



REPUBLIQUE ALGERIENNE DEMOCRATIQUE ET POPULAIRE
MINISTRE DE L'ENSEIGNEMENT SUPERIEUR ET DE LA RECHERCHE SCIENTIFIQUE

UNIVERSITE ABOU-BEKR BELKAID De TLEMCEN

THÈSE

Présentée à :

FACULTE DES SCIENCES – DEPARTEMENT DE PHYSIQUE

Pour l'obtention du diplôme de :

DOCTORAT EN SCIENCES

Spécialité: Physico-Chimie des matériaux

Par :

Mr GUEDDOUH Ahmed

sur le thème

Calcul ab-initio des propriétés physiques de quelques borures de métaux de transitions

Soutenue publiquement le 06 juillet 2017 à Tlemcen devant le jury composé de :

Mr. Benmansour Abdelhalim	Professeur	Université de Tlemcen	Président
Mr. Bentria Bachir	Professeur	Université de Laghouat	Directeur de thèse
Mr. Chikhaoui Abdelhak	Maître de Conférences A	Université de Tlemcen	Examineur
Mr. Cheknane Ali	Professeur	Université de Laghouat	Examineur
Mr. Ouahrani Tarik	Maître de Conférences A	EPST de Tlemcen	Examineur
Mr. Merad Abdelkrim	Professeur	Université de Tlemcen	Examineur

Laboratoire de Physique des Matériaux(LPM)
BP37G, Laghouat 03000, Algerie



DEMOCRATIC AND PEOPLE'S REPUBLIC OF ALGERIA
MINISTRY OF HIGHER EDUCATION AND SCIENTIFIC RESEARCH

UNIVERSITY ABOU-BEKR BELKAID – TLEMCEEN

THESIS

Presented at:

FACULTY OF SCIENCE - DEPARTMENT OF PHYSICS

To obtain the diploma of:

DOCTORATE IN SCIENCE

Speciality: Physical Chemistry of Materials

By:

Mr GUEDDOUH Ahmed

on the subject

**Ab-initio calculation of the physical properties
of some transition metal borides.**

Publicly defended on on July 6, 2017 In Tlemcen before the jury consisting of:

Mr Benmansour Abdelhalim	Professor	University of Tlemcen	President
Mr Bentria Bachir	Professor	University of Laghouat	Thesis supervisor
Mr Chikhaoui Abdelhak	Lecturer	University of Tlemcen	Examiner
Mr Cheknane Ali	Professor	University of Laghouat	Examiner
Mr Ouahrani Tarik	Associate Professor	EPST of Tlemcen	Examiner
Mr Merad Abdelkrim	Professor	University of Tlemcen	Examiner

Laboratory of Physics of Materials (LPM)
BP37G, Laghouat 03000, Algeria

Dedication

This thesis is dedicated

To my parents,

To my wife Aicha,

To my son Ayoub,

To my daughters Imane, Kaouthar, Bouchra and Hiba,

To my brothers and sisters,

To my friends and colleagues,

To all my teachers in my life.

Acknowledgments

First of all, I thank Allah Almighty for the immense blessings and help provided to me for writing this thesis and also His assistance throughout my life.

This thesis could not have been written without the help of Allah and the support of many people who have contributed by many different ways.

First of all, I would like to thank Prof. Bachir Bentría, Professor at University, Amar Telidji of Laghouat, my supervisor most sincerely for his support, his patience and the new ideas he put in this thesis. Thanks again, dear Bachir for allowing me to travel in Czech Republic where I met Prof. Mojmír Šob, professor at the Institute of Physics of Material (IPM) and Masaryk University, Brno (Czech Republic), Faculty of Science, Department of Chemistry, whom I have benefited of him by the fruitful discussions and their support for me. Furthermore, my thanks also go to Prof. Lefkeir Ibn Khaldoun, director of the Laboratory of physics of Materials (LPM), which make me more cheerful when I meet him.

I express my sincere thanks to Mr. Benmansour Abdelhalim, Professor at the University of Tlemcen, for agreeing to chair the jury of this thesis.

I also thank all jury members, namely: Mr. Chikhaoui Abdelhak, lecturer at the University of Tlemcen, Mr. Cheknane Ali, Professor at the University of Laghouat, Mr. Ouahrani Tarik, lecturer at EPST of Tlemcen and Mr. Merad Abdelkrim, Professor at the University of Tlemcen, for reviewing this doctoral thesis.

I would like to extend my gratitude to the scientific Committee of faculty of science and through them the staff in Department of physics at the reception, and the facility in the registry for every academic year.

I would also like to thank my colleagues at the LPM, who always spared some of their time for discussion with me. Special thanks go to Lagoun Brahim, Dahame Tahar and Benghia Ali.

I should address most special acknowledgements to my parents and particularly my wife for her patience and whose support is indispensable to me.

I apologize to my children for my preoccupation sometimes and take part of their time.

Table Of Content

Dedication.....	i
Acknowledgments	ii
List Of Figures.....	x
List Of Tables	xiii
CHAPTER 1: General introduction.....	1
1. Introduction	2
1.1. General context and objective	2
1.2. Thesis structure.....	5
CHAPTER 2: Borides	6
2. Borides.....	7
2.1. Crystallographic structure of semi-borides TM_2B compounds	9
2.2. Crystallographic structure of mono-borides TMB compounds.....	11
2.3. Boriding	15
2.4. Types of boriding	15
2.4.1. Pack boriding.....	15
2.4.2. Past boriding.....	16
2.4.3. Liquid boriding.....	16
2.4.4. Plasma boriding	17
2.4.5. Gas boriding	17
2.5. Borided layer characteristics	17
2.6. Advantages and disadvantages of boriding	20
2.7. Industrial application	21
CHAPTER 3: Theoretical frame work, Concept and formalism.....	22
3. Theoretical Framework, Concept and Formalism	23
3.1. Theoretical framework	23
3.1.1. Density Functional Theory	25
3.1.2. The Hohenberg-Kohn (HK) Theorems.....	26
3.1.3. The Kohn-Sham equations	27
3.1.4. Magnetism in the Density Functional Theory	29
3.1.5. Approximations	29
3.1.5.1. Local Density Approximations (LDA).....	29

3.1.5.2. Generalized-Gradient Approximation (GGA).....	30
3.1.6. Pseudo-potential	31
3.2. Concept and formalism.....	32
3.2.1. Magnetism in materials	32
3.2.1.1. Localized moments in solids	33
3.2.1.2. Itinerant-electron magnetism.....	35
3.2.2. Abrupt phase transitions	38
3.2.2.1. Phase transition.....	38
3.2.2.2. Quantum Phase Transitions	40
3.2.3. Equation Of State Calculation	43
3.2.4. Population analysis	44
3.2.5. Hardness	44
3.2.6. Elastic properties	48
3.2.6.1. Relationship stress-strain.....	49
3.2.6.2. Elastic constants and stability criteria under pressure	52
3.2.6.3. Polycrystalline elastic modulus	53
3.2.7. Elastic anisotropy	54
3.2.8. Acoustic sound velocities and Debye temperatures	56
3.2.9. Disorder In Solids.....	58
3.2.9.1. Disorder and first principles calculations	59
3.3. Conclusions	60
CHAPTER 4: Semi-Borides TM_2B (TM=Fe, Co, Ni) Under Pressure.....	62
4. Structure, magnetic, hardness and anisotropic elastic properties of boride coating TM_2B (TM=Fe, Co, Ni) under pressure.	63
4.1. Structure aspects and calculation methods	64
4.1.1. Structural properties and stability.....	66
4.1.2. Pressure effects.	69
4.1.3. Hardness	75
4.1.4. Elastic properties under pressure.....	76
4.1.5. Elastic anisotropy	80
4.1.6. Acoustic sound velocities and Debye temperatures	88
4.2. Conclusions	90

CHAPTER 5: Mono-Borides TMB (TM = Mn, Fe, Co) Under Pressure.....	92
5. Hardness and anisotropic elastic properties of mono-boride.....	93
TMB (TM=Mn, Fe, Co) under pressure. A first-principles study.	93
5.1. Structure aspects and calculation methods	94
5.1.1. Structural properties and stability.....	96
5.1.2. Effect of pressure and magnetic moment on the structural properties.	99
5.1.3. Density of states and bond structure under pressure	102
5.1.4. Hardness	106
5.1.5. Elastic properties under pressure.....	107
5.1.6. Elastic anisotropy	112
5.1.7. Acoustic sound velocities and Debye temperature.....	119
5.2. Conclusions	120
CHAPTER 6: Physical properties of solid solution	122
of $Fe_{(1-x)}Mn_xB$	122
6. Ab initio calculations of structural, magnetic and anisotropic elastic properties of $Fe_{(1-x)}Mn_xB$	123
6.1. Method of calculation.....	124
6.1.1. Structural properties and stability.....	125
6.1.2. Density Of States	129
6.1.3. Elastic properties	131
6.1.4. Elastic anisotropy	135
6.1.5. Acoustic sound velocities and Deby temperature.....	141
6.2. Conclusions	142
7. General conclusions and outlook.....	145
Annex	148
I. CASTEP: Description and calculation principle	149
I.1. Presentation of the CASTEP package	149
I.2. SCF Electronic minimization technique in CASTEP.....	150
I.3. Geometry optimization with castep.....	151
I.4. Band structure and state density	152
I.4.1. Electronic band structure	152
I.4.2. Density of electronic states.....	153
I.5. Method of calculating elastic constants.....	153
I.6. Spin polarization.....	154
Bibliography	155
Scientific Publications	
Abstract:	

List Of Abbreviations

HS	High Spin
LS	Low Spin
QPT	Quantum Phase Transitions
GPa	Giga Pascal
DFT	Density Functional Theory
GGA	Generalized Gradient Approximation
VCA	Virtual Crystal Approximation
TM	Transition Metal
PP-LAPW	Pseudo Potential Linearized Augmented Plane Wave
CASTEP	Cambridge Serial Total Energy Package
PBE	Perdew-Burke Ernzerhof
C_{ij}	Elastic Constants
Mn, Fe, Co, Ni	Manganese, Iron, Cobalt, Nickel
LSDA	Local Spin Density Approximation
\hat{H}	the Hamiltonian
\hat{T}_N	kinetic energy of nuclei
\hat{T}_e	kinetic energy of electrons
BOA	Born-Oppenheimer Approximation
ψ	wave function
$V_{\text{ext}}(\mathbf{r})$	Static external potential
HK	Hohenberg-Kohn
$n(\mathbf{r})$	Density
KS	Kohn and Sham
LDA	Local Density Approximations.
T_C	<i>Curie</i> temperature
FM	Ferromagnetic
$N(E_F)$	Density Of States at the Fermi level
B	Bulk modulus of a material

EOS	Equation Of State
MPA	Mulliken Population Analysis
LCAO	Linear Combined Atomic Orbitals
σ_{ij}	Stress Tensor
ε_{ij}	Strain Tensor
\tilde{C}_{ij}	Elastic Constants under pressure
VRH	Voigt-Reuss-Hill
G	Shear modulus
E	Young modulus
ν	Poisson ratio
A_G	shear anisotropic factor
A_B	Bulk anisotropic factor
A_U	Universal anisotropic factor
S_{ij}	Compliance Matrix
l_1, l_2 and l_3	The direction cosines
Θ_D	Debye temperature
V_l	longitudinal velocity
ν_t	transverse sound velocity
BFGS	Broydene-Fletchere-Goldarbe-Shanno
3D	Three dimensional
E_{coh}	Cohesive energy
E_f	Formation energy
E_{iso}	Isolate energy
μ_B	Bohr magneton
E_{total}	Total cell energy
DOS	Density of state

USP	Ultra soft pseudo potentiel
H^u	Hardness of u type bond
N^u	Nearest-neighbor for different pairs of atoms
d^u	Average bond length of nearest-neighbor atoms
SG	Space groupe

List Of Figures

Figure 1. Saturation magnetization based on the average atomic number:	9
Figure 2. Crystal structure of TM_2B projecting onto the (100), (010) and (001) planes and the metal transition, boron atoms environment.	10
Figure 3. Crystal structure of TMB projecting onto the (100), (010) and (001) planes, the metal transition; boron atoms environment and for a section perpendicular to the plane (010) showing the zigzag B-B chain.....	13
Figure 4. Periodic table of the elements, transition metals are shown in light Green and the transition metals which are included in this study are represented by Yellow color	14
Figure 5. The pack-powder boriding treatment.	16
Figure 6. The image of AISI 304 specimen surface before and after boriding.	18
Figure 7. SEM images of the cross-sections of low-carbon microalloyed steels boronized for 4 h at: a) 973 K, b) 1073 K, c) 1173 K, and d) 1273 K	19
Figure 8: Boride layers thickness and Microhardness profiles.	20
Figure 9. Schematic illustration of pseudo-potential. Comparison of a wave function in the Coulomb potential of the nucleus (blue) to the one in the pseudo-potential (red). The real and the pseudo wave function and potentials match above a certain cutoff radius r_c	31
Figure 10. Schematic illustrations of possible coupling mechanisms between localized magnetic moments: (a) direct exchange between neighboring atoms, (b) superexchange mediated by non-magnetic ions, and (c) indirect exchange mediated by the conduction electrons.	35
Figure 11 a) the Stoner parameter, b) the density of states at Fermi level,	37
Figure 12. Qualitative illustration of first order (1) and second order (2) transitions of the magnetic moment (m) under pressures, and their corresponding free energy (E), respectively, adapted from Pfleiderer	42
Figure 13. Hardness-resistance to penetration of a hard indenter.	46
Figure 14. Schematics of indenter tips	46

Figure 15. Loads in the range of 10 to 300 mN were applied to the “pure” zone of the FeB layer at a distance of 10 μm from the surface.	47
Figure 16 Origin of linear elasticity	49
Figure 17. The crystal structure of TM_2B illustrated by ball and stick model.	65
Figure 18 Pressure dependence of of magnetic moment and the normalized volume V/V_0 for Fe_2B and Co_2B	69
Figure 19 Pressure dependence of structure parameters and elastic constants for Fe_2B	71
Figure 20. Pressure dependence of structure parameters and elastic constants for Co_2B	72
Figure 21 The calculated total and partial DOS of TM_2B , Left panel with spin polarization	74
Figure 22. Pressure dependence on the elastic constants	78
Figure 23. The calculated percentage change of parameters by the top: volume, cohesive and formation energy, hardness, bulk, Young and shear modulus.	82
Figure 24. Illustration of directional dependent Young’s modulus of TM_2B compounds: Left panel with 0 GPa pressure and right panel under pressure.	84
Figure 25. Illustration of directional dependent bulk modulus of TM_2B compounds: Left panel with 0 GPa pressure and right panel under pressure.	85
Figure 26. Illustration of directional dependent torsion modulus of TM_2B compounds: Left panel with 0 GPa pressure and right panel under pressure.	86
Figure 27. The projection of Young, bulk and torsion moduli at 0 GPa and under pressure for different crystal planes for TM_2B compounds.	88
Figure 28. The crystal structure of TMB illustrated by ball and stick model.	95
Figure 29 Dependance of magnetic moment vs pressure.	99
Figure 30 Pressure dependence of total energy, Volume and lattice parameters of: MnB (left panel) and FeB (right panel). Dashed line represents the critical pressures.	101
Figure 31. The calculated total and partial DOS of TMB at 0 GPa and a critical pressure. Dashed line represents the Fermi level.	103
Figure 32. The calculated band structures for FeB compound near Fermi level.	105
Figure 33. Pressure dependence on the elastic constants.	109

Figure 34. The calculated relative change of parameters by the top: volume cohesive and formation energy, hardness, bulk, Young and shear modulus Poisson ratio and Debye temperature.....	113
Figure 35. Illustration of directional dependent Young's modulus of TMB compounds: With 0 GPa pressure and critical pressure.	115
Figure 36. Illustration of directional dependent bulk modulus of TMB compounds:.....	116
Figure 37. The projection of Young moduli at several different.....	117
Figure 38. The projection of bulk moduli at several	118
Figure 39. The calculated total magnetic moment, cohesive and formation energies.....	128
Figure 40. The calculated lattice parameter and bulk modulus as a function Mn content(x).....	128
Figure 41. The calculated total and partial DOS of $(Fe_{1-x}Mn_x)B$	130
Figure 42. Illustration of elastic constant's as a function of Mn content of $(Fe_{1-x}Mn_x)B$ compounds.	133
Figure 43 Illustration of directional dependent Young's modulus of $(Fe_{1-x}Mn_x)B$ compounds: With 0 GPa pressure critical pressure.	137
Figure 44. Illustration of directional dependent bulk modulus of $(Fe_{1-x}Mn_x)B$ compounds.....	138
Figure 45. The projection of Young modul at 0 GPa for different crystal planes for $Fe_{1-x}Mn_xB$ compounds.....	139
Figure 46. The projection of Bulk modul at 0 GPa for different crystal planes for $Fe_{1-x}Mn_xB$ compounds.....	140

List Of Tables

Table 1. Crystallographic parameters for the tetragonal transition-metal semi-borides. TM-TM, TM-B and B-B are the distances between neighbouring atoms in Å; V (Å ³) is the volume(per formula unit).....	11
Table 2. Crystallographic parameters for the orthorhombic transition-metal mono-borides.	12
Table 3. Fe and boron atoms environment in FeB compound	12
Table 4. The number of independent elastic constants for different crystalline structure with their point group.	50
Table 5. The calculated ground state properties of pure elements, Fe, Co, Ni and B with experimental and other theoretical works.....	67
Table 6. The calculated ground state properties of TM ₂ B. Experimental and theoretical values are listed in parentheses. Total cell energy E_{total} (eV/f.u.), cell parameters (a , b , c in Å), fractional coordinates of TM and B atoms(x , y and z), volume V (Å ³), Bulk modulus (GPa), magnetic moment (μ_B /atom), cohesive energy E_{coh} (eV/f.u.), formation energy E_f (eV/f.u).	68
Table 7. The predicted hardness of TM ₂ B. Experimental and theoretical values are listed in parentheses. Different pairs of atoms (B–B, TM–B). Average bond length of nearest-neighbor atoms d^u (Å), average overlap population of u type bond, nearest-neighbor numbers N^u for different pairs of atoms, cell volume Ω (Å ³), volume of a bond of u type v^u , hardness of u type bond H^u (GPa) and hardness H (GPa).	76
Table 8. The calculated full set elastic constants of TM ₂ B (under 0 and a critical pressure, in GPa) with other theoretical works.....	78
Table 9. The calculated bulk, Young (E) and shear modulus (G) (under 0 and critical pressure, in GPa), Poisson’s ratio (ν), B/G ratio and the relative change (in %) for TM ₂ B compounds.....	79
Table 10. Polycrystalline elastic properties and Anisotropic factors of TM ₂ B compounds.....	81

Table 11. The calculated bulk, Young (E) and shear modulus (G) (under 0 and critical pressure, in GPa), Poisson's ratio (ν), B/G ratio and the relative change (in %) for TM_2B compounds.....	81
Table 12. The density (in g/cm^3), anisotropic sound velocities (in m/s), average sound velocity (in m/s), Debye temperature (in K) and relative change (in %) for the TM_2B compounds.....	89
Table 13. The calculated ground state properties of pure elements, Mn, Fe, Co, Ni and B. Experimental and theoretical (eV/f.u.), cohesive energy E_{coh} (eV/f.u.) and volume V (\AA^3).....	97
Table 14. The calculated ground state properties of TMB. Experimental and theoretical values are listed in parentheses. Total cell energy E_{total} (eV/f.u.), cell parameters (a, b, c in \AA), atomic positions for TM and B atoms (fractional coordinates), volume V (\AA^3), Bulk modulus (GPa), magnetic moment (μ_B/atom), cohesive energy E_{coh} (eV/f.u.), formation energy E_f (eV/f.u).	98
Table 15. The predicted hardness of TMB. Experimental and theoretical values are listed in parentheses. Different pairs of atoms (B–B, TM–B). Average bond length of nearest-neighbor atoms $d^u(\text{\AA}^\circ)$, average overlap population of u type bond, nearest-neighbor numbers N^u for different pairs of atoms, cell volume Ω (\AA^3), volume of a bond of u type $\nu\nu u$, hardness of u type bond H^u (GPa) and hardness H (GPa).	107
Table 16. The calculated full set elastic constants of TMB (under 0 and critical pressure, in GPa) along with other available values.....	108
Table 17. Polycrystalline elastic properties and Anisotropic factors of TM-B system.....	110
Table 18. The calculated bulk, Young (E) and shear modulus (G) of TM_2B (under 0 and critical pressure, in GPa), Poisson's ratio (ν) and B/G ratio along with other available values.....	111
Table 19. The density (in g/cm^3), anisotropic sound velocities (in m/s), average sound velocity (in m/s) and Debye temperature (in K) for the TM_2B compounds.....	120
Table 20. The calculated ground state properties of $(\text{Fe}_{1-x}\text{Mn}_x)\text{B}$. Experimental values are listed in parentheses. Total cell energy E_{total} (eV/f.u.), cell parameters (a, b, c in \AA) volume V (\AA^3), Bulk modulus (GPa), magnetic moment (MM in μ_B), cohesive energy E_{coh} (eV/f.u.) and formation energy E_f (eV/f.u).....	127

Table 21. The stability of the $(\text{Fe}_{1-x}\text{Mn}_x)\text{B}$ mono-borides according to Stoner model.	131
Table 22. The calculated full set elastic constants of $(\text{Fe}_{1-x}\text{Mn}_x)\text{B}$ along with other available values.....	132
Table 23. Polycrystalline elastic properties and Anisotropic factors of $\text{Fe}_{1-x}\text{Mn}_x\text{B}$ compounds.....	134
Table 24. The calculated bulk, Young (E) and shear modulus (G) of $\text{Fe}_{1-x}\text{Mn}_x\text{B}$ (in GPa), Poisson's ratio (ν) and B/G ratio along with other available values.	135
Table 25. The density (in g/cm^3), anisotropic sound velocities (in m/s), average sound velocity (in m/s) and Debye temperature (in K) for the $(\text{Fe}_{1-x}\text{Mn}_x)\text{B}$ compounds.	142

CHAPTER 1: General introduction

1. Introduction

1.1. General context and objective

Materials are crucial in the development of civilization and the improvement of human life. As an example of these materials: boride layers, which offer excellent surface properties in terms of high hardness, increase the wear and corrosion resistance and stability of mechanical properties at high temperature [1-4]. The transition metal borides are important due to their considerable practical importance and fundamental interest in science, technology and industrial applications [5-8]. Iron borides (Fe_2B and FeB) in particular are widely used as hard and protective coatings on steel surfaces for improved wear and corrosion resistance to the material [9, 10]. The coating is produced via the process of boriding, also called boronizing, which includes the deposition of boron and an additional heat treatment, for example, in the form of a thermochemical process [9] to form the borides. Boronizing results are provided by the powder-pack boronizing using Ekabor Ni powder, specially prepared for Ni-based alloys [11, 12]. The layers, produced on nickel, are characterized by a high hardness (about 18 GPa) and thickness of 100 μm [11]. Cobalt boride (CoB and Co_2B) coatings are developed on the surface of a CoCrMo alloy using the powder-pack boriding process at temperatures between 1223 and 1273 K using different exposure times for each temperature [13]. Furthermore, magnetism of some borides plays a crucial role for the development of memories for mass storage, and in sensors to name a few; spintronics is an integration of the magnetic materials, to realize nanosized devices with better features.

Transition metal borides have large outstanding physical properties. The combination of metals with slight covalent-bond forming atoms like B often leads to materials, it does not have

only a high melting point, but also has a very low compressibility and high hardness compared with the pure metal [14]. In addition, transition metal borides possess other properties, such as good electrical-thermal conductivity, catalytic activity, and magnetic properties [15-19]. They are widely used for cutting tools and hard coatings [20, 21].

In recent decades, interest in borides increased, as well as, many useful applications have been found in nanomaterial science. It is well demonstrated that reverse micelles are good candidates for the production of nanoparticles [22], where nano size cobalt boride particles are prepared [23]. Nanocrystalline nickel boride powders are successfully prepared by ball milling of the elemental components in Ref. [24]. Feng *et al.* [25] prepared the nanocrystalline Ni₂B via a solvo-thermal method and Shi *et al.* [26] used an electro less deposition technique to synthesize nanocrystalline Ni–B coating, Ni₂B and Ni₃B are formed in layers during heat treatment. The manganese mono-boride is important due to potential spintronic applications [27]. The reported experimental magnetic moments give values of 1.83 μ_B for MnB, 1.12 μ_B for FeB, and 0 μ_B for CoB [28].

Experiments under pressure provide a unique tool to characterize materials; high pressure has the advantage that the chemical bonding can be modified without changing the composition. Specifically, chemical substitution introduces disorder and local strain in the atomic lattice, while external pressure preserves the lattice homogeneity [29]. Furthermore, the presence and nature of unconventional magnetic phases of semi-borides (Fe₂B and Co₂B), and mono-borides (FeB and MnB) may be clarified by tuning them systematically with the help of an external parameter such as pressure, which will provide much information of structures concerning behavior under pressure. For example, magnetic collapse, either being a transition from ferromagnetic state to paramagnetic state, or from high spin (HS) state to low spin (LS) state, under pressure, is a widely observed phenomenon, and it is very interesting to study it. This character of magnetic

collapse is perhaps the earliest prediction of what may be called a ‘novel’ phase of magnetic metals near a quantum phase transition (QPT) has been magnetically mediated superconductivity. The emergence of superconductivity in the ferromagnetic state in the presence of strong first order QPT may be reconciled in a model proposed by Sandeman *et al.* [30].

Modern experiments can reach hydrostatic pressure beyond 200 GPa [31]. The pressure changes at least the inter-atomic interaction. The itinerancy of the electrons will be changed accordingly. The improving experimental facilities enable us to extend our theoretical work to high pressures, to understand, and predict new phenomena. The main phenomenon I am going to address is the quantum magnetic phase transition at high pressures and the related effect on structure, magnetic, hardness and anisotropic elastic properties on the boride coating (semi and mono borides). These borides are isomorphic, i.e. it preserves the symmetry of both the lattice and the atomic sites.

Many experimental techniques have been developed to measure and discover new properties of materials such as X-rays [32], infrared spectroscopy [33], Berkovich Nano indentation[34]...etc. On the other hand, understanding of how materials behave like they do and why they differ in properties is possible with the electronic states understanding allowed by quantum mechanics. Electronic state of materials is fundamental to understand their macroscopic properties, such as thermal, electrical conductivity, structure, etc., people use a variety of quantum methods to predict these electronic states and, hence, material properties at the most fundamental level.

Quantum methods allow us to study transition states and unusual structures and conformations, which are difficult, if not impossible, to study experimentally. Ab initio methods are based entirely on quantum mechanics and basic physical constants. Other methods are called empirical or semi-empirical because they employ additional empirical parameters. Density functional theory (DFT) is among the most popular and useful Ab initio methods available in

condensed-matter physics. DFT was put on a safe theoretical stability by the two Hohenberg-Kohn theorems [35].

In order to show the effects of pressure on the structural, electronic, magnetic, hardness, anisotropic elastic and Debye temperature properties, I examined these structural properties at 0 GPa and under pressure within GGA for the transition metal mono and semi-borides: TMB (TM= Mn, Fe, Co and Ni) and TM_2B (TM= Fe, Co and Ni) compounds, Furthermore, the Fe-Mn-B systems are studied by calculate the ferromagnetic variation of transition metal mono boride by the method of virtual crystal approximation (VCA), based on density-functional theory (DFT) with generalized gradient approximation (GGA). The variations of ferromagnetism of $Fe_{1-x}Mn_xB$ alloys by the first-principle spin-polarized calculations are in agreement with the experimental results. All calculations are performed using the pseudo potential linearized augmented plane wave (PP-LAPW) method, which is implemented in the CASTEP software [36]. The results are compared with experimental and other theoretical results in the litterature.

1.2. Thesis structure

This thesis is divided into six Chapters. Following this introductory part (chapter 1), is Chapter 2, where I will present the crystallographic structure of borides, the different types of boriding, the physical characteristics of boride layers and industrial applications. Chapter 3 is dedicated to the basic concepts of density functional theory (DFT) and introduced the concept and formalism of calculations used at the present work. Chapter 4 presents the results of our calculations for semi-borides TM_2B . Chapter 5 is dedicated to our calculations results for mono-borides TMB. Chapter 6 shows the results of calculations for Fe-Mn-B system. I close my thesis, with a general conclusions and some perspectives.

CHAPTER 2: Borides

2. Borides

Borides, carbides and nitrides are interesting class of compounds because they have a unique combination of different properties such as electronic, optical, elastic thermal and magnetic properties. They might be characterized by the following properties: metallic to insulating or superconducting, absorption/emission bands from UV (ultraviolet) to the visible, NIR (near infrared) region, low to high thermal conductivity, negative to positive thermal expansion, paramagnetic to ferromagnetic and soft to extreme hardness. In addition, they have high chemical and thermal stability [37]. Particularly, transition metal borides usually have good properties of large hardness, high melting point, and good wear resistance. They are widely used for coating and cutting tools. Since defects presented by metal alloys, such as corrosion, wear and contact fatigue, several studies have been conducted to improve the surface properties of these alloys. So surface treatments such as Boriding, Nitriding, Carburizing and Carbonitriding are applied to meet these requirements on an industrial scale.

Borides are classified as boron-rich or metal-rich. Borides which are formed with a metal to boron ratio equal or higher than four are in the class of metal-rich borides and borides with metal to boron ratio less than four are called as boron-rich borides.

Several of the metal borides are ferromagnetic and in many ways their magnetic behavior resembles those of the transition series metals. Transition metals and boron form a large number of intermetallic compounds with chemical formulas TM_2B , TMB , TMB_2 , TMB_4 , TMB_6 , TMB_{12} [38]. These materials are known in many industrial areas as; superhard materials, electronic devices, and the discovery of superconductivity in MgB_2 at 39K [39] has reinforced the importance of borides. These properties make them as a potential candidate for several applications.

The mono-borides occur with three structures: the orthorhombic CrB (B_f) and FeB (B_{27}) and the tetragonal MoB type. The semi-borides have the tetragonal CuAl_2 structure (C_{16}).

The mono-borides from (Cr, Mn)B to CoB and the half-borides from (Mn, Fe) $_2$ B to (Co, Ni) $_2$ B and are ferromagnetic (Figure 1), and have a magnetization versus composition curve analogous to the Slater-Pauling magnetization curve for the transition metals (Figure 1))[40].

In this chapter I present the crystal structure of the transition-metal semi-borides, mono-borides, and different types of boriding such as pack boriding, past boriding, liquid boriding, plasma boriding, gas boriding. I also present the characteristics of borided layers such as color, thickness, hardness. Then, I will show some advantages and disadvantages of boriding. Finally, I present some industrial applications of borided components.

In this study, I treated two sets of borides of elements of the first transition series, which are mainly magnetic: the mono-borides TMB (TM = Mn, Fe, Co, Ni) and semi-borides TM_2B (TM=Fe, Co, Ni) (Figure 1).

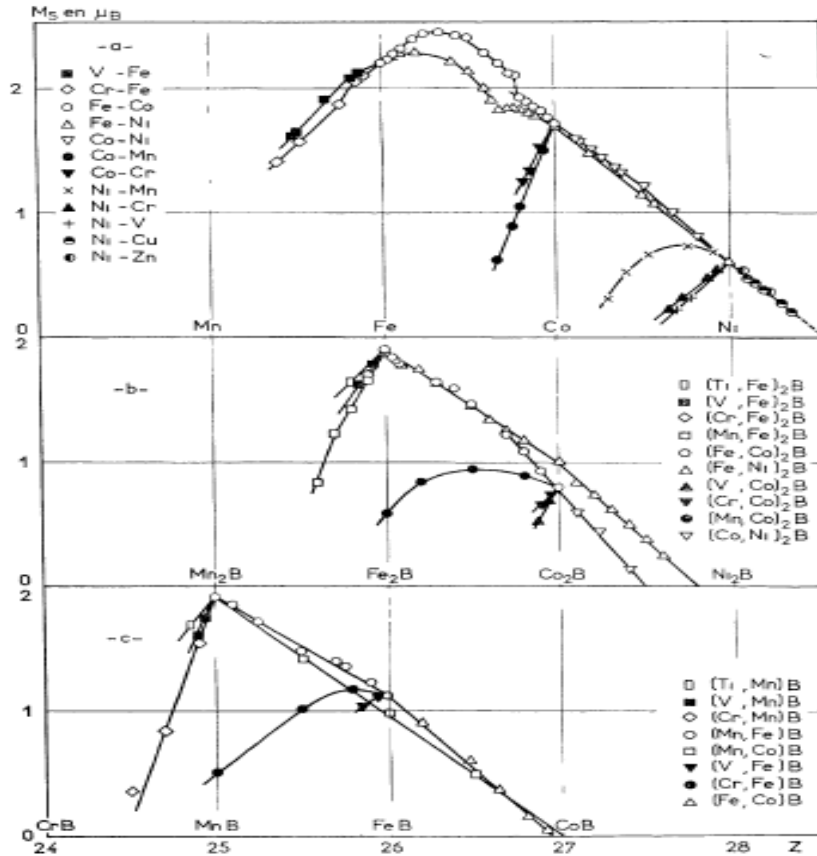


Figure 1. Saturation magnetization based on the average atomic number:
 a) The Slater-Pauling curve (alloys); b) semi borides; c) mono-borides [40].

2.1. Crystallographic structure of semi-borides TM_2B compounds

The crystal structure of the transition-metal semi-borides described in this chapter is isomorphous to the Al_2Cu structure; space group $14/mcm$. The tetragonal unit cell contains four molecular units. The atoms are found in the following special positions in the space group specified as:

B	0,0,1/4	0,0,3/4
TM	u, u+1/2,0	-u, 1/2 - u,0
	u+1/2,-u, 0	1/2 - u, u, ,0

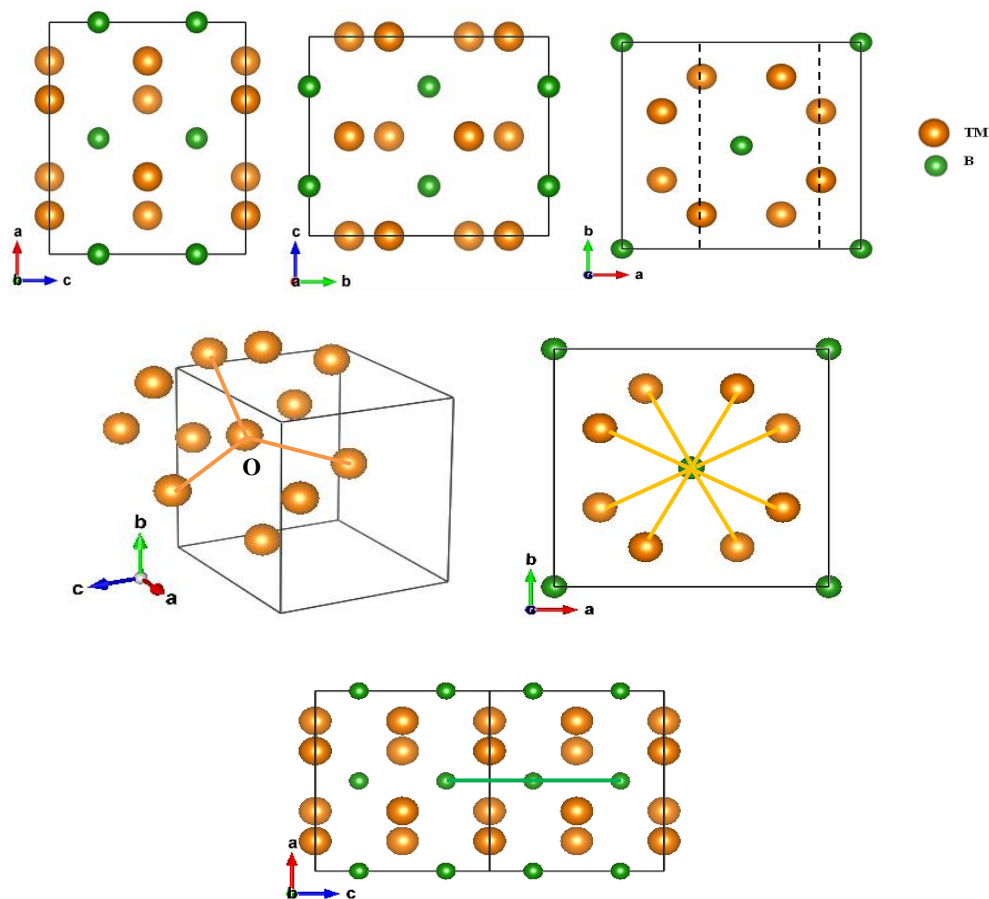


Figure 2. Crystal structure of TM_2B projecting onto the (100), (010) and (001) planes and the metal transition, boron atoms environment.

As the symmetry of the crystal structure is basically tetragonal body centered, the remaining six atom positions can be calculated by adding $(1/2, 1/2, 1/2)$. For all compounds investigated, $u = 1/6$.

Figure 2 shows a projected view of the $A1_2Cu$ structure along (by the left) b, a, and c axes.

The boron atoms (small green balls) form a quadratic lattice (view along the c axis), which is repeated with a periodicity at $0, 0, 1/2$. The metal transition atoms (large orange balls) form two layers:

One at 0, 0, 1/4. (Dashed line) and one of 0, 0, 3/4. Each boron atom is therefore surrounded by eight transition metal atoms which are about 2.14 Å, apart, and two boron atoms at a distance of about 2.145 Å. Each transition-metal atom has 11 transition-metal neighbours: three at 2.4 Å, eight at 2.65 Å, and four boron atoms at 2.2 Å.

Table 1 gives the crystallographic data for TM₂B compounds investigated.

Table 1. Crystallographic parameters for the tetragonal transition-metal semi-borides. TM-TM, TM-B and B-B are the distances between neighbouring atoms in Å; V (Å³) is the volume(per formula unit).

Compound	a	c	c/a	TM-TM	TM-B	B-B	V
Fe ₂ B	5.109	4.249	0.83	2.44	2.18	2.12	27.73
Co ₂ B	5.016	4.220	0.84	2.42	2.15	2.11	26.54
Ni ₂ B	4.990	4.245	0.85	2.43	2.14	2.12	26.43

2.2. Crystallographic structure of mono-borides TMB compounds

The structure of TMB, belongs to the orthorhombic lattice, B27 type, with space group Pnma(N° 62) and the structure contains four formula units per cell with atoms in the positions (Table 3). Figure 3. Illustrates the dispositions and separations of nearest neighbours in the structure, which is composed of layers at y(b axis) = 1/4, 3/4 containing TM and boron atoms.

Table 2. Crystallographic parameters for the orthorhombic transition-metal mono-borides.

Compound	a (Å)	b (Å)	c (Å)
MnB	5.560 ^c	2.977 ^c	4.145 ^c
	5.560 ^d	2.977 ^d	4.151 ^d
	5.560 ^e	2.976 ^e	4.147 ^e
Fe B	5.505 ^a	2.952 ^a	4.059 ^a
	5.495 ^c	2.946 ^c	4.053 ^c
	5.506 ^d	2.952 ^d	4.081 ^d
CoB	5.254 ^b	3.314 ^b	3.956 ^b
	5.253 ^c	3.043 ^c	3.956 ^c
NiB			

^aRef.[41], ^bRef. [42], ^cRef. [16], ^dRef. [43], ^eRef. [44].

Table 3. Fe and boron atoms environment in FeB compound [41].

Atoms	Number	Distance	Atoms	Number	Distance
				2	2,171
TM-TM	2	2,628	TM-B	1	2,184
	4	2,636		1	2,196
TM-B	1	2,157	B-B	2	1,783
	2	2,167			

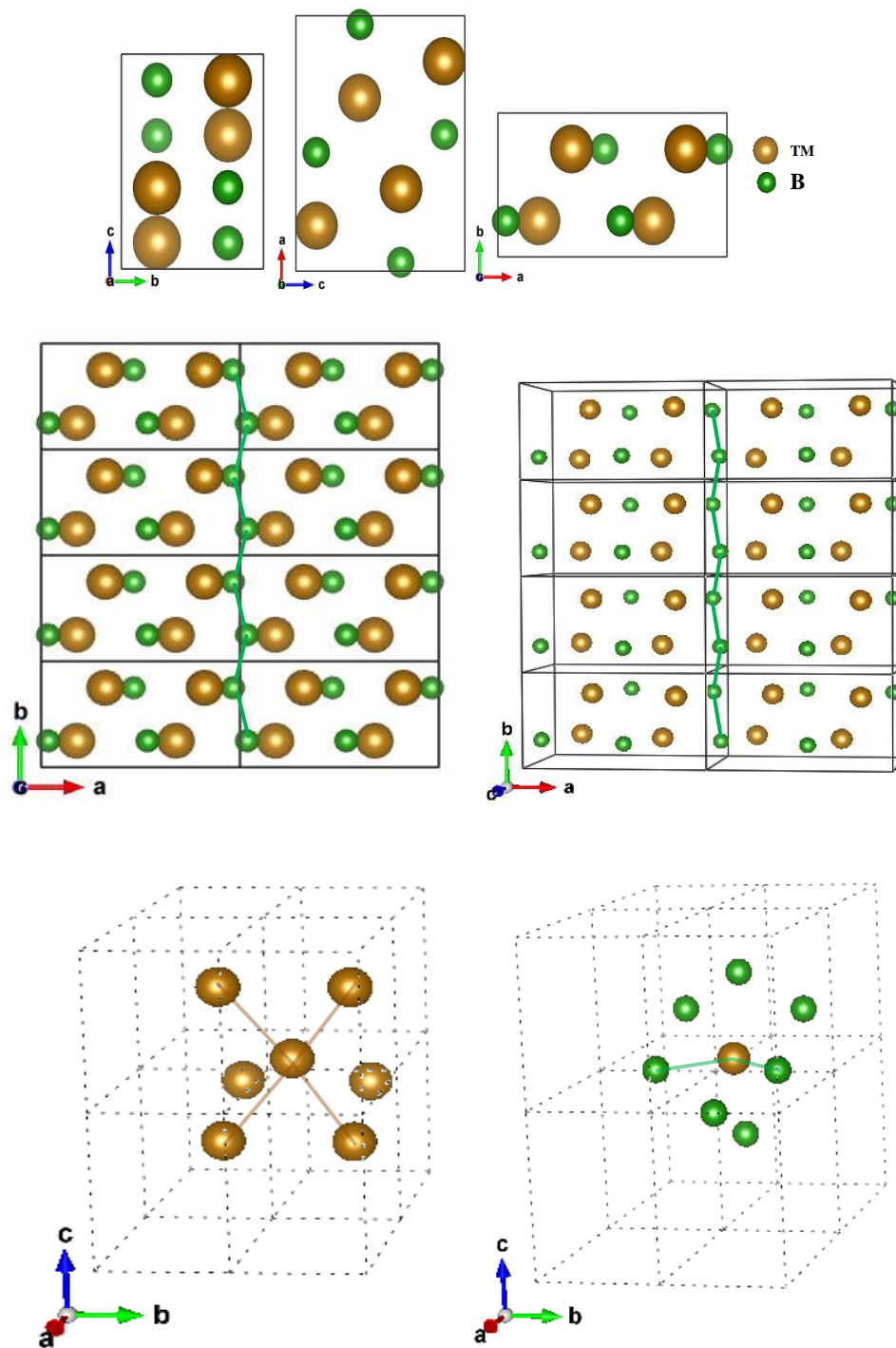


Figure 3. Crystal structure of TMB projecting onto the (100), (010) and (001) planes, the metal transition; boron atoms environment and for a section perpendicular to the plane (010) showing the zigzag B-B chain.

According to the crystal structure of TMB, B atoms form zigzag chains are in the interstices surrounded by TM atoms, and the distance between two B atoms is 3.36Å, and the interaction between B atoms is slightly strong. The strong interaction between B atoms causes a 2s-p hybridization and leads to strong covalent bonds. It is clearly shown that there exists an even stronger bond (zigzag chains) between the two B atoms. It is this strong covalent bond which makes the B atoms form linear zigzag chains in FeB.

Periodic Table of the Elements

Key:																	
element name	atomic number	symbol	atomic weight														
hydrogen 1 H 1.00794	beryllium 4 Be 9.012182	boron 5 B 10.811	carbon 6 C 12.0107	nitrogen 7 N 14.00674	oxygen 8 O 15.9994	fluorine 9 F 18.9984	neon 10 Ne 20.1797	lithium 3 Li 6.941	beryllium 4 Be 9.012182	boron 5 B 10.811	carbon 6 C 12.0107	nitrogen 7 N 14.00674	oxygen 8 O 15.9994	fluorine 9 F 18.9984	neon 10 Ne 20.1797		
sodium 11 Na 22.98977	magnesium 12 Mg 24.3050	aluminum 13 Al 26.981538	silicon 14 Si 28.0855	phosphorus 15 P 30.97376	sulfur 16 S 32.065	chlorine 17 Cl 35.453	argon 18 Ar 39.984	sodium 11 Na 22.98977	magnesium 12 Mg 24.3050	aluminum 13 Al 26.981538	silicon 14 Si 28.0855	phosphorus 15 P 30.97376	sulfur 16 S 32.065	chlorine 17 Cl 35.453	argon 18 Ar 39.984		
potassium 19 K 39.0983	calcium 20 Ca 40.078	scandium 21 Sc 44.95591	titanium 22 Ti 47.867	vanadium 23 V 50.9415	chromium 24 Cr 51.9961	manganese 25 Mn 54.93805	iron 26 Fe 55.845	cobalt 27 Co 58.9332	nickel 28 Ni 58.6934	copper 29 Cu 63.546	zinc 30 Zn 65.409	gallium 31 Ga 69.723	germanium 32 Ge 72.64	arsenic 33 As 74.9216	seelenium 34 Se 78.96	bromine 35 Br 79.904	krypton 36 Kr 83.798
rubidium 37 Rb 85.4678	strontium 38 Sr 87.62	yttrium 39 Y 88.90585	zirconium 40 Zr 91.224	niobium 41 Nb 92.90638	molybdenum 42 Mo 95.94	technetium 43 Tc [98]	ruthenium 44 Ru 101.07	rhodium 45 Rh 102.9055	palladium 46 Pd 106.42	silver 47 Ag 107.8682	cadmium 48 Cd 112.411	indium 49 In 114.818	tin 50 Sn 118.710	antimony 51 Sb 121.760	tellurium 52 Te 127.60	iodine 53 I 126.9045	xenon 54 Xe 131.29
cesium 55 Cs 132.90545	barium 56 Ba 137.327	lutetium 71 Lu 174.967	hafnium 72 Hf 178.49	tantalum 73 Ta 180.9479	tungsten 74 W 183.84	rhenium 75 Re 186.207	osmium 76 Os 190.23	iridium 77 Ir 192.217	platinum 78 Pt 195.078	gold 79 Au 196.96655	mercury 80 Hg 200.59	thallium 81 Tl 204.3833	lead 82 Pb 207.2	bismuth 83 Bi 208.980	polonium 84 Po [209]	astatine 85 At [210]	radon 86 Rn [222]
francium 87 Fr [223]	radium 88 Ra [226]	lawrencium 103 Lr [262]	rutherfordium 104 Rf [261]	dubnium 105 Db [262]	seaborgium 106 Sg [266]	bohrium 107 Bh [264]	hassium 108 Hs [269]	meitnerium 109 Mt [268]	darmstadtium 110 Ds [271]	roentgenium 111 Rg [272]	unnilium 112 Uub [265]	ununquadium 114 Uuq [289]					

Figure 4. Periodic table of the elements, transition metals are shown in light Green and the transition metals which are included in this study are represented by Yellow color

2.3. Boriding

Boriding, also called boronizing, is the process by which boron is introduced to a metal or alloy. It is a type of surface hardening. In this process, boron atoms diffuse into the surface of a metal component. This diffusion is a thermochemical diffusion, which takes place in the temperature range (800-1050 °C) for times ranging from 0.5 to 10 h using a borurant agent which releases boron in an atomic state [45]. The resulting surface contains the metallic boride layer about 20-300 µm thick with either a single-phase boride or a poly-phase boride layer. The parts of metal boronized are extremely wear resistant and will often last two to five times longer than components treated with conventional heat treatments [46].

2.4. Types of boriding

2.4.1. Pack boriding

Pack boriding is the most widely used process of all the types due to various reasons. Pack boriding is conducted using a source of boron in the solid state. Boron powder is used as the coating medium in pack boriding. This technique is the most preferred due to safety, the possibility to change the composition of the powder mixture. This process usually uses a powder boriding mixture that consists of boron yielding substance, activators and diluents and a container where it will happen the boriding. So, the material which will be borided is immersed in the container with the boron powder, then it is heated until determined temperature (900 ~ 1000 °C) and time. The boron is diffused to the metal forming the boride layer. The powder grants a boron layer quality and suitable for applications of small size [47].

The samples are packed along with a Durborid fresh powder mixture in a closed cylindrical case as shown in Figure 5. a. This powder mixture has an average size of 30 µm as illustrated on Figure 5. b [48].

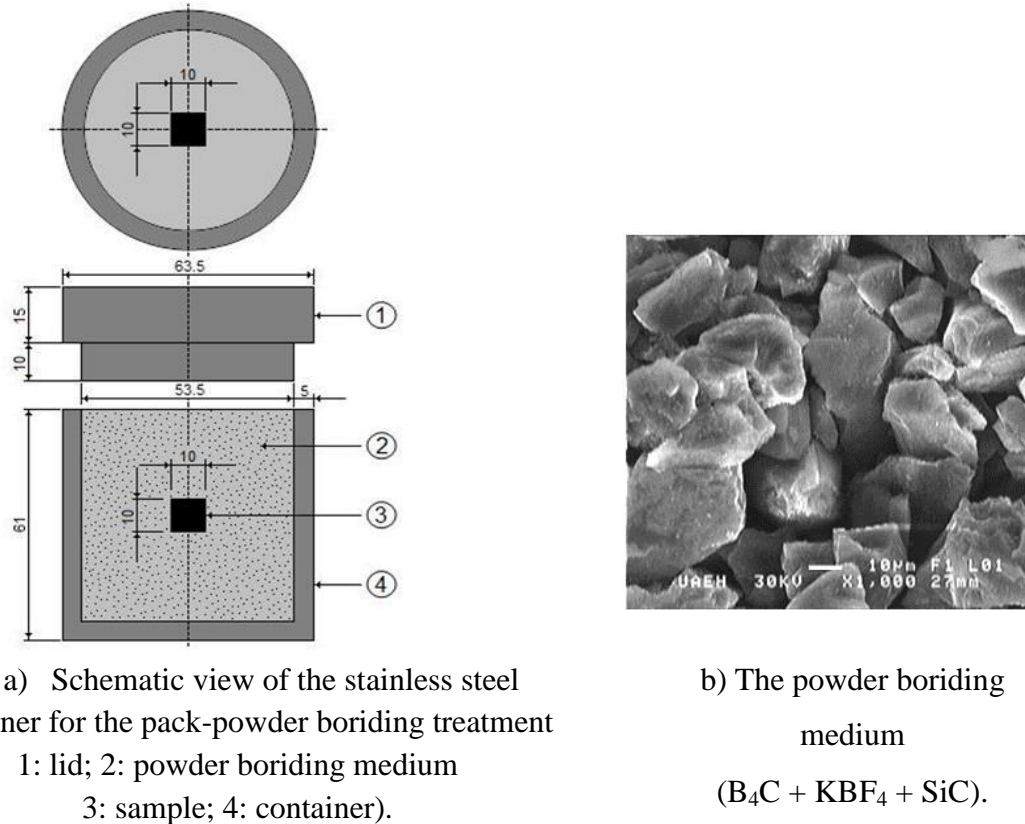


Figure 5. The pack-powder boriding treatment [48].

2.4.2. Past boriding

Paste boriding is considered to be a commercial process, while powder boriding is not a manufacturable process. In this process, a boriding paste of 55% B_4C (grain size 200- 40 μ m) and 45% cryolite [49], in a binding agent is brushed or sprayed over the entire or selected portions of parts, after drying, a layer of about 1-2 μ m thickness is obtained. Then, these parts are placed in the furnace and heated in an inert or vacuum atmosphere. After the heat treatment and by blast cleaning, brushing or washing the paste is separated from the components.

2.4.3. Liquid boriding

Liquid boriding is grouped into electroless and electrolytic salt bath processes. Electroless method is carried out in a Borax-based melt at 900-950 $^{\circ}C$ to which of 30% of B_4C is added.

Another salt bath composition can be used. In electrolytic salt bath boriding, the metallic part acting as the cathode and a graphite anode are immersed in the electrolytic molten Borax at 950 °C. The fused salt bath decomposes into boric acid (B_2O_3), and sodium ions react with boric acid to liberate boron. These processes have several disadvantages such as difficulties to remove the excess salt, quality of the salt, environment [50].

2.4.4. Plasma boriding

Mixtures of $B_2H_6-H_2$ or BCl_3-H_2-Ar may be used in the plasma boriding. The control of composition and depth of the borided layer is possible, but the use of a very toxic gas and difficulties of obtain good layer uniformity limit the diffusion of this technology [50].

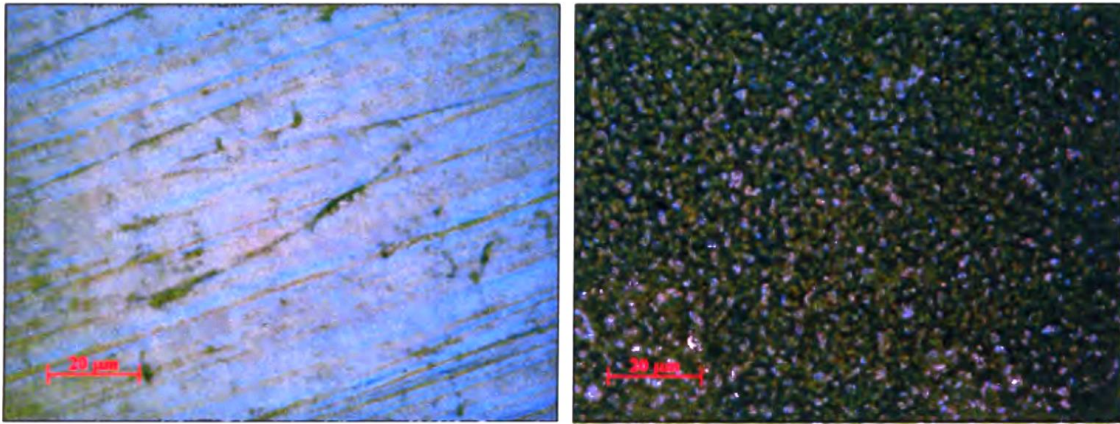
2.4.5. Gas boriding

Gas boriding is another type of boriding in which the boron source is in the gaseous phase. At high temperature boron gas diffuses into the metal and hard borides are formed. The boron source which is commonly used in gas boriding are boron chloride (BCl_3), diborane (B_2H_6) etc. This is not one of the common and most widely used techniques of boriding because of toxicity. The problems with the explosion of the gas and the toxicity of boron limit the usage of the gas boriding technique. The BCl_3-H_2 gas mixture has previously been attempted to boronize steel, but the high concentration of BCl_3 causes the corrosion of the substrate and results in poor adherent layers. To improve the technique, the dilute (1:15) BCl_3-H_2 gas mixture is commonly used at 700- 900 °C and under the pressure of about 67 kPa. This process can be used with titanium and its alloys [51].

2.5. Borided layer characteristics

The image of the specimen's surface before and after boriding heat treatment is illustrated in Figure 6. The sample surface is seen in dark grey color, which is a color of iron-boron

compound (FeB and Fe_2B). The boride layer that occurred during the boriding process increased the roughness of specimen's surface.



a) The specimen surface before boriding b) The specimen surface after boriding

Figure 6. The image of AISI 304 specimen surface before and after boriding [52].

Many studies, have shown that the surface- boriding treatment can form FeB and Fe_2B layers on the surface of a steel substrate (Figure 6). For a double phase boride layer, the near surface is the FeB phase and the Fe_2B phase is between the FeB layer and the substrate [53]. This morphology is one characteristic property of the boride layer in steels and depends on the concentration of alloying elements as well as on the treatment temperature and time [54]. Commonly known, the relative concentration of boron should be high at the surface and it then decreases with distance. This behavior is a typical characteristic of a thermochemical treatment such as boriding [55].

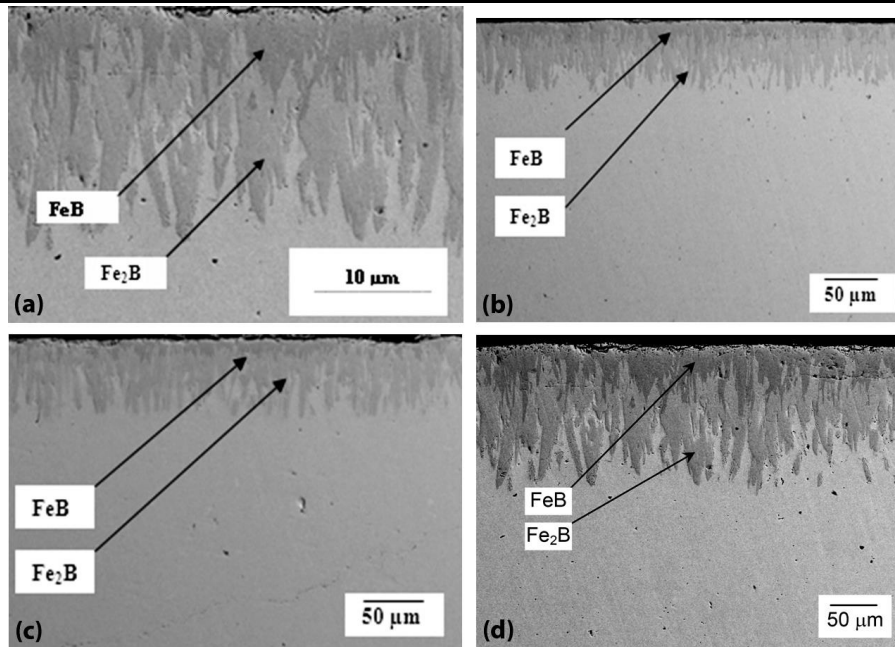


Figure 7. SEM images of the cross-sections of low-carbon microalloyed steels boronized for 4 h at: a) 973 K, b) 1073 K, c) 1173 K, and d) 1273 K [56].

shows a graphical representation of the variation of a boride layer thickness with temperature obtained from optical and SEM (scanning electron microscope) photographs; it is easy to see that the thickness of the boride layer increases with increasing temperature [56]. In various previous studies, it has been pointed out that the thickness of a boride layer depends strongly on the boriding time, the chemical composition of the material to be boronized, the process temperature, and the techniques used, such as gas, liquid and pack boriding [57-61]. The hardness measurements carried out by means of the Vickers indentations from the surface to the interior of the specimen showed that the hardness of the boride layer is much higher than that of the matrix (Figure 8). This is a consequence of the presence of hard FeB and Fe₂B phases as determined by different methods.

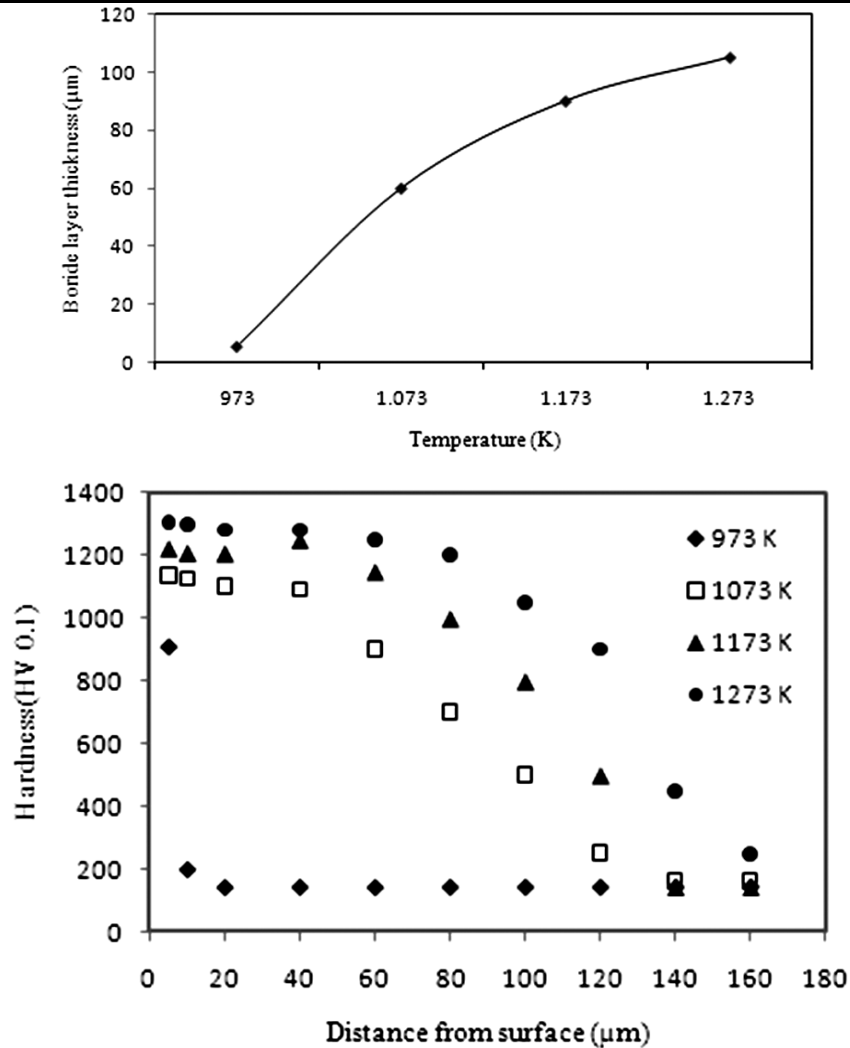


Figure 8: Boride layers thickness and Microhardness profiles[56].

2.6. Advantages and disadvantages of boriding

➤ Advantages

- High hardness and wear resistance retained in elevated temperatures.
- Enhance chemical corrosion resistance against acids and molten metals.
- The combination of a high surface hardness and a low surface coefficient of friction in boronized steel provides the outstanding of wear mechanisms, including adhesion, tribooxidation, abrasion, and surface fatigue.
- Lubricant surface that prevents the metal of aqueous corrosion.
- Increased fatigue life.

➤ Disadvantages

- The process of boriding is inflexible and labor intensive.
- The conventional thermochemical process for boriding is very slow.
- The boride thickness cannot be well controlled because the thickness growth depends on the substrate composition and the consistency of boronized powder composition.
- The partial removal of a layer for tolerance is only done by an expensive method.
- It is mostly applied to components with a large cross sectional area.
- The brittleness of the compound layer, especially the FeB phase.

2.7. Industrial application

Borided parts have been used in a wide variety of industrial applications. The high hardness of borided materials make them suited to resisting wear, particularly to that caused by abrasive particles. The hardness of boride layers on iron materials is about 1800 to 2100 HV and higher for alloyed alloys. Parts used in sliding wear situations have had their service life increased. Industrial application includes: extrusion screws, cylinders, textile nozzles, punching dies, stamping dies, molds for plastic and ceramic, die-casting molds pressing rollers, mandrels, hot forming dies Borided steel parts have been used for molten, nonferrous metals (Al, Zn, Sn). Boriding can increase the resistance of low alloy steel to acids. Borided austenitic steels are resistant to HCl acid. Large scale boriding is applied, on small drive gears for oil pump in a Volkswagen diesel engine, to increase resistance to adhesive wear [50].

CHAPTER 3: Theoretical frame work, Concept and formalism

3. Theoretical Framework, Concept and Formalism

3.1. Theoretical framework

The term *ab initio* is taken from the first principles of Physics. It does not mean that we are solving the Schrödinger equation exactly, but selecting a method that in principle with no inclusion of experimental data can lead to a reasonable approximation to the solution of the Schrödinger equation, and then selecting a basis set that will implement this method in a reasonable way [62]. *Ab initio* electronic structure methods have the advantage that they can be made to converge to the exact solution, when all approximations are sufficiently small in magnitude and when the finite set of basis functions tends toward the limit of a complete set.

In this case, using Density functional theory (DFT), which was originally found and developed by Kohn, Hohenberg, and Sham in the middle of the sixties, provides a modern tool to study the ground state properties of atoms, molecules, and solids. It is based on exact theorems, in particular, the Hohenberg-Kohn theorems. Kohn and Sham, later on, put this general theorem into a practical way where the problem can be solved by a single particle-like Hamiltonian with an approximated effective potential. The electronic structure calculations provide a quantitative way to discuss the phase stability at temperature $T = 0$, and are even extendable to $T \neq 0$ with certain model assumptions. They also provide the microscopic explanation of phase transitions. Bonding characters, energy dispersions or topology of Fermi surfaces, *etc.* all can play a role in the different phase transitions. Magnetic properties are natural outputs of the calculations.

In the non-relativistic case, the magnetic moment is the difference between the populations of the spin up and spin down states. Electronic structure calculations also provide quantitative justification of the model considerations. For example, in the Stoner model, the density of states and

the Stoner parameter are available by DFT calculations. Thus the itinerant magnetism can be discussed in a more quantitative way. It has been shown that the local spin density approximation (LSDA) and its extension the general gradient approximation (GGA) are quite successful in understanding itinerant magnetism and structure trends in metals and intermetallic compounds.

DFT within Born-Oppenheimer approximation can find the non-relativistic solution of the electronic Schrödinger equation :

$$\hat{H}\psi = E\psi \quad (3-1)$$

Where ψ is an N-body wave function, E denotes the energy of either the ground or an excited state of the system. H is the Hamiltonian, the total energy operator for a system, and is written as the sum of the kinetic energy of all the components of the system and the internal potential energy. Thus for the kinetic and potential energy in a system of M nuclei and N electrons (atomic unit):

$$\hat{T}_N = -\sum_A^M \frac{1}{2M_A} \nabla_A^2 \quad (3-2)$$

$$\hat{T}_e = -\sum_i^N \frac{1}{2} \nabla_i^2 \quad (3-3)$$

$$\hat{V}_{NN} = \sum_{A>B}^M \frac{Z_A Z_B}{r_{AB}} \quad (3-4)$$

$$\hat{V}_{ee} = \sum_{i>j}^N \frac{1}{r_{ij}} \quad (3-5)$$

$$\hat{V}_{eN} = -\sum_A^M \sum_i^N \frac{Z_A}{r_{iA}} \quad (3-6)$$

Since, $\hat{H} = \hat{T} + \hat{V}$

$$\hat{H} = -\sum_A^M \frac{1}{2M_A} \nabla_A^2 - \sum_i^N \frac{1}{2} \nabla_i^2 + \sum_{A>B}^M \frac{Z_A Z_B}{r_{AB}} + \sum_{i>j}^N \frac{1}{r_{ij}} - \sum_A^M \sum_i^N \frac{Z_A}{r_{iA}} \quad (3-7)$$

A common and very reasonable approximation used in the solution of Eq. 3.7 is the Born-Oppenheimer Approximation (BOA). Since the nuclei are much heavier than electrons (the mass of a proton is about 1836 times the mass of an electron), the nuclei move much slower (about two order of magnitude slower) than the electrons. Therefore, we can separate the movement of nuclei and electrons. The last two terms can be removed from the total Hamiltonian to give the electronic Hamiltonian, \hat{H}_e , since $\hat{V}_{NN} = K$, and $\nabla_A^2 = 0$.

$$\hat{H}_e = -\sum_i^N \frac{1}{2} \nabla_i^2 - \sum_A^M \sum_i^N \frac{Z_A}{r_{iA}} + \sum_{i>j}^N \frac{1}{r_{ij}} \quad (3-8)$$

The success of the BO approximation is due to the high ratio between nuclear and electronic masses, which we can separate the movement of electrons and nuclei. Now we can consider that the electrons are moving in a static external potential $V_{\text{ext}}(\mathbf{r})$ formed by the nuclei. The approximation is an important tool of quantum chemistry, even in the cases where the BO approximation breaks down, it is used as a point of departure for the computations for a wide range of ab initio methods, such as Hartree-Fock (HF), post-HF approaches and Density-functional theory (DFT), but we will restrict ourselves to the Density-functional theory, which the calculation is based on.

3.1.1. Density Functional Theory

Density functional theory (DFT) is a powerful, formally exact theory [63, 64]. DFT is widely used method in condensed matter physics, computational physics and quantum chemistry to describe properties of condensed matter systems, which include not only standard bulk materials, but also complex materials such as molecules, proteins, interfaces and nanoparticles. The principal feature of density functional method is that the many problems are solved directly for the charge density, $n(\mathbf{r})$ rather than for the many-electron wave function ψ . This is a massive simplification, as we only need consider a function of three variables x , y and z rather than the $3N$ variable problem above.

Its basis is the well-known Hohenberg-Kohn (HK) theorem[35], which claims that all properties of a system can be considered to be unique functional of its ground state density.

3.1.2. The Hohenberg-Kohn (HK) Theorems

Prior to the work of Hohenberg and Kohn in 1964 the use of the electron density as a fundamental variable was thought of as a special approach. However, Hohenberg and Kohn showed that this method may enable the calculation of the exact ground-state energy. The Hohenberg and Kohn first theorem states that for any system of interacting particles in an external potential $V_{ext}(\mathbf{r})$, the density is uniquely determined (in other words, the external potential is a unique functional of the density). Thus the ground state particle density determines the full Hamiltonian. In principle, all the states, including ground and excited states of the many-body wave functions can be calculated. This means that the ground state particle density uniquely determines all properties of the system completely.

The second theorem of HK states that there exists a universal functional $F[n(\mathbf{r})]$ of the density, independent of the external potential $V_{ext}(\mathbf{r})$, such that the global minimum value of the energy functional $E[n(\mathbf{r})] \equiv \int n(\mathbf{r})V_{ext}(\mathbf{r})d\mathbf{r} + F[n(\mathbf{r})]$ is the exact ground state energy of the system and the exact ground state density $n_0(\mathbf{r})$ minimizes this functional. Thus the exact ground state energy and density are fully determined by the functional $E[n(\mathbf{r})]$.

The universal functional $F[n(\mathbf{r})]$ written as

$$F[n(\mathbf{r})] \equiv T[n(\mathbf{r})] + E_{int}[n(\mathbf{r})] \quad (3-9)$$

Where $T[n(\mathbf{r})]$ is the kinetic energy and $E_{int}[n(\mathbf{r})]$ is the interaction energy of the particles. According to the variational principle, for any wave function ψ' , the energy functional $E[\psi']$:

$$E[\psi'] < \langle \psi' | \hat{T} + \hat{V}_{int} + \hat{V}_{ext} | \psi' \rangle \quad (3-10)$$

According to the theorem I, ψ' correspond to a ground state with particle density $n'(\mathbf{r})$ and external potential $V'_{\text{ext}}(\mathbf{r})$, and then $E[\psi']$ is a functional of $n'(\mathbf{r})$. According to the variational principle:

$$\begin{aligned}
 E[\psi'] &\equiv \langle \psi' | \hat{T} + \hat{V}_{\text{int}} + \hat{V}_{\text{ext}} | \psi' \rangle \\
 &= E[n'(\mathbf{r})] \\
 &= \int n'(\mathbf{r}) V'_{\text{ext}}(\mathbf{r}) dr + F[n'(\mathbf{r})] \\
 &> E[\psi_0] = \int n_0(\mathbf{r}) V_{\text{ext}}(\mathbf{r}) dr + F[n_0(\mathbf{r})] = E[n_0(\mathbf{r})]
 \end{aligned} \tag{3-11}$$

By minimizing the total energy functional $E[n(r)] \equiv \int n(\mathbf{r}) V_{\text{ext}}(\mathbf{r}) dr + F[n(\mathbf{r})]$ we can obtain the ground state energy $E[n_0(\mathbf{r})]$ of the system with respect to variations in the density $n(\mathbf{r})$. The HK theorems put particle density $n(\mathbf{r})$ as the basic variable, it is still impossible to calculate any property of a system because the universal functional $F[n(\mathbf{r})]$ is unknown. This difficulty was overcome by Kohn and Sham [65] in 1965.

3.1.3. The Kohn-Sham equations

The Hohenberg-Kohn theorem offers no practical guide to the explicit construction of the $F[n(\mathbf{r})]$ universal function. For this it is necessary to confront the complexities of the many-body problems. The KS equation is to replace the original many-body system by an auxiliary independent-particle system and assume that the two systems have exactly the same ground state density. Kohn and Sham (KS) addressed this problem in 1966, by introducing an auxiliary system containing N non interacting electrons in a background potential $V_{\text{eff}}(\mathbf{r})$, chosen such that the charge density in this auxiliary system is exactly the same as that in the full interacting system:

$$n(\mathbf{r}) = \sum_{i=1}^N |\psi_i(\mathbf{r})|^2 \tag{3-12}$$

It is simple to calculate the kinetic energy of the *non-interacting* system of electrons where the electrons are in these states using

$$T_s[n(\mathbf{r})] = -\frac{1}{2} \sum_{i=1}^N \psi_i^*(\mathbf{r}) \nabla^2 \psi_i(\mathbf{r}) d\mathbf{r} \quad (3-13)$$

The true kinetic energy of the interacting system will of course differ from this, and the difference between this term and the exact result is treated separately. The total energy is given by

$$E[n(\mathbf{r})] \equiv \int n(\mathbf{r}) V_{ext}(\mathbf{r}) d\mathbf{r} + F[n(\mathbf{r})] \quad (3-14)$$

Then the universal functional $F[n(\mathbf{r})]$ was rewritten as

$$F[n(\mathbf{r})] = T_s[n(\mathbf{r})] + E_H[n(\mathbf{r})] + E_{XC}[n(\mathbf{r})] \quad (3-15)$$

T_s is the Kohn–Sham kinetic energy for non-interacting system and $E_H[n(\mathbf{r})]$ is the classic electrostatic (Hartree) energy of the electrons:

$$E_H[n(\mathbf{r})] = \frac{1}{2} \int \int \frac{n(\mathbf{r})n(\mathbf{r}')}{|\mathbf{r}-\mathbf{r}'|} d\mathbf{r}d\mathbf{r}' \quad (3-16)$$

$E_{XC}[n(\mathbf{r})]$ contains the exchange and correlation energies and the correction to the kinetic energy. In order to obtain the ground state energy they minimize the energy of Eq. 3.17 (theorem 2), subject to the constraint the number of electrons N is conserved.

$$\delta[E[n(\mathbf{r})] - (\mu \int n(\mathbf{r}) d\mathbf{r} - N)] = 0 \quad (3-17)$$

And the resulting equation is

$$\mu = \frac{\delta F[n(\mathbf{r})]}{\delta n(\mathbf{r})} + V_{ext}[n(\mathbf{r})] \quad (3-18)$$

$$\mu = \frac{\delta T_s[n(\mathbf{r})]}{\delta n(\mathbf{r})} + V_{KS}[n(\mathbf{r})] \quad (3-19)$$

Where μ is the chemical potential.

$$V_{KS}(\mathbf{r}) = V_{ext}(\mathbf{r}) + V_H(\mathbf{r}) + V_{XC}(\mathbf{r}) \quad (3-20)$$

$$V_{KS}(\mathbf{r}) = V_{ext}(\mathbf{r}) + \frac{\delta E_H[n(\mathbf{r})]}{\delta n(\mathbf{r})} + \frac{\delta E_{XC}[n(\mathbf{r})]}{\delta n(\mathbf{r})} \quad (3-21)$$

To find the ground-state density $n_0(\mathbf{r})$ for this non-interacting system we simply solve the one-electron Schrödinger equations;

$$\left(\frac{1}{2}\nabla^2 + V_{KS}\right)\psi_i(\mathbf{r}) = \varepsilon_i\psi_i(\mathbf{r}) \quad (3-22)$$

Equations (3.15), (3.24), (3.25) together are the well-known KS equations, which must be solved self-consistently because $V_{KS}(\mathbf{r})$ depends on the density through the XC potential.

3.1.4. Magnetism in the Density Functional Theory

3.1.5. Approximations

Both the Hohenberg-Kohn formulation as well as the approach by Kohn-Sham are formally exact and therefore allow an exact solution, provided that the functional $E_{xc}[n(\mathbf{r})]$ is exactly known. In practice this is never the case, which reveals the crucial point in density functional theory. Every calculatory approach in DFT stands and falls with the quality of the approximation for the unknown functional $E_{xc}[n(\mathbf{r})]$. We will now review some of the common approximations made for E_{xc} .

3.1.5.1. Local Density Approximations (LDA).

Local-density approximations (LDA) are a class of approximations to the exchange–correlation (XC) energy functional that depend solely upon the value of the electronic density at each point in space (and not, for example, derivatives of the density or the Kohn–Sham orbitals). Many approaches can yield local approximations to the XC potential energy. However, overwhelmingly successful local approximations are those that have been derived from the

homogeneous electron gas (HEG) model. The total exchange-correlation functional $E_{XC}[n(\mathbf{r})]$ can be written as,

$$\begin{aligned} E_{XC}^{LDA}[n(\mathbf{r})] &= \int n(\mathbf{r}) \varepsilon_{XC}^{hom}(n(\mathbf{r})) d\mathbf{r} \\ &= \int n(\mathbf{r}) [\varepsilon_X^{hom}(n(\mathbf{r})) + \varepsilon_C^{hom}(n(\mathbf{r}))] d\mathbf{r} \\ &= E_X^{LDA}[n(\mathbf{r})] + E_C^{LDA}[n(\mathbf{r})] \end{aligned} \quad (3-23)$$

The local spin density approximation (LSDA) [66] has two quantities, the spin-up and spin down charge densities, and it is a straightforward generalization of the LDA to include electron spin.

$$E_{XC}^{LDA}[n_\uparrow(\mathbf{r}), n_\downarrow(\mathbf{r})] = \int n(\mathbf{r}) \varepsilon_{XC}^{hom}(n_\uparrow(\mathbf{r}), n_\downarrow(\mathbf{r})) d\mathbf{r} \quad (3-24)$$

3.1.5.2. Generalized-Gradient Approximation (GGA)

As the LDA approximates the energy of the true density of the energy of a local constant density, it neglects the inhomogeneities of the real charge density, which could be very different from the HEG (homogenous electronic gas). The XC energy of inhomogeneous charge density can be significantly different from the HEG results. An improvement to this can be made by considering the gradient of the electron density, the so-called Generalized Gradient Approximation (GGA). Symbolically, this can be written as:

$$E_{XC}^{GGA} = E_{XC}^{GGA}[n(\mathbf{r}), \nabla n(\mathbf{r}), \nabla n(\mathbf{r})] \quad (3-25)$$

$$E_{XC}^{GGA}[n_\uparrow, n_\downarrow] = \int n(\mathbf{r}) \varepsilon_{XC}[n_\uparrow, n_\downarrow, \nabla n_\uparrow, \nabla n_\downarrow] d\mathbf{r}$$

GGA also reproduces the binding energies, atomic energies, bond lengths better than LSDA, Nevertheless, there still exist some system which cannot be described properly by GGA because of its semi-local nature. What is the worst that no systematic way has been developed to improve the functional for exchange and correlation. The problems are severe in materials in which the electrons

tend to be localized and strongly interacting, such as transition metal nitrides and rare earth elements and compounds [67].

3.1.6. Pseudo-potential

In physics, a pseudo-potential (Figure 9) or effective potential is used as an approximation for the simplified description of complex systems. Using pseudo-potential in DFT calculations corresponds to simplify and accelerate the computational time. In this approach, only the effects of the valence electrons are explicitly covered in the calculation, contrary to the effects due to core electrons. The latter, strongly related to the atomic nucleus, are much localized. Therefore, they participate very little in the chemical bond and thus influence weakly the solid properties of interest. However, the potential created by the core electrons is strongly oscillating and generates significant costs in terms of computation time. The idea therefore of potential nickname is to replace the complex potential due to core electrons by an effective ionic potential that would have the same effect on the valence electrons.

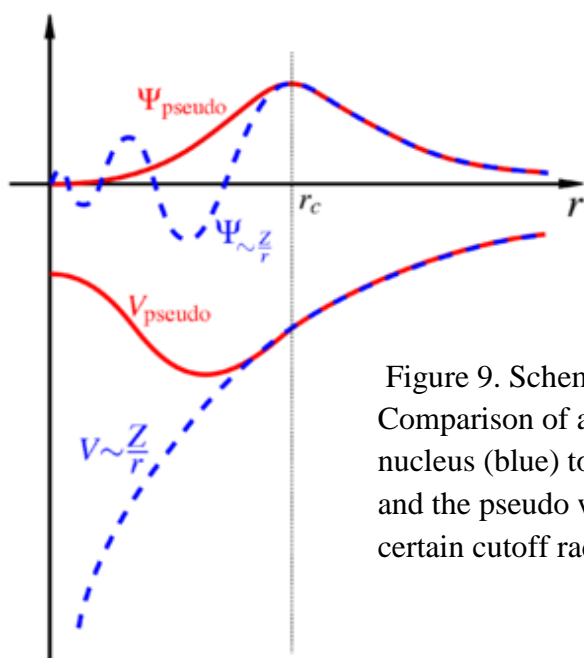


Figure 9. Schematic illustration of pseudo-potential. Comparison of a wave function in the Coulomb potential of the nucleus (blue) to the one in the pseudo-potential (red). The real and the pseudo wave function and potentials match above a certain cutoff radius r_c

3.2. Concept and formalism

Magnetism, the phenomenon by which materials assert an attractive or repulsive force or influence on other materials, has been known for thousands of years. However, the underlying principles and mechanisms that explain the magnetic phenomenon are complex and subtle, and their understanding has eluded scientists until relatively recent times [68]. Magnetism plays a crucial role in the development of memories for mass storage, and in sensors to name a few, Spintronics is an integration of the magnetic material with semiconductor technology, to realize nanosized devices with better features like non-volatility, scaling, etc.

I will discuss in this part the origin of magnetism and the various phenomena of diamagnetism, paramagnetism, ferromagnetism, anti-ferromagnetism and ferrimagnetism. I presented the two basic theories of magnetism-localized moment theory (Heisenberg model) and itinerant electron theory (Stoner model).

3.2.1. Magnetism in materials

There are two basic theories of magnetism, localized moment theory and itinerant electron theory. In localized moment theory, the valence electrons are attached to the atoms and cannot move about the crystal. The valence electrons contribute a magnetic moment, which is localized at the atom. In the itinerant electron magnetic theory, electrons responsible for magnetic effects are ionized from the atoms and are able to move through the crystal. There are materials for which one or the other model is a rather good approximation [69].

The non-integral values of magnetic moment per atom, the high values of specific electronic heat coefficient, which are not compatible with localized model, impose the use of the itinerant model in the case of transition metals and their alloys. But, this model cannot explain the

Curie-Weiss law observed for all ferromagnetic metals for $T > T_C$, and the calculated value of Curie temperature is too big comparing to the experimental one, problems that are easily resolved by localized model [70].

It is very clear that d electrons should be treated as localized electrons in magnetic insulator compounds and as correlated itinerant electrons in transition metals. However, they are still in the stage of development and in many cases they cannot be separated from each other. For a deep understanding of magnetism in condensed matter there has been a trend to combine both models to develop a unified theory [71].

3.2.1.1. Localized moments in solids

The modern theory of magnetism has started with the concept of a local magnetic moment of a fixed size. Within this concept Langevin gave an explanation for the Curie law of magnetic susceptibility [72]. Subsequently Weiss introduced the notion of an interaction (molecular field) between the atomic magnetic moments to explain the spontaneous magnetic order in solids.

Combining this new concept with the studies of Langevin, Weiss was able to explain the finite temperature properties of ferromagnetic $3d$ transition metals [73].

In 1928 Heisenberg attributed the origin of Weiss molecular field to the quantum mechanical exchange interaction between the magnetic moments and proposed a more general model [74]. The magnetic interaction between localized moments, the magnetic coupling, determines the behavior of a compound when placed in a magnetic field and may favor magnetic ordering. The magnetic coupling is usually described using the *Heisenberg* Hamiltonian:

$$H = -\sum_{i,j} J_{ij} \vec{S}_i \vec{S}_j \quad (3-26)$$

Where J is the exchange integral, positive values of the Heisenberg coupling constant J corresponds to parallel spin orientation (ferromagnetic coupling), negative ones to antiparallel spin orientation (antiferromagnetic coupling). The i and j can be restricted to run over all nearest neighbors or next nearest neighbor pairs of magnetic moments on account of the fact that the magnetic interaction is weak and decreases exponentially with distance. A spin operator of this form was first deduced from the Heitler-London results by Dirac [75] and first extensively applied in the theory of magnetism by Van Vleck [76]. If the orbitals of two neighbor atoms present a sufficient space extension so that an overlap is possible, the correlation effects lead to a direct interaction between the atoms spins. This phenomenon is known as direct exchange. The direct exchange is characteristic for 3d intermetallic compounds, and represents the strong interatomic interaction, being responsible for the magnetic order up to high temperatures. When magnetic orbitals of two neighboring atoms are too localized to overlap, as in the case for the 4f series, the exchange process can occur through conduction electrons if the system is metallic. This leads to an indirect exchange of RKKY type (Ruderman, Kittel, Kasuya, Yosida) [77-79]. If there are no conduction electrons, as in ceramics where magnetic atoms are separated by non-magnetic atoms like oxygen, the external electrons of the latter participate in covalent binding and mediate the exchange interaction. This is the superexchange interaction, which was introduced by Kramers [80] (1934) in an early attempt to explain the magnetic interaction in antiferromagnetic ionic solids. The three main exchange mechanisms between localized moments are presented in Figure 10. The Heisenberg model is actually justified when well-defined local atomic moments exist, like in the case of magnetic insulators and in the majority of rare-earth metals.

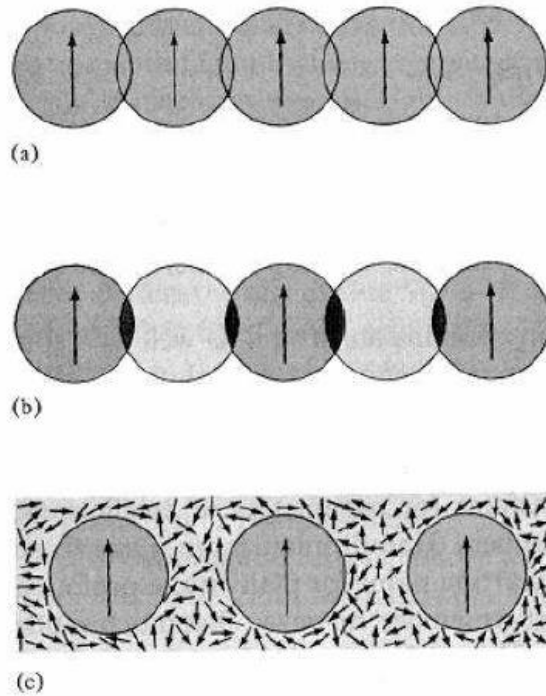


Figure 10. Schematic illustrations of possible coupling mechanisms between localized magnetic moments: (a) direct exchange between neighboring atoms, (b) superexchange mediated by non-magnetic ions, and (c) indirect exchange mediated by the conduction electrons.

3.2.1.2. Itinerant-electron magnetism

Opposite to the localized model is the itinerant (or band) model which considers that the magnetic carrier are the so called Bloch electrons which are itinerant through the solid. One of the main reasons for this is that the atomic moments in Fe, Co and Ni are not multiples of the Bohr magneton but rather odd fraction of it.

Bloch first discussed the possibility of ferromagnetism in an electron gas on the basis of Hartree-Fock approximation [81]. Later Wigner pointed out the importance of electron electron interactions on the suppression of the occurrence of ferromagnetism in electron gas [82]. Thus the occurrence of ferromagnetism in transition metals is considered to be connected with the atomic character of 3d electrons and mainly intra-atomic exchange interactions.

The Stoner model [83] is the simplest model of itinerant-electron magnetism, which has mainly been used to account for the existence of ferromagnetism in itinerant systems. If the relative gain in the exchange interaction (the interaction of electrons via Pauli's exclusionary principle) is larger than the loss in kinetic energy, the spin up and spin down electron bands will split spontaneously. The instability of non-magnetic state with respect to formation of ferromagnetic order is given by the Stoner criterion which is defined by:

$$I.N(E_F) > 1 \quad (3-27)$$

where: I is the intra-atomic exchange integral and $N(E_F)$ is the density of states at the Fermi level. The conditions favoring magnetic moments in metallic systems are obviously: a large value of the exchange energy, but also a large density of state at the Fermi level. In Figure 11 the density of states at Fermi level of d transition elements are presented. However, the Stoner theory fails to explain the Curie-Weiss magnetic susceptibility observed in almost all ferromagnets and the measured T_C for $3d$ metals are too high in comparison to the observed ones. Improvements to the Stoner model have been made that take into account the effect of spin fluctuations in a self-consistent renormalized (SCR) way [71]. These studies built a bridge between two extreme limits of models (localized and itinerant) and unified them into one picture. In particular, these new theories have been very successful in describing several properties of weak itinerant ferromagnets [84].

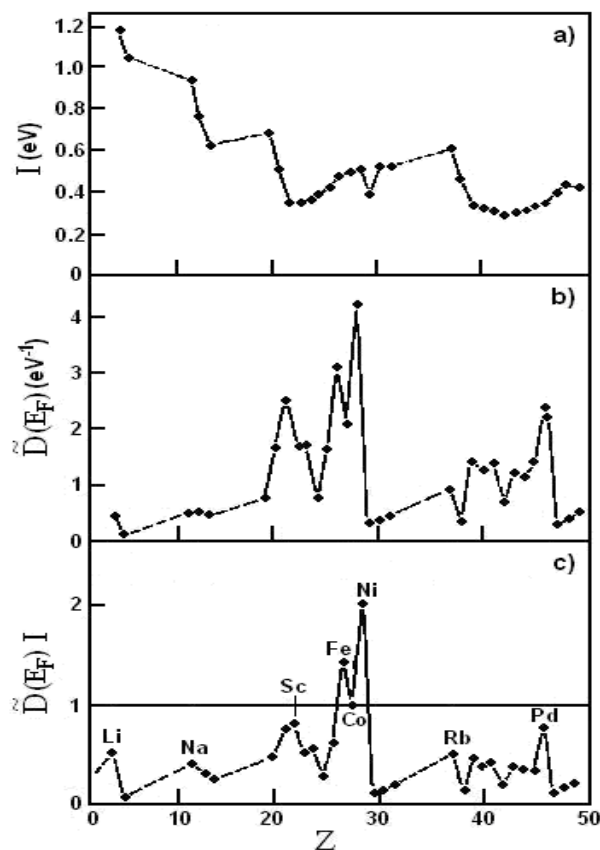


Figure 11 a) the Stoner parameter, b) the density of states at Fermi level,
c) the Stoner criterion

In addition, I also relate the result of calculation to the Stoner model [85-88], which is used for explaining the mechanism of spontaneous spin polarization and the Slater–Pauling curve. The existence of a Slater–Pauling magnetization curve is well known in the transition metal compounds, specifically in the formula types TM_2B and TMB , where TM belongs to the first row of transition metal [89-91]. With the half-d-band occupied in compounds, such a curve describing saturation magnetization decreases linearly with a slope of 1 by progressively adding valence electrons to higher split half-d-band orbital. Because of the independence of the curve from the crystal structure,

I can draw a single Slater–Pauling curve to predict the magnetization for different crystal structures of transition metal borides.

The question I want to analyze then is whether the magnetization of $\text{Fe}_{1-x}\text{Mn}_x\text{B}$ is dependent on a Slater–Pauling magnetization curve. In order to fully understand the characteristics of Fe and Mn in $\text{Fe}_{1-x}\text{Mn}_x\text{B}$, I treated the mixture of TM1 and TM2 as the singular TM in the boride compounds, TM as transition metals.

3.2.2. Abrupt phase transitions

Phase transitions occur in all fields of the physical sciences and are crucial in engineering as well; abrupt changes from one state of matter to another are apparent everywhere we look, from the freezing of rivers to the steam rising up from the tea kettle. But why should it be only temperature and pressure that drive such abrupt transitions? In fact, quantum fluctuations can replace thermal fluctuations, a phase transition can occur even at zero temperature, and the concept of a phase transition turns out to be a lot more general than it is made out to be in elementary thermodynamics. Over the last twenty or so years the field of *quantum phase transitions* (QPTs) has seen steady growth.

3.2.2.1. Phase transition

Under certain conditions (temperature, pressure, magnetic and electric fields or doping) a number of systems in nature undergo phase transitions, for example, of a gas to a liquid or a solid, ferromagnetic-paramagnetic transition; normal metal to a superconducting phase, etc.

These remarkable phenomena occur as a consequence of the inter-particle correlations. Their description is made with the help of the thermodynamics and the statistical physics.

The thermodynamics provides a general framework for the description of phases and phase transitions (classical phase transitions). Within the thermodynamic approach the phase transition is

considered as an abrupt change of one phase into another caused by the variation of the parameters of the state like the temperature T , the pressure P , the magnetic field H , etc. Usually the thermodynamic systems are defined for fixed external conditions-temperature, volume V , etc.

For a given set of fixed parameters there always exists a function called thermodynamic potential having a minimum in the states, for which the system is in a thermodynamic equilibrium. As an example I would like to mention the Gibbs potential Φ ; it depends on intensive parameters like T , P , and H . In order to make an appropriate use of the introduced thermodynamic potentials I should apply to them the Gibbs stability conditions. This gives the opportunity to outline the main properties of the phase transitions and the phase diagrams.

Depending on whether the phases can coexist in an equilibrium contact or their distinctions vanish as the transition point is approached, two different types of thermodynamic behavior may exist. The first one is referred to the first-order transitions while the latter usually characterizes the second-order phase transitions. The order and the main properties of the phase transition depend on the way, in which the exchange of the stability between the possible phases participating in it takes place. There is another important point for discussion-the so-called critical state. This is a homogeneous thermodynamic state occurring at the second-order transition point, i.e., the critical point T_c where the phases are indistinguishable (Gibbs, 1876-1878; see Gibbs, 1948). On approaching the critical state the distinctive features of the phases gradually disappear and the phase transition is continuous; a special type of continuous transitions is the second-order phase transition.

The phenomena taking place in a close vicinity of the critical points (or lines) are called critical phenomena. The critical behavior at (and near to) the critical point is a special subject of the "critical" thermodynamics. The "phases" in the critical state and in the near-to-critical states have almost equal stability. For example, let us consider paramagnetic to ferromagnetic transition, below the Curie point T_c the low-temperature (ferromagnetic) phase is stable.

It possesses a nonzero spontaneous magnetization M in a zero external magnetic field ($H = 0$). When the temperature approaches T_c from the low-temperature side the stability of the ferromagnetic phase is reduced and at T_c the high-temperature ($T > T_c$) paramagnetic ($M = 0$) phase becomes stable. The ordered (ferromagnetic) phase cannot exist above T_c either as stable or metastable state and this is a characteristic feature of the second-order phase transitions.

Within the framework of the rational thermodynamics the possibility of the critical points to appear is related to the existence of nonanalytic singularities of the thermodynamic functions. For instance, the thermodynamic susceptibilities, i.e., the second derivatives of the thermodynamic potential Φ may exhibit at the transition point either simple discontinuities or power and logarithmic singularities.

The thermodynamics itself allows all these possibilities but it does not answer to the question concerning which of them actually occur in real systems.

Phase transitions occur when the thermodynamic free energy of a system is non-analytic for some choice of thermodynamic variables. This condition generally stems from the interactions of a large number of particles in a system, and does not appear in systems that are too small. It is important to note that phase transitions can occur and are defined for non-thermodynamic systems, where temperature is not a parameter. Examples include: quantum phase transitions, dynamic phase transitions, and topological (structural) phase transitions. In these types of systems other parameters take the place of temperature.

3.2.2.2. Quantum Phase Transitions

In physics, a quantum phase transition (QPT) is a phase transition between different quantum phases (phases of matter at zero temperature). Quantum phase transitions can only be accessed by varying a physical parameter, such as magnetic field or pressure at absolute zero temperature.

The transition describes an abrupt change in the ground state of a many-body system due to its quantum fluctuations [92]. Classical phase transitions occur at a regime where quantum fluctuations do not play an important role, usually at high enough temperatures.

In recent years the scientific interest has shifted towards two new fields, viz. non-equilibrium phase transitions and quantum phase transitions.

The investigation of quantum phase transitions was pioneered by Hertz [93]. In recent years quantum phase transitions in electronic systems have gained particular attention since some of the most exciting discoveries in contemporary condensed matter physics, viz. the integer and fractional quantum Hall effects and high-temperature superconductivity are often attributed to quantum critical points [94-96]. There are now quite a number of excellent textbooks available on the physics of phase transitions and critical behavior [97, 98].

A continuous phase transition can usually be characterized by an order parameter, a concept first introduced by Lev Davidovich Landau (Fermi liquid theory) [99]. An order parameter is a thermodynamic quantity that is zero in one phase (the disordered) and non-zero and non-unique in the other (the ordered) phase. Very often the choice of an order parameter for a particular transition is obvious as, e.g., for the ferromagnetic transition where the total magnetization is an order parameter. Sometimes, however, finding an appropriate order parameter is a complicated problem by itself, e.g., for the disorder-driven localization-delocalization transition of non-interacting electrons.

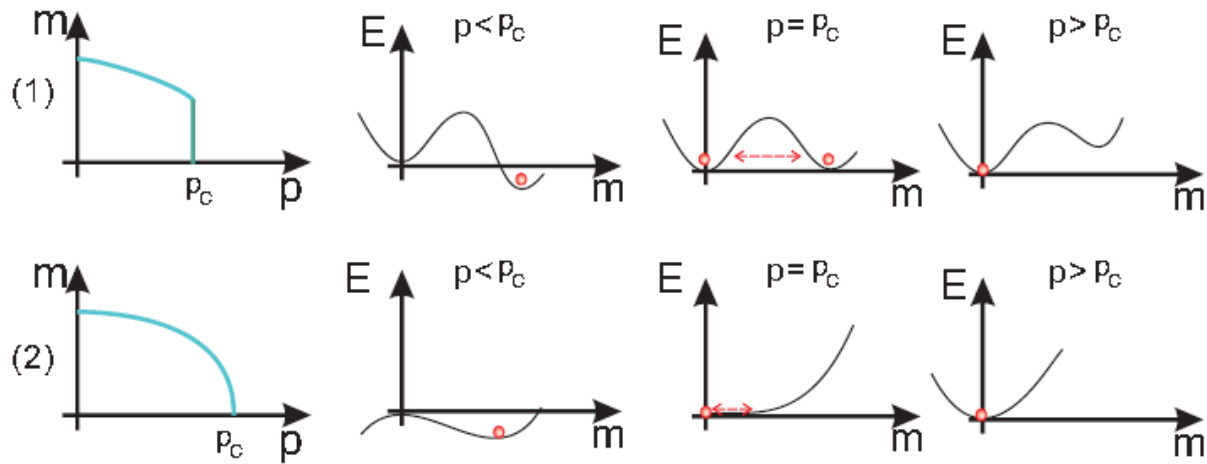


Figure 12. Qualitative illustration of first order (1) and second order (2) transitions of the magnetic moment (m) under pressures, and their corresponding free energy (E), respectively, adapted from Pfeleiderer [93].

The transition of the magnetic moment can be either a first order (a discontinuous transition) or a second order (a continuous transition). The free energy (E) landscape at $T = 0$ of first and second order phase transition is schematically illustrated in Figure 12. This different behavior when approaching the quantum phase transition can be of interest both experimentally and theoretically.

The nature of unconventional magnetic phases of metals may be clarified by tuning them systematically with the help of an external parameter such as pressure or field. In this thesis, I present studies on the magnetic state of semi and mono borides TM_2B ($TM=Fe, Co, Ni$) and TMB ($TM=Mn, Fe, Co, Ni$) at high pressure. This group, consisting of transition metals belongs to the class of so-called nearly or weakly ferromagnetic materials. Thus, are characterized by strongly enhanced spin fluctuations, their ground state is close to a ferromagnetic instability which makes them good candidates for actually reaching the ferromagnetic quantum phase transition in experiment by changing the chemical composition or applying pressure.

One of the most remarkable findings about the magnetic phase transition in TM_xB ($x=1, 2$) are at a certain pressure the magnetic moment of the ferromagnetic compounds shows a pronounced abrupt avalanche (first order as is the case experimentally for the transition in MnSi [100]) as is shown in Figure 12. This phenomenon was explained by Landau-Ginzburg-Wilson theory of the ferromagnetic quantum phase transition [101]. It will be quite interesting for the experimentalist to perform high pressure (tens of GPa) measurements, comparing the magnetic and transport properties in this series of compounds. It can help to reveal the analogies and differences in the QPT

3.2.3. Equation Of State Calculation

Geometry optimization under applied hydrostatic pressure can be used to determine the bulk modulus of a material, B , and its pressure derivative, $B' = dB/dP$. The procedure involves calculating a theoretical equation of state, EOS, which describes the dependence of the cell volume on the external hydrostatic pressure. The methodology is very similar to the real experiment: the external pressure is fixed using the Minimizer tab on the Geometry Optimization dialog and the cell volume at that pressure is found by carrying out geometry optimization with CASTEP.

The subsequent analysis of the P-V dataset is exactly the same as in experimental studies [102]. An analytical expression is chosen to describe the EOS and its parameters are fitted to the calculated data points. The most popular form of EOS is the third order Birch-Murnaghan equation [103]:

$$P = \frac{3}{2} B \left[\left(\frac{V_0}{V} \right)^{2/3} - \left(\frac{V_0}{V} \right)^{5/3} \right] * \left\{ 1 + \frac{3}{4} (4 - B') \left[\left(\frac{V_0}{V} \right)^{2/3} - 1 \right] \right\} \quad (33.28)$$

where V_0 is the equilibrium volume. A detailed comparative study of various analytical forms of EOS was performed by Cohen *et al.*[104].

3.2.4. Population analysis

Mulliken population analysis (MPA)[105] is a method for calculating partial atomic charges based on the population of linear combined atomic orbitals (LCAO) bases. This is implemented in CASTEP by Segall *et al.* [36] based on the method of Sanchez-Portal [106] which provides the link between methods using LCAO and those using plane waves. Owing to the difference of electronegativity between the TM and B atoms, ionic bonds are formed where TM atoms donate some electrons to B atoms and thus become slightly positively charged. MPA method is applied to overlap population and charge calculations. I use the following relations to calculate the average bond length and the average overlap population:

$$L_{\text{moy}}(\text{AB}) = \frac{\sum_i L_i N_i}{\sum_i N_i} \quad , \quad P^u = \bar{n}_{\text{AB}} = \frac{\sum_i n_i^{AB} N_i}{\sum_i N_i} \quad (3.29)$$

Here, $L_{\text{moy}}(\text{AB})$ and \bar{n}_{AB} are the average bond length and the mean bond population, respectively; N_i is the total number of i bond in the cell and L_i is the bond length of i type. These parameters will be used for the calculation of bond hardness.

3.2.5. Hardness

Hardness is a measure of the resistance of materials against permanent deformations. It is usually measured by traditional techniques such as in Brinell, Rockwell, Vickers, or Knoop [107] and Berkovich Nano indentation [34] (Figure 15). Materials with high hardness are technologically important for cutting tools and wear resistant coatings. It has been recognized that the hardness of strongly covalent/ionic bonded crystals is associated directly with the bond strength [108-110].

Nano-indentation is an instrumented hardness testing technique (also called depth sensing indentation), with precise indent location, high-resolution load control and displacement measurement [111] .

During indentation one can measure continuous load–displacement, and after indentation the modulus and hardness results can be calculated from the unloading portion of the experiment [112].

Nanoindentation probes a very small volume around the indenter and when combined with a fully characterized large grained polycrystalline material, a wide variety of crystal orientations can be probed, which provides information on the materials performance on the nano- and micro-scales. Increasingly, these tests are being used to improve our understanding of materials performance on these scales.

T. B. Britton *et al.*[113] confirm that there are correlations between the orientations of the titanium crystals, specifically the declination angle, and both the elastic and the plastic behavior during nanoindentation. When the indentation load is applied parallel to the *c*-axis the material is both stiffer and harder. Variations in stiffness are due to the different positions of Ti atoms within the hexagonal lattice; as the material is indented, the load will be applied to different configurations of atoms and will resolve onto different combinations of atomic bonds. Zarkades & Larsson [114] demonstrated this variation as a function of orientation, by considering the anisotropy in the stiffness and compliance constants.

Consequently, the measured values of hardness of materials are very sensitive to many parameters including loading and unloading speed (Figure 13), applied load, indenter tips (Figure 14), anisotropy of materials, defects in the sample, method of measurement, temperature, etc. Additionally, for polycrystalline materials hardness is a function of grain size; in case of thin films and coatings, their hardness depends on the repulsive barrier for the movement of dislocations across the interface between two materials and the results may vary critically (by a factor of three) with the nature of the substrate [115-118]. Therefore, it seems that there are no available methods for determining the “absolute” hardness of a material.

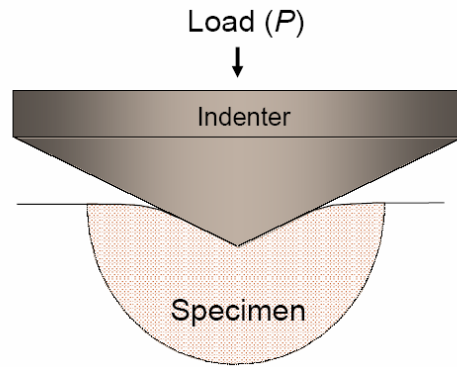


Figure 13. Hardness-resistance to penetration of a hard indenter [117].

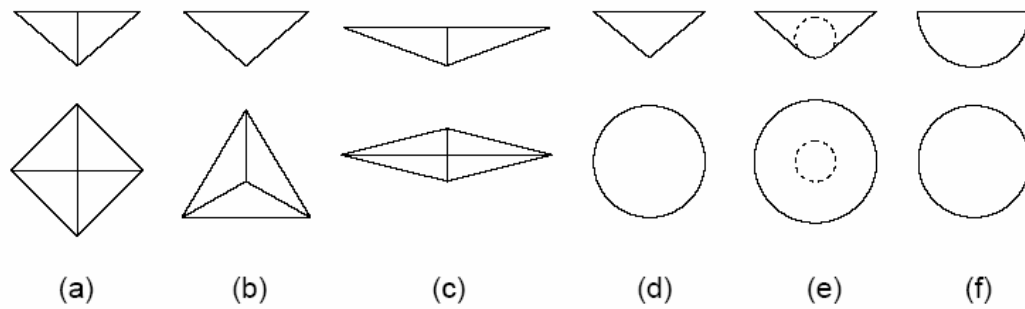


Figure 14. Schematics of indenter tips [117]

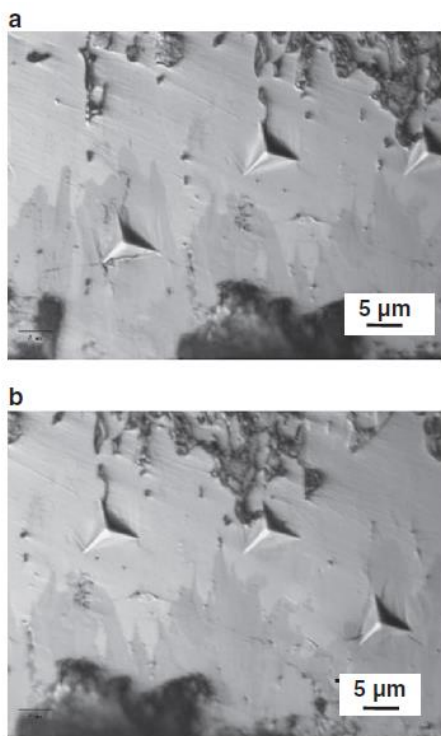


Figure 15. Loads in the range of 10 to 300 mN were applied to the “pure” zone of the FeB layer at a distance of 10 μm from the surface [56].

In this thesis, the hardness of TM–B and B–B bonds in each of compounds TMB and TM_2B are evaluated and compared. The proposed analytical expressions have been used to determine the hardness from first-principles theory [119]. I consider the hardness of B–B and TM–B bonds only. The hardness of TM–TM bond, however, is not taken into consideration in this work, because the hardness of metallic bond is ill defined in this method. The strength of the bond per the unit volume can be characterized by average overlaps populations. For complex multi-bonding compounds, the hardness of the u type bond can be calculated as follows:

$$H_v^u(GPa) = 740P^u(v_b^u)^{-5/3}$$

$$v_b^u = \frac{(d^u)^3 \Omega}{\sum_v [(d^v)^3 N_b^v]} \quad (3.30)$$

$$H = ((H^{Fe-B})^{N^u} (H^{B-B})^{N^v})^{1/(N^u+N^v)}$$

H_v^u is the hardness of u type bond; Ω is the cell volume, d^u is the bond length; N_b^v refers to the v type bond density per cubic angstrom and the sum is over the total number of v type bonds in the cell; and P^u is overlap population of u type bond. I use Mulliken population analysis as implemented in CASTEP in order to estimate bond overlap population.

Using ab-initio calculations and previous works of Gao *et al* [120]; Zhang *et al.* showed that GGA PBE gives better values of bond hardness (H). It is find that GGA-PBE (USP) method can be effectively used to predict the H value [119].

3.2.6. Elastic properties

It is well known that elastic properties can reflect interatomic interactions and are related to some fundamental physical properties, such as thermal expansion, phonon spectra and equations of state [121].

$$\sigma = \frac{\partial E}{\partial r} \quad (3.31)$$

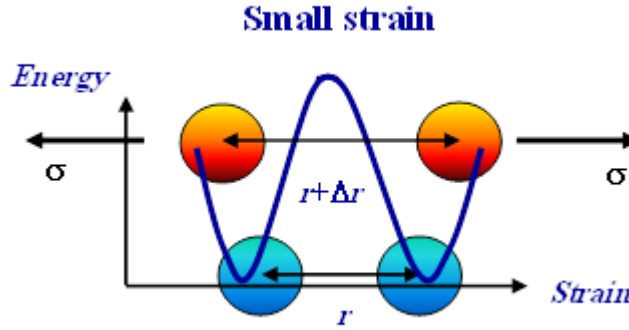


Figure 16 Origin of linear elasticity

3.2.6.1. Relationship stress-strain

Elasticity begins by defining two tensors of order 2: the stress tensor σ_{ij} and the strain tensor ε_{ij} which are both symmetrical, ie that $\sigma_{ij} = \sigma_{ji}$ and in theory of linear elasticity is assumed that there is a linear relationship between σ_{ij} and ε_{ij} given by (generalized Hooke's law):

$$\sigma_{ij} = C_{ijkl} \varepsilon_{kl} \tag{3.32}$$

C_{ijkl} is an 4 order tensor. The number of possible combinations of four indices ijkl is $3^4=81$ éléments called tensor elastic stiffness. This tensor defines the elastic constants of the material.

By reason of symmetry of σ_{ij} and ε_{kl} and by applying the relation of Maxwell $C_{ijkl} = C_{klij}$ [122], the items are reduced to 21 independent elements in the most general case. In addition, the symmetry of the crystalline solid substantially reduces this number. The constants C_{ijkl} are denoted by a new notation, namely $C_{\alpha\beta}$, such as ij or kl indexes are abbreviated by replacing each pair of indices initially quadruplets by a single α or β index. Thus, the abbreviations are as follows:

11 \longrightarrow 1 32 or 23 \longrightarrow 4
 22 \longrightarrow 2 31 or 13 \longrightarrow 5
 33 \longrightarrow 3 21 or 12 \longrightarrow 6

Example:

$$C_{1111} = C_{11}, C_{1112} = C_{16}, C_{2232} = C_{24}.$$

The equation (), in matrix form is:

$$\begin{pmatrix} \sigma_{11} \\ \sigma_{22} \\ \sigma_{33} \\ \sigma_{23} \\ \sigma_{31} \\ \sigma_{12} \end{pmatrix} = \begin{pmatrix} C_{11} & C_{12} & C_{13} & C_{14} & C_{15} & C_{16} \\ C_{21} & C_{22} & C_{23} & C_{24} & C_{25} & C_{26} \\ C_{31} & C_{32} & C_{33} & C_{34} & C_{35} & C_{36} \\ C_{41} & C_{42} & C_{43} & C_{44} & C_{45} & C_{46} \\ C_{51} & C_{52} & C_{53} & C_{54} & C_{55} & C_{56} \\ C_{61} & C_{62} & C_{63} & C_{64} & C_{65} & C_{66} \end{pmatrix} \begin{pmatrix} \varepsilon_{11} \\ \varepsilon_{22} \\ \varepsilon_{33} \\ \varepsilon_{23} \\ \varepsilon_{31} \\ \varepsilon_{12} \end{pmatrix} \tag{3.33}$$

The number of independent coefficients $C_{\alpha\beta}$ depends on the symmetry of the material. If the symmetry of the crystal is cubic it is reduced at 3, hexagonal crystal 5, 9 for an orthorhombic ... etc.

Table 4. The number of independent elastic constants for different crystalline structure with their point group[123].

Structure (with point group)	Number of independent constants
Triclinic	21
Monoclic	13
Orthorhombique	9
Tetragonal (4,-4,4/m)	7
Tetragonal (422,4mm,-4 2/m, 4/mmm)	6
Hexagonal and rhomboedric (3,-3)	7
Hexagonal et rhomboedric (32,3m,-32/m)	6
Hexagonal (6,-6,6/m, 622,6mm,-62m,-6/mmm)	5
Cubic	3

For TM_2B with tetragonal structures, there are six independent elastic constants, C_{11} , C_{12} , C_{13} , C_{33} , C_{44} , C_{66} , because of $C_{22} = C_{11}$, $C_{23} = C_{13}$, $C_{44} = C_{55}$ as a result of the crystal symmetry.

$$C_{(\alpha\beta)} = \begin{pmatrix} C_{11} & C_{12} & C_{13} & 0 & 0 & 0 \\ C_{12} & C_{11} & C_{13} & 0 & 0 & 0 \\ C_{13} & C_{13} & C_{33} & 0 & 0 & 0 \\ 0 & 0 & 0 & C_{44} & 0 & 0 \\ 0 & 0 & 0 & 0 & C_{44} & 0 \\ 0 & 0 & 0 & 0 & 0 & C_{66} \end{pmatrix} \quad (3.34)$$

Generally, the elastic constants C_{11} and C_{33} are very high, which indicates the high resistance to the axial compression in these directions. Moreover, it is well known that the elastic constant C_{44} is the most significant parameter which indirectly determines the indentation hardness of a solid [124]. A large C_{44} implies a strong resistance to monoclinic shear in the (100) plane. Notably, the values of C_{11} (C_{66}) are larger than that of C_{33} (C_{44}); implying that the intra-layer chemical bonds are stronger than those between the layers.

For TMB with orthorhombic structures, there are nine independent elastic constants, C_{11} , C_{22} , C_{12} , C_{13} , C_{23} , C_{33} , C_{44} , C_{55} and C_{66} as a result of the crystal symmetry.

$$C_{(\alpha\beta)} = \begin{pmatrix} C_{11} & C_{12} & C_{13} & 0 & 0 & 0 \\ C_{12} & C_{22} & C_{23} & 0 & 0 & 0 \\ C_{12} & C_{12} & C_{33} & 0 & 0 & 0 \\ 0 & 0 & 0 & C_{44} & 0 & 0 \\ 0 & 0 & 0 & 0 & C_{55} & 0 \\ 0 & 0 & 0 & 0 & 0 & C_{66} \end{pmatrix} \quad (3.35)$$

The mechanical stability criteria can be represented in a uniform manner for orthorhombic structure [125]:

$$\begin{aligned}
 & C_{ii} > 0 (i = 1; 2; 3; 4; 5; 6), \\
 & C_{11} + C_{22} + C_{33} + 2(C_{12} + C_{13} + C_{23}) > 0, (C_{11} + C_{22} - \\
 & 2C_{12}) > 0; (C_{11} + C_{33} - 2C_{13}) > 0, (C_{22} + C_{33} - 2C_{23}) > 0
 \end{aligned} \tag{3.36}$$

3.2.6.2. Elastic constants and stability criteria under pressure

For tetragonal structure the elastic constants under pressure (P) are related to those under zero pressure, shown as follows [126]:

$$\begin{aligned}
 \tilde{C}_{ij} &= C_{ij} \quad (i = 1, 2, 3; j = 4, 5, 6), \quad \tilde{C}_{ii} = C_{ii} - P (i = 1, 2, 3, 4, 5, 6), \\
 \tilde{C}_{12} &= C_{12} + P, \quad \tilde{C}_{13} = C_{13} + P, \quad \tilde{C}_{23} = C_{23} + P, \quad \tilde{C}_{45} \\
 &= C_{45}, \quad \tilde{C}_{46} = C_{46}, \quad \tilde{C}_{56} = C_{56}
 \end{aligned} \tag{3.37}$$

The stability criteria of material under pressure are similar to those under zero pressure, just replacing C_{ij} with \tilde{C}_{ij} ($i, j = 1, 2, 3, 4, 5, 6$) [127]. The single crystal elastic coefficients (C_{ij}) satisfy the stability criteria, which leads to the following restrictions on the elastic coefficients under isotropic pressure as follows:

$$\begin{aligned}
 & \tilde{C}_{ii} > 0, (i = 1, 2, 3, \dots 6), \quad \tilde{C}_{11} + \tilde{C}_{33} - 2\tilde{C}_{13} > 0, \\
 & (2\tilde{C}_{11} + \tilde{C}_{33} + 2\tilde{C}_{12} + 4\tilde{C}_{13}) > 0, (\tilde{C}_{11} - \tilde{C}_{12}) > 0.
 \end{aligned} \tag{3.38}$$

On the other hand, the mechanical stability for orthorhombic structure leads to restrictions on the elastic coefficients under isotropic pressure as follows:

$$\begin{aligned} \tilde{C}_{ii} = C_{ii} - P > 0, (i = 1, 2, 3, 4, 5, 6), (C_{11} + C_{22} - 2C_{12} - 4P) > 0, \\ (C_{11} + C_{33} - 2C_{13} - 4P) > 0, \quad (C_{22} + C_{33} - 2C_{23} - 4P) > 0, \\ (C_{11} + C_{22} + C_{33} + 2C_{12} + 2C_{13} + 2C_{23} + 3P) > 0 \end{aligned} \quad (3.39)$$

Where: C_{ij} are the elements of elastic coefficient matrix

3.2.6.3. Polycrystalline elastic modulus

The arithmetic average of the Voigt and Reuss bounds is known as the Voigt-Reuss-Hill (VRH) average, which is regarded as the best estimate for the theoretical value of polycrystalline elastic modulus [128]:

$$G_H = (G_R + G_V)/2, \quad B_H = (B_R + B_V)/2 \quad (3.40)$$

Where: B_V (G_V) and B_R (G_R) are the bulk modulus (shear modulus) in the Voigt and Reuss approximations respectively.

The Young modulus and Poisson ratio can be computed from the formula [128]:

$$E = 9BG / (3B + G), \quad \nu = (3B - 2G) / (6B + 2G) \quad (3.41)$$

A larger B/G value (>1.75) for a solid indicates ductile behavior while a smaller B/G value (<1.75) usually means brittle material. Similarly, Poisson ratio $\nu > 0.26$ corresponds for ductile compounds usually [129].

3.2.7. Elastic anisotropy

It is known that elastic anisotropy correlates with anisotropic plastic deformation and behavior of micro cracks in the material. Hence it is important to study the elastic anisotropy in intermetallic structures in order to further understand these properties and improve their mechanical durability. Most of crystals exhibit elastic anisotropies to some extent, and several criteria have been developed to describe it. The elastic anisotropy of a crystal can be characterized by the universal anisotropic index A^U and by the indexes describing the behavior in shear and compression (A_G and A_B). The universal elastic anisotropy index A^U and indexes A_G and A_B for a crystal with any symmetry may be proposed as follows [130, 131]:

$$A^U = 5 \frac{G_V}{G_R} + \frac{B_V}{B_R} - 6 \geq 0 \quad (3.42)$$

$$A_G = \frac{G_V - G_R}{G_V + G_R} 100, \quad A_B = \frac{B_V - B_R}{B_V + B_R} 100 \quad (3.43)$$

For an isotropic crystal, all three factors must be one, while any value smaller or greater than one is a measure of the degree of elastic anisotropy possessed by the crystal. $A^U = 0$ corresponds to an isotropic crystal. The deviation of A^U from zero indicates the extent of single crystal anisotropy and accounts for both the shear and the bulk contributions unlike all other existing anisotropy measures. Thus, A^U represents a universal measure to quantify the single crystal elastic anisotropy. $A_B = A_G = 0$ represents the elastic isotropy, while $A_B = A_G = 1$ means the maximum elastic anisotropy [132]. The shear anisotropic factors provide measures of the degrees of anisotropy in atomic bonding in different crystallographic planes.

The elastic anisotropy of a tetragonal crystal can be measured by two shear anisotropy factors (Zener ratios) [124]:

$$A_1 = \frac{2C_{66}}{C_{11} - C_{12}} = A_2, \quad A_3 = \frac{C_{44}}{C_{11} + C_{33} - 2C_{13}} \quad (3.44)$$

For an orthorhombic crystal the three shear anisotropy factors (Zener ratios):

1. The anisotropic factor for the $\{1\ 0\ 0\}$ shear planes between (011) and (010) directions is define as:

$$A_1 = \frac{4C_{44}}{C_{11} + C_{33} - 2C_{13}} \quad (3.45)$$

2. The anisotropic factor for the $\{0\ 1\ 0\}$ shear planes between (101) and (001) directions is:

$$A_2 = \frac{4C_{55}}{C_{22} + C_{33} - 2C_{23}} \quad (3.46)$$

and

3. The anisotropic factor for the $\{0\ 0\ 1\}$ shear planes between (110) and (010) directions is:

$$A_3 = \frac{4C_{66}}{C_{11} + C_{22} - 2C_{12}} \quad (3.47)$$

The simplest way to illustrate the anisotropy of mechanical moduli is to plot them in the three-dimensional space as a function of direction. For tetragonal crystal class, the directional dependence of Young modulus (E) or bulk modulus (B) and torsion modulus can be written as [121, 133]:

$$\frac{1}{E} = S_{11}(l_1^4 + l_1^4) + (2S_{13} + S_{44})(l_1^2 l_3^2 + l_2^2 l_3^2) + S_{33}l_3^4 + (2S_{12} + S_{66})l_1^2 l_2^2 \quad (3.48)$$

$$\frac{1}{B} = (S_{11} + S_{12} + S_{13})(l_1^2 + l_2^2) - (2S_{13} - S_{33})l_3^2 \quad (3.49)$$

$$\frac{1}{T} = S_{44} + \frac{4(S_{11} - S_{12} - S_{44})}{2}(l_1^2 l_2^2 + l_2^2 l_3^2 + l_1^2 l_3^2) \quad (3.50)$$

For orthorhombic crystal system [133]:

$$\begin{aligned} \frac{1}{E} = & (S_{11} + S_{22} + S_{33})l_1^4 + (2S_{12} + S_{66})l_1^2 l_2^2 + (2S_{23} + S_{44})l_2^2 l_3^2 \\ & + (2S_{13} + S_{55})l_1^2 l_3^2 \end{aligned} \quad (3.51)$$

$$\frac{1}{B} = (S_{11} + S_{12} + S_{13})l_1^2 + (S_{12} + S_{22} + S_{23})l_2^2 + (S_{13} + S_{23} + S_{33})l_3^2 \quad (3.52)$$

In the equations above, S_{ij} represents the compliance matrix and l_1 , l_2 and l_3 are the direction cosines, which are given as $l_1 = \sin\theta \cos\varphi$, $l_2 = \sin\theta \sin\varphi$ and $l_3 = \cos\theta$ in the spherical coordinates.

3.2.8. Acoustic sound velocities and Debye temperatures

The phase velocities of pure transverse and longitudinal modes of the TMB and TM₂B compounds can be calculated from the single crystal elastic constants following the procedure of Brugger [134].

The sound velocities are determined by the symmetry of the crystal and propagation direction. For example, the pure transverse and longitudinal modes can only be found in [001], [110] and [111] directions in a cubic crystal and the sound propagating modes in other directions are the quasi-transverse or quasi-longitudinal waves. In the principal directions, the acoustic velocities for tetragonal system can be expressed by:

$$\begin{aligned} [100]v_l = [010]v_l = \sqrt{C_{11}/\rho}; \quad [001]v_{t1} = \sqrt{C_{44}/\rho}; \quad [010]v_{t2} = \sqrt{C_{66}/\rho} \\ [001]v_l = \sqrt{C_{33}/\rho}; \quad [100]v_{t1} = [010]v_{t2} = \sqrt{C_{66}/\rho} \end{aligned} \quad (3.53)$$

$$[110]v_l = [010]v_l = \sqrt{(C_{11} + C_{12} + 2C_{66})/2\rho}; [001]v_{t1} = \sqrt{C_{44}/\rho};$$

$$[1\bar{1}0]v_{t2} = \sqrt{(C_{11} - C_{12})/2\rho}$$

For orthorhombic system can be expressed by:

$$[100]v_l = \sqrt{C_{11}/\rho}; [010]v_{t1} = \sqrt{C_{66}/\rho}; [001]v_{t2} = \sqrt{C_{55}/\rho}$$

$$[010]v_l = \sqrt{C_{22}/\rho}; [100]v_{t1} = \sqrt{C_{66}/\rho}, [001]v_{t2} = \sqrt{C_{44}/\rho} \quad (3.54)$$

$$[001]v_l = \sqrt{C_{33}/\rho}; [100]v_{t1} = \sqrt{C_{55}/\rho}, [010]v_{t2} = \sqrt{C_{44}/\rho}$$

Where: ρ is the compound density; v_l is the longitudinal sound velocity; v_{t1} and v_{t2} refer the first transverse mode and the second transverse mode, respectively. The anisotropic properties of sound velocities indicate the elastic anisotropy in these crystals. For example, the C_{11} , C_{22} and C_{33} determine the longitudinal sound velocities along $[100]$, $[010]$ and $[001]$ directions, respectively, and C_{44} , C_{55} and C_{66} correspond to the transverse modes [135].

As a fundamental parameter for the materials' thermodynamic properties, Debye temperature Θ_D is related to specific heat, thermal expansion and elastic constants. The Debye temperature can be estimated from the average sound velocity by the following equation based on elastic constant evaluations [136]:

$$\Theta_D = \frac{h}{k} \left(\frac{3nN_A}{4\pi M} \right)^{\frac{1}{3}}$$

$$v_m = \left[\frac{1}{3} \left(\frac{1}{v_t^3} + \frac{1}{v_l^3} \right) \right]^{-\frac{1}{3}} \quad (3.55)$$

$$v_t = \sqrt{\frac{G}{\rho}}, v_l = \sqrt{\frac{(B + \frac{4G}{3})}{\rho}}$$

Where: B and G are isothermal bulk modulus and shear modulus, respectively, v_l is the longitudinal velocity and v_t is the transverse sound velocity.

3.2.9. Disorder In Solids

Many crystal structures possess static positional disorder. The crystal may either contain fewer atomic species than there are crystallographically equivalent sites to populate, or there might, for example, be statistical occupancy of a given crystallographic site by more than one type of atom in different unit cells. This positional disorder is typically manifested in site occupancy factors of less than unity for the average unit cell.

Castep code allows us to model positional disorder by specifying atom occupancy and by defining mixture atoms.

The vast majority of atoms will have occupancy of unity. However, in the case of an atom on a partially occupied interstitial position, it can specify an occupancy ranging from 0.0 to 1.0.

Atom occupancies can be modified in the Properties Explorer.

Atomic sites in a crystal can also be described in terms of a hybrid atom that consists of two or more element types. The relative concentrations can be set for any number of atoms, but the total concentration must not exceed 100%. The mixture atoms description is the most often used representation of solid solutions, metallic alloys, disordered minerals, etc.

3.2.9.1. Disorder and first principles calculations

There are a number of different approaches for dealing with disorder in first principles calculations:

1. Virtual crystal approximation (VCA): this offers technically the simplest approach, allowing calculations on disordered systems to be carried out at the same cost as calculations for ordered structures. VCA ignores any possible short range order and assumes that on each potentially disordered site there is a virtual atom which interpolates between the behavior of the actual components. This approach neglects such effects as local distortions around atoms and cannot be expected to reproduce the finer details of the disordered structures very accurately.
2. Using large ordered supercells followed by configurational averaging: this is a very expensive approach with limited applicability. For example, it is not possible to treat arbitrary and particularly small concentrations.
3. Coherent potential approximation (CPA): this method approximates a configurationally random alloy with an effective medium that is determined self-consistently from the condition of stationary scattering. The CPA technique is used extensively with model

Hamiltonians with well-known scattering properties or in the context of multiple scattering methods of band structure calculation (KKR, LMTO). CPA is not well suited to total energy calculations or geometry optimization tasks.

4. "Computational alchemy": this method uses the perturbation theory to calculate the response to the difference between the true and VCA potentials. This approach is very demanding computationally, as are all linear response calculations.

The basic ideas for the workable VCA implementation for DFT methods, in particular for the pseudopotential-based techniques, were set out by [137]. The main statement of the implementation of VCA with ultrasoft potentials can be expressed as:

$$V_{ent}(r, r') = \sum_I \sum_{\alpha} w_{\alpha}^I V_{ps}^{\alpha}(r - R_{I\alpha}, r' - R_{I\alpha})$$

Where the total external potential is generated as the sum of the nonlocal potentials of each atomic species, α , taken with the weights, w , of the component atoms in the mixture atom. This means that all the key components of the ultrasoft potentials, i.e., the local part, V_{loc} , and the D and Q matrices, are all weighted according to the site occupancies.

3.3. Conclusions

DFT calculations allow us to calculate many properties of crystalline solids with a lower cost such as electronic structure, magnetic moment, elastic constants. Furthermore, other properties can be calculated using semi-empirical formalism that uses DFT results.

In this chapter I have discussed all properties which are dealt in this thesis, starting by magnetism in materials through the phase transition, population analysis, hardness, elastic properties, elastic anisotropy, acoustic sound velocities and debye temperatures up to virtual crystal approximation (VCA) approach.

CHAPTER 4: Semi-Borides TM_2B (TM=Fe, Co, Ni)

Under Pressure.

4. Structure, magnetic, hardness and anisotropic elastic properties of boride coating TM₂B (TM=Fe, Co, Ni) under pressure.

It is known that Fe₂B and Co₂B compounds are ferromagnetic with magnetic moment 1.96 and 1.18 μ B, whereas Ni₂B carry no magnetic moment [138-140]. Meneses-Amadoreta *et al.* [141], used indentation for the mechanical characterization of Fe₂B layers and found that their hardness ranged from 9 to 14.2 GPa depending on boriding temperature and time. Furthermore, the mechanical properties of FeB and Fe₂B layers are estimated by Berkovich Nano indentation on boride steels. Their measurements show that hardness range between 14.5 GPa and 19 GPa for FeB and from 13 to 16.3 GPa for Fe₂B depending on temperature and boriding time, the hardness of CoB and Co₂B range between 15 and 16 GPa respectively [1, 142-144]. The hardness of nickel borides is measured after different diffusion processes of boriding using Knoop [11, 145] or Vickers methods [12, 146]. Ni₂B borides hardness of about 12.75 GPa [11] and measured by Nano indenter 17.98 GPa [147].

Britton *et al.* [113] show that there are correlations between crystals anisotropy and both the elastic and the plastic behavior during Nano indentation. The electronic and elastic properties of the semi borides X₂B (X=Cr, Mn, Fe, Co, Ni, Mo, W) compounds have been investigated in detail [139, 148]. However, anisotropic elastic properties and pressure effects for these compounds have not been presented. They are able to provide much insight on structures concerning behavior under pressure. The understanding of borides as protective coatings on steel surfaces especially mechanical properties needs the knowledge of their elastic constants and polycrystalline elastic moduli.

In this chapter, I present first-principles calculations results for the structure, magnetic, hardness and anisotropic elastic properties of Fe₂B, Co₂B and Ni₂B compounds under pressure in the range from 0 to 90 GPa, in order to predict the critical transition pressure from ferromagnetic (FM) to nonmagnetic states (NM). Furthermore, mechanical anisotropies in both cases are discussed by calculating different anisotropic properties indexes and factors. I plot the three dimensional (3D) surfaces and planar contours of bulk, Young and torsion moduli of TM₂B (TM=Fe, Co and Ni) compounds along (100) and (001) crystallographic planes in order to reveal their elastic anisotropy. I demonstrate that all previous properties change strongly with increasing pressure.

4.1. Structure aspects and calculation methods

Boride TM₂B (Figure 17) belongs to the body-centered tetragonal Bravais lattice, with I4/mcm space group where the unit cell contains four equivalent TM atoms in the positions of point group mm and two equivalent B atoms in the positions of point group 42 [128]. The B atoms in TM₂B are located between two layers of TM atoms in a distorted closely packed arrangement.

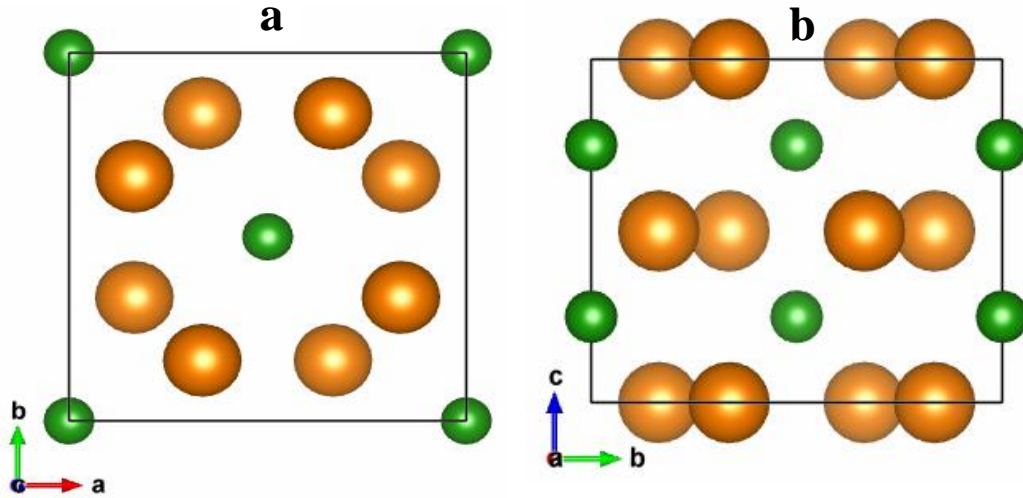


Figure 17. The crystal structure of TM₂B illustrated by ball and stick model.

(a) View along c axis; (b) view along a axis; the big ball refers to B and the small ball refers to TM atom.

CASTEP code is used for the whole study, which uses the plane wave expansion method in reciprocal space [149]. Ultra-soft Vanderbilt pseudo-potentials are employed to represent the electrostatic interactions between valence electrons and ionic cores [150] which are used with the following valence electronic configurations Fe: $3d^64s^2$, Co: $3d^74s^2$, Ni: $3d^84s^2$ and B: $2s^22p^1$. Generalized gradient approximation PBE-GGA was used for exchange-correlation energy calculations [151]. The kinetic energy cut-off value is selected as 500eV, which is sufficient to obtain reliable results. Total energies are evaluated in the first irreducible Brillouin zone with the following Monk-horst–Pack grids [152]: (10 x10x 10) for all compounds.

The convergence criteria of total energy and structure optimization are set to fine quality with the energy tolerance of 10^{-6} eV/atom. BFGS (Broydene-Fletcher-Goldarbe-Shanno) optimization method was performed to obtain the equilibrium crystal structures of TM₂B with maximum atom displacement and force set to 0.002 \AA and 10^{-4} eV/\AA .

Structure, hardness and anisotropic elastic properties are calculated at 0 GPa and high pressure (above critical transition pressure for Fe₂B and Co₂B).

The cohesive energy (E_{coh}) of a material, (a useful fundamental property), is a measure of the relative binding forces. The stability of our compounds can be evaluated by calculating two energy parameters, cohesive energy E_{coh} and formation energy E_f defined as follows:

$$E_{coh}(TM_2B) = \frac{E_{total}(TM_2B, Cell) - 2nE_{iso}(TM) - nE_{iso}(B)}{n} \quad (4.1-1)$$

$$E_f(TM_2B) = E_{coh}(TM_2B) - 2E_{coh}(TM) - E_{coh}(B) \quad (4.1-2)$$

Where: $E_{coh}(TM_2B)$ is the cohesive energy of TM₂B per unit formula; $E_f(TM_2B)$ is its formation energy; $E_{coh}(TM)$ is the cohesive energy of transition metal element per atom; $E_{total}(TM_2B, Cell)$ is the total calculated energy of TM₂B per conventional unit cell; $E_{iso}(TM)$ is the total energy of an isolated TM atom and finally n refer to the number of unit formula TM₂B in the conventional cell. The calculation method for $E_{coh}(TM_2B)$ can also be used to evaluate the cohesive energy of pure elements B and TM. *Eqs.* (1) and (2) require negative values of $E_{coh}(TM_2B)$ and $E_f(TM_2B)$ to refer to a thermodynamically stable structure. The crystal structures of TM₂B studied in this thesis are built based on experimental results.

4.1.1. Structural properties and stability

The calculated lattice parameters, unit cell volumes, bulk modulus, cohesive energy and the formation energy of pure elements and TM₂B along with the available experimental and previous theoretical data for comparison, are shown in Table 5 and Table 6. These results show that the calculated structure parameters are in good agreement with the experimental values. At equilibrium, calculations show that Fe₂B and Co₂B compounds carry magnetic moment with

values 1.83 and 1.12 μ_B respectively, while Ni₂B shows the paramagnetic behavior. The calculated magnetic moments of our compounds, at 0 GPa, are in good agreement with theoretical and experimental values (Table 6). These moments are smaller than the magnetic moments of pure elements Fe, Co and Ni which behave as weak ferromagnetic with a magnetic moment 2.217 μ_B for iron, while both cobalt and nickel behave as strong ferromagnetic with a magnetic moment: 1.753 μ_B and 0.616 μ_B , respectively [153, 154]. Indeed, when B atoms are inserted in TM crystals, the volume concentration of metallic TM–TM bonds decrease and are replaced by the newly formed covalent TM–B and B–B. The calculated values of cohesive energy of Fe₂B, Co₂B and Ni₂B are, respectively, -18.92, -18.58 and -22.06eV per formula unit. Furthermore, the formation energies are -1.475, -0.98 and -1.068eV for Fe₂B, Co₂B and Ni₂B respectively, indicating that all of these TM₂B compounds are stable.

Table 5. The calculated ground state properties of pure elements, Fe, Co, Ni and B with experimental and other theoretical works.

Parameters	Fe	Co	Ni	B
E_{iso}	-859.821 (-855.913) ^a	-1037.55	-1347.162	-70.501 (-70.492) ^a
E_{total}	-865.315 (865.335) ^a	-1043.113	-1354.431	-76.953 (-76.875) ^a
E_{coh}	-5.494 (-4.28) ^{exp} (-9.422) ^a	-8.344	-7.2697	-6.452 (-6.383) ^a
volume	11.775 (11.82) ^{exp}	11.16 (10.90) ^b	11.04 (10.87) ^b	8.652 (8.763) ^a

^{exp}Ref. [153]. ^aRef. [139], ^bRef. [154].

Table 6. The calculated ground state properties of TM₂B. Experimental and theoretical values are listed in parentheses. Total cell energy E_{total} (eV/f.u.), cell parameters (a , b , c in Å), fractional coordinates of TM and B atoms (x , y and z), volume V (Å³), Bulk modulus (GPa), magnetic moment (μ_B /atom), cohesive energy E_{coh} (eV/f.u.), formation energy E_f (eV/f.u.).

Parameters	Fe ₂ B	Co ₂ B	Ni ₂ B
E_{total}	-3618,115	-4328.344	-5573.764
(a, b, c)	5.012, 4.209 (5.110, 4.240) ^{exp}	4.981, 4.289 (5.015, 4.22) ^{exp}	4.988, 4.295 (4.9910, 4.247) ^{exp}
TM (x, y, z)	0.1666, 0.666, 0 (0.1649, 0.6649, 0) ^{exp}	0,1686, 0,6686, 0 (0.168, 0.668, 0) ^{exp}	0.1686, 0,6686, 0 (0.1677, 0.6677, 0) ^{exp}
B(x, y, z)	0, 0, 0.25	0, 0, 0.25	0, 0, 0.25
V	52.87	53.22	53.66
B	244.59 (249.7) ^d	257.46 (247.26) ^d	262.88 (238.12) ^d
μ_B /atom	1.83 (1.62) ^{exp2} , (1.96) ^b	1.12 (1.182) ^b	0
E_{coh}	-18.92, (-26.70) ^b	-18.58(-24.14) ^b	-22.06(-22.10) ^b
E_f	-1.475, (-1.475) ^b , (-0.85) ^c	-0,98(-1.022) ^b	-1,068(-1.18) ^b

^{exp}Ref. [155], ^bRef. [139], ^cRef. [156], ^dRef. [148].

4.1.2. Pressure effects.

Usually, in order to induce some significant change in the structures, high pressures are needed for the study of materials. I applied increasing pressure on my three compounds and examined the corresponding magnetic moment for each compound. Figure 18 presents the evolution of the magnetic moment and the V/V_0 ratio of Fe₂B and Co₂B with increasing pressure. As it can be seen in this figure, there is an abrupt transition from magnetic to nonmagnetic state which causes an extinction of the magnetic moment; the critical transition pressures are: 85 GPa for both Fe₂B and Co₂B.

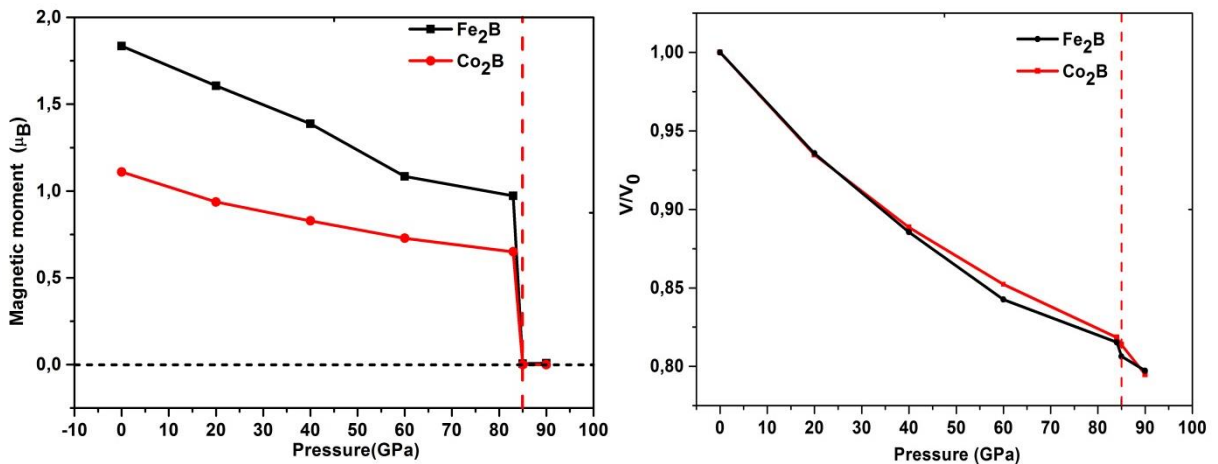


Figure 18 Pressure dependence of of magnetic moment and the normalized volume V/V_0 for Fe₂B and Co₂B.

I applied increasing pressure on my compounds and examined the corresponding total energy, volume, lattice parameters, c/a ratio and magnetic moment for each compound. Figure 19 and Figure 20, presents the evolution of these parameters of Fe₂B and Co₂B compounds with increasing pressure, because they are ferromagnetic.

It is obvious that the V/V_0 decreases (Figure 18) with the increase of pressure, and the values of V/V_0 for Fe₂B and Co₂B at a critical pressure (85 GPa) are 0.806 and 0.8137, respectively.

Up to ≈ 84 GPa, TM₂B compounds show a linear decrease in their lattice parameters and c/a ratio of similar magnitude. There is a discontinuous change in slope for the structure parameters between 84 GPa and 85 GPa for Fe₂B and Co₂B (Figure 18), this abrupt change of lattice parameters are linked with the magnetic state transition (FM to NM), and there are two changes of lattice parameters at the critical pressure: one with the decrease of a and the increase of c for Fe₂B and the other, the increase of a and the decrease of c for Co₂B.

Near QPT (Figure 19), the abrupt changes of lattice parameters between 84 and 85 GPa are obvious. It can be seen that the parameter a of Fe₂B has a tiny decrease between 84 and 85 GPa (1.2%), while the parameter c has a tiny increase (1.5%), which mean that the easy axes of magnetization for Fe₂B are the direction $\langle 100 \rangle$, $\langle 010 \rangle$ and the hard axis is the direction $\langle 001 \rangle$, this is confirmed experimentally by Edström *et al.* [157]. Contrary, the parameter, a of Co₂B has a tiny increase between 84 and 85 GPa (0.4%), while the parameter c has a tiny decrease (1.3%), which mean that the easy axis of magnetization for Co₂B is the direction $\langle 001 \rangle$, and the hard axes are the direction $\langle 100 \rangle$, $\langle 010 \rangle$, also, this is confirmed experimentally by Edström *et al.* [157]. Here, I can note that the percentage of relative change is due to value of the magnetic moment.

From the comparison of Fe₂B and Co₂B calculation data, it is possible to assign the sudden change of c/a ratio at 85 GPa pressure to a magneto-elastic transition, in Figure 19 and Figure 20, where c/a ratio decrease (increase) with increasing pressure (decreasing volume). All the abrupt changes of parameters are due to the a pronounced abrupt collapse of the magnetic moment (first order quantum phase transitions) from FM to PM state, which causes an extinction of the magnetic moment and a possible origin of this dependence is the magneto-volume effect [158].

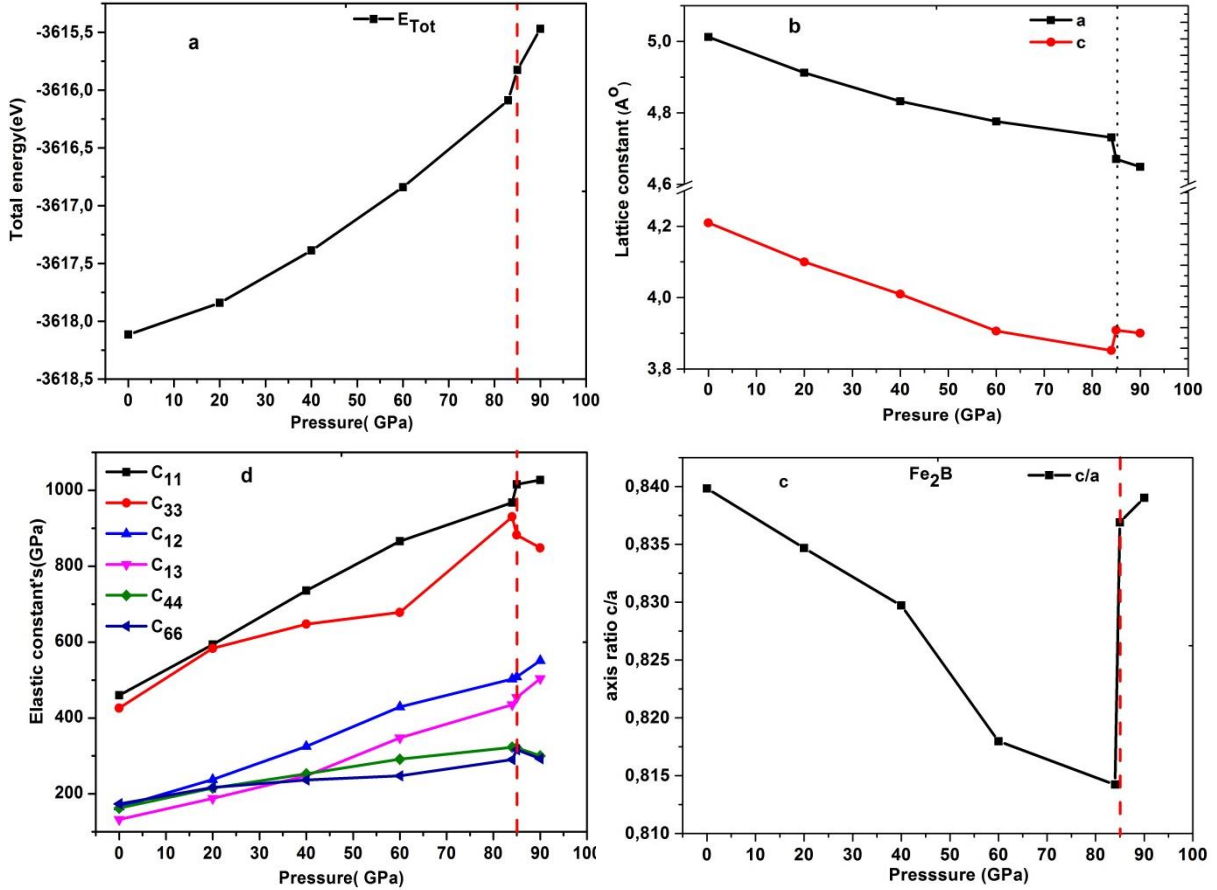


Figure 19 Pressure dependence of structure parameters and elastic constants for Fe₂B.

In order to show the dependence of pressure at 0 GPa (FM) and at a critical pressure (NM), I calculate the relative change of all parameters between the ferromagnetic and nonmagnetic states, they are obtained as:

$$\frac{\Delta X}{X} = \frac{X_{FM} - X_{NM}}{X_{FM}}, X = V, E_{coh}, E_f, B, H... \quad 4.1-3$$

The calculated percentage change of volume at 0 GPa and at transition pressure of our compounds, show a volume compression of 20%, 17.74% and 19.2% for Fe₂B, Co₂B and Ni₂B respectively, in applied pressure, which increase the bulk modulus of our compounds by 62%, 60% and 57%.

The formation energy E_f , is calculated to check the probability of thermodynamic existence of TM₂B under pressure. All formation energies are negative indicating that structures in two pressures conditions are thermodynamically stable. The formation energies of TM₂B at 0 GPa are less than TM₂B under pressure by 82.14%, 98.23% and 97.4% for both Fe₂B, Co₂B and Ni₂B respectively, implying that they have more thermodynamic stability without applied pressure.

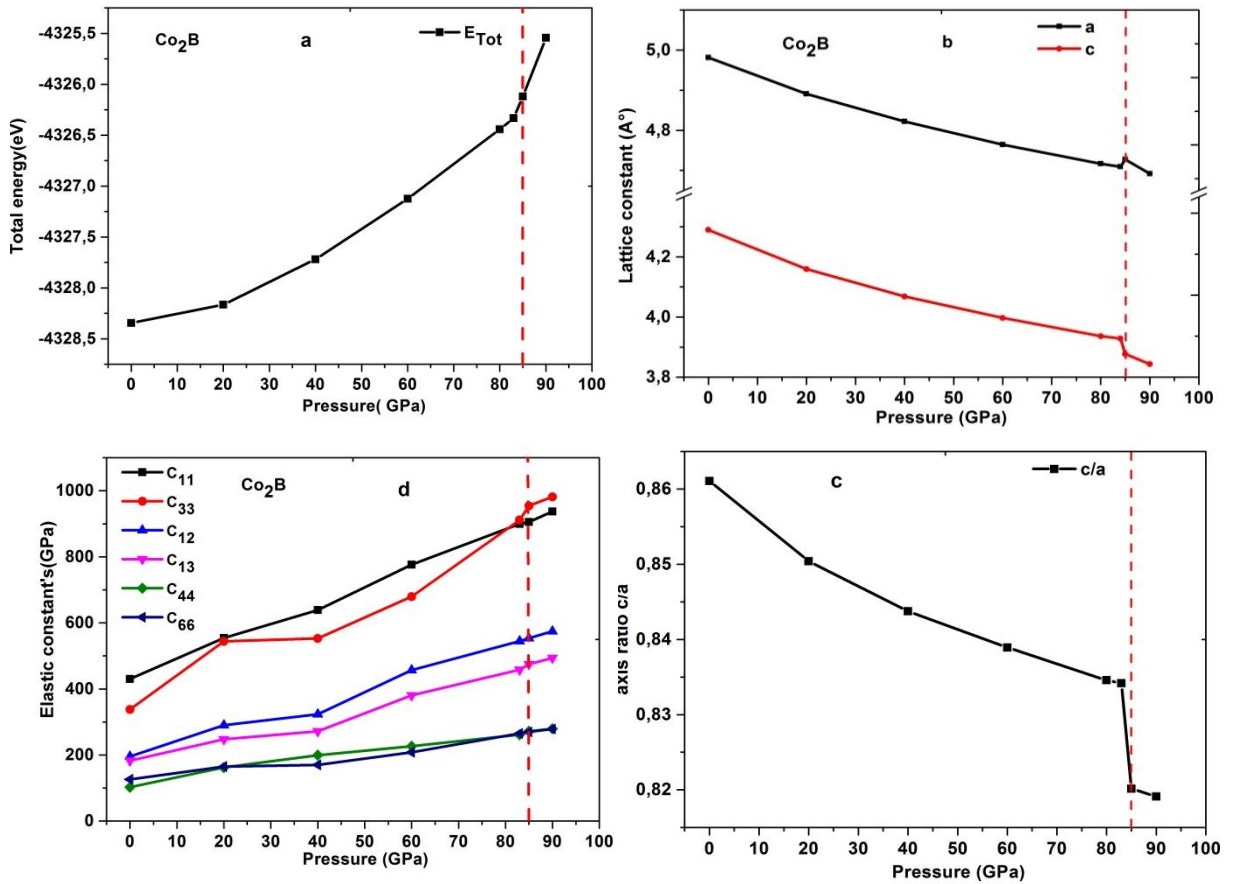


Figure 20. Pressure dependence of structure parameters and elastic constants for Co₂B.

Figure 21 presents the density of states for spin-up and spin-down electrons of TM₂B(TM=Fe, Co, Ni) at 0GPa and 85 GPa.

The calculated magnetic moments of our compounds, at 0 GPa, are in good agreement with theoretical and experimental values from literature (Table 6).

As shown in Figure 21 the difference between the density of spin-up and spin-down electrons corresponds to the saturated magnetic moment, μ_{sat} , at $T=0$. Indeed, when B atoms are inserted in TM crystals, the volume concentration of metallic TM–TM bonds decrease and are replaced by the newly formed covalent TM–B and B–B.

The magnitude of the magnetic moment is strongly related to the volume. Thus the values of equilibrium volume obtained in the magnetic case are larger than in NM case. A possible origin of this dependence is the magneto-volume effect [158]. Because the Pauli Exclusion Principle operates for parallel spins, the electron kinetic energy of the spin-polarized state is higher, and volume expansion relaxes the kinetic energy. Consequently the magnetic (high-spin) state has a larger volume than the non-magnetic state [159].

The bulk modulus is increased from 0 to 62.4% for Fe₂B and from 0 to 60% for Co₂B. In the NM state the bulk modulus B is systematically larger than in the magnetic state. The low value of bulk modulus in the magnetic case points to a larger compressibility. This means that Fe₂B and Co₂B are “softer” when are magnetically ordered and “harder” when are not. The calculations are important to obtain the correct ground state properties of TM₂B compounds due to the presence of magnetic elements Fe, Co and Ni. Total DOS at the Fermi level for Fe₂B and Co₂B increases under pressure by 50.6% and 22.8% and decrease by 17.4% for Ni₂B(Figure 21.) respectively, this enhanced $N(E_f)$ is derived entirely from the TM 3d states, with negligible contribution from the B 2p states. Following the above arguments I may predict the appearance of superconductivity in Fe₂B and Co₂B under pressure as is in the case of iron that undergoes a transition to superconducting phase above 30GPa when it loses its magnetic moment [160].

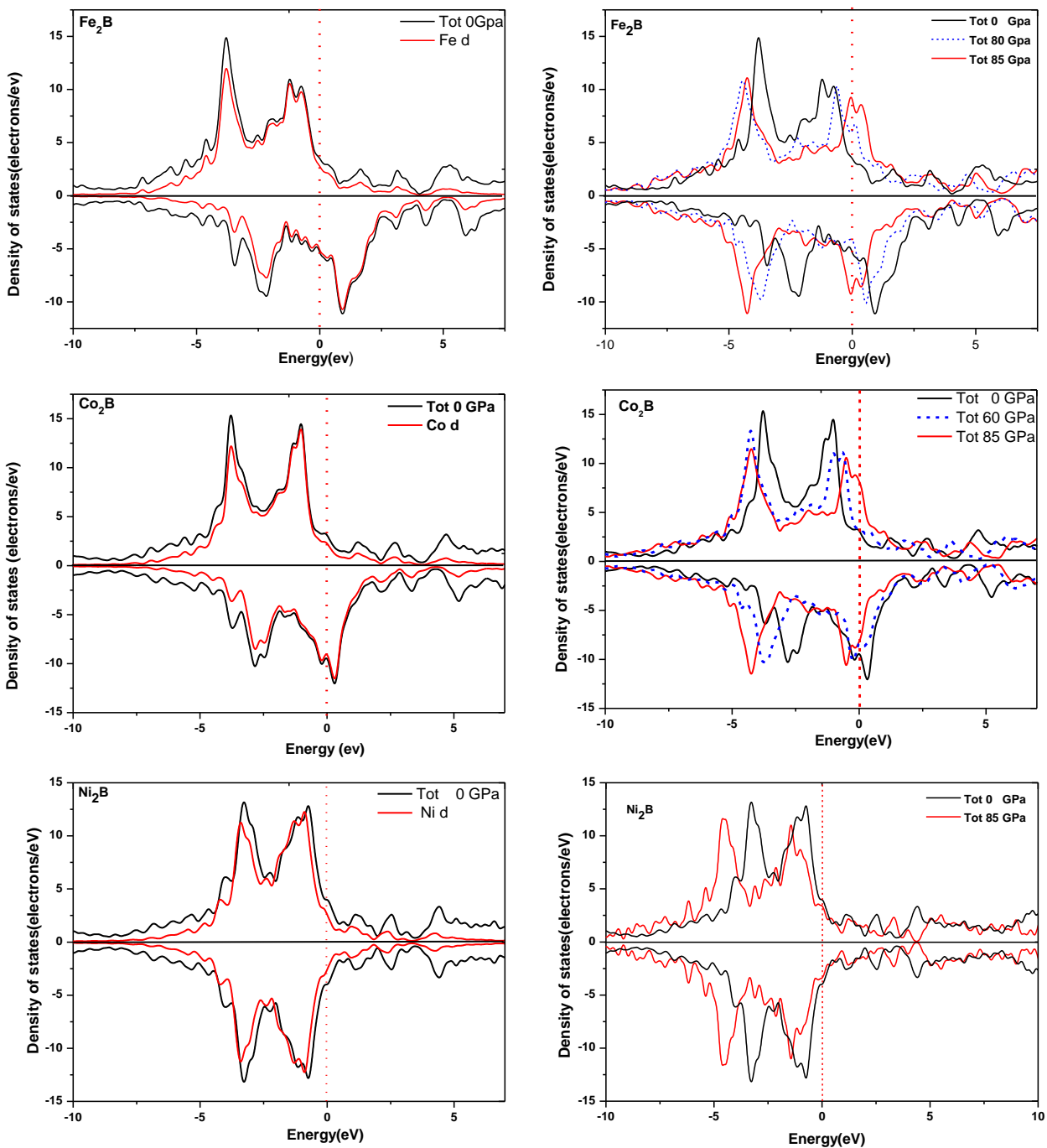


Figure 21 The calculated total and partial DOS of TM₂B, Left panel with spin polarization and right panel under pressure. Dashed line represents the Fermi level.

4.1.3. Hardness

Quite recently developed semi-empirical models used for preliminary theoretical estimation of intrinsic hardness. One of the first models has been proposed for the description of covalent crystals Based on the works of Gao *et al.* [120], the hardness of TM–B and B–B bonds in each of our three compounds TM₂B are evaluated and compared. It is find that GGA-PBE (USP) method can be effectively used to predict the H value, and the proposed analytical expressions have been used to determine the hardness from first-principles theory [119]. I consider the hardness of B-B and TM-B bonds only. The hardness of TM–TM bond, however, is not taken into consideration in this work, because the hardness of metallic bond is ill defined in this method. The strength of the bond per the unit volume can be characterized by average overlap populations. For complex multi-bonding compounds, the hardness of the u type bond can be calculated (relation 0 3.30). In Table 7; I use MPA (3.29) to estimate the bond overlap population

The longest TM–B bond length considered in this work is limited to 3.1Å because the interaction between TM atom and the second nearest neighbor B atom is assumed to be weaker than that between the nearest-neighbor boron atoms.

The calculated bond length, population overlaps and the contribution of TM–B and B-B bonds to the hardness H_v in Fe₂B, Co₂B and Ni₂B are listed in Table 7, with material hardness of our three compounds. The hardness of B–B bond H_u is significantly larger than TM–B bond in TM₂B compounds because of the large bond overlap population. In the case of Fe₂B the B–B bond is harder than the other B–B bond in Co₂B and Ni₂B because B–B bond has the shortest bond length in this compound and hence maximum overlap population.

The calculated hardness as follows: Fe₂B (18.34 GPa), Co₂B (18.07 GPa) and Ni₂B (17.82 GPa) are in fairly good agreement with the experimental values of $(16.2 \pm 0.017 \text{ GPa})$ for Fe₂B, (17.99 GPa) for Co₂B [142] and (17.98 GPa) for Ni₂B [147].

Table 7. The predicted hardness of TM₂B. Experimental and theoretical values are listed in parentheses. Different pairs of atoms (B–B, TM–B). Average bond length of nearest-neighbor atoms d^u (Å), average overlap population of u type bond, nearest-neighbor numbers N^u for different pairs of atoms, cell volume Ω (Å³), volume of a bond of u type v_v^u , hardness of u type bond H^u (GPa) and hardness H (GPa).

Species	Bond	d^u	p^u	N^u	Ω	v_v^u	H^u	H
	B-B	2.105	0.64	2		2.952	85.270	
Fe ₂ B	Fe-B	2.144	0.15	32	105.76	3.121	16.658	18.34 (18.2) ^a (16.2±0.011) ^{exp}
Co ₂ B	B-B	2.145	0.58	2	106.456	3.152	63.83	
	Co-B	2.140	0.15	32		3.130	16.70	18.07 (17.99) ^{exp}
Ni ₂ B	B-B	2.148	0.57	2	107.310	3.173	62.04	
	Ni-B	2.144	0.15	32		3.155	16.48	17.82 (17.98) ^{exp1}

^a Ref. [148], ^{exp} Ref. [142], ^{exp1} Ref. [147].

4.1.4. Elastic properties under pressure

There are six independent elastic constants for TM₂B with tetragonal structures, C_{11} , C_{12} , C_{13} , C_{33} , C_{44} , C_{66} , because of $C_{22} = C_{11}$, $C_{23} = C_{13}$, $C_{44} = C_{55}$ as a result of the crystal symmetry. The elastic constants of single crystalline TM₂B compounds are presented in Table 8. Generally, the elastic constants C_{11} and C_{33} are very high, both at zero and at high pressure, which indicates the high resistance to the axial compression in these directions.

Moreover, it is well known that the elastic constant C_{44} is the most significant parameter which indirectly determines the indentation hardness of a solid [124]. A large C_{44} implies a strong resistance to monoclinic shear in the (100) plane. Fe₂B has the highest C_{44} among our compounds which means its ability to resist shear distortion in the (100) plane is the strongest. The highest C_{44} for Fe₂B than those for the other compounds means that its ability to resist shear distortion in the (100) plane is the strongest. The results in Table 8 indicate that TM₂B have relatively strong anisotropic elastic constants resulting in the directional dependence of the moduli. Notably, the values of C_{11} (C_{66}) are larger than that of C_{33} (C_{44}) at 0 GPa and under pressure, implying that the intra-layer chemical bonds are stronger than those between the layers. Moreover the calculated percentage change in lattice parameters a and c between FM and NM cases are 6.8% and 7.34% for Fe₂B, while for Co₂B are 5.15% and 9.65%. The other compression moduli (C_{12} and C_{13}) are significantly smaller for Fe₂B, while for Co₂B and Ni₂B are significantly larger. They correspond to the intra and inter-layer moduli under bi-axial stress conditions.

The stability criteria of material under pressure are similar to those under zero pressure, just replacing C_{ij} with \tilde{C}_{ij} ($i, j = 1, 2, 3, 4, 5, 6$) [127] where \tilde{C}_{ij} are given by relations (3.37).

The single crystal elastic coefficients (C_{ij}) satisfy the stability criteria on the elastic coefficients under isotropic pressure given by (3.38).

Table 8. The calculated full set elastic constants of TM₂B (under 0 and a critical pressure, in GPa) with other theoretical works.

Species	Elastic constants					
	C_{11}	C_{33}	C_{12}	C_{13}	C_{44}	C_{66}
Fe ₂ B (0 GPa)	459.7	426.3	165.6	132.3	162.6	173.7
	413 ^b	389 ^b	154 ^b	132 ^b	148 ^b	157 ^b
Fe ₂ B (85 GPa)	1010.4	839	541.3	488.4	298	288.4
Co ₂ B (0 GPa)	430	337.68	195.7	183	102.9	126.4
	417.7 ^a	310.3 ^a	207.2 ^a	183.1 ^a	103.9 ^a	109.5 ^a
Co ₂ B (85 GPa)	892.2	887.2	552.1	493.3	242.1	227.8
Ni ₂ B (0 GPa)	410.8	351.3	218	180.4	86.7	126.6
	397.2 ^a	351.8 ^a	191.2 ^a	158.2 ^a	79.6 ^a	126.9 ^a
Ni ₂ B (85 GPa)	864.68	906.29	523.46	447.5	225.46	284.23

^aRef. [148], ^bRef. [161]

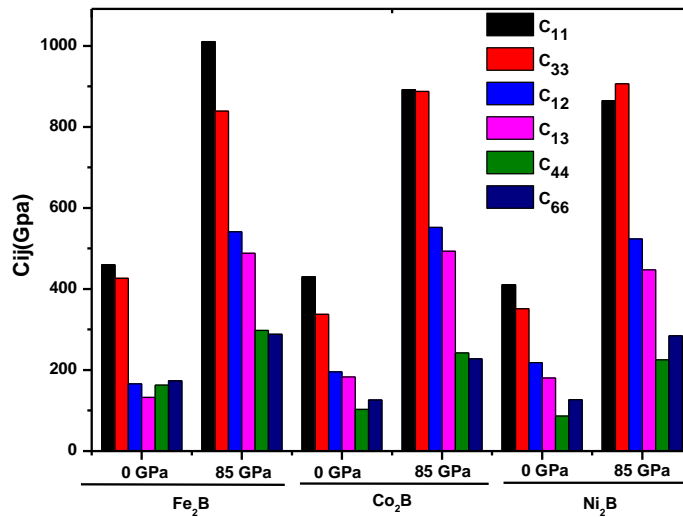


Figure 22. Pressure dependence on the elastic constants

The arithmetic average of the Voigt and Reuss bounds is known as the Voigt-Reuss-Hill (VRH) average, which is regarded as the best estimate for the theoretical value of polycrystalline elastic modulus (3.40). The Young modulus and Poisson ratio can be computed from the formula (3.41).

A larger B/G value (>1.75) for a solid indicates the ductile behavior while a smaller B/G value (<1.75) usually means brittle material. Similarly, Poisson ratio $\nu > 0.26$ corresponds for ductile compounds usually [129]. At both 0 GPa and above critical pressure, B/G is larger than 1.75 and $\nu > 0.26$ for Co₂B and Ni₂B (Table 9), which indicate that they are ductile. The values of B/G and ν for Fe₂B are 1.52 and 0.23, respectively at 0 GPa pressure which mean Fe₂B is brittle. In contrast, at critical pressure Fe₂B is ductile since B/G=2.48, $\nu=0.32$.

Table 9. The calculated bulk, Young (E) and shear modulus (G) (under 0 and critical pressure, in GPa), Poisson's ratio (ν), B/G ratio and the relative change (in %) for TM₂B compounds.

Species	B	E	G	ν	B/G	$\Delta B/B$	$\Delta E/E$	$\Delta G/G$	$\Delta \nu/\nu$	$\Delta (B/G)/(B/G)$
Fe ₂ B (0 GPa)	244.6	395.2	160.5	0.23	1.524					
	222.3 ^a	355 ^a	144 ^a	0.23 ^a	1.54 ^a					
Fe ₂ B (85 GPa)	651	695.4	263	0.32	2.48	62.4	43.2	39	28.1	38.5
Co ₂ B (0 GPa)	257.46	287.69	109.49	0.31	2.35					
	247.2 ^b		89.7 ^b		2.76 ^b					
Co ₂ B (85 GPa)	644.35	583.82	216.39	0.35	2.97	60	50.7	49.4	11.4	20.8
Ni ₂ B (0 GPa)	262.88	255.51	95.48	0.34	2.75					
	238.1 ^b		105.4 ^b		2.26 ^b	57	58	58	0	-2
Ni ₂ B (85 GPa)	607.97	601.28	225.17	0.34	2.70					

^aRef. [162], ^bRef.[148].

4.1.5. Elastic anisotropy

The mechanical anisotropy is characterized by calculating several different anisotropic indexes AU, AG and AB as defined in chapter 3 (3.42) and (3.43).

The shear anisotropic factors provide measures of the degrees of anisotropy in atomic bonding in different crystallographic planes.

The calculated values of anisotropic factors for semi- borides TM₂B are shown in Table 10. For an isotropic crystal, all three factors must be one, while any value smaller or greater than one is a measure of the degree of elastic anisotropy possessed by the crystal.

The elastic anisotropy of a tetragonal crystal can be measured by two shear anisotropy factors (Zener ratios) (3.44).

Obviously, the order in the universal elastic anisotropic index for the considered TM₂B compounds is Ni₂B > Co₂B > Fe₂B. The elastic modulus of Ni₂B is strongly dependent on different directions and the calculated AG, AB and shear anisotropic factors (A1, A2 and A3) values support this conclusion, that means iron boride Fe₂B has very small anisotropy ($A^u \cong 0$).

Magnetic moment in Fe₂B and Co₂B has reduced the anisotropic factors A1 and A3 to 4% and 23.5% and to 19.4% and 16.1% respectively. For the universal anisotropic index AU is augmented when pressure is applied by 84.6% for Fe₂B and 20% for Co₂B. Notably, the values of C11 (C66) are larger than that of C33 (C44) at 0 GPa and under pressure for both compounds Fe₂B and Co₂B, moreover the calculated percentage change in lattice parameters a and c between FM and NM cases are 6.8% and 7.34% for Fe₂B, while for Co₂B are 5.15% and 9.65%.

Table 10. Polycrystalline elastic properties and Anisotropic factors of TM₂B compounds.

Species	BV	BR	GV	GR	A ₁	A ₂	A ₃	A _u	A _G	A _B
Fe ₂ B (0 GPa)	245.11	244.07	160.82	160.21	1.18	1.18	0.26	0.02	0.19	0.21
	222.7 ^a	221.8 ^a	144.4 ^a	143.6 ^a	1.07 ^a	1.07 ^a	1.23 ^a	0.03 ^a	0.28 ^a	0.20 ^a
Fe ₂ B (85 GPa)	655.09	646.32	266.31	260.30	1.23	1.23	0.34	0.13	1.14	0.67
Co ₂ B (0 GPa)	259.26	255.67	110.22	108.76	1.08	1.08	0.26	0.08	0.01	0.01
Co ₂ B (85 GPa)	644.69	644.00	218.47	214.31	1.34	1.34	0.31	0.10	0.01	0.00
Ni ₂ B (0 GPa)	265.19	260.56	96.76	94.21	1.31	1.31	0.22	0.15	0.01	0.01
Ni ₂ B (85 GPa)	608.06	607.88	228.17	222.17	1.67	1.67	0.26	0.14	1.33	0.01

^aRef. [162].

Table 11. The calculated bulk, Young (*E*) and shear modulus (*G*) (under 0 and critical pressure, in GPa), Poisson's ratio (*ν*), *B/G* ratio and the relative change (in %) for TM₂B compounds.

Species	<i>B</i>	<i>E</i>	<i>G</i>	<i>ν</i>	<i>B/G</i>	Δ <i>B/B</i>	Δ <i>E/E</i>	Δ <i>G/G</i>	Δ <i>ν/ν</i>	Δ (<i>B/G</i>)/ (<i>B/G</i>)
Fe ₂ B (0 GPa)	244.6	395.2	160.5	0.23	1.524					
	222.3 ^a	355 ^a	144 ^a	0.23 ^a	1.54 ^a					
Fe ₂ B (85 GPa)	651	695.4	263	0.32	2.48	62.4	43.2	39	28.1	38.5
Co ₂ B (0 GPa)	257.46	287.69	109.49	0.31	2.35					
	247.2 ^b		89.7 ^b							
Co ₂ B (85 GPa)	644.35	583.82	216.39	0.35	2.97	60	50.7	49.4	11.4	20.8
Ni ₂ B (0 GPa)	262.88	255.51	95.48	0.34	2.75					
	238.1 ^b		105.4 ^b			57	58	58	0	-2
Ni ₂ B (85 GPa)	607.97	601.28	225.17	0.34	2.70					

^aRef.[162]. Ref.[148]

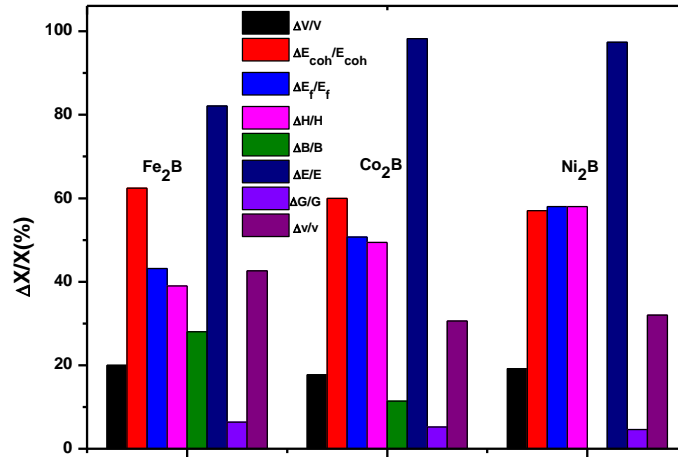


Figure 23. The calculated percentage change of parameters by the top: volume, cohesive and formation energy, hardness, bulk, Young and shear modulus.

The previously calculated A^U , A_B , A_G and A_1 , A_2 , A_3 cannot describe the size and shape of anisotropy directly. To conduct a careful inspection of the changes of elastic modulus in all directions, drawing a three-dimensional graph for TM₂B compounds is necessary, as shown in Figure 24, Figure 25 and Figure 26.

From Eqs: (3.48), (3.49) and (3.50) the three-dimensional surface representations showing the variation of the Young, bulk and torsion modulus are plotted in Figure 24, Figure 25 and Figure 26, and the plane projections ((100) plane and (001) plane) of the directional dependences of the Young, bulk and torsion modulus are given in Figure 27 for comparisons. It can be clearly seen that Fe₂B exhibits a pronounced anisotropy ($A_B = 0.67$, $A_G = 1.14$) under pressure, in contrast Co₂B ($A_B = 0.00$, $A_G = 0.01$) with the spherical nature in Figure 24 and Figure 25. Moreover, it is interesting to note that the directional bulk modulus along the c-axis is smaller than those along a= b-axes, which is consistent with the predicted elastic constants along different axes (Table 8).

Thus, compared to the in-plane isotropy in (001) plane, a significant in-plane elastic anisotropy in (100) planes are revealed. It can be seen that the Young modulus anisotropy of Ni₂B is stronger than in the other structures.

The shear anisotropic factors provide measures of the degrees of anisotropy in atomic bonding in different crystallographic planes.

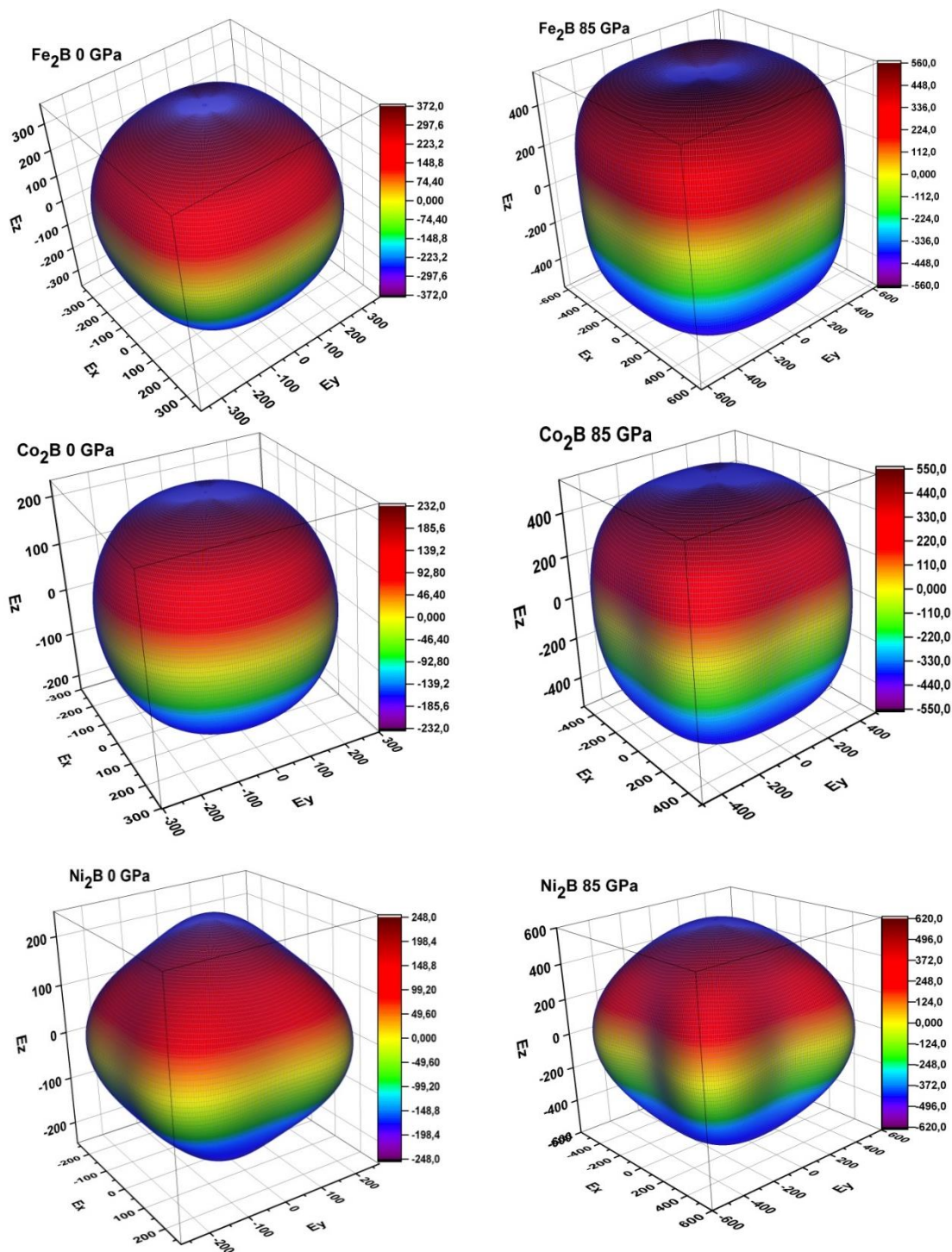


Figure 24. Illustration of directional dependent Young's modulus of TM₂B compounds: Left panel with 0 GPa pressure and right panel under pressure.

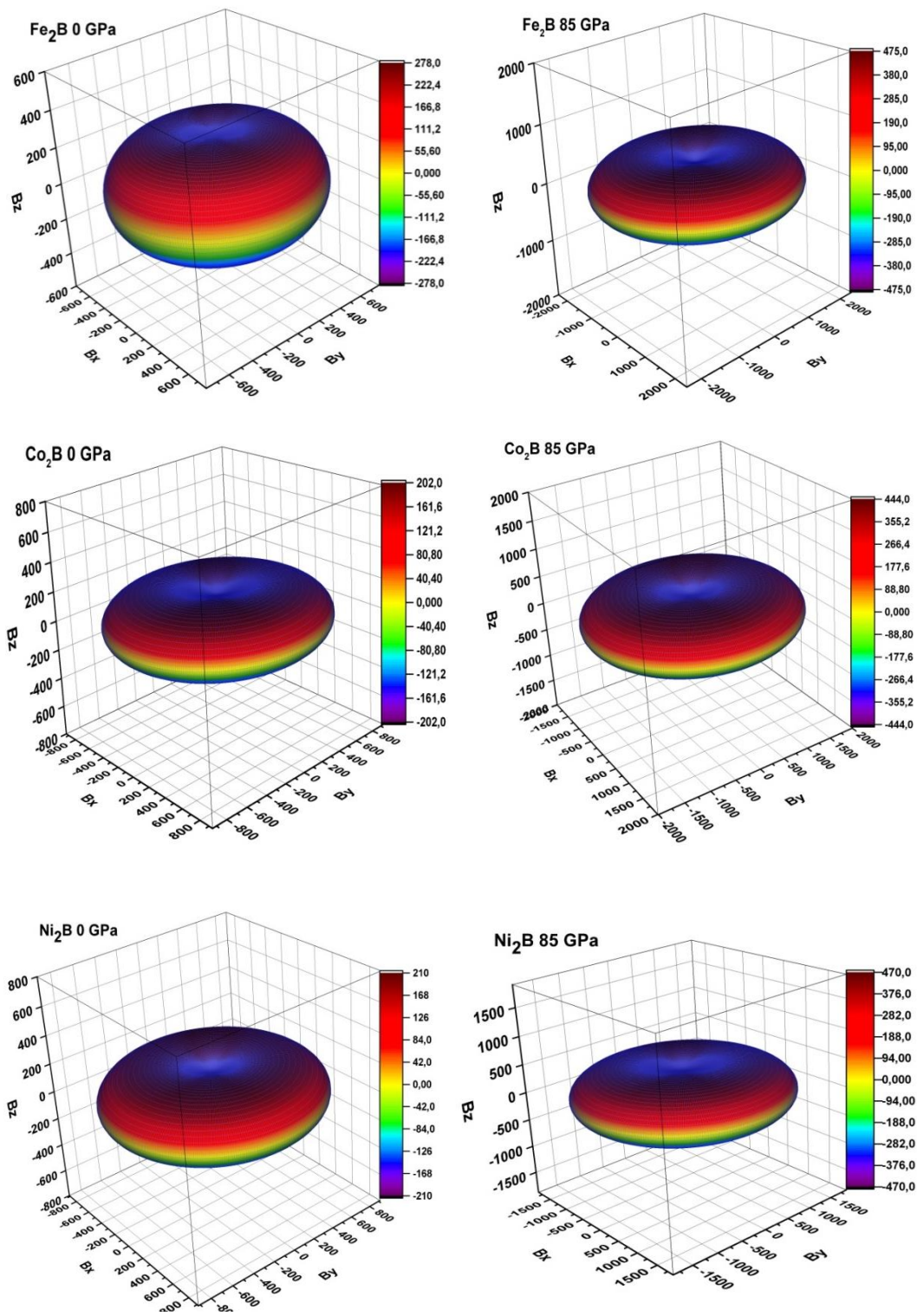


Figure 25. Illustration of directional dependent bulk modulus of TM₂B compounds: Left panel with 0 GPa pressure and right panel under pressure.

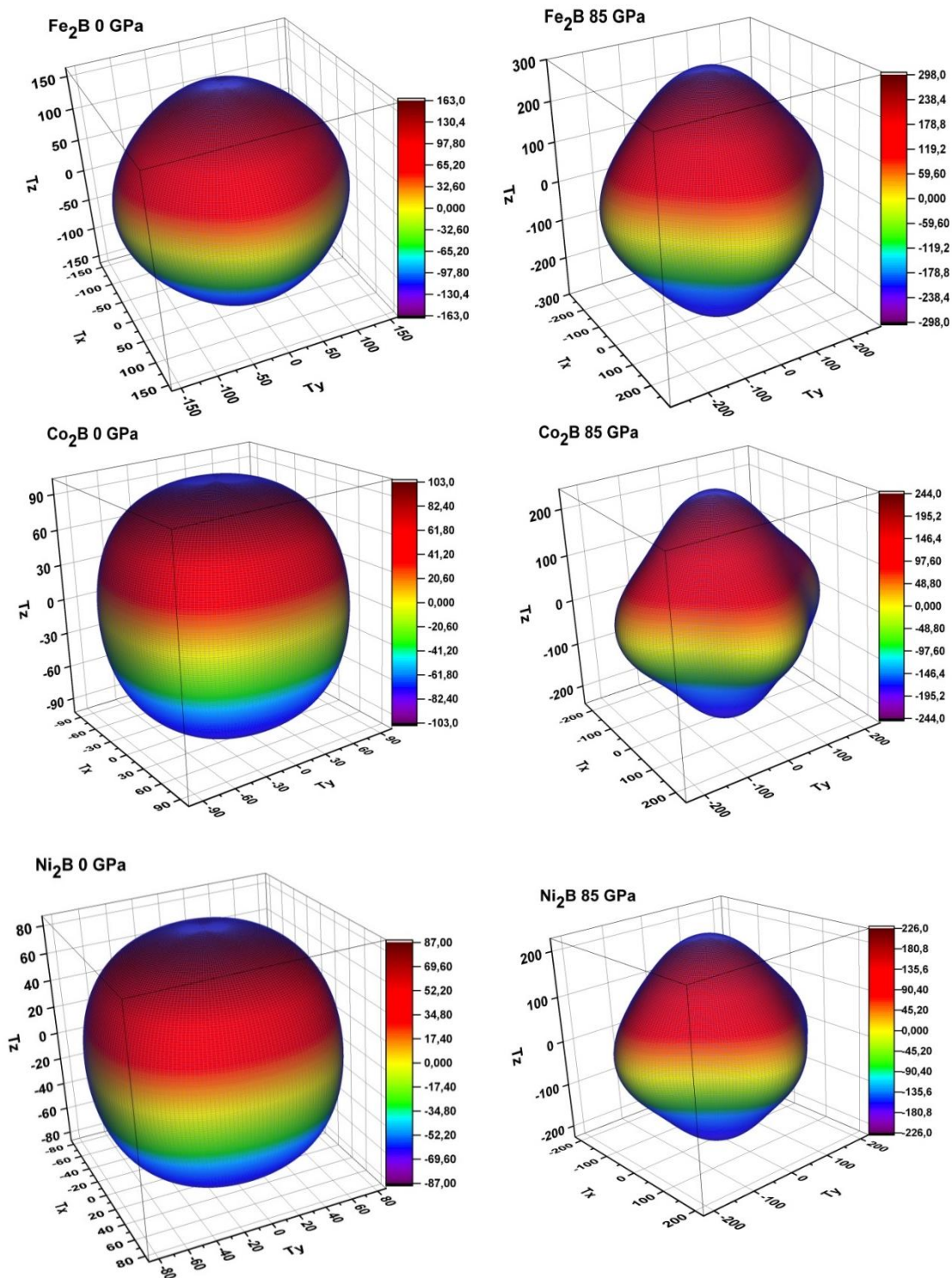
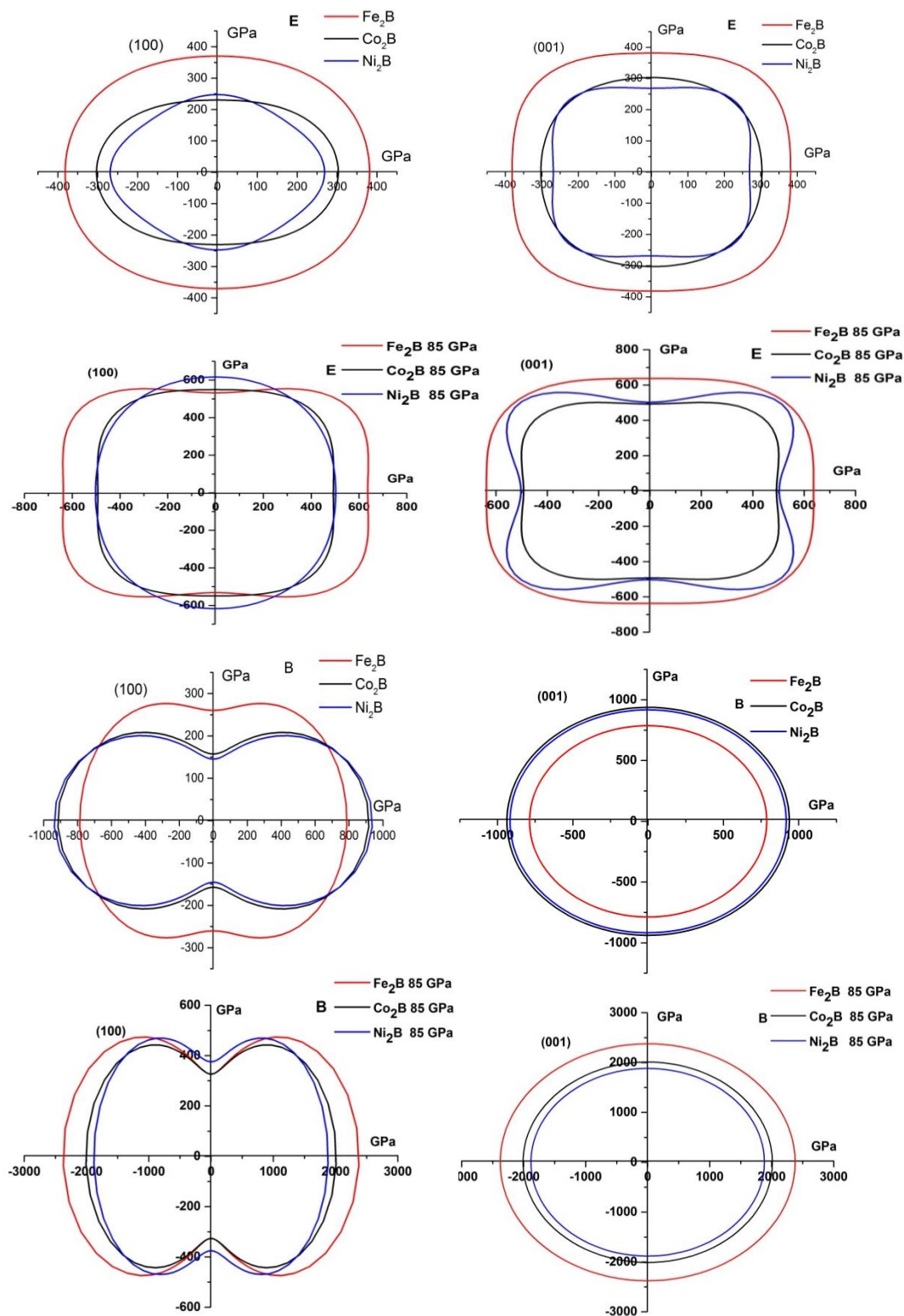


Figure 26. Illustration of directional dependent torsion modulus of TM₂B compounds: Left panel with 0 GPa pressure and right panel under pressure.



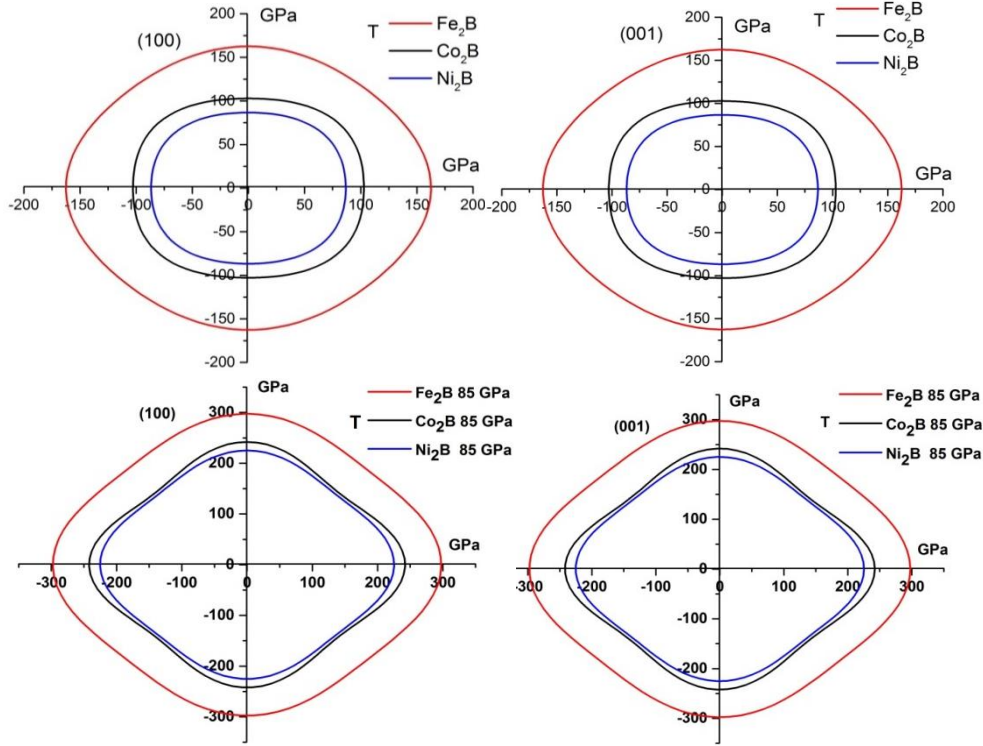


Figure 27. The projection of Young, bulk and torsion moduli at 0 GPa and under pressure for different crystal planes for TM₂B compounds.

4.1.6. Acoustic sound velocities and Debye temperatures

In the principal directions, the acoustic velocities for a tetragonal system are related to elastic coefficients by relation in (3.53).

The calculated densities, sound velocities and Debye temperatures at 0 GPa and critical pressure for TM₂B compounds are presented in Table 12. It is obvious that Fe₂B has large sound velocities, since its elastic constants (C_{11} , C_{33} , C_{44} and C_{66}) are larger than the other compounds: Co₂B and Ni₂B. The anisotropic properties of sound velocities indicate the elastic anisotropy of these crystals. For example, the C_{11} and C_{33} determine the longitudinal sound velocities along [100] and [001] directions, respectively, and C_{44} and C_{66} correspond to the transverse modes [135].

As a fundamental parameter for the materials' thermodynamic properties, Debye temperature Θ_D is related to specific heat, thermal expansion and elastic constants. The Debye temperature can be estimated from the average sound velocity using equations 3.54 and 3.55 based on elastic constant. The calculated Debye temperatures of our compounds are listed in Table 12. The elastic wave velocities of these compounds are relatively large, because our compounds have large mechanical moduli and large densities. For Debye temperatures the largest Θ_D is 505 K (630K) for Fe₂B while the lowest one is 396 K for Ni₂B and the order of Θ_D for TM₂B compounds is: Fe₂B > Co₂B > Ni₂B. It is well known that the Θ_D is the inverse to molecular weight and can be used to characterize the strength of covalent bonds in the solids. Therefore, I conclude that the covalent bonds in Fe₂B are stronger than the other borides. Ni₂B has the smallest Θ_D which implies the strong metallic bonds among Ni atoms.

Table 12. The density (in g/cm³), anisotropic sound velocities (in m/s), average sound velocity (in m/s), Debye temperature (in K) and relative change (in %) for the TM₂B compounds.

Species	ρ	vl	Vt	vm	Θ_D	$\Delta\rho/\rho$	$\Delta vl/vl$	$\Delta vt/vt$	$\Delta vm/vm$	$\Delta\Theta_D/\Theta_D$
Fe ₂ B (0 GPa)	7.69	7722.4	4568.5	5060.7	505.8					
		(6560.8) ^a	(2802.9) ^a	(3167.9) ^a	(456.3) ^a	20.2	24.2	12.5	13.5	19.8
Fe ₂ B (85 GPa)	9.64	10193.5	5223.2	5850.8	630.5					
Co ₂ B (0 GPa)	7.64	7266.9	3785.7	4235.9	422.5					
		(6759.6) ^a	(3342.6) ^a	(3752.2) ^a	(539.9) ^a	22.7	25.2	19.1	19.5	24.8
Co ₂ B (85 GPa)	9.88	9717	4679.9	5261	562.3					
Ni ₂ B (0 GPa)	7.58	7174.7	3549.1	3983.9	396.3					
		(6887.3) ^a	(3633.7) ^a	(4062.5) ^a	(584.2) ^a	23	25	26	26	31
Ni ₂ B (85 GPa)	9.82	9616.9	4788.5	5373.1	573.8					

^aRef.[148].

4.2. Conclusions

Magnetic moment, hardness, elastic moduli, elastic anisotropy properties, and Debye temperatures of the TM₂B (TM = Fe, Co and Ni) compounds at 0 GPa and high pressure are investigated and discussed from the first-principles calculations. The calculated ground-state parameters are in good agreement with the other available theoretical data and experiments values. The equilibrium structure and formation energy show that Fe₂B and Co₂B are energetically more stable at 0 GPa than at each critical pressure. Both Fe₂B and Co₂B have a magnetic transition when the pressure is about 85 GPa. The hardness, elastic constants, bulk, shear, Young's modulus and acoustic velocities for Fe₂B and Co₂B compounds increase with the applied pressure. The increasing B/G and ν of these compounds indicate that Fe₂B and Co₂B are ductile phases under high pressures. The TM₂B compounds show a certain degree of mechanical anisotropy. The Debye temperatures increase with increasing pressure and Fe₂B has a higher Debye temperature in two pressures 0 GPa and Critical pressure. The calculated sound velocities along [100] and [001] directions for TM₂B under high pressure also imply the anisotropic. I believe that my findings serve as guidance for experimental investigations

CHAPTER 5: Mono-Borides TMB (TM = Mn, Fe, Co)

Under Pressure.

5. Hardness and anisotropic elastic properties of mono-boride

TMB (TM=Mn, Fe, Co) under pressure. A first-principles study.

Among the transition metal borides, manganese mono-boride is important due to potential spintronic applications [163]. Iron borides in particular are widely used as hard and protective coatings on steel surfaces for improved wear and corrosion resistance of the material [9, 10]. Nanosize cobalt boride particles are prepared in reverse micelles or in a di-phase system[164]. A review of different methods of Boriding and control parameters is exposed in chapter 2.

The mechanical properties of FeB layers are estimated by Berkovich Nano indentation on boride steels; their measurements show that hardness range between 14.5 GPa and 19 GPa for FeB depending on temperature and boriding time [165]. For CoB provides 15–16 GPa [143, 144], Moreover, Campos *et al.* [1] obtained hardness values in a range of 25– 30 GPa with a maximum value of 5 μm from the free surface; regardless of the duration and boriding temperature. The hardness of nickel borides is measured for samples with different diffusion processes of boriding using Knoop [11, 145] or Vickers method [12, 146]. Ni-B borides have a hardness around 12.75 GPa [11] and measured by Nano indenter 17.98 GPa [147].

Britton *et al.*[113] show that there are correlations between the anisotropy of crystals, and both the elastic and the plastic behavior during Nano indentation. The structure and magnetic properties of the 3d transition-metal mono-borides TM–B (TM=Mn, Fe, Co) under pressures, have been investigated in detail [166].

However, hardness, anisotropic elastic properties of these compounds have not been presented yet. They can be used to provide much insight of structural behavior under pressure, as protective coatings on metal surfaces.

In this chapter, I use ab-initio calculation for the structure, magnetic, hardness and anisotropic elastic properties of MnB, FeB, CoB and NiB compounds under pressure ranging between 0 and 145 GPa. I also determine the transition pressure at which the material loses its magnetic moment. Mechanical anisotropies in both cases (0 GPa and after transition pressure) are discussed by calculating different anisotropic indexes and factors. I plot the three dimensional (3D) surfaces and planar contours of Young and bulk moduli of my mono-borides at several crystallographic planes, ((100), (010) and (001)) to reveal their elastic anisotropy.

5.1. Structure aspects and calculation methods

The TM–B compounds (MnB, FeB, CoB and NiB) crystallize in space group Pnma of the orthorhombic system with four units formula per cell. FeB prototype structure is presented in Figure 28. A characteristic of the structures is the presence of strong interaction between non-metallic atoms in continuous zig zag like chains [166].

Total energy calculations are performed within density functional theory (DFT) [167] using CASTEP code [36] for the whole study which uses the plane wave expansion method in reciprocal space [149]. The Ultra-soft Vanderbilt pseudo-potentials are employed to represent the electrostatic interactions between valence electrons and ionic cores [150] which are used with the following valence electronic configurations Mn: $3d^5 4s^2$, Fe: $3d^6 4s^2$, Co: $3d^7 4s^2$, Ni: $3d^8 4s^2$ and B: $2s^2 2p^1$. Generalized gradient approximation PBE-GGA was used for exchange-correlation energy calculations [151]. The kinetic energy cut-off value is selected as 500eV, which is sufficient to obtain the reliable results.

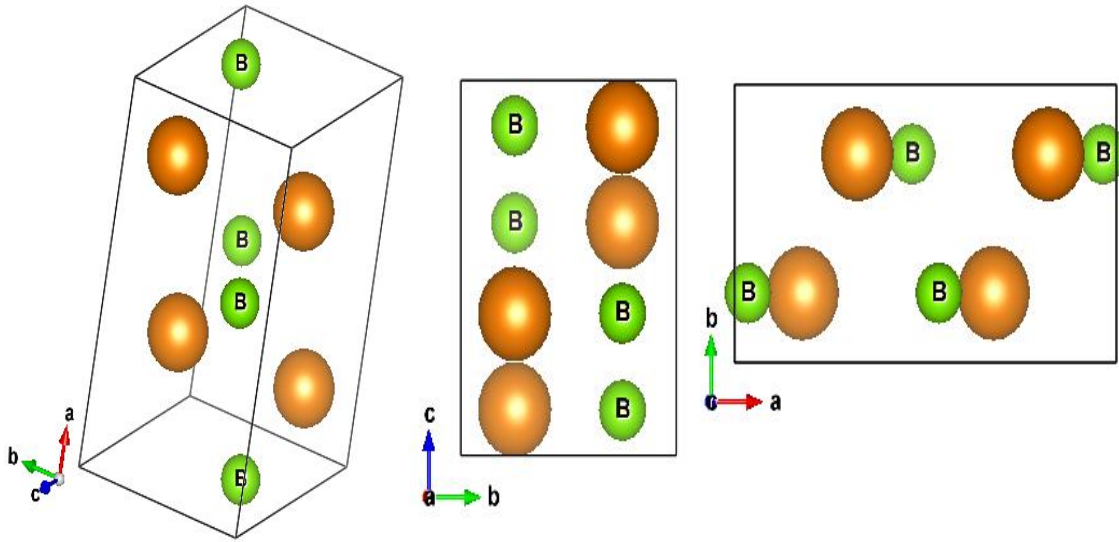


Figure 28. The crystal structure of TMB illustrated by ball and stick model. The big ball refers to B and the small ball refers to TM atom.

Total energies are evaluated in the first irreducible Brillouin zone with the following Monkhorst-Pack grids [152]: (8 x10x 12) for all compounds. It is known that the ground states of MnB and FeB compounds are ferromagnetic [138-140].

The convergence criteria of total energy and structure optimization are set to fine quality with the energy tolerance of 10^{-6} eV/atom. BFGS (Broydene-Fletcher-Goldarbe-Shanno) optimization method was performed to obtain the equilibrium crystal structures of TMB with maximum atom displacement and force set to 0.002 \AA and 10^{-4} eV/\AA .

The stability of our compounds can be evaluated by calculating two energy parameters, cohesive energy E_{coh} and formation energy E_f defined as follows:

$$E_{coh}(TMB) = \frac{E_{total}(TMB, Cell) - nE_{iso}(TM) - nE_{iso}(B)}{n} \quad (5.1-1)$$

$$E_f(TMB) = E_{coh}(TMB) - E_{coh}(TM) - E_{coh}(B) \quad (5.1-2)$$

5.1.1. Structural properties and stability

The calculated lattice parameters, unit cell volumes, bulk modulus, cohesive and the formation energies for pure metals and TMB along with the available experimental and previous theoretical data for comparison, are shown in Table 13 and Table 14. These results show that the calculated structure parameters are in good agreement with the experimental values. At equilibrium, calculations show that MnB and FeB compounds carry magnetic moment with values 1.83 and 1.12 μ_B respectively. Our calculations also show that the magnetic moments of both CoB and NiB compounds are very close to zero. The calculated magnetic moments of our compounds are in good agreement with theoretical and experimental values. These moments for FeB and MnB are larger than the magnetic moment of pure element Fe and Mn respectively. In fact Mn behave as paramagnetic, and pure iron is ferromagnetic and carry smaller magnetic moment 2.217 μ_B than FeB [153].

The calculated values of cohesive energy of MnB, FeB, CoB and NiB are respectively, -17.01, -13.153, -13.10 and -14.46 eV per unit formula. Furthermore, the formation energies are -1.35, -1.207, -1.075 and -0.735 eV for MnB, FeB, CoB and NiB respectively, indicating that all of these TMB compounds are stable. Moreover the calculated percentage change in lattice parameters a, b and c between 0GPa and high pressure are 7.1%, 12.96% and 8.4% for MnB, while for FeB are 9.6%, 0.3% and 6.8%, which mean that the easy axis of magnetization for MnB is the direction $\langle 010 \rangle$ and the hard axes are the direction $\langle 100 \rangle$, $\langle 001 \rangle$.

However the easy axis of magnetization for FeB is the direction $\langle 100 \rangle$ and the hard axes are the direction $\langle 010 \rangle$, $\langle 001 \rangle$.

Table 13. The calculated ground state properties of pure elements, Mn, Fe, Co, Ni and B. Experimental and theoretical (eV/f.u.), cohesive energy E_{coh} (eV/f.u.) and volume V (\AA^3).

Ground state properties	Mn	Fe	Co	Ni	B
E_{iso}	-644.390	-859.821 (-855.913) ^a	-1037.55	-1347.162	-70.501 (-70.492) ^a
E_{total}	-653.60	-865.315 (865.335) ^a	-1043.113	-1354.431	-76.953 (-76.875) ^a
E_{coh}	-9.21	-5.494 (-4.28) ^{exp}	-8.344	-7.2697	-6.452 (-6.383) ^a
V	11.09	11.775 (11.82) ^{exp}	11.16 (10.90) ^b	11.04 (10.87) ^b	8.652 (8.763) ^a

^{exp}Ref. [153], ^aRef. [139], ^bRef. [154].

Table 14. The calculated ground state properties of TMB. Experimental and theoretical values are listed in parentheses. Total cell energy E_{total} (eV/f.u.), cell parameters (a, b, c in Å), atomic positions for TM and B atoms (fractional coordinates), volume V (Å³), Bulk modulus (GPa), magnetic moment (μ_B /atom), cohesive energy E_{coh} (eV/f.u.), formation energy E_f (eV/f.u.).

Parameters	MnB	FeB	CoB	NiB
E_{total}	-2927.6114	-3773.900	-4484.547	-5728.472
(a, b, c)	5.493, 2.992, 4.147 (5.459, 2.984, 4.126) ^a	5.317, 2.950, 3.964 (5.495, 2.946, 4.053) ^b	5.206, 3.068, 3.927 (5.503, 2.946, 4.064) ^{exp1}	5.535, 2.979, 3.972
TM (x, y, z)	0.175 0.25 0.123	0.178 0.25 0.122	0.177 0.25 0.126	0.179 0.25 0.117
B(x, y, z)	0.033 0.25 0.614	0.0348 0.25 0.620	0.032 0.25 0.623	0.0328 0.25 0.614
V	68.153	62.176	62.73	65.51
B	261.90	305.58 (286.6) ^a	262.88 (238.12) ^d	245.28
μ_B /atom	1.93	1,126 (1.12) ^{exp1} , (1.20) ^b , (0.95) ^{exp2}	0	0
E_{coh}	-17.01	-13.153	-13.10	-14.456
E_f	-1.35	-1.207	-1.075	-0.735

^{exp}Ref. [155], ^aRef[168], ^bRef. [139], ^cRef. [156], ^{exp1} Ref[169].

5.1.2. Effect of pressure and magnetic moment on the structural properties.

In this part of my work, I am interested in the variation of the magnetic moment with increasing pressure. I calculate the magnetic moment of my compounds FeB and MnB as a function of pressure. The results are presented in Figure 29. As can be noted, the magnetic moment of our materials slowly decreases with applied pressure and suddenly disappears at a specific pressure. The extinction of the magnetic moment in our compounds is characterized by a very precise critical value: 77 GPa for FeB and 143 GPa for MnB.

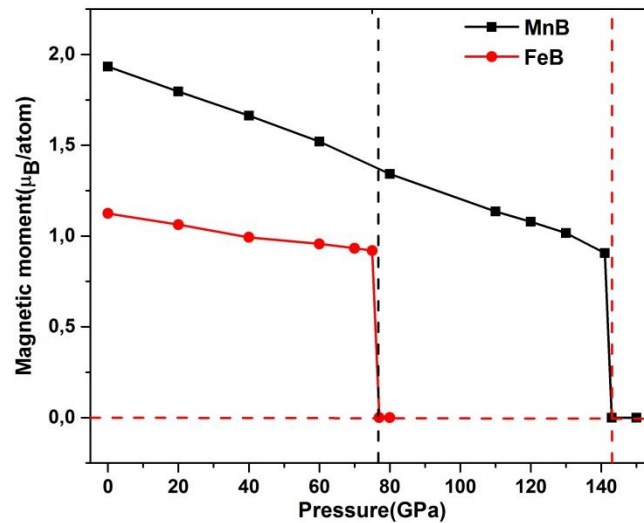


Figure 29 Dependence of magnetic moment vs pressure.

The calculated percentage change of volume between 0 GPa and transition pressure of ferromagnetic compounds, show a volume compression of 26% and 15% for MnB and FeB respectively, with an increase of the bulk modulus of our compounds by 67.8% and 50.5% (Figure 34).

The formation energy E_f , is calculated to check the probability of thermodynamic existence of TMB under pressure excepted CoB and NiB. All formation energies are negative indicating that structures in two pressures conditions are thermodynamically stable (Table 14). The formation energies of TMB in magnetic state are less than TMB in NM case by 85.94%, and 68.35% for both MnB and FeB respectively, implying that they have more thermodynamic stability FM case.

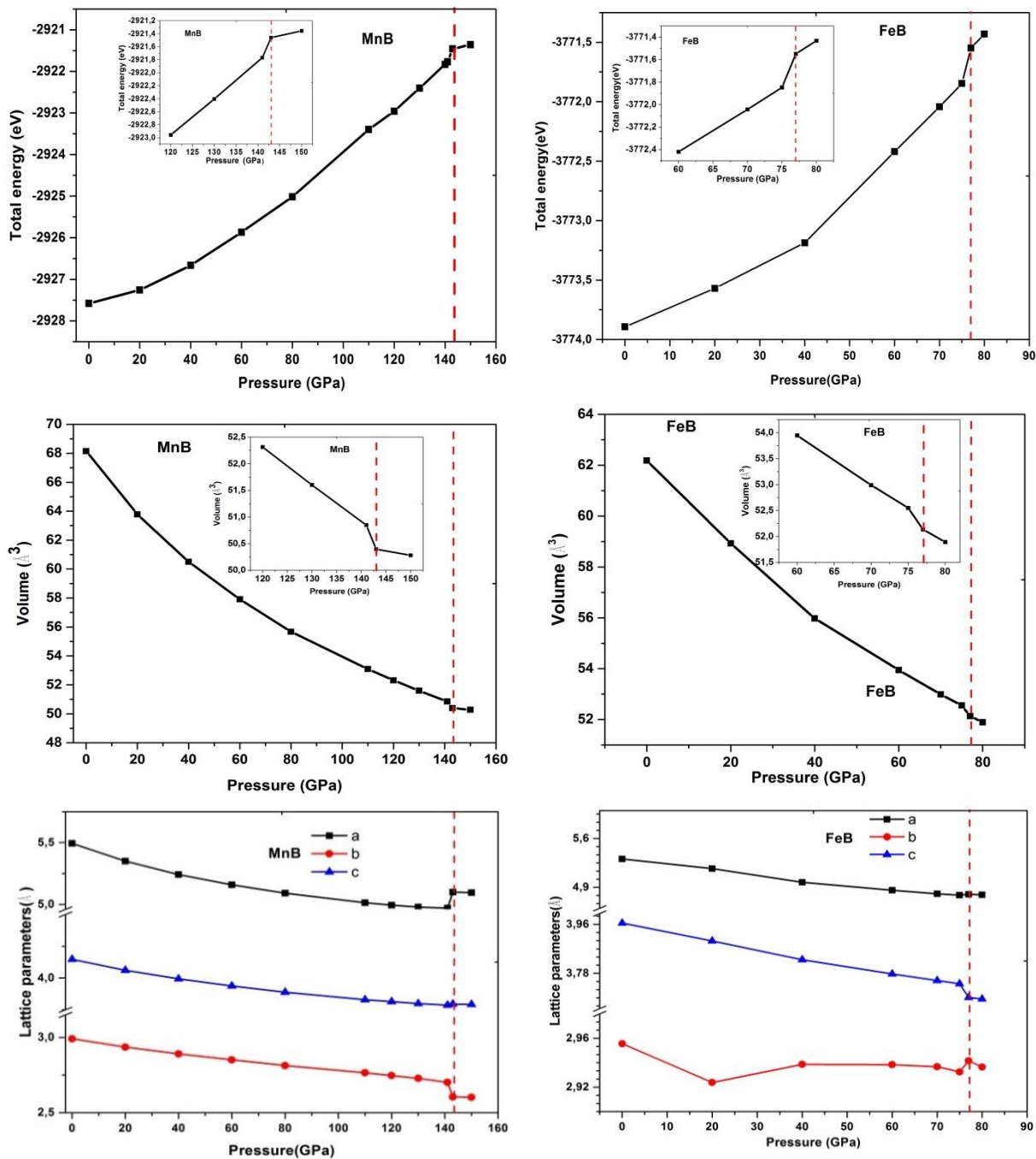


Figure 30 Pressure dependence of total energy, Volume and lattice parameters of: MnB (left panel) and FeB (right panel). Dashed line

5.1.3. Density of states and bond structure under pressure

As I showed in Figure 31, the total DOS is dominated by the density of d electrons in the majority and minority bands of MnB and FeB. As the Fermi energy is pinned above the pure d states, both compounds behave as strong ferromagnets. Total DOS at the Fermi level for MnB and FeB increases under pressure by 48.8% and 21% for MnB and FeB (Figure 31) respectively, this enhanced $N(E_f)$ is derived entirely from the TM 3d states, with a negligible contribution from the B 2p states. Following the above arguments I may be predict the appearance of superconductivity in MnB and FeB under pressure as is in the case of iron that undergoes a transition to superconducting phase above 30GPa when it loses its magnetic moment [160].

The bulk modulus increased by 67.8% for MnB and 50.5% for FeB. In the NM state the bulk modulus B is systematically larger than the magnetic state. The low value of bulk modulus in the magnetic case points to a larger compressibility. This means that MnB and FeB compounds are “softer” when are magnetically ordered and “harder” when are not.

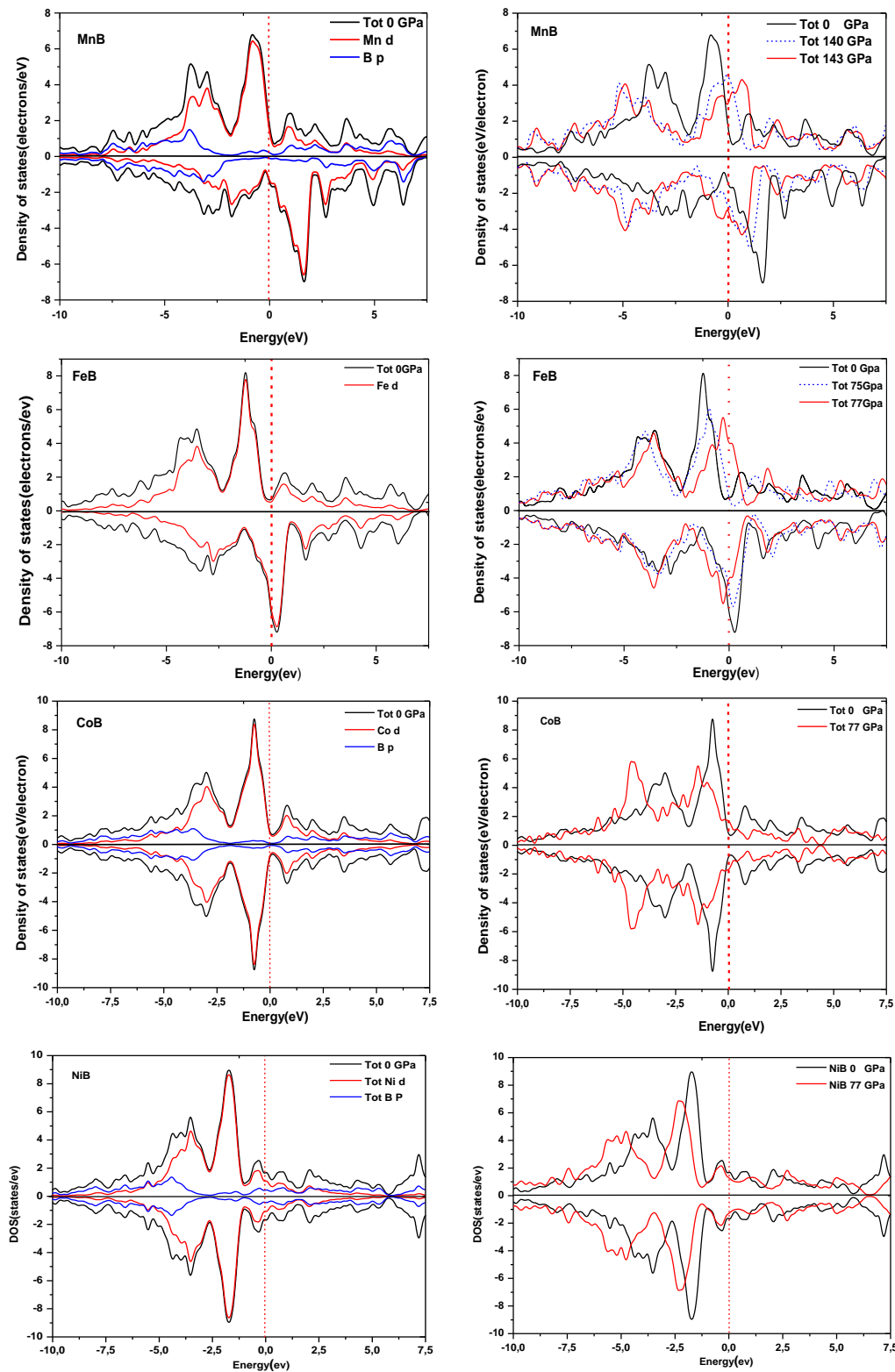


Figure 31. The calculated total and partial DOS of TMB at 0 GPa and a critical pressure. Dashed line represents the Fermi level.

Figure 32 depicts the electronic band structure of FeB at 0 and 77 GPa along the symmetry directions Γ -Z-T-Y-S-X-U-R for orthorhombic structure. For comparison, I gave the electronic band structure spin up and spin down (Figure 32). The valence band generated in the K_y direction (S -X, U -R,) and K_z (T -Y, Γ - Z, X-U) are narrower than those bands in the K_x (Y-S,) directions. This indicates that the principal bonding interactions lie along the y and z directions in the crystal, while the x direction is limited. Both the continuous zigzag chains of B atoms and the metal atom chains lie in the YZ plane of the crystal. It is clearly indicating that the B-B bonding chains are very important in the chemical stability of TM-B compounds. The conduction bands are less well characterized than the valence bands, but it is clear that they are also somewhat broadly in the y and z direction and are consistent with the known metallic nature of these compounds.

At normal pressure (Figure 32) band structure of FeB shows that there is an overlapping of the valence band and the conduction band, confirming the metallic nature of iron boride under normal conditions. The bands just above the Fermi energy are due to the empty 3d states of TM elements (Mn and Fe). The band structure of FeB exhibits characteristic features similar to other mono-borides (MnB and NiB). It can see in Figure 32, the entire band structure is slowly shifted up in energy as pressure increases.

As pressure increases, the conduction band width increases because of the enhanced overlap of the wave function with the neighboring atoms. Visible changes are seen in the band structures along all symmetry line (Figure 32) since the electronic system is strongly coupled to the lattice under pressure.

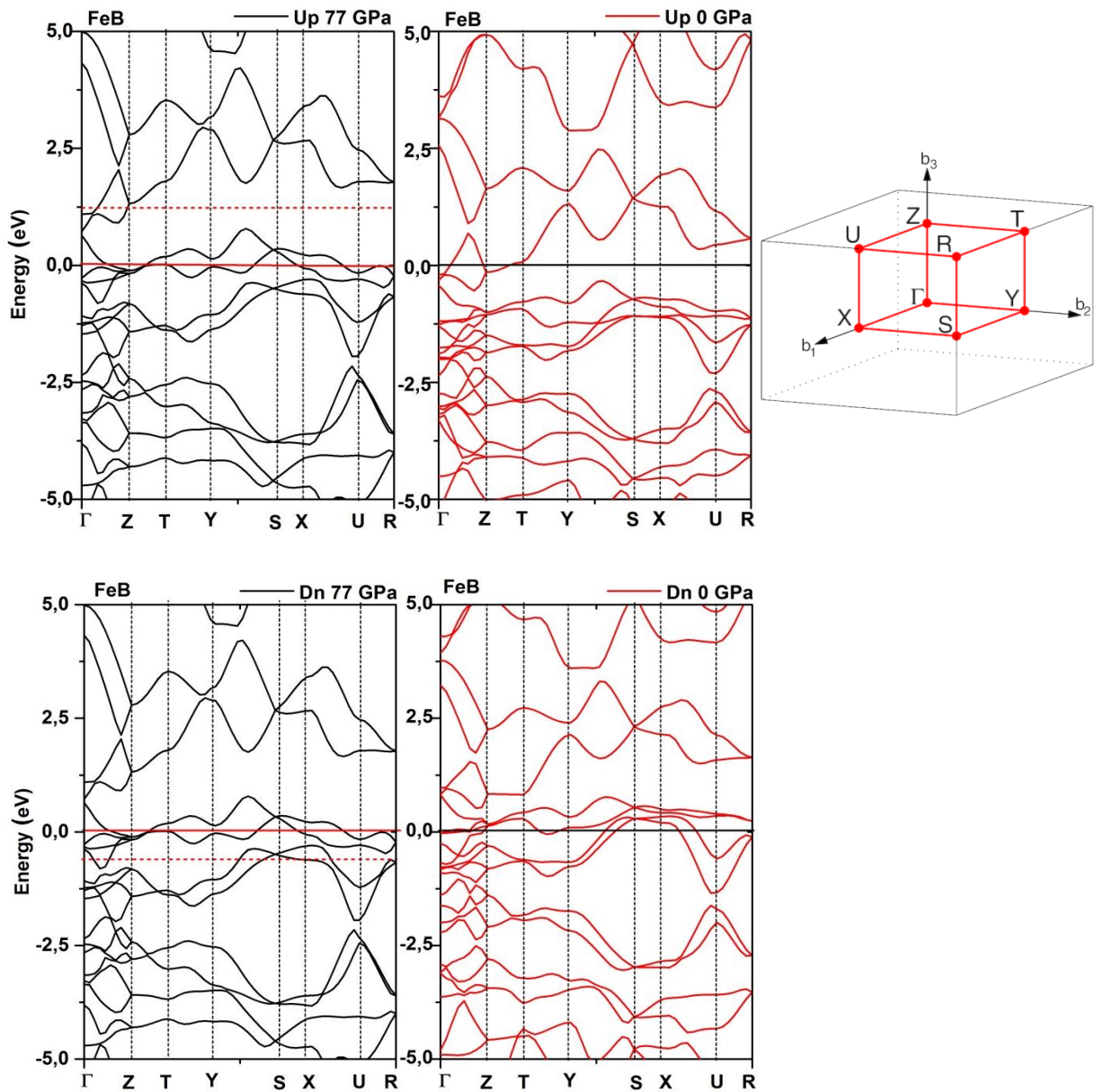


Figure 32. The calculated band structures for FeB compound near Fermi level at 0 GPa and 77 GPa, sin up (left panel) and spin down(right panel).

5.1.4. Hardness

Based on the semi-empirical approach of Gao *et al.* [120], the hardness of TM–B and B–B bonds in each of our three compounds TMB are evaluated and compared. Semi-empirical models and first principles calculations are widely used for theoretical search of hard materials [119]. I, only consider the hardness of B-B and TM-B bonds. The hardness of TM–TM bond, however, is not taken into consideration in this work, because the hardness of metallic bond is ill defined in this method. The strength of the bond per the unit volume can be characterized by average overlap populations. For complex multi-bonding compounds, the hardness of the *u* type bond is calculated using equation (3.30) . I use Mulliken population analysis as implemented in CASTEP in order to estimate the bond overlap population.

The longest TM–B bond length considered in this work is limited to 3.1Å because the interaction between TM atom and the second nearest neighbor B atom is weaker than that between the near-neighbor boron atoms.

The calculated bond length, population overlap, contribution of TM–B and B-B bonds to the hardness H^v as well as material hardness of our four compounds are listed in Table 15. The hardness of B–B bond H^u is significantly larger than TM–B bond in TMB compounds because of the large bond overlap population. The value of B–B hardness in NiB is 54.92 GPa, which is harder than the other B–B bond in MnB, FeB and CoB because B–B bond has a large overlap population.

The calculated hardness of MnB (20 GPa), FeB (26.25 GPa), CoB (26.70 GPa) and NiB (25.71 GPa) are in fairly good agreement with the experimental values of (16.2 ± 0.017) GPa for MnB, (26.28 GPa) for FeB [142], and the maximum value of hardness (27 GPa) was obtained near-surface region at a distance of 8 μm in the CoB phase.

Table 15. The predicted hardness of TMB. Experimental and theoretical values are listed in parentheses. Different pairs of atoms (B–B, TM–B). Average bond length of nearest-neighbor atoms $d^u(\text{Å})$, average overlap population of u type bond, nearest-neighbor numbers N^u for different pairs of atoms, cell volume $\Omega (\text{Å}^3)$, volume of a bond of u type v_v^u , hardness of u type bond H^u (GPa) and hardness H (GPa).

Species	Bond	d^u	p^u	N^u	Ω	v_v^u	H^u	H
	B-B	2.390	0.765	4		4.192		20.66
MnB	Mn-B	2.187	0.155	16	68.153	3.212	51.95	$(16.2 \pm 0.017)^{\text{exp}}$
							16.41	
	B-B	2.322	0.725	4		3.840	56.966	26.25
FeB	Fe-B	2.121	0.175	16	62.176	2.926	21.629	$(26.28)^{\text{exp1}}$
								$(20.4 \pm 0.017)^{\text{exp2}}$
CoB	B-B	2.316	0.68	4		3.876	52.62	26.70
					62.73			
	Co-B	2.115	0.185	16		2.952	22.54	$(27)^{\text{exp3}}$
NiB	B-B	2.375	0.775	4		4.08	54.92	
					65.51			25.705
	Ni-B	2.164	0.173	16		2.94	21.26	

^{exp}Ref. [142], ^aRef. [148], ^{exp1}Ref. [26], ^{exp2}Ref. [147], ^{exp3}Ref[170].

5.1.5. Elastic properties under pressure

The calculated elastic constants for single crystal TMB compounds, at both 0GPa and high pressure pressures, are presented in Table 16.

Table 16. The calculated full set elastic constants of TMB (under 0 and critical pressure, in GPa) along with other available values.

Species	Elastic constants								
	C_{11}	C_{22}	C_{33}	C_{12}	C_{13}	C_{23}	C_{44}	C_{55}	C_{66}
MnB (0 GPa)	392.05	510.74	497.17	181.33	154.92	148.61	212.11	167.69	211.28
	414.4 ^a	527.7 ^a	504.8 ^a	171.1 ^a	147.5 ^a	127.7 ^a	215.8 ^a	218.4 ^a	175.8 ^a
MnB (143GPa)	1035	905	1300	745.2	667	560.76	442	203	561.21
FeB (0 GPa)	389.82	438.36	557.07	286.85	183.12	239.76	218.8	132.25	212.01
	373.7 ^b	434.1 ^b	503.4 ^b	246 ^b	184.4 ^b	209.1 ^b	207.4 ^b	117.7 ^b	193.7 ^b
FeB (77 GPa)	718.5	752.6	993.9	583.2	350.1	492.4	296.4	243.3	354.4
CoB (0 GPa)	411.46	481.97	620.61	239	279.21	275.12	206.23	144.53	157.85
CoB (77 GPa)	891	914	1053	533,3	463.94	479.24	346.5	279.27	344.98
NiB (0 GPa)	339.83	424.67	415.51	192.50	202.26	176.43	123.61	111.93	102.82
NiB (77 GPa)	736.6	775.88	919.91	502.83	428.81	415.22	236.4	214.75	272.96

^aRef[168], ^bRef. [162].

Generally, the elastic constants C_{11} , C_{22} and C_{33} are very high, at both zero and high pressure, which indicates the high resistance to the axial compression in these directions. Moreover, it is shown in Table 16 that the elastic constants C_{11} , C_{22} and C_{33} are larger than C_{44} , C_{55} and C_{66} , indicating that TMB are mechanically anisotropic and the shear deformation is easier to take place than other deformation forms.

It is well known that the elastic constant C_{44} is the most significant parameter which indirectly determines the indentation hardness of a solid [124]. A large C_{44} implies a strong resistance to monoclinic shear in the (100) plane. The highest C_{44} for FeB than those for the other

compounds means that its ability to resist shear distortion in the (100) plane is the strongest. The results in Table 16 indicate that TMB have relatively strong anisotropic elastic constants resulting in the directional dependence of the moduli. Notably, the values of C_{11} (C_{66}) are relatively smaller than that of C_{33} (C_{44}) at 0 GPa and under pressure, implying that the intra-layer chemical bonds are weaker than those between the layers.

The other compression moduli (C_{12} , C_{13} and C_{23}) are significantly different; they correspond to the intra and inter-layer moduli under bi-axial stress conditions.

The mechanical stability criteria can be represented in a uniform manner for orthorhombic structure (the relation (3.36)). On the other hand, the mechanical stability under isotropic pressure, leads to restrictions on the elastic coefficients using relation (3.39).

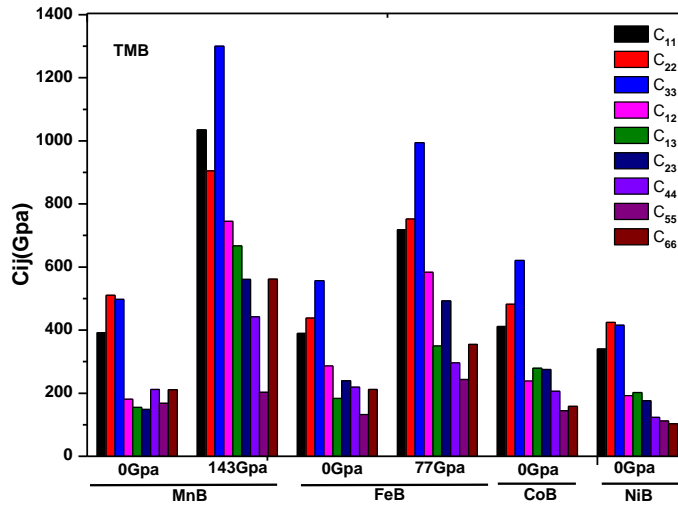


Figure 33. Pressure dependence on the elastic constants.

The arithmetic average of the Voigt and Reuss bounds is known as the Voigt-Reuss-Hill (VRH) average, which is regarded as the best estimate for the theoretical value of the

polycrystalline elastic modulus (3.40). The Young modulus and Poisson ratio can be computed from the formula (3.41).

Table 17. Polycrystalline elastic properties and Anisotropic factors of TM-B system

Species	B_V	B_R	G_V	G_R	A_1	A_2	A_3	A_u	A_G	A_B
MnB (0 GPa)	263.30	260.5	179.22	172.45	1.464	0.944	1.565	0.21	1.93	0.53
MnB (143 GPa)	824.88	801.02	327.69	236.63	1.766	0.749	4.993	1.95	16.14	1.47
FeB (0 GPa)	308.37 287.8 ^a	302.80 284.6 ^a	155.66 148.5 ^a	125.47 130.9 ^a	1.57 1.63 ^a	1.04 0.91 ^a	3.38 2.45 ^a	1.22 0.68 ^a	10.74 5.85 ^a	0.91 0.62 ^a
FeB (77 GPa)	621.69	612.49	260.17	190.38	1.17	1.28	4.65	1.85	15.49	0.75
CoB (0 GPa)	344.52	330.27	149.77	140.56	1.742	1.047	1.520	0.37	3.17	2.11
CoB (77 GPa)	645.6	644.37	286.25	271.5	1.364	1.108	1.869	0.27	2.64	0.10
NiB (0 GPa)	245.38	245.20	110.66	108.95	0.08	0.78	0.04	1.409	0.919	1.084
NiB (77 GPa)	569.57	568.3	217.2	202.07	1.184	0.993	2.154	0.38	3.61	0.11

^aRef. [162].

Table 18. The calculated bulk, Young (E) and shear modulus (G) of TM_2B (under 0 and critical pressure, in GPa), Poisson's ratio (ν) and B/G ratio along with other available values.

Species	B	E	G	ν	B/G	$\Delta B/B$	$\Delta E/E$	$\Delta G/G$	$\Delta \nu/\nu$	$\Delta (B/G)/(B/G)$
MnB (0 GPa)	261.90	431.04	175.84	0.23	1.49					
	259.1 ^a	450.2 ^a	186 ^a	0.21 ^a	1.49 ^a	67.8	43.2	37.7	32.4	48.3
MnB (143 GPa)	812.95	758.70	282.16	0.34	2.88					
FeB (0 GPa)	305.6	365.7	140.6	0.30	2.174					
	286.6 ^b	360.5 ^b	139.7 ^b	0.29 ^b	2.05 ^b	50.5	35.6	37.6	11.8	21.2
FeB (77 GPa)	617.1	567.5	225.3	0.34	2.76					
CoB (0 GPa)	337.39	380.87	145.16	0.31	2.32	47.6	26.7	80.1	0	0
CoB (77 GPa)	644.99	278.88	731.24	0.31	2.31					
NiB (0 GPa)	245.28	286.63	109.80	0.31	2.23	56.8	26.8	80.39	8.8	17.7
NiB (77 GPa)	568.94	209.64	560.11	0.34	2.71					

^aRef[168], ^bRef. [162].

Poisson's ratio ν characterizes the stability of the crystal against shearing strain. For a typical metal, the value is supposed to be 0.33; for the ionic-covalent crystal, the value is situated between 0.2 and 0.3; the strong covalent crystal has even smaller Poisson's ratio, which is usually below 0.15 [171], the calculated Poisson's ratios of our compounds range between 0.23 and 0.32. This indicates the bond's mixture character in these materials. It is also noted that the studied Poisson's ratios of MnB compound is smaller than other compounds.

A larger B/G value (>1.75) for a solid indicates the ductile behavior while a smaller B/G value (<1.75) usually means brittle material. Similarly, Poisson ratio $\nu > 0.26$ corresponds usually for ductile compounds [129]. At both 0 GPa and the critical pressure, FeB, CoB and NiB are ductile ($B/G > 1.75$ and $\nu > 0.26$), while MnB is brittle ($B/G < 1.75$ and $\nu < 0.26$), see Table 18.

5.1.6. Elastic anisotropy

Most crystals exhibit elastic anisotropy of varying degree. These effects are very important for the layered mono-borides; in particular, significant elastic anisotropy is related to the occurrence of microcracks in materials, and can be expressed by the universal anisotropic index A^U and by the indexes describing the behavior in shear and compression A_G and A_B , respectively, and may be proposed as follows (3.42) and (3.43). Using equations (3.51) and (3.52), the three-dimensional surface representations showing the variation of the Young, and bulk modulus are plotted in Figure 35 and Figure 36. The plane projections ((100), (010) and (001) plans) of the directional dependences of the Young and bulk modulus are given in Figure 37 and Figure 38 for comparisons.

The calculated values of anisotropic factors for mono- borides TMB are shown in Table 17. For an isotropic crystal, all three factors must be equal to unity, while any value deviation from 1 is a measure of the degree of elastic anisotropy in the crystal.

The shear anisotropic factor for an orthorhombic crystal can be measured by three factors (Zener ratios):

- The anisotropic factor for the $\{1\ 0\ 0\}$ shear planes between (011) and (010) directions as define in (3.45):
- The anisotropic factor for the $\{0\ 1\ 0\}$ shear planes between (101) and (001) directions is(3.46) and The anisotropic factor for the $\{0\ 0\ 1\}$ shear planes between (110) and (010) directions is (3.47):

The applied high pressure reduces the anisotropic factors A_1 and A_3 by 17% and 68.6% for MnB, while for FeB has the reduced anisotropic factors A_2 (18.7%) and A_3 (27.3%).

For the universal anisotropic index A^U is augmented when pressure is applied by 89.2% for MnB and 30% for FeB.

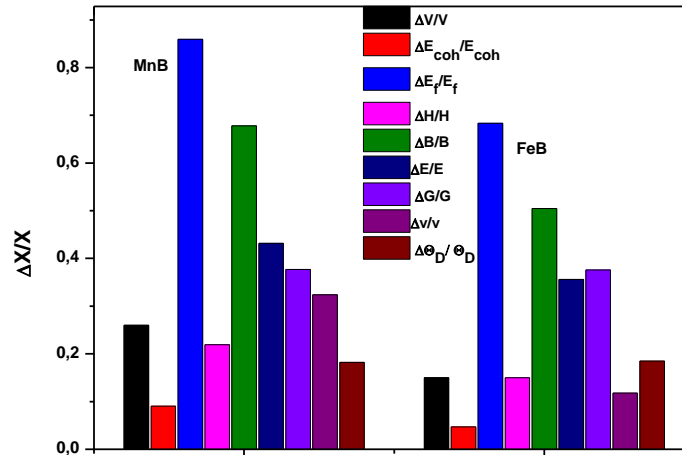


Figure 34. The calculated relative change of parameters by the top: volume cohesive and formation energy, hardness, bulk, Young and shear modulus Poisson ratio and Debye temperature.

For orthorhombic system the 3D figures of directional dependencies of the reciprocal of Young's and Bulk modulus for the TM-B binary compounds can be defined by (3.51) and (3.52). The surface constructions of Young and bulk modulus of MnB, FeB, CoB and NiB compounds are shown in Figure 35 and Figure 36. These surfaces have similar features. The projections of the mechanical moduli are plotted in Figure 37 and Figure 38. It can be clearly seen that TMB exhibits a pronounced anisotropy with the non-spherical nature (Figure 35 and Figure 36). Thus, $A_u=0.21(1.95)$ and $A_u=1.22(1.85)$ at 0 GPa (high pressure) for both MnB and FeB respectively, while for CoB ($A_u=0.37$) and NiB ($A_u=1.41$) (Table 17). The obtained results for TM-B are plotted in Fig. 10, 11 and 12. The variation of Young modulus in all planes and directions show that our compounds possess a minimum of Young modulus along [100] direction and a maximum along [001] direction.

As example FeB exhibits a minimum of $E_{[100]} = 195.45$ GPa, a maximum of $E_{[001]} = 407.06$ GPa and for $E_{[010]} = 201.81$ GPa. Therefore, the ordering of Young's modulus as a function of the principal crystal tensile $[u\ v\ w]$ for TM-B are:

$E_{[100]} < E_{[010]} < E_{[001]}$. Additionally, it is remarkable to note that the variation of bulk modulus with B_{\min} along $[100]$ directions and B_{\max} along $[010]$ directions, for the compounds MnB, FeB and CoB, but for NiB the minimum of B is along $[100]$ directions and the maximum is along $[001]$ direction, which is consistent with the predicted elastic constants along different axes

(Table 16).

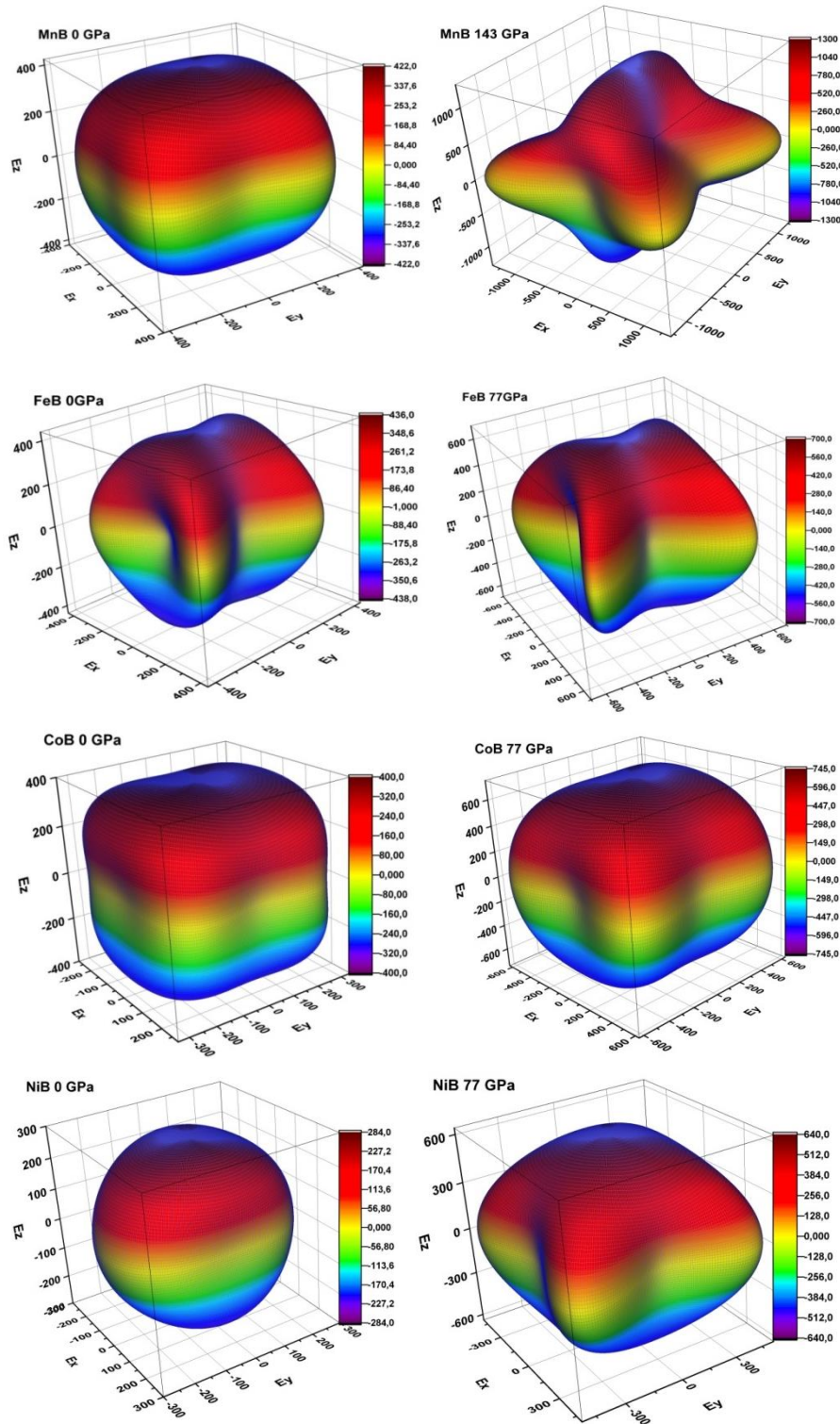


Figure 35. Illustration of directional dependent Young's modulus of TMB compounds: With 0 GPa pressure and critical pressure.

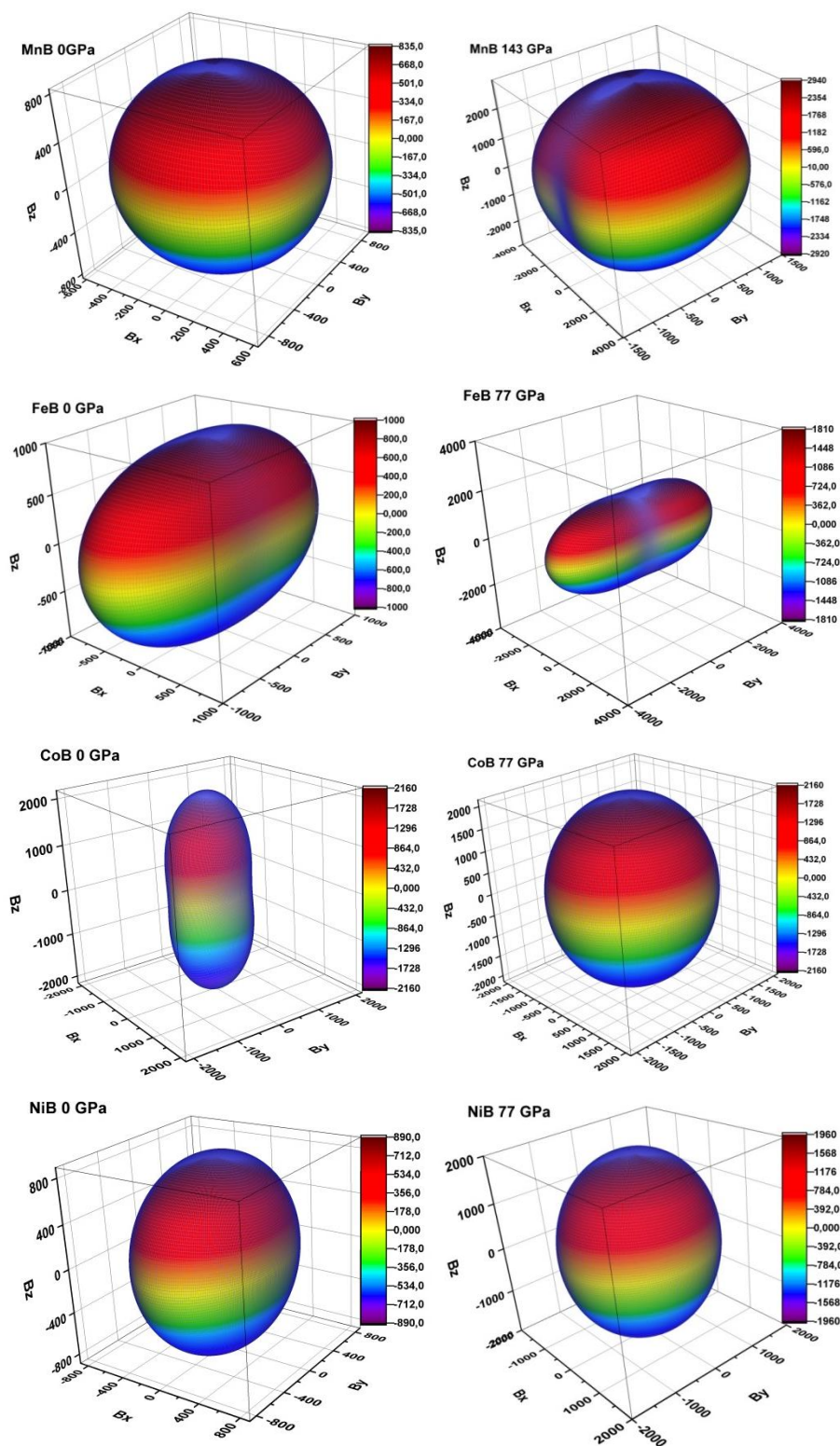


Figure 36. Illustration of directional dependent bulk modulus of TMB compounds:
With 0 GPa pressure and critical pressure.

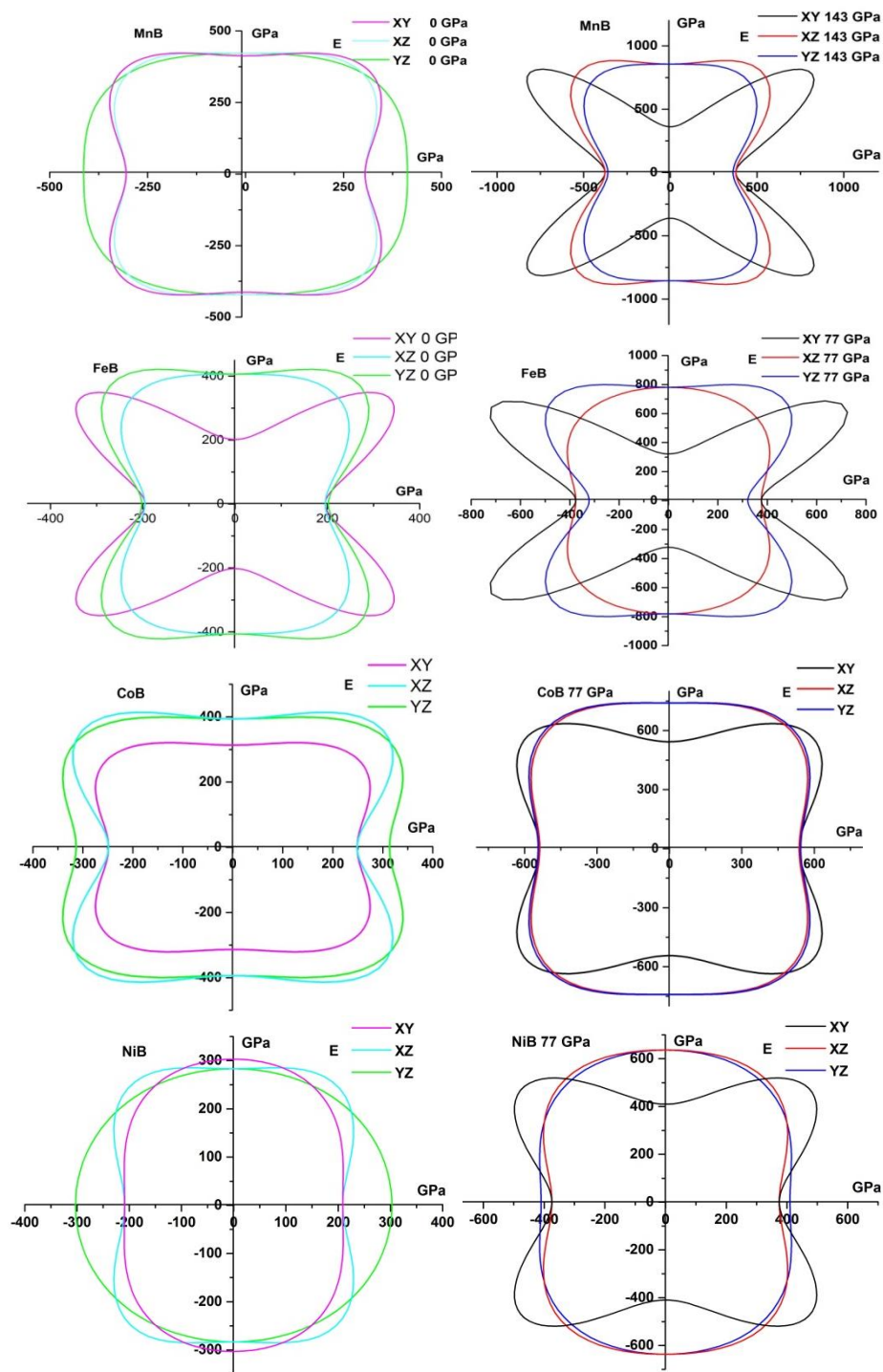


Figure 37. The projection of Young moduli at several different crystal planes for TMB compounds.

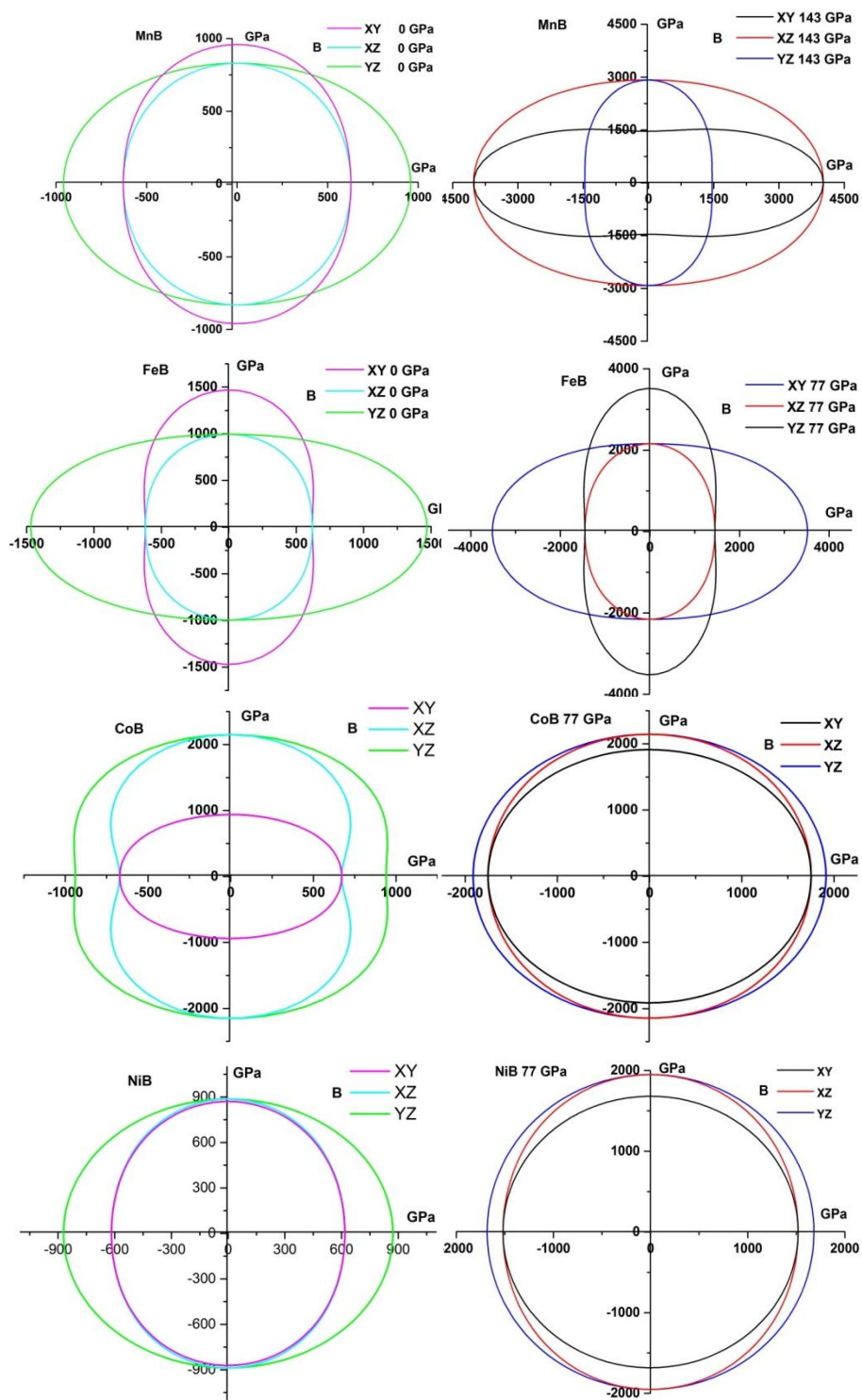


Figure 38. The projection of bulk moduli at several different crystal planes for TMB compounds.

5.1.7. Acoustic sound velocities and Debye temperature

The calculated densities, sound velocities and Debye temperatures at 0 GPa and high pressure for TMB compounds are shown in Table 19. The anisotropic properties of sound velocities indicate the elastic anisotropy in these crystals. For example, the C_{11} , C_{22} , C_{33} determines the longitudinal sound velocities along [100], [010] and [001] directions, respectively, the C_{44} , C_{55} and C_{66} correspond to the transverse modes [135].

The Debye temperature can be estimated from the average sound velocity using equation 3.8.7-3 based on elastic constants.

Our compounds have large mechanical moduli and large densities, which causes relatively large elastic wave velocities. For Debye temperatures the largest Θ_D is 671 K for MnB while the lowest one is 581.96 K for NiB and the order of Θ_D for TMB compounds is: MnB > FeB > CoB > NiB. It is well known that the Θ_D is the inverse to molecular weight and can be used to characterize the strength of covalent bonds in the solids. From Table 19, I conclude that the covalent bonds in MnB are stronger than the other borides. In the case of NiB, the smallest Θ_D implies the strong metallic bonds among Ni atoms.

Table 19. The density (in g/cm^3), anisotropic sound velocities (in m/s), average sound velocity (in m/s) and Debye temperature (in K) for the TM_2B compounds.

Species	ρ	v_l	V_t	vm	Θ_D	$\Delta\rho/\rho$	$\Delta v_l/v_l$	$\Delta v_t/v_t$	$\Delta vm/vm$	$\Delta\Theta_D/\Theta_D$
MnB (0 GPa)	6.41	8800	5238	5799	671 356 ^{exp}					
MnB (143 GPa)	8.66	11718	5708	6413	821	26	25	8.24	9.6	18.23
FeB (0 GPa)	7.085	8342	4455	4976	593					
FeB (77 GPa)	8.78	10223	5066	5686	728	19.3	18.4	12.06	12.47	18.5
CoB (0 GPa)	7.38	8482	4435	4961	590 669 ^{exp}					
CoB (77 GPa)	8.91	10678	5592	6255	792					
NiB (0 GPa)	7.05	7454	3947	4411	582					
NiB (77 GPa)	8.56	9955	4948	5553	695	17.6	25.12	20.24	20.56	16.23

^aRef.[148].^{exp}Ref[172]

5.2. Conclusions

The phase stability, magnetic moment, mechanical properties as well as Debye temperatures of the TMB (TM = Mn, Fe, Co and NiB) compounds are investigated and discussed from the first-principles calculations. The equilibrium structure and formation energy show that MnB and FeB are energetically more stable at 0 GPa than at each critical pressure. For both MnB and FeB, at a certain pressure (143 GPa for MnB and 77 GPa for FeB) a pronounced abrupt collapse of the magnetic moment (first order quantum phase transitions), this character might a sign of superconducting. The difference of the topology of DOS near the Fermi level is observed. The hardness, elastic constants, bulk, shear, Young's modulus, acoustic velocities and Debye temperature for MnB and FeB compounds increase with the applied pressure. The calculated ground-state parameters are in good agreement with the other available theoretical data and

experiments values. The increasing B/G and ν of these compounds indicate that MnB is ductile phases under high pressures. The TMB compounds show a certain degree of mechanical anisotropy. The Debye temperatures increase with increasing pressure and MnB has a higher Debye temperature at 0 GPa and Critical pressure. The calculated sound velocities along [100], [010] and [001] directions for TMB under high pressure also reveal the anisotropic nature of our compounds.

CHAPTER 6: Physical properties of solid solution

of $\text{Fe}_{(1-x)}\text{Mn}_x\text{B}$.

6. Ab initio calculations of structural, magnetic and anisotropic elastic properties of Fe_(1-x)Mn_xB.

The properties of transition metal alloys and transition metal borides have been under intense study for decades [173, 174]. Among these properties, magnetization has been given special attention because of its applications in the electronics industry. Previous studies have provided us with insights on the role of d-orbital electrons in iron borides, indicating that the electrons are hybridized in a subtle way [175]. In addition, the magnetic properties are shown to be correlated with the electronic structure [176], as well as the long-range spin interaction [177]. Various transition metal alloy and transition metal boride materials have been studied, in both experimental analysis and theoretical calculations, for example, MnB [178], Fe_(1-x)B_x [179, 180], Fe_xMn_(1-x) [181], Fe_xB [128], Fe_{80-x}Mn_xB₂₀ [182] and Fe_(1-x)(Mn_x)₇₈B₂₂ [183]. However, there is relatively little research done with the transition metal alloy borides Fe_(1-x)Mn_xB. Both FeB and MnB have the same orthorhombic (Pnma) structure [163, 184], and it is interesting to investigate the profile of the change in magnetic properties of the material if some of the Mn atoms are replaced by Fe in MnB.

In this chapter, I investigate the electronic structure and the anisotropic elastic properties of Fe_(1-x)Mn_xB alloys in the whole compositional range ($0 \leq x \leq 1$) at 0 GPa by first-principles calculations within the virtual crystal approximation VCA framework [185]. The VCA approach ignores any possible short range order and assumes that on each potentially disordered site there is a virtual atom which interpolates between the behaviors of the actual components.

This approach neglects the alloying effects as local distortions around atoms and cannot be expected to reproduce the finer details of the disordered structures very accurately. Despite this limitation, it often produces acceptable and useful results. The VCA allows calculations on disordered systems to be carried out at the same cost as calculations for ordered structures. For example, in the case of Fe_{0,5}Mn_{0,5}B alloys, the virtual transition metal atom will have atomic number 25.5. However, there are no data available in the literature about theoretical C_{ij} on these solid solution alloys and are given only for single-crystals (FeB and MnB). Thus, these values are not directly comparable to elastic moduli deduced from experiments made on polycrystalline films and bulk materials. The lattice parameters and of the single-crystal elastic constants are determined and discussed. Furthermore, the anisotropic elastic constants and moduli at the polycrystalline scale are computed and plotted in the three dimensional (3D) surfaces and planar contours of Young and bulk moduli of Fe_{1-x}Mn_xB compounds at several crystallographic planes, ((100), (010) and (001)) to reveal their elastic anisotropy.

6.1.Method of calculation

In order to calculate electronic structures, magnetic and anisotropic elastic properties of Fe_{1-x}Mn_xB, I use the pseudo-potential plane wave (PPPW) method implemented by the CASTEP packages [36].

For the method of virtual crystal approximation, the electron number used to calculate the density of state (DOS) and magnetism is the mean electron number of the linear combination of TM1 and TM2. In this approximation, the nuclear and valence charges of the TM atom are continuously altered from Mn= 25 to Fe = 26 to represent different cases in Fe_{1-x}Mn_xB.

The crystal structures of FeB and MnB calculated here refer to Bjurstroem's experimental work [16], with the space group Pnma and lattice parameters for FeB : a =5.317 Å, b = 2.95 Å

and $c = 3.964 \text{ \AA}$; and for MnB $a = 5.493 \text{ \AA}$, $b = 2.992 \text{ \AA}$ and $c = 4.147 \text{ \AA}$ (chapter 5). The lattice constants of Fe_{1-x}Mn_xB are determined by the structure relaxation. The kinetic energy cut-off value was selected as 500eV, which is sufficient to obtain the reliable results.

Total energies are evaluated in the first irreducible Brillouin zone with the following Monkhorst-Pack grids [152]: (8 x12x 10) for all compounds. The fraction x in the method of virtual crystal approximation plays the role of mean electron number. For the treatment of the disordered ternary alloy, I used the virtual crystal approximation VCA, in which the alloy pseudo potentials are constructed within a first-principles VCA scheme. Elemental ionic pseudo potentials of FeB and MnB are combined to construct the virtual pseudo potential of the Fe_{1-x}Mn_xB.

$$V_{VCA} = xV_{FeB} + (1 - x)V_{MnB} \quad (6.1-1)$$

The formation energy (E_f) of the Fe_{1-x}Mn_xB alloys is determined as follows:

In TM1_(1-x)TM2_xB, $Z = Z1(1 - x) + Z2(x)$ is the average of electron number, where $Z1$ and $Z2$

$$E_f(x) = E_T(Fe_{1-x}Mn_xB) - (1 - x)E_T(FeB) - xE_T(MnB) \quad (6.1-2)$$

represent the electron number of TM1 and TM2, respectively.

6.1.1. Structural properties and stability

The ternary Fe_{1-x}Mn_xB ($x=0, 0.25, 0.5, 0.75$ and 1) ferromagnetic alloys with space group Pnma (SG: 62) are studied in the orthorhombic phase. Figure 39 shows the total magnetic moment of Fe_{1-x}Mn_xB vs. fraction of Mn. The magnetic moments of FeB and MnB are about 1.12 and 1.83 μ_B /atom, respectively, which agree well with the previous studies.

When the fraction of manganese (x) becomes larger, the magnetic moment gradually increases. As the fraction x increases from 0 to 1, the occupation of the minority state decreases (Figure 41).

The calculated formation and cohesive energies of Fe_{1-x}Mn_xB (x=0, 0.25, 0.5, 0.75 and 1) are presented in Table 20. The formation energy is positive in the entire composition range from x=0.25 to x=0.75, which implies that orthorhombic (Fe_{1-x}Mn_x)B solid solutions are not stable, and will decompose into FeB and MnB. It has been shown that the mixing enthalpy of alloys can be represented as the sum of a negative contribution due to electron transitions during alloy formation and positive contribution due to the difference between the widths of the d-bands of the pure components [186].

The optimized equilibrium lattice constant and bulk modulus of (Fe_{1-x}Mn_x)B with GGA for various x concentrations are summarized in Table 20 and shown in Figure 40. It must be noted that the equilibrium lattice parameter is computed from the structural optimization, using the Broyden–Fletcher–Goldfarb–Shanno minimization [187-190]. Our calculated equilibrium lattice parameters for (Fe_{1-x}Mn_x)B, are in reasonable agreement with the experimental data [163, 172, 191]. The computed lattice constant for (Fe_{1-x}Mn_x)B is plotted against Mn fraction in Figure 40. The deviation from the linear dependence is distinct. Also, the bulk modulus B of (Fe_{1-x}Mn_x)B is calculated using the stress–strain method, and by applying the Voigt–Reuss–Hill approximation, is plotted against Mn fraction in Figure 40. A comparison of the lattice constant and bulk modulus of these alloys shows that an increase in the earlier parameter is accompanied by a decrease in the later one.

Table 20. The calculated ground state properties of (Fe_{1-x}Mn_x)B. Experimental values are listed in parentheses. Total cell energy E_{total} (eV/f.u.), cell parameters (a, b, c in Å) volume V (Å³), Bulk modulus (GPa), magnetic moment (MM in μ_B), cohesive energy E_{coh} (eV/f.u.) and formation energy E_f (eV/f.u.).

Parameters	X=0	X=0.25	X=0.5	X=0.75	X=1
E_{total}	-3773.90	-3511.63	-3305.60	-3093.16	-2927.61
a	5.317 (5.495) ^{exp1}	5.510 (5.521) ^{exp2}	5.483 (5.532) ^{exp2}	5.517 (5.553) ^{exp2}	5.493 (5.56) ^{exp3}
b	2.950 (2.946) ^{exp1}	2.986 (2.951) ^{exp2}	2.982 (2.961) ^{exp2}	2.989 (2.968) ^{exp2}	2.992 (2.977) ^{exp3}
c	3.964(4.053) ^{exp1}	4.052 (4.043) ^{exp2}	4.077 (4.104) ^{exp2}	4.122 (4.125) ^{exp2}	4.147 (4.145) ^{exp3}
V	62.176	66.66	66.68	67.97	68.153
MM	4.49	5.93	6.61	7.43	7.73
E_{coh}	-13.153	-1.44	-3.79	-4.54	-17.01
E_f	-1.207	12.67	11.29	11.50	-1.35

^{exp1}[191], ^{exp2}[172] and ^{exp3}[163]

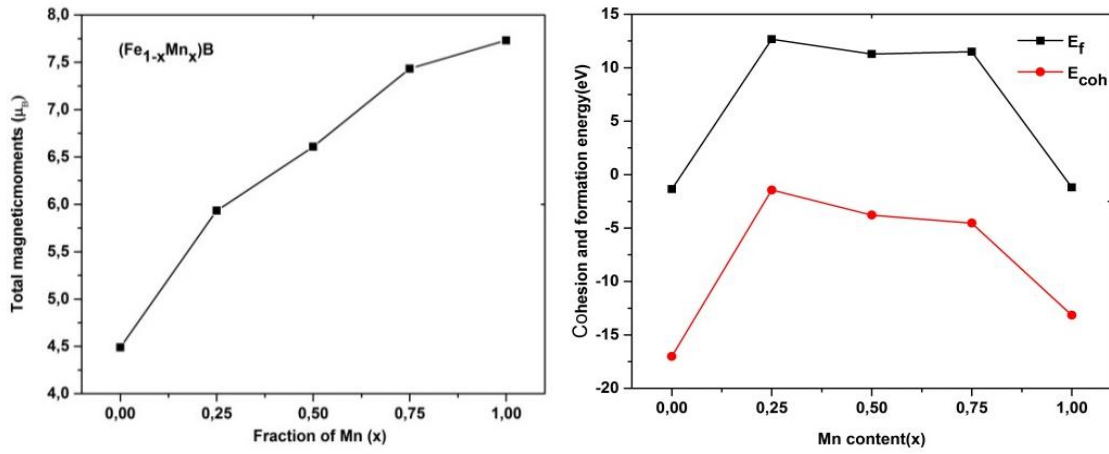


Figure 39. The calculated total magnetic moment, cohesive and formation energies as a function Mn content(x) at 0 GPa.

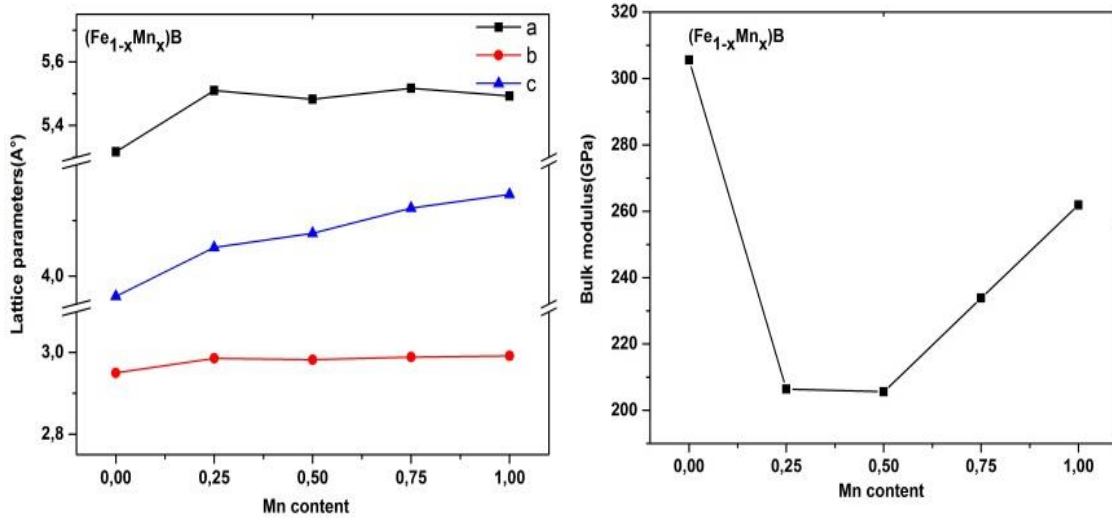


Figure 40. The calculated lattice parameter and bulk modulus as a function Mn content(x).

6.1.2. Density Of States

Total densities of state DOS for (Fe_{1-x}Mn_x)B compounds are illustrated in Figure 41. The most obvious feature of (Fe_{1-x}Mn_x)B compounds is the metallic character at the Fermi level. It can be seen that the total density of minority is shifted considerably from $x = 0.0$ to $x = 1.0$ from the left to the right of Fermi level, which mean the difference between the density of spin-up and spin-down increase and magnetic moment increased.

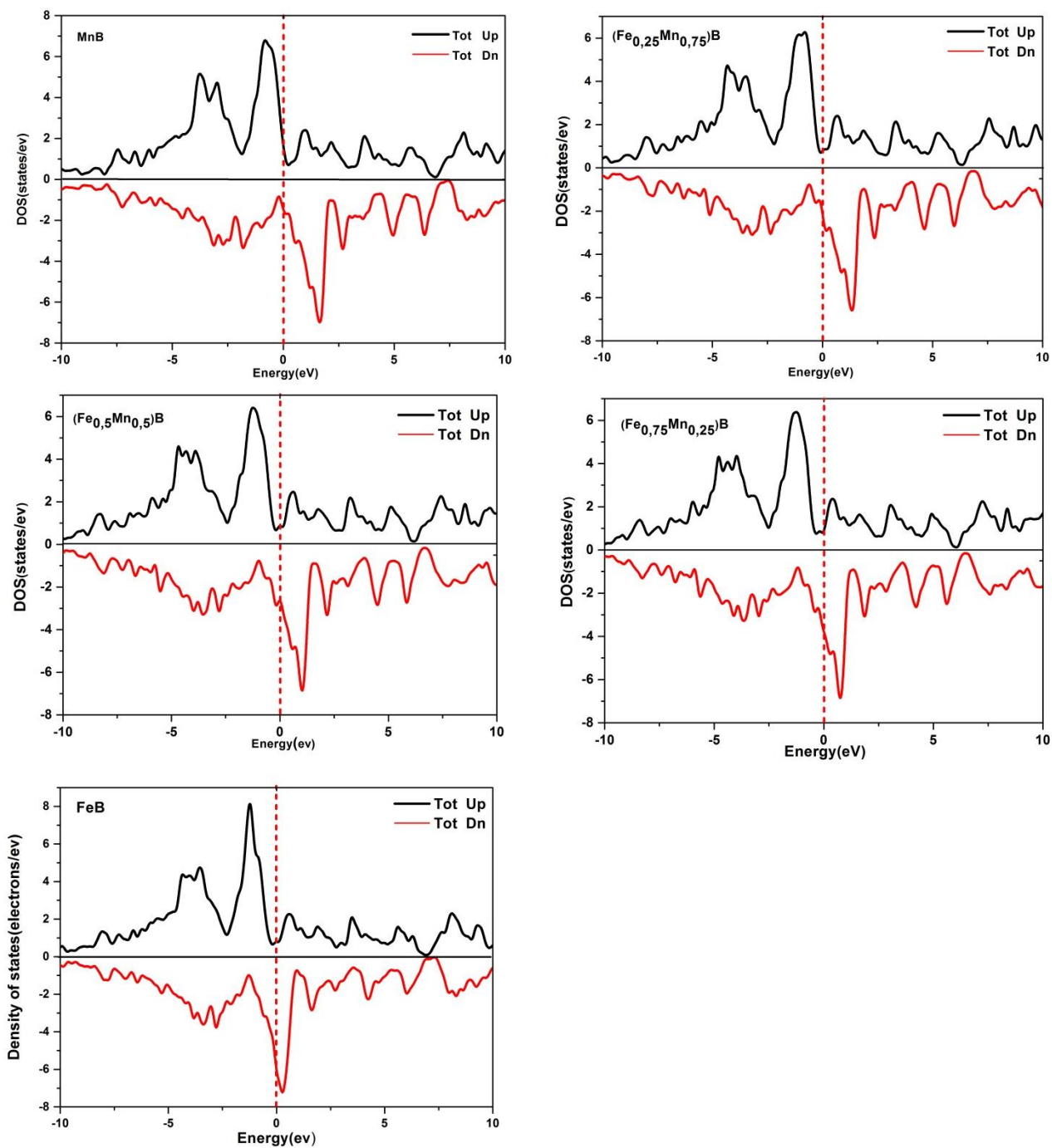


Figure 41. The calculated total and partial DOS of $(\text{Fe}_{1-x}\text{Mn}_x)\text{B}$. Dashed line represents the Fermi level.

Table 21. The stability of the (Fe_{1-x}Mn_x)B mono-borides according to Stoner model.

	$N_{TM}(E_F)$	I_{TM}	$N_{TM}(E_F) * I_{TM}$
X=0	8,02	0.46	3.69
X=0.25	6,2	0,45	2,79
X=0.5	5,1	0,44	3
X=0.75	5,81	0,42	2.46
X=1	6	0.41	2.46

6.1.3. Elastic properties

The elastic constants of orthorhombic crystalline (Fe_{1-x}Mn_x)B compounds are presented in Table 22. Generally, the elastic constants C_{11} , C_{22} and C_{33} are very high, both at zero and critical pressure, which indicates the high resistance to the axial compression in these directions. Moreover, it is shown in Table 22 that the elastic constants C_{11} , C_{22} and C_{33} are larger than C_{44} , C_{55} and C_{66} , indicating that (Fe_{1-x}Mn_x)B are mechanically anisotropic and the shear deformation is easier to take place than other deformation forms. It is well known that the elastic constant C_{44} is the most significant parameter which indirectly determining the indentation hardness of a solid [124]. A large C_{44} implies a strong resistance to monoclinic shear in the (100) plane. The highest C_{44} at 0 GPa for FeB(x=0) than those for the other compounds means that its ability to resist shear distortion in the (100) plane is the strongest.

The results in Table 22 indicate that (Fe_{1-x}Mn_x)B have relatively strong anisotropic elastic constants resulting in the directional dependence of the moduli. Notably, the values of C_{11} (C_{66}) are relatively small than that of C_{33} (C_{44}) at 0 GPa, implying that the intra-layer chemical bonds are weaker than those between the layers,

Table 22. The calculated full set elastic constants of (Fe_{1-x}Mn_x)B along with other available values.

Species	Elastic constants								
	C_{11}	C_{22}	C_{33}	C_{12}	C_{13}	C_{23}	C_{44}	C_{55}	C_{66}
MnB	392.05	510.74	497.17	181.33	154.92	148.61	212.11	167.69	211.28
	414.4 ^a	527.7 ^a	504.8 ^a	171.1 ^a	147.5 ^a	127.7 ^a	215.8 ^a	218.4 ^a	175.8 ^a
Fe _{0.25} Mn _{0.75} B	359.25	462.46	478.41	159.16	126.96	121	205.63	157.76	201.06
Fe _{0.5} Mn _{0.5} B	352	420	464.22	149.08	100	94.72	202.37	151.26	210.67
Fe _{0.75} Mn _{0.25} B	347	377.4	474.7	139.5	92.6	111	203	155	179
FeB	389.82	438.36	557.07	286.85	183.12	239.76	218.8	132.25	212.01
	373.7 ^b	434.1 ^b	503.4 ^b	246 ^b	184.4 ^b	209.1 ^b	207.4 ^b	117.7 ^b	193.7 ^b

^aRef[168], ^bRef[162].

The mechanical stability criteria at 0 GPa can be represented in a uniform manner for orthorhombic structure (criteria: (3.36)).

It is clear from Table 22 that all elastic constants are consistent with the restrictions of orthorhombic crystal, which reveals that all these (Fe_{1-x}Mn_x)B compounds are mechanically stable.

The elastic constant C_{11} , C_{22} and C_{33} characterizes the x, y and z directions resistance to linear compression; while C_{44} , C_{55} and C_{66} characterize the shear deformation.

It is obvious that the calculated elastic constants C_{33} for (Fe_{1-x}Mn_x)B compounds are larger than C_{22} and C_{11} at zero and critical pressure for the concentration(0.25, 0.5, 0.75 and 1) which indicates that these compounds are more incompressible under uniaxial stress along the z axis (c

direction) than the x and y axes (a and b direction)($C_{33} > C_{22} > C_{11}$). While MnB ($x=0$) is stronger against compression in b direction at 0 GPa and z direction under critical pressure.

Their elastic anisotropic nature can be explained by the ratios of C_{11}/C_{22} and C_{11}/C_{33} .

The C_{11}/C_{22} and C_{11}/C_{33} ratio = 1.0 means the same resistance to linear compression along the x, y and z axes. If C_{11}/C_{22} and C_{11}/C_{33} are larger than 1.0 for a crystal, the y and z axis are more compressible than the x axis; while the x axis is more compressible than the y and z axis with C_{11}/C_{22} and C_{11}/C_{33} smaller than 1.0. A larger deviation of C_{11}/C_{22} and C_{11}/C_{33} ratio from 1.0 means the larger difference in linear compression along the x, y and z axes. Moreover The C_{44}/C_{11} , C_{55}/C_{22} and C_{66}/C_{22} ratio for all x concentration are lesser than 1.0 which showing a weaker resistance to shear deformation compared with the resistance to the unidirectional compression.

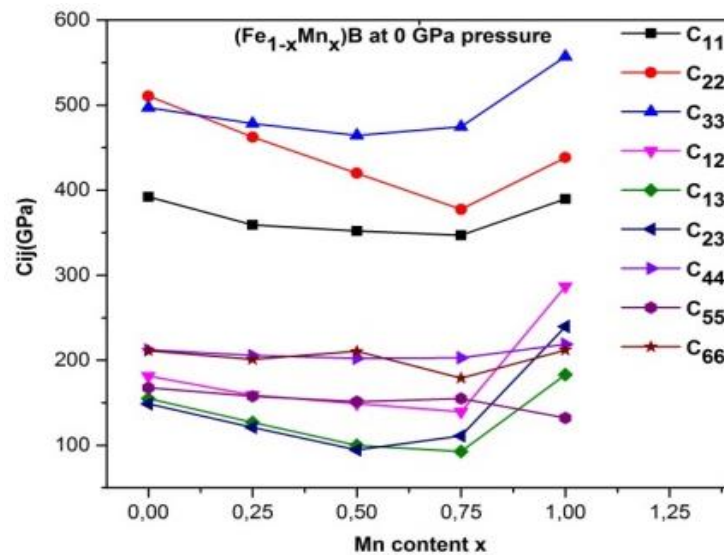


Figure 42. Illustration of elastic constant's as a function of Mn content of $(Fe_{1-x}Mn_x)B$ compounds.

The arithmetic average of the Voigt and Reuss bounds is known as the Voigt-Reuss-Hill (VRH) average, which is regarded as the best estimate for the theoretical value of polycrystalline elastic modulus eq:(3.40).

The Young modulus and Poisson ratio can be computed using relations (3.41).

The calculated polycrystalline bulk modulus B, shear modulus according Voigt-Reuss-Hill approach, Young's modulus E and Poisson's ratio ν are tabulated in Table 23 and Table 24.

(Fe_{1-x}Mn_x)B at concentration (x=0) is ductile since $B/G > 1.75$ and $\nu > 0.26$, while (Fe_{1-x}Mn_x)B is brittle ($B/G < 1.75$ and $\nu < 0.26$) at 0 GPa for the 0.25, 0.5, 0.75 and 1 concentrations.

Table 23. Polycrystalline elastic properties and Anisotropic factors of Fe_{1-x}Mn_xB compounds.

Species	B _V	B _R	G _V	G _R	A ₁	A ₂	A ₃	A _u	A _G	A _B
MnB	263.30	260.5	179.22	172.45	1.46	0.94	1.57	0.21	1.93	0.53
Fe _{0.25} Mn _{0.75} B	207.26	205.60	163.18	155.6	1.41	0.90	1.60	0.25	2.38	0.40
Fe _{0.5} Mn _{0.5} B	205.99	205.20	169.08	160.30	1.31	0.87	1.78	0.28	2.67	0.19
Fe _{0.75} Mn _{0.25} B	235.14	232.52	172.76	165.83	1.28	0.98	1.61	0.22	2.05	0.56
FeB	308.37	302.80	155.66	125.47	1.57	1.04	3.38	1.22	10.74	0.91
	287.8 ^a	284.6 ^a	148.5 ^a	130.9 ^a	1.63 ^a	0.91 ^a	2.45 ^a	0.68 ^a	5.85 ^a	0.62 ^a

^aRef[162].

Table 24. The calculated bulk, Young (E) and shear modulus (G) of Fe_{1-x}Mn_xB (in GPa), Poisson's ratio (ν) and B/G ratio along with other available values.

Species	B	E	G	ν	B/G
MnB	261.90	431.04	175.84	0.23	1.49
	259.1 ^a	450.2 ^a	186 ^a	0.21 ^a	1.49 ^a
Fe _{0.25} Mn _{0.75} B	206.43	380.29	159.39	0.19	1.30
Fe _{0.5} Mn _{0.5} B	205.60	389.95	164.69	0.18	1.25
	233.83	409.14	169.30	0.21	1.38
Fe _{0.75} Mn _{0.25} B	305.6	365.7	140.6	0.30	2.17
FeB					

^aRef[168], ^bRef[162]

6.1.4. Elastic anisotropy

The three-dimensional surface representations showing the variation of the Young, and bulk modulus are plotted in Figure 43 and Figure 44. The plane projections ((100), (010) and (001) plane) of the directional dependences of the Young and bulk modulus are given in Figure 43 for comparisons.

The calculated values of anisotropic factors for mono- borides (Fe_{1-x}Mn_x)B are shown in Table 23. For an isotropic crystal, all three factors must be one, while any value smaller or greater than one is a measure of the degree of elastic anisotropy possessed by the crystal.

The shear anisotropic factor for an orthorhombic crystal can be measured by three factors (Zener ratios) (3.45), (3.46) and (3.47).

Here, I plot the Young modulus (E), and bulk modulus (B) in different directions using spherical coordinates for Fe_{1-x}Mn_xB compounds. For orthorhombic crystal class, the directional dependence of Young modulus (E) and bulk modulus (B) can be written as:

For orthorhombic system [133] (3.51) and (3.52).

For an isotropic system, 3D directional dependence would give rise to a spherical shape, while the deviation degree from spherical shape reflects the content of anisotropy. The surface constructions of Young and bulk modulus of Fe_{1-x}Mn_xB compounds are shown in Figure 45 and Figure 46. The surface constructions of Young moduli and bulk modulus are respectively similar to each other. The projections of the mechanical moduli are plotted in Figure 45 and Figure 46. It can be clearly seen that Fe_{1-x}Mn_xB exhibits a pronounced with the non-spherical nature. Thus, the calculated values of anisotropic factors (A_u, A_G and A_B) for mono- borides (Fe_{1-x}Mn_x)B are shown in Table 23, which are all some different to zero. The variation of Young's modulus in all planes and directions shows that our compounds possess a minimum of Young's modulus E, in [100] direction, and a maximum of E [001] direction. As example FeB exhibits a minimum of E_[100] = 195.45GPa, a maximum of E [001] = 407.06GPa and for E_[010] = 201.81GPa. Therefore, the ordering of Young's modulus as a function of the principal crystal tensile [u v w] for TM-B are:

$$E_{[100]} < E_{[010]} < E_{[001]}.$$

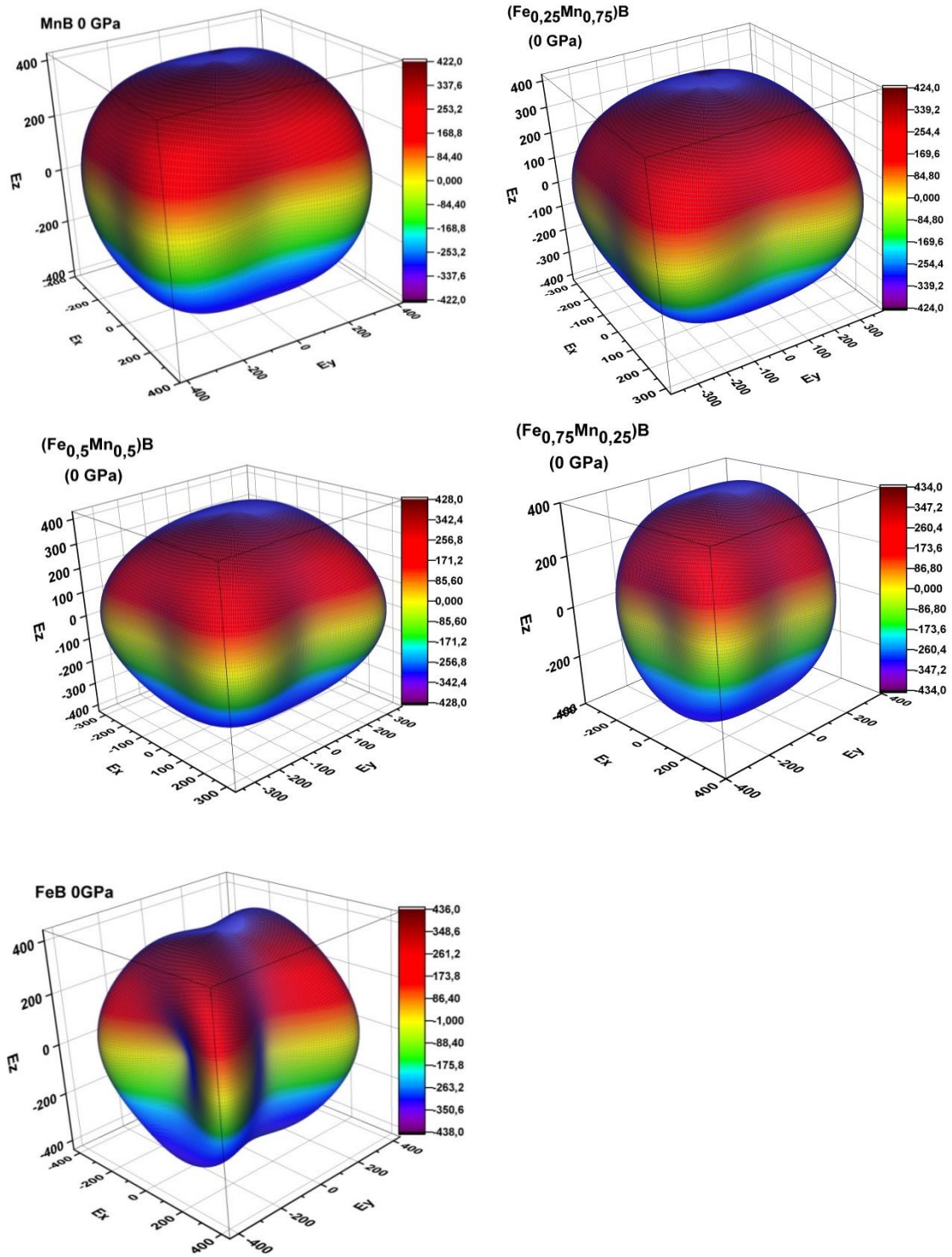


Figure 43 Illustration of directional dependent Young's modulus of (Fe_{1-x}Mn_x)B compounds: With 0 GPa pressure critical pressure.

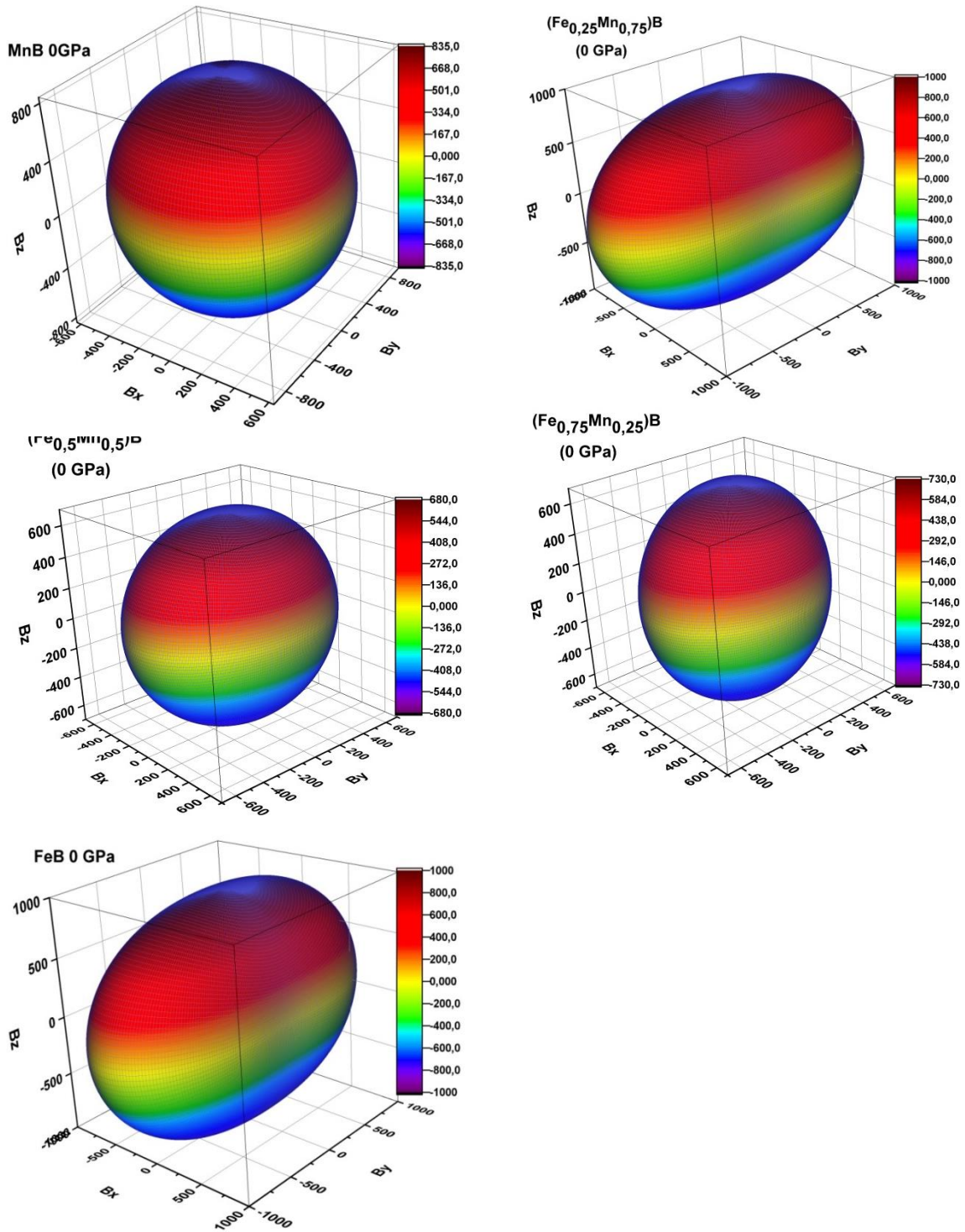


Figure 44. Illustration of directional dependent bulk modulus of (Fe_{1-x}Mn_x)B compounds

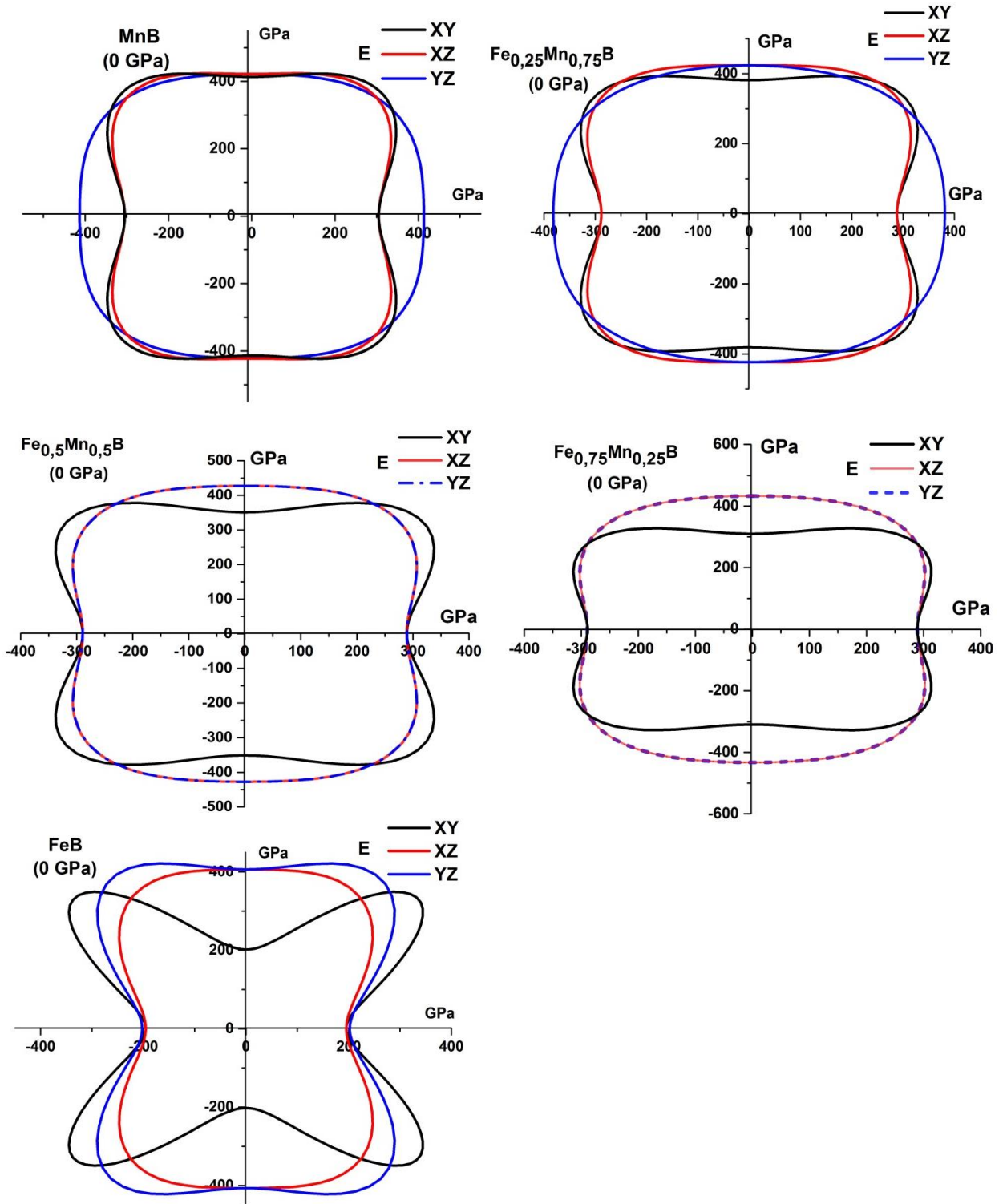


Figure 45. The projection of Young modul at 0 GPa for different crystal planes for Fe_{1-x}Mn_xB compounds.

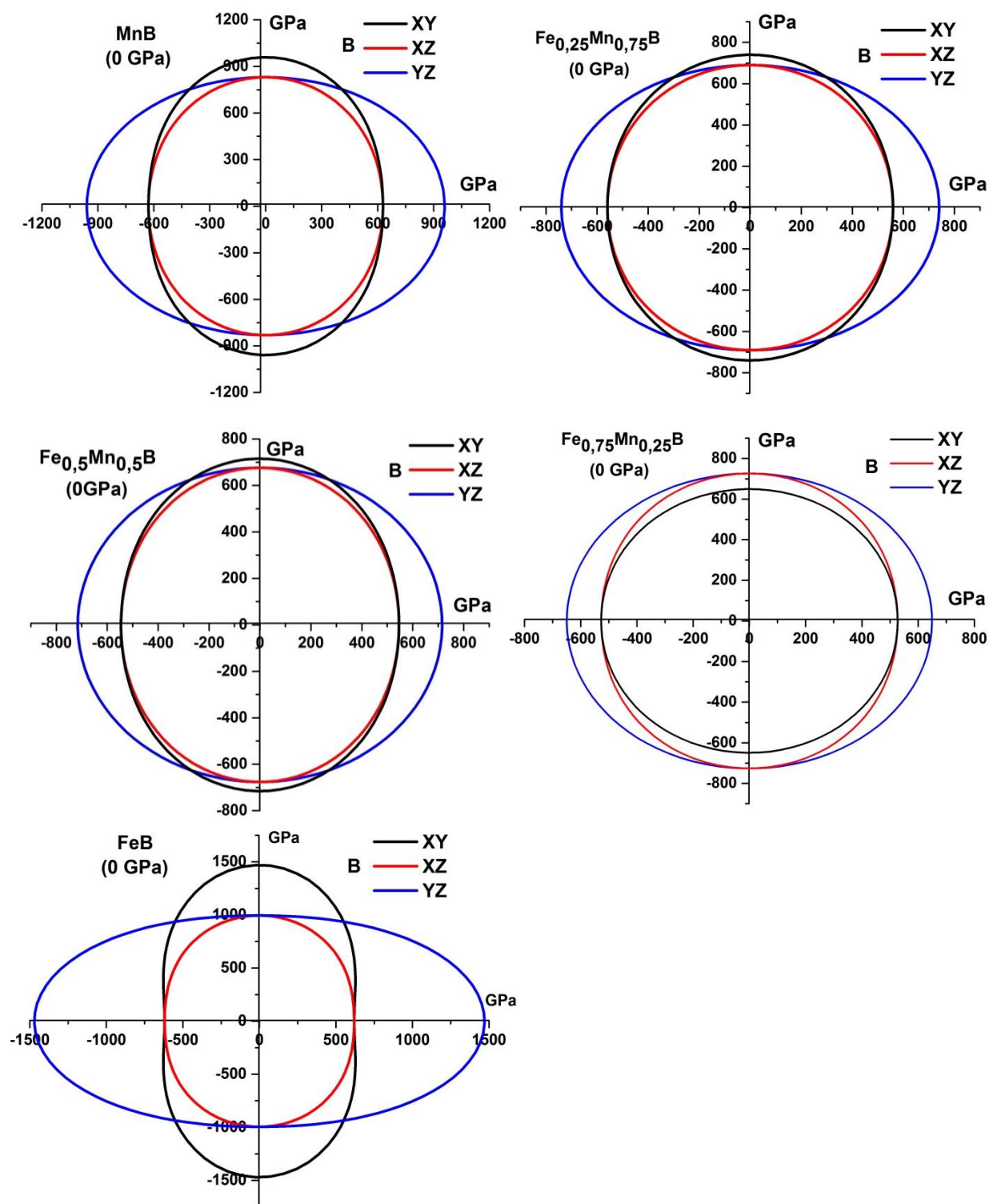


Figure 46. The projection of Bulk modul at 0 GPa for different crystal planes for $\text{Fe}_{1-x}\text{Mn}_x\text{B}$ compounds.

6.1.5. Acoustic sound velocities and Deby temperature

The acoustic velocities for (Fe_{1-x}Mn_x)B compounds in the principal directions can be expressed by (3.54).

Where ρ is the density of (Fe_{1-x}Mn_x)B compounds; v_1 is the longitudinal sound velocity; v_{t1} and v_{t2} refer the first transverse mode and the second transverse mode, respectively. The calculated densities, sound velocities and Debye temperatures for (Fe_{1-x}Mn_x)B compounds are shown in Table 25. It is obvious that MnB compound has large sound velocities, because for two causes, the first one is that its density is lesser than the other structures and the other is due to the high magnetic moment. The anisotropic properties of sound velocities indicate the elastic anisotropy in these crystals. For example, the C_{11} , C_{22} , C_{33} determine the longitudinal sound velocities along [100], [010] and [001] directions, respectively, the C_{44} , C_{55} and C_{66} correspond to the transverse modes [135].

As a fundamental parameter for the materials' thermodynamic properties, Debye temperature Θ_D is related to specific heat, thermal expansion and elastic constants. The Debye temperature can be estimated from the average sound velocity by the following equation(3.55) based on elastic constant evaluations [136].

The elastic wave velocities of these compounds are relatively large, because our compounds have large mechanical moduli and large densities. For Debye temperatures the largest Θ_D is 671 K for MnB ($x=1$), while the lowest one is 592.78 K for FeB($x=0$). It is well known that the Θ_D can be used to characterize the strength of covalent bonds in the solids. From Table 25, I conclude that the covalent bonds in MnB are stronger than the other borides. In the case of FeB, the smallest Θ_D implies the strong metallic bonds among Fe atoms.

Table 25. The density (in g/cm³), anisotropic sound velocities (in m/s), average sound velocity (in m/s) and Debye temperature (in K) for the (Fe_{1-x}Mn_x)B compounds.

Species	ρ	v_l	v_t	v_m	Θ_D
MnB	6.41	8799.67	5237.57	5798.51	671 356 ^{exp}
(Fe _{0.25} Mn _{0.75})B	6.45	8059.37	4971.08	5483.87	635.14 645 ^{exp}
(Fe _{0.5} Mn _{0.5})B	6.6	8026.35	4995.30	5505.34	641.76 602 ^{exp}
(Fe _{0.75} Mn _{0.25})B	6.62	8331.89	5057.08	5587.98	651.43 562 ^{exp}
FeB	7.085	8342.24	4454.74	4976.19	592.78 740 ^a 403 ^{exp}

^{exp}Ref[172], ^aRef[162]

6.2. Conclusions

The phase stability, magnetic moment, hardness, elastic moduli, elastic anisotropy properties, and Debye temperatures of the (Fe_{1-x}Mn_x)B (X = 0, 0.25, 0.5, 0.75 and 1) compounds as a function of pressure are investigated and discussed from the first-principles calculations. The equilibrium structure and formation energy show that (Fe_{1-x}Mn_x)B (x=1) and x=0 are energetically more stable than the other concentration. The calculated ground-state parameters are in good agreement with the other available theoretical data and experiments values. The increasing B/G and ν of these compounds indicate that are ductile phases under high pressures. The (Fe_{1-x}Mn_x)B compounds show a certain degree of mechanical anisotropy.

The calculated sound velocities along [100], [010] and [001] directions for (Fe_{1-x}Mn_x)B imply the anisotropic.

General Conclusions and Outlook

7. General conclusions and outlook

In this thesis three kinds of compounds are investigated by density functional calculations in generalized gradient spin density approximation.

The first one is the tetragonal semi-borides TM_2B ($TM = Fe, Co$ and Ni) compounds where the phase stability, magnetic moment, hardness, elastic moduli, elastic anisotropy properties, and Debye temperatures are investigated and discussed from the first-principles calculations at 0 GPa and high pressure. The equilibrium structure and formation energy show that Fe_2B and Co_2B are energetically more stable at 0 GPa than at each critical pressure. Both Fe_2B and Co_2B have an abrupt magnetic collapse when the pressure is about 85 GPa. The hardness, elastic constants, bulk, shear, Young's modulus, acoustic velocities and Debye temperature for Fe_2B , Co_2B and Ni_2B compounds increase with the applied pressure. The calculated ground-state parameters are in good agreement with the other available theoretical data and experiments values. The increasing B/G and ν of these compounds indicate that Fe_2B and Co_2B are ductile phases under high pressures. The TM_2B compounds show a certain degree of mechanical anisotropy. The Debye temperatures increase with increasing pressure and Fe_2B has a higher Debye temperature in two pressures 0 GPa and Critical pressure. The calculated sound velocities along [100] and [001] directions for TM_2B under high pressure also imply the anisotropic.

The second kind consists of the orthorhombic mono-borides TMB ($TM = Mn, Fe, Co$ and NiB) compounds where also the phase stability, magnetic moment, hardness, elastic moduli, elastic anisotropy properties, and Debye temperatures are investigated and discussed from the first-principles calculations as a function of pressure. The equilibrium structure and formation energy

General conclusions and outlook

show that MnB and FeB are energetically more stable at 0 GPa than at each critical pressure. Both MnB and FeB have a magnetic transition when the pressure is about 143 GPa and 77 GPa. The hardness, elastic constants, bulk, shear, Young's modulus, acoustic velocities and Debye temperature for MnB and FeB compounds increase with the applied pressure. The calculated ground-state parameters are in good agreement with the other available theoretical data and experiments values. The increasing B/G and ν of these compounds indicate that MnB is ductile phases under high pressures. The TMB compounds show a certain degree of mechanical anisotropy. The Debye temperatures increase with increasing pressure and MnB has a higher Debye temperature in two pressures 0 GPa and Critical pressure. The calculated sound velocities along [100], [010] and [001] directions for TMB under high pressure also imply the anisotropic. At last the Substitution of Fe by Mn in FeB or Mn by Fe in MnB: $Fe_{1-x}Mn_xB$ ($X = 0, 0.25, 0.5, 0.75$ and 1) compounds are investigated and discussed from the first-principles calculations using Virtual Crystal Approximation (VCA), this offers technically the simplest approach, allowing calculations on disordered systems to be carried out at the same cost as calculations for ordered structures. The calculated ground-state parameters are in good agreement with the other available theoretical data and experiments values. The elastic constants, Young's, bulk, shear, modulus, acoustic velocities and Debye temperature for $(Fe_{1-x}Mn_x)B$ compounds are calculated and discussed. $Fe_{1-x}Mn_xB$ at concentration ($x=0$) is ductile, while $Fe_{1-x}Mn_xB$ is brittle for the concentrations 0.25, 0.5, 0.75 and 1. The $(Fe_{1-x}Mn_x)B$ compounds show a certain degree of mechanical anisotropy.

The calculated sound velocities along [100], [010] and [001] directions for $(Fe_{1-x}Mn_x)B$ are anisotropic. My perspective is to complete my ab initio calculation by the experiments research

General conclusions and outlook

that lends further credibility of research, and try to discover the superconductivity for transition metal borides under pressure.

ANNEX

CASTEP: Description and calculation principle

I. CASTEP: Description and calculation principle

I.1. Presentation of the CASTEP package

CASTEP (Cambridge Serial Total Energy Package) is a software based on quantum mechanics, specifically for solid-state materials science. It employs the density functional theory plane-wave pseudopotential method, with both formulations; norm conserving pseudopotential and ultra-soft (ultrasoft) pseudopotential, which allows us to perform first-principles quantum mechanics calculations that explore the properties of crystals. All calculations presented in my manuscript were carried out using this package developed in 1988 by Payne *et al.*[36, 192]. It is an ab initio calculation code and is part of a set of numerical simulation software called Material Studio (MS) marketed by Accelrys ©. CASTEP uses the DFT to solve the Schrödinger equation. Direct energy minimization procedures are used to obtain, in a self-consistent manner, the electronic wave functions and the corresponding charge density. Only the Kohn-Sham orbitals whose vector G belongs to the irreducible part of the ZB are computed because the electron density can be constructed only from these states, with a symmetrization step which uses the matrices of the group space. A symmetrization step is also necessary for forces and stress. As a result, the electron density is explicitly symmetrized. The use of symmetry makes it possible to reduce the computation time significantly, especially for small meshes containing many points- k because CASTEP is effectively parallelized as a function of the k -points. As mentioned previously, CASTEP uses the Monkhorst-Pack method for sampling the Brillouin zone [152]. This method makes it possible to generate a uniform grid along the three axes of the reciprocal space. The symmetry of the system is used to reduce the number of k -points of the primitive cell. The forces

exerted on the atoms, the tensor of the stresses and consequently the atomic displacements and the variations of the parameters of the crystal lattice are always symmetrized.

Furthermore, the vibrational properties of solids (phonon dispersion, total and projected density of phonon states, thermodynamic properties) can be calculated with CASTEP using either the linear response methodology or the finite displacements technique.

The time required for a CASTEP calculation increases with the cube of the number of atoms in the system. As an example, which I have two systems tetragonal body centred (semi borides) and orthorhombic (orthorhombic), the time of calculation take several days for geometry optimization and properties calculation.

I.2. SCF Electronic minimization technique in CASTEP

In order to determine the electronic ground state of the studied systems, two SCF (Self-consistent field) algorithms are implemented in the CASTEP code: Density Mixing (DM)[193] and EDFT [194]. Although the DM algorithm is generally faster, Is not a variational algorithm and, therefore, it may be subject to convergence instabilities. The EDFT algorithm is variational but is generally slower, especially in the presence of empty bands. The choice of one or the other algorithm is governed by the convergence difficulties of CASTEP for a given system.

In the DM algorithm, the sum of the electronic eigenvalues is minimized in the fixed potential instead of the self-consistent minimization of the total energy. The new electronic density obtained at the end of the minimization (ρ_{out}) is mixed with the initial density (ρ_{in}) and the process is repeated until the convergence is reached. In this scheme, CASTEP supports four mixing methods: linear mixing, Kerker mixing, Broyden mixing, and Pulay mixing in the

increasing order of robustness . The conjugate gradient-based approach is used to minimize the sum of eigenvalues.

The CASTEP code also supports a more traditional scheme for electronic relaxation (All bands / EDFT), involving the minimization of total energy. The electronic wave functions are projected using a flat wave set and the expansion coefficients are varied so as to minimize the total energy. This minimization is performed using an all-bands method that allows simultaneous updating of all wave functions. The scheme uses a preconditioned conjugate gradient technique[195].

The main advantage of the density-mixing method is its robustness for metallic systems, especially for metal surfaces. The traditional technique of minimizing total energy could become unstable in a metal system with the elongated cell in one dimension, which is the typical configuration for supercell calculations on surfaces. The density-mixing technique converges both for insulating and metallic cases, and offers at least a factor of three in increasing the speed for medium-sized insulation.

I.3. Geometry optimization with castep

The optimization of equilibrium geometries is often the first step in the theoretical study of a molecule or a solid. The determination of the optimized structure of such a system requires the calculation and then the minimization of the forces (these forces are obtained from the Hellmann-Feynman theorem[196, 197]), that apply to each of the atoms that constitute them. That means is based on reducing the magnitude of calculated forces and stresses until they become smaller than defined convergence tolerances. It is also possible to specify an external stress tensor to model the behavior of the system under tension, compression, shear, etc. In these cases the internal stress tensor is iterated until it becomes equal to the applied external stress..

In the CASTEP package, the optimization of the geometries is carried out in a self-consistent by an algorithm named BFGS (Broyden, Fletcher, Goldfarb and Shannon), from the configuration chosen by the user to initialize the calculation. By default, CASTEP uses the BFGS geometry optimization method. This method usually provides the fastest way of finding the lowest energy structure and this is the only scheme that supports cell optimization in CASTEP. The minimization is carried out in such a way that the overall minimum of energy is reached. Optimization of geometry is an indispensable procedure for accessing a molecular or crystalline structure and a static energy that are comparable to experimental values. Moreover, even if the structure chosen for the initialization is close to the experimental structure, an optimization of precise geometry is a prerequisite for the calculation of the vibrational properties of a system.

I.4. Band structure and state density

I.4.1. Electronic band structure

The electronic tape structure of the solids reveals the eigenvalues associated with the conduction and valence bands along specific directions in the Brillouin zone of a particular crystal structure. One of the most important reasons for calculating the electronic band structure is to determine the band gap (energy gap), ie, the difference between the higher valence band energy values and the lower conduction band because This may give an idea of the potential uses for optical device applications. However, the energy gap calculated from the Kohn-Sham eigenvalues using the LDA and GGA methods is underestimated with respect to the energy gap obtained experimentally. In fact, it is a property where the GGA does not bring improvement

beyond LDA. Generally, the difference between the gap obtained using the pure DFT and the experimental gap is of the order of 50% to 100%.

In order to determine the structure of electronic bands of such a material, a single-point energy calculation is first performed to determine the self-consistent density of the ground state. This fixes the form of the Kohn-Sham Hamiltonian, which is solved to give the corresponding Kohn-Sham eigenvalues. The eigenvalues are calculated at a greater number of k-points, along the specific directions in the Brillouin zone, than that used in the calculation of the energy.

The eigenvalues obtained by solving the Kohn-Sham equations can be used to generate energy band structure diagrams and the density of electronic states.

I.4.2. Density of electronic states

A second tool for analyzing the results consists of the Total Density of States (TDOS) or Partial Density of States (PDOS) curves. The TDOS presents, in the form of a histogram, the number of monoelectronic states as a function of the energy. PDOSs are based on the Mulliken population analysis [105] and are performed by projection of monoelectronic orbitals on a basis of atomic orbitals located around the different nuclei of the mesh. The PDOSs provide an approximate identification of the type of orbitals constituting each band, in terms of the orbitals (s, p, d, or f) of the atoms constituting the system.

The density of states (DOS) counts the number of electronic states having a given energy. For a band n , the density of states

I.5. Method of calculating elastic constants

The CASTEP Elastic Constants task allows us to run a set of CASTEP calculations which provides all of the information necessary to obtain the full 6×6 tensor of elastic constants for a

3D periodic structure with any symmetry. CASTEP automatically generates the set of distorted structures that is required by symmetry to produce the fullset of elastic constants, then submits jobs for the idealstructure and for all the distorted structures. The actual calculation of elastic constants, based on the values of initialstrains and calculated stresses. The accuracy of the elastic constants, especially of the shear constants, depends strongly on the quality of the SCF calculation and in particular, on the quality of the Brillouin zone sampling and the degree of convergence of wavefunctions. Therefore, you should use the Fine setting for SCF tolerance and for kpoint sampling and a Fine derived FFT (Fast Fourier transforms) grid. It is not necessary to perform geometry optimization before calculating elastic constants, so you can generate C_{ij} data for the experimentally observed structure. However, more consistent results are obtained if you perform full geometry optimization, including cell optimization and then calculate the elastic constants for the structure which corresponds to the theoretical ground state.

I.6. Spin polarization

Magnetic systems can be studied by carrying out spin-polarized DFT calculations with CASTEP. This setting is recommended for transition metal oxides, certain inorganic surface studies, and metallic systems containing magnetic elements (Fe, Co, Mn, Ni).

Spin-polarized CASTEP calculations are normally carried out with a variable magnetic moment. The most commonly obtained solutions correspond to high spin and low spin states. The state generated by CASTEP depends on the initial magnetic configuration, since the solution is likely to converge to the nearest local minimum rather than to the global minimum.

There are two ways of defining the initial magnetic configuration: either specify the total magnetic moment per unit cell, which gets uniformly distributed over the space, or provide

detailed information on the absolute values and direction (up or down) of the spins for each atom in the unit cell. The former method can be used for relatively simple systems where only two solutions are expected (magnetic and non-magnetic). The latter method, which specifies the spin state of the atoms in the system, is more general and gives much more flexibility. It is possible to set up ferromagnetic, ferrimagnetic, or antiferromagnetic calculations to get different starting spin arrangements.

BIBLIOGRAPHY

- [1] I. Campos-Silva, D. Bravo-Bárceñas, A. Meneses-Amador, M. Ortiz-Dominguez, H. Cimenoglu, U. Figueroa-López and J. Andraca-Adame, *Surface and Coatings Technology*, 237 (2013) 402.
- [2] G. Kartal, O. Kahvecioglu and S. Timur, *Surface and Coatings Technology*, 200 (2006) 3590.
- [3] K. Stewart, *Advanced materials and processes*, 151 (1997).
- [4] O. Allaoui, N. Bouaouadja and G. Saindernan, *Surface and Coatings Technology*, 201 (2006) 3475.
- [5] S. Jayaraman, E.J. Klein, Y. Yang, D.Y. Kim, G.S. Girolami and J.R. Abelson, *Journal of Vacuum Science and Technology-Section A*, 23 (2005) 631.
- [6] Q. Gu, G. Krauss and W. Steurer, *Advanced Materials*, 20 (2008) 3620.
- [7] A. Ivanovskii, *Progress in Materials Science*, 57 (2012) 184.
- [8] H.-Y. Chung, M.B. Weinberger, J.B. Levine, A. Kavner, J.-M. Yang, S.H. Tolbert and R.B. Kaner, *Science*, 316 (2007) 436.
- [9] I. Campos, M. Palomar, A. Amador, R. Ganem and J. Martinez, *Surface and Coatings Technology*, 201 (2006) 2438.
- [10] M. Eroglu, *Surface and Coatings Technology*, 203 (2009) 2229.
- [11] N. Ueda, T. Mizukoshi, K. Demizu, T. Sone, A. Ikenaga and M. Kawamoto, *Surface and Coatings Technology*, 126 (2000) 25.
- [12] O. Torun and I. Çelikyürek, *Materials & Design*, 30 (2009) 1830.
- [13] I. Campos-Silva, D. Bravo-Bárceñas, M. Flores-Jiménez, I. Arzate-Vazquez, C. López-García and S. Bernabé-Molina, *Metallography, Microstructure, and Analysis*, 4 (2015) 158.
- [14] A. Friedrich, B. Winkler, E.A. Juarez-Arellano and L. Bayarjargal, *Materials*, 4 (2011) 1648.
- [15] P.H. Lee, Z.R. Xiao, K.L. Chen, Y. Chen, S.W. Kao and T.S. Chin, *Physica B: Condensed Matter*, 404 (2009) 1989.
- [16] P. Mohn and D.G. Pettifor, *Journal of Physics C: Solid State Physics*, 21 (1988) 2829.
- [17] S.T. Oyama, *The Chemistry of Transition Metal Carbides and Nitrides*, Springer, 1996.
- [18] O. Ozdemir, M. Usta, C. Bindal and A.H. Ucisik, *Vacuum*, 80 (2006) 1391.
- [19] L.E. Toth, *Transition Metal Carbides and Nitrides*, Academic Press, New York, 1971.
- [20] J. Yang, J.H. Wang, H.G. Fu and D.Z. Ren, *Foundry Technol.*, 27 (2006) 1079.
- [21] C.B. Li, M.K. Li, F.Q. Liu and X.J. Fan, *Modern Physics Letters B*, 18 (2004) 281.
- [22] V. Pillai, P. Kumar, M. Hou, P. Ayyub and D. Shah, *Advances in Colloid and Interface Science*, 55 (1995) 241.
- [23] C. Petit and M.P. Pileni, *Journal of Magnetism and Magnetic Materials*, 166 (1997) 82.
- [24] A. Corrias, G. Ennas, G. Marongiu, A. Musinu, G. Paschina and D. Zedda, *Materials Science and Engineering: A*, 204 (1995) 211.
- [25] X. Feng, Y.-J. Bai, B. Lü, Y.-R. Zhao, J. Yang and J.-R. Chi, *Inorganic Chemistry Communications*, 7 (2004) 189.
- [26] S. Ziyuan, W. Deqing and D. Zhimin, *Applied Surface Science*, 253 (2006) 1051.
- [27] H. Zhu, C. Ni, F. Zhang, Y. Du and J.Q. Xiao, *Journal of Applied Physics*, 97 (2005).
- [28] C. Cadeville, PhD thesis, Strasbourg, 1965.

BIBLIOGRAPHY

- [29] H. Rosner, D. Koudela, U. Schwarz, A. Handstein, M. Hanfland, I. Opahle, K. Koepernik, M. Kuz'min, K.-H. Müller and J. Mydosh, *Nature Physics*, 2 (2006) 469.
- [30] K. Sandeman, G. Lonzarich and A. Schofield, *Physical review letters*, 90 (2003) 167005.
- [31] W. Zhang, (2007).
- [32] E. Lifshin, *X-ray Characterization of Materials*, Wiley, 2008.
- [33] B.H. Stuart, *Infrared Spectroscopy: Fundamentals and Applications*, Wiley, 2004.
- [34] E. Berkovich, *Ind. Diamond Rev*, 11 (1951) 129.
- [35] P. Hohenberg and W. Kohn, *Physical Review*, 136 (1964) B864.
- [36] M. Segall, P.J. Lindan, M.a. Probert, C. Pickard, P. Hasnip, S. Clark and M. Payne, *Journal of Physics: Condensed Matter*, 14 (2002) 2717.
- [37] R.S. Ningthoujam and N.S. Gajbhiye, *Progress in Materials Science*, 70 (2015) 50.
- [38] D.E. Garrett, *Borates: handbook of deposits, processing, properties, and use*, Academic Press, 1998.
- [39] D. Larbalestier, L. Cooley, M. Rikel, A. Polyanskii, J. Jiang, S. Patnaik, X. Cai, D. Feldmann, A. Gurevich and A. Squitieri, *Nature*, 410 (2001) 186.
- [40] M. Cadeville and E. Daniel, *Journal de Physique*, 27 (1966) 449.
- [41] R. Perkins and P. Brown, *Journal of Physics F: Metal Physics*, 4 (1974) 906.
- [42] S.B. Hendricks and P.R. Kosting, *Z.Kristallogr. Kristallgeom. Kristallphys. Kristallchem.*, 74 (1930) 511.
- [43] J.P. Perdew, K. Burke and M. Ernzerhof, *Physical Review Letters*, 77 (1996) 3865.
- [44] P.K. Liao and K.E. Spear, *Bulletin of Alloy Phase Diagrams*, 7 (1986) 543.
- [45] A.K. Sinha, *Boronizing, Heat treatment- ASM International Handbook*, 1991.
- [46] H. Kunst, B. Haase, J.C. Malloy, K. Wittel, M.C. Nestler, A.R. Nicoll, U. Erning and G. Rauscher, *Ullmann's Encyclopedia of Industrial Chemistry*, (1991).
- [47] J.R. Davis, *Surface Hardening of Steels: Understanding the Basics*, A S M International, 2002.
- [48] M. Elias-Espinosa, J. Zuno-Silva, M. Ortiz-Domínguez, J. Hernández-Ávila and O. Damián-Mejía, *Nova Scientia*, 7 (2015) 74.
- [49] R. Petrova and Z.T. Zahariev, *Bulg Chem Comm*, 26 (1985) 82.
- [50] W. Gissler and H.A. Jehn, *Advanced Techniques for Surface Engineering*, Springer, 1992.
- [51] R. Vangaveti, *Boron induced surface modification of transition metals*, Committee for the Interdisciplinary Program in Materials Science and Engineering, New Jersey Institute of Technology 2006.
- [52] R.S. Petrova and N. Suwattananont, *Journal of electronic materials*, 34 (2005) 575.
- [53] I. Uslu, H. Comert, M. Ipek, O. Ozdemir and C. Bindal, *Materials & Design*, 28 (2007) 55.
- [54] S. Sen, U. Sen and C. Bindal, *Vacuum*, 77 (2005) 195.
- [55] M. Keddad and S.M. Chentouf, *Applied Surface Science*, 252 (2005) 393.
- [56] N. Ucar, O.B. Aytar and A. Calik, *Materiali in Tehnologije*, 46 (2012) 621.
- [57] C. Li, B. Shen, G. Li and C. Yang, *Surface and Coatings Technology*, 202 (2008) 5882.
- [58] A.G.v. Matuschka, *Boronizing*, Carl Hanser Verlag, Munich, FRG, 1980.
- [59] A. Pertek, *Materials Science Forum*, 323 (1994) 163.
- [60] C. Meriç, S. Sahin and S.S. Yilmaz, *Materials Research Bulletin*, 35 (2000) 2165.
- [61] D. Mu, C. Yang, B.I. Shen and H. Jiang, *Journal of Alloys and Compounds*, 479 (2009) 629.

- [62] D.C. Young, Computational Chemistry, John Wiley & Sons, Inc., 2002.
- [63] R.G. Parr and R.G.P.W. Yang, Density-Functional Theory of Atoms and Molecules, Oxford University Press, USA, 1989.
- [64] R.M. Dreizler and E.K.U. Gross, Density Functional Theory, Springer-Verlag Berlin Heidelberg, 1990.
- [65] W. Kohn and L.J. Sham, Physical Review, 140 (1965) A1133.
- [66] U. Von Barth and L. Hedin, Journal of Physics C: Solid State Physics, 5 (1972) 1629.
- [67] D. Wu, First-principles Study on Hard/soft Samarium-cobalt/cobalt-iron Nanocomposite Magnetic Materials, University of Texas at Arlington 2008.
- [68] W.D. Callister, Materials Science and Engineering: An Introduction, Wiley, 2002.
- [69] N.A. Spaldin, Magnetic Materials: Fundamentals and Applications, Cambridge University Press, 2010.
- [70] L. Rednic, electronic structure and magnetic properties of metallic systems based on rare earths and *d* transition elements PhD thesis, Babeş-Bolyai University, 2010.
- [71] T. Moriya, Spin Fluctuations in Itinerant Electron Magnetism, Springer Berlin Heidelberg, 2012.
- [72] P. Langevin, J. Phys. Theor. Appl., 4 (1905) 678.
- [73] P. Weiss, J. Phys. Radium, 6 (1907).
- [74] W. Heisenberg, Z. Phys., 49 (1928) 619.
- [75] P.A.M. Dirac, Quantum Mechanics of Many-Electron Systems, 1929.
- [76] J.H. Van Vleck, The Theory of Electric and Magnetic Susceptibilities, BiblioBazaar, 2011.
- [77] M.A. Ruderman and C. Kittel, Physical Review, 96 (1954) 99.
- [78] T. Kasuya, Progress of Theoretical Physics, 16 (1956) 58.
- [79] K. Yosida, Physical Review, 106 (1957) 893.
- [80] H.A. Kramers, Physica, 1 (1934) 825.
- [81] F. Bloch, Z. Phys., 57 (1929).
- [82] E. Wigner, Physical Review, 46 (1934) 1002.
- [83] E.C. Stoner, Collective Electron Ferromagnetism, 1938.
- [84] v. der, First-principles study of the exchange interactions and Curie temperature in Heusler alloys, PhD thesis, Mathematisch-Naturwissenschaftlich-Technischen Fakultät, der Martin-Luther-Universität, 2006.
- [85] E.C. Stoner, Proceedings of the Royal Society of London. Series A, Mathematical and Physical Sciences, (1939) 339.
- [86] P. Marcus and V. Moruzzi, Physical Review B, 38 (1988) 6949.
- [87] G. Stollhoff, A.M. Oleś and V. Heine, Physical Review B, 41 (1990) 7028.
- [88] J. Janak, Physical Review B, 16 (1977) 255.
- [89] J.C. Slater, Journal of Applied Physics, 8 (1937) 385.
- [90] Y. Tyan and L. Toth, Journal of Electronic Materials, 3 (1974) 1.
- [91] L. Pauling, Physical Review, 54 (1938) 899.
- [92] C. Pfleiderer, Journal of Physics: Condensed Matter, 17 (2005) S987.
- [93] J.A. Hertz, Physical Review B, 14 (1976) 1165.
- [94] P. Sachdev, Treatment of drug-induced akathisia, Akathisia and Restless Legs. New York: Cambridge University Press, 1995.
- [95] S. Sondhi, S. Girvin, J. Carini and D. Shahar, Reviews of Modern Physics, 69 (1997) 315.
- [96] S.-C. Zhang, Science, 275 (1997) 1089.

- [97] Y. Imry and S.-k. Ma, *Physical Review Letters*, 35 (1975) 1399.
- [98] N. Goldenfeld, (1992).
- [99] L.D. Landau, E.M. Lifshitz, J.B. Sykes, J.S. Bell and E. Dill, *Electrodynamics of continuous media*, AIP, 1961.
- [100] C. Pfleiderer, C. Thessieu, A. Stepanov, G. Lapertot, M. Couach and J. Flouquet, *Physica B: Condensed Matter*, 230 (1997) 576.
- [101] S. Sachdev, *Quantum phase transitions*, Wiley Online Library, 2007.
- [102] B. Winkler, *Zeitschrift für Kristallographie*, 214 (1999) 506.
- [103] F. Birch, *Journal of Geophysical Research: Solid Earth*, 83 (1978) 1257.
- [104] R.E. Cohen, O. Gülseren and R.J. Hemley, *American Mineralogist*, 85 (2000) 338.
- [105] R.S. Mulliken, *The Journal of Chemical Physics*, 23 (1955) 1833.
- [106] D. Sanchez-Portal, E. Artacho and J.M. Soler, *Solid State Communications*, 95 (1995) 685.
- [107] B.G. Pfrommer, M. Côté, S.G. Louie and M.L. Cohen, *Journal of Computational Physics*, 131 (1997) 233.
- [108] A. Šimůnek and J. Vackář, *Physical review letters*, 96 (2006) 085501.
- [109] S.-H. Jhi, S.G. Louie, M.L. Cohen and J. Ihm, *Physical Review Letters*, 86 (2001) 3348.
- [110] J. He, E. Wu, H. Wang, R. Liu and Y. Tian, *Physical review letters*, 94 (2005) 015504.
- [111] W.C. Oliver and G.M. Pharr, *Journal of materials research*, 19 (2004) 3.
- [112] G. Pharr and A. Bolshakov, *Journal of Materials Research*, 17 (2002) 2660.
- [113] T. Britton, H. Liang, F. Dunne and A. Wilkinson, *Proceedings of the Royal Society of London A: Mathematical, Physical and Engineering Sciences* 2010.
- [114] A. Zarkades and F.R. Larson, *ELASTICITY OF TITANIUM SHEET ALLOYS*, Army Materials and Mechanics Research Center, Watertown, Mass., 1970.
- [115] V.V. Brazhkin, A.G. Lyapin and R.J. Hemley, *Philosophical Magazine A*, 82 (2002) 231.
- [116] J.B. Levine, S.H. Tolbert and R.B. Kaner, *Advanced Functional Materials*, 19 (2009) 3519.
- [117] J. Rau, A. Latini, A. Generosi, V.R. Albertini, D. Ferro, R. Teghil and S. Barinov, *Acta Materialia*, 57 (2009) 673.
- [118] N. Lecture, Dept. of Material Science and Engineering KAIST, Korea.
- [119] X. Zhang, X. Luo, J. Han, J. Li and W. Han, *Computational materials science*, 44 (2008) 411.
- [120] F. Gao, J. He, E. Wu, S. Liu, D. Yu, D. Li, S. Zhang and Y. Tian, *Physical review letters*, 91 (2003) 015502.
- [121] J.F. Nye, *Physical properties of crystals: their representation by tensors and matrices*, Oxford university press, 1985.
- [122] A.C. Ugural and S.K. Fenster, *Advanced strength and applied elasticity*, Pearson Education, 2003.
- [123] M. Levy, *Experimental Methods in the Physical Sciences*, 39 (2001) 1.
- [124] X. Gao, Y. Jiang, R. Zhou and J. Feng, *Journal of Alloys and Compounds*, 587 (2014) 819.
- [125] O. Beckstein, J. Klepeis, G. Hart and O. Pankratov, *Physical Review B*, 63 (2001) 134112.
- [126] S. Patil, S. Khare, B. Tuttle, J. Bording and S. Kodambaka, *Physical Review B*, 73 (2006) 104118.

BIBLIOGRAPHY

- [127] Z. Zhou and B. Joos, *Physical Review B*, 54 (1996) 3841.
- [128] A. Gueddouh, B. Bentría and I. Lefkaier, *Journal of Magnetism and Magnetic Materials*, 406 (2016) 192.
- [129] J. Lewandowski*, W. Wang and A. Greer, *Philosophical Magazine Letters*, 85 (2005) 77.
- [130] Y. Liu, W.-C. Hu, D.-J. Li, K. Li, H.-L. Jin, Y.-X. Xu, C.-S. Xu and X.-Q. Zeng, *Computational Materials Science*, 97 (2015) 75.
- [131] K. Ali, A. Arya, P. Ghosh and G. Dey, *Computational Materials Science*, 112 (2016) 52.
- [132] H. Ozisik, K. Colakoglu and E. Deligoz, *Computational Materials Science*, 51 (2012) 83.
- [133] Y. Duan, Y. Sun, M. Peng and S. Zhou, *Journal of Alloys and Compounds*, 595 (2014) 14.
- [134] K. Brugger, *Journal of Applied Physics*, 36 (1965) 768.
- [135] L. Sun, Y. Gao, B. Xiao, Y. Li and G. Wang, *Journal of Alloys and Compounds*, 579 (2013) 457.
- [136] D. Music, A. Houben, R. Dronskowski and J.M. Schneider, *Physical Review B*, 75 (2007) 174102.
- [137] L. Bellaiche and D. Vanderbilt, *Physical Review B*, 61 (2000) 7877.
- [138] K.A. Murphy and N. Hershkovitz, *Physical Review B*, 7 (1973) 23.
- [139] C. Zhou, J. Xing, B. Xiao, J. Feng, X. Xie and Y. Chen, *Computational Materials Science*, 44 (2009) 1056.
- [140] T. Kanomata, Y. Ise, N. Kumagai, A. Haga, K. Kamishima, T. Goto, H. Kimura, H. Yoshida, T. Kaneko and A. Inoue, *Journal of alloys and compounds*, 259 (1997) L1.
- [141] A. Meneses-Amador, I. Campos-Silva, J. Martínez-Trinidad, S. Panier, U. Figueroa-López and A. Torres-Hernández, *Surface and Coatings Technology*, 215 (2013) 285.
- [142] I. Campos-Silva, J. Martínez-Trinidad, M. Doñu-Ruiz, G. Rodríguez-Castro, E. Hernandez-Sanchez and O. Bravo-Bárceñas, *Surface and Coatings Technology*, 206 (2011) 1809.
- [143] P. Dearnley and T. Bell, *Surface Engineering*, 1 (1985) 203.
- [144] A. Minkevich, *Metal Science and Heat Treatment*, 3 (1961) 347.
- [145] R.S. Petrova, N. Suwattananont and V. Samardzic, *Journal of Materials Engineering and Performance*, 17 (2008) 340.
- [146] D. Lou, J. Solberg, O. Akselsen and N. Dahl, *Materials Chemistry and Physics*, 115 (2009) 239.
- [147] C. Domínguez-Ríos, A. Hurtado-Macias, R. Torres-Sánchez, M.A. Ramos and J.s. González-Hernández, *Industrial & Engineering Chemistry Research*, 51 (2012) 7762.
- [148] B. Xiao, J. Feng, C. Zhou, J. Xing, X. Xie, Y. Cheng and R. Zhou, *Physica B: Condensed Matter*, 405 (2010) 1274.
- [149] S. Medeiros, E. Albuquerque, F. Maia, E. Caetano and V. Freire, *Chemical physics letters*, 435 (2007) 59.
- [150] Y. Xu and H. Wang, *Journal of Alloys and Compounds*, 457 (2008) 239.
- [151] Y. Wang, K. Burke and J. PERDEW, *Phys. Rev. B*, 54 (1996) 16533.
- [152] H.J. Monkhorst and J.D. Pack, *Physical Review B*, 13 (1976) 5188.
- [153] C. Kittel, *Introduction to solid state physics*, Wiley, 2005.
- [154] I. Shein, N. Medvedeva and A. Ivanovskii, *Physica B: Condensed Matter*, 371 (2006) 126.
- [155] E. Havinga, H. Damsma and P. Hokkelling, *Journal of the Less Common Metals*, 27 (1972) 169.
- [156] Y. Liang, Y. Che, X. Liu and N. Li, *Thermodynamical data for inorganic compounds*, NorthEastern University Press, 1993.

- [157] A. Edström, M. Werwiński, D. Iuşan, J. Ruzs, O. Eriksson, K. Skokov, I. Radulov, S. Ener, M. Kuz'min and J. Hong, *Physical Review B*, 92 (2015) 174413.
- [158] S. Chikazumi and C.D. Graham, *Physics of Ferromagnetism 2e*, Oxford University Press on Demand, 2009.
- [159] T. Egami, B. Fine, D. Singh, D. Parshall, C. de La Cruz and P. Dai, *Physica C: Superconductivity*, 470 (2010) S294.
- [160] K. Shimizu, T. Kimura, S. Furomoto, K. Takeda, K. Kontani, Y. Onuki and K. Amaya, *Nature*, 412 (2001) 316.
- [161] A. Bialon, T. Hammerschmidt, R. Drautz, S. Shah, E. Margine and A. Kolmogorov, arXiv preprint arXiv:1104.2136, (2011).
- [162] L.-H. Li, W.-L. Wang, L. Hu and B.-B. Wei, *Intermetallics*, 46 (2014) 211.
- [163] H. Zhu, C. Ni, F. Zhang, Y. Du and J.Q. Xiao, *Journal of applied physics*, 97 (2005) 10M512.
- [164] C. Petit and M. Pileni, *Journal of Magnetism and Magnetic Materials*, 166 (1997) 82.
- [165] G. Rodríguez-Castro, I. Campos-Silva, E. Chávez-Gutiérrez, J. Martínez-Trinidad, E. Hernandez-Sanchez and A. Torres-Hernández, *Surface and Coatings Technology*, 215 (2013) 291.
- [166] Y. Bourourou, L. Beldi, B. Bentria, A. Gueddouh and B. Bouhafis, *Journal of Magnetism and Magnetic Materials*, 365 (2014) 23.
- [167] W. Kohn, *Reviews of Modern Physics*, 71 (1999) 1253.
- [168] H. Niu, X.-Q. Chen, W. Ren, Q. Zhu, A.R. Oganov, D. Li and Y. Li, *Physical Chemistry Chemical Physics*, 16 (2014) 15866.
- [169] W.B. Pearson, P. Villars and L.D. Calvert, *Pearson's handbook of crystallographic data for intermetallic phases*, American Society for Metals, 1985.
- [170] G.A. Rodríguez-Castro, C. Reséndiz-Calderón, L. Jiménez-Tinoco, A. Meneses-Amador, E.A. Gallardo-Hernandez and I.E. Campos-Silva, *Surface and Coatings Technology*, 284 (2015) 258.
- [171] Y. Ding, M. Chen and W. Wu, *Physica B: Condensed Matter*, 428 (2013) 97.
- [172] B. Hanson, M. Mahnig and L.E. Toth, *Zeitschrift für Naturforschung A*, 26 (1971) 739.
- [173] P. Mohn and D. Pettifor, *Journal of Physics C: Solid State Physics*, 21 (1988) 2829.
- [174] A. Malozemoff, A. Williams and V. Moruzzi, *Physical Review B*, 29 (1984) 1620.
- [175] W. Ching, Y.-N. Xu, B. Harmon, J. Ye and T. Leung, *Physical Review B*, 42 (1990) 4460.
- [176] C. Hausleitner and J. Hafner, *Physical Review B*, 47 (1993) 5689.
- [177] W. Zhong, G. Overney and D. Toma, *Physical Review B*, 47 (1993) 95.
- [178] S. Kervan, *Journal of superconductivity and novel magnetism*, 24 (2011) 815.
- [179] J. Hafner, M. Tegze and C. Becker, *Physical Review B*, 49 (1994) 285.
- [180] J. Taylor, J. Duffy, A. Bebb, M. Cooper, S. Dugdale, J. McCarthy, D. Timms, D. Greig and Y. Xu, *Physical Review B*, 63 (2001) 220404.
- [181] C. Jing, S. Cao and J. Zhang, *Physical Review B*, 68 (2003) 224407.
- [182] R. Wisniewski, A. Rostocki, A. Magiera and W. Zych, *Journal of magnetism and magnetic materials*, 81 (1989) 121.
- [183] T. Soumura, K. Takeda, T. Wakano, K. Terasawa and T. Maeda, *Journal of magnetism and magnetic materials*, 58 (1986) 202.
- [184] A. Bratkovsky, S. Rashkeev and G. Wendin, *Physical Review B*, 48 (1993) 6260.
- [185] L. Nordheim, *Annalen der Physik*, 401 (1931) 607.

BIBLIOGRAPHY

- [186] M. Turchanin and P. Agraval, Powder Metallurgy and Metal Ceramics, 47 (2008) 26.
- [187] C.G. Broyden, IMA Journal of Applied Mathematics, 6 (1970) 76.
- [188] R. Fletcher, The computer journal, 13 (1970) 317.
- [189] D. Goldfarb, Mathematics of computation, 24 (1970) 23.
- [190] D.F. Shanno, Mathematics of computation, 24 (1970) 647.
- [191] T. Bjurström, Röntgenanalyse der Systeme Eisen-Bor, Kobalt-Bor und Nickel-Bor, Almqvist & Wiksell, 1933.
- [192] S.J. Clark, M.D. Segall, C.J. Pickard, P.J. Hasnip, M.I. Probert, K. Refson and M.C. Payne, Zeitschrift für Kristallographie-Crystalline Materials, 220 (2005) 567.
- [193] G. Kresse and J. Furthmüller, Physical Review B, 54 (1996) 11169.
- [194] N. Marzari, D. Vanderbilt and M.C. Payne, Physical review letters, 79 (1997) 1337.
- [195] M.C. Payne, M.P. Teter, D.C. Allan, T. Arias and J. Joannopoulos, Reviews of Modern Physics, 64 (1992) 1045.
- [196] H. Hellmann, Einführung in die quantenchemie: Texte imprimé, F. Deuticke, 1937.
- [197] R.P. Feynman, Physical Review, 56 (1939) 340.

Scientific Publications



ELSEVIER

Contents lists available at ScienceDirect

Journal of Magnetism and Magnetic Materials

journal homepage: www.elsevier.com/locate/jmmmFirst-principle investigations of structure, elastic and bond hardness of Fe_xB ($x=1, 2, 3$) under pressureAhmed Gueddouh^{a,b,*}, Bachir Bentria^a, I.K. Lefkaier^a^a Laboratoire de Physique des Matériaux, Université Amar Telidji de Laghouat, BP37G, Laghouat 03000, Algeria^b Département de Physique, Faculté des Sciences, Université A.B. Belkaid Tlemcen, BP 119, Tlemcen 13000, Algeria

ARTICLE INFO

Article history:

Received 20 August 2015

Received in revised form

30 October 2015

Accepted 4 January 2016

Available online 6 January 2016

Keywords:

DFT

Magnetic moment

Mulliken population

Elastic constants

Hardness

Pressure effect

ABSTRACT

First-principles calculations are performed to study pressure effects on structure, magnetic and mechanical properties of Fe_xB ($x=1, 2, 3$) compounds using density functional theory (DFT) within GGA approximation. The three structures are studied in the pressure range from 0 to 90 GPa, in order to predict the critical transition pressure from magnetic to nonmagnetic states (NM) and a possibility of superconductivity in this state was predicted. The density of states of Fe_xB ferromagnetic compounds are significantly modified with increasing pressure and at particular critical pressures, our compounds undergo an abrupt loss of ferromagnetic character that cause mirror in upper and lowers half panels on both spin channels. Furthermore, the relationship between crystal structure and material hardness of Fe_xB is also investigated by calculating hardness of Fe–B and B–B bonds using Mulliken population analysis and semi empirical hardness theory. This model proved effective in hardness prediction of metal borides and agrees well with the experimental values. By the elastic stability criteria, it is predicted that Fe_xB are stable up to the selected pressures.

© 2016 Elsevier B.V. All rights reserved.

1. Introduction

Physical properties of metal borides such as hardness, high melting point, wear resistance, corrosion resistance, and ferromagnetism are important for both basic research and technological applications [1–3]. Their notable mechanical properties are due to the B–B covalent bonding associated with hybrid metal–nonmetal bonding. Iron borides are metallic in nature and exhibit ferromagnetism. The thickness of iron boride layers in the thermo-chemical surface hardening process of steel depend on the chemical composition of the boronizing environment, temperature and duration of treatment. The obtained boride layer is either single-phase (Fe_2B only) or double-phase (FeB and Fe_2B) [4]. A metastable phase, Fe_3B , appears in the formation of Fe_2B [5]. Kneller et al. have drawn the phase diagram B–Fe system [6]. Physical properties such as structure parameters, hardness, Young modulus and fracture toughness of iron boride layer that depend on process time and temperature have been well investigated experimentally [7,8]. On the other hand, Fe_2B can also be prepared as bulk single crystals [9]. FeB was prepared in the form of nanoparticles by the chemical reduction method for the improvement of the cycle stability of the

PuNi3- type hydrogen storage electrode [10–12].

Recently, Meneses-Amador et al. used indentation for the mechanical characterization of Fe_2B layers and found that layer hardness ranged from 9 to 14.2 GPa depending on boriding temperature and time [7]. Furthermore, the mechanical properties of FeB and Fe_2B layers were estimated by Berkovich nano indentation on boride steels. Their measurements showed that hardness ranged between 14.5 GPa and 19 GPa for FeB and from 13 to 16.3 GPa for Fe_2B depending on temperature and boronizing time [8].

In this paper we calculate the density of states of Fe_xB ferromagnetic compounds to evaluate the magnetic moment and also used, *ab-initio* based Mulliken population analysis method [13] to calculate the hardness of our three compounds Fe_xB . In order to predict the transition pressure between ferromagnetic and nonmagnetic states, we have increased pressure on these compounds until the extinction of the magnetic moment and appear a higher DOS at the Fermi level, which usually improves superconducting properties. Also we calculate the relative change in volume, elastic modulus, hardness and other parameters between the ferromagnetic and nonmagnetic state.

Finally, we notice that pressure affects the structure, mechanical and magnetic properties of iron borides, there spin-polarized calculations are important to obtain the correct ground state properties of Fe_xB compounds. We demonstrate that the structure properties and magnetic moment change strongly with increasing pressure. At the end of results presentation, we show the pressure

* Corresponding author at: Laboratoire de Physique des Matériaux, Université Amar Telidji de Laghouat, BP37G, Laghouat 03000, Algeria.

E-mail addresses: a.gueddouh@mail.lagh-univ.dz, gueddouh_a@yahoo.fr (A. Gueddouh).

effect on the magnetic moment and all calculated parameters (see Fig. 3) by the relative change of these parameters between the ferromagnetic and nonmagnetic state.

We dedicate the last section to the most important conclusions of this work.

2. Structure aspects and calculation methods

FeB and Fe₃B belong to the orthorhombic space group *Pnma* [14–17]. Both structures contain four formula per cell, Fig. 1. In Fe₃B, an isotype of Fe₃C, iron atoms are distributed over two distinct lattice sites: the general Fe (I) sites (Wyckoff position 8d) and the special Fe(II) sites (Wyckoff position 4c). On the other hand, Fe₂B belongs to the body-centered tetragonal Bravais lattice with *I4/mcm* space group where contains four equivalent Fe atoms in the positions of point group *mm* and two equivalent B atoms in the positions of point group 42 [14]. The B atoms in Fe₂B are located between two layers of Fe atoms in a distorted closely packed arrangement, as shown in Fig. 1. It is known that the ground states of Fe_xB compounds are ferromagnetic [18,19].

The total energy calculations were performed within density functional theory (DFT) [20–23]. CASTEP code was employed for the whole study uses the plane wave expansion method in reciprocal space [24,25]. The ultrasoft Vanderbilt pseudopotentials were employed to represent the electrostatic interactions between valence electrons and ionic cores [26] which were used with the following valence electron configurations Fe: 3d⁶4s² and B: 2s²2p¹. Generalized gradient approximation PBE-GGA was used for exchange–correlation energy calculations [27]. Kinetic energy cut-off value was set to 500 eV, which was sufficient to obtain the reliable results.

Total energies were evaluated with the following Monkhorst–Pack grids [28]: (6 × 10 × 8) for FeB, (10 × 10 × 10) for Fe₂B and (10 × 12 × 8) for Fe₃B. The convergence criteria of total energy and structure optimization were set to fine quality with the energy tolerance of 10^{−6} eV/atom. BFGS (Broyden–Fletcher–Goldfarbe–Shanno) optimization method was used to obtain the equilibrium crystal structures of Fe_xB with maximum atom displacement and force set to 0.002 Å and 0.001 eV/Å respectively. The crystal structures of Fe_xB studied in this paper were built based on experimental results.

In package code spin polarized indicates that the calculation will be performed using different wave functions for different spins. This is known as a ‘spin-polarized’ calculation. Use formal spin as initial: indicates that the initial value for the number of unpaired electrons for each atom will be taken from the formal spin specified for each atom. This starting value will be subsequently optimized during the calculation.

The stability of our compounds can be evaluated by calculating two energy parameters, cohesive energy E_{coh} and formation energy E_f defined as follows:

$$E_{coh}(Fe_xB) = \frac{E_{total}(Fe_xB, Cell) - x n E_{iso}(Fe) - n E_{iso}(B)}{n} \quad (1)$$

$$E_f(Fe_xB) = E_{coh}(Fe_xB) - x E_{coh}(Fe) - E_{coh}(B) \quad (2)$$

where $E_{coh}(Fe_xB)$ is the cohesive energy of Fe_xB per formula; $E_f(Fe_xB)$ is its formation energy; $E_{coh}(Fe)$ is the cohesive energy of bcc-iron per atom; $E_{total}(Fe_xB, Cell)$ is the total calculated energy of Fe_xB per conventional unit cell; $E_{iso}(Fe)$ is the total energy of an isolated Fe atom and finally n refers to the number of formula Fe_xB in the conventional cell. The calculation method for $E_{coh}(Fe_xB)$ can also be used to evaluate the cohesive energy of pure elemental B and Fe. Eqs. (1) and (2) require negative values of $E_{coh}(Fe_xB)$ and $E_f(Fe_xB)$ in order to refer to a thermodynamically stable structure.

3. Results and discussion

3.1. Structure properties and stability

The calculated lattice parameters, unit cell volumes, bulk modulus, cohesive energy and the formation energy for Fe_xB along with the available experimental and previous theoretical data for comparison, are shown in Tables 1 and 2. These results show that the calculated structure parameters are in good agreement with the experimental values. The calculated values of cohesive energy of FeB, Fe₂B and Fe₃B are respectively −13.13, −18.91 and −24.36 eV per atom indicate that all of these Fe_xB compounds are stable. Furthermore, the cohesive energies decreases from FeB to Fe₃B, this is mainly caused by the increase in the volume concentration of Fe atoms.

3.2. Pressure effects

Usually, in order to induce some significant change in the structures, high pressures are needed for the study of materials. By increasing the pressure, there is a transfer from state magnetic to nonmagnetic state which causes an extinction of the magnetic moment; the theoretical critical (transition) pressure is estimated to be 77 GPa, 85 GPa and 55 GPa for FeB, Fe₂B and Fe₃B respectively, as shown Fig. 2. The critical pressure at which a ferromagnetic material undergoes transition to a NM state is defined as $P_c = -\Delta E/\Delta V$ where ΔE is the difference between NM and spin-polarized (SP) equilibrium total energy by unit cell and ΔV is the corresponding difference between NM and SP equilibrium

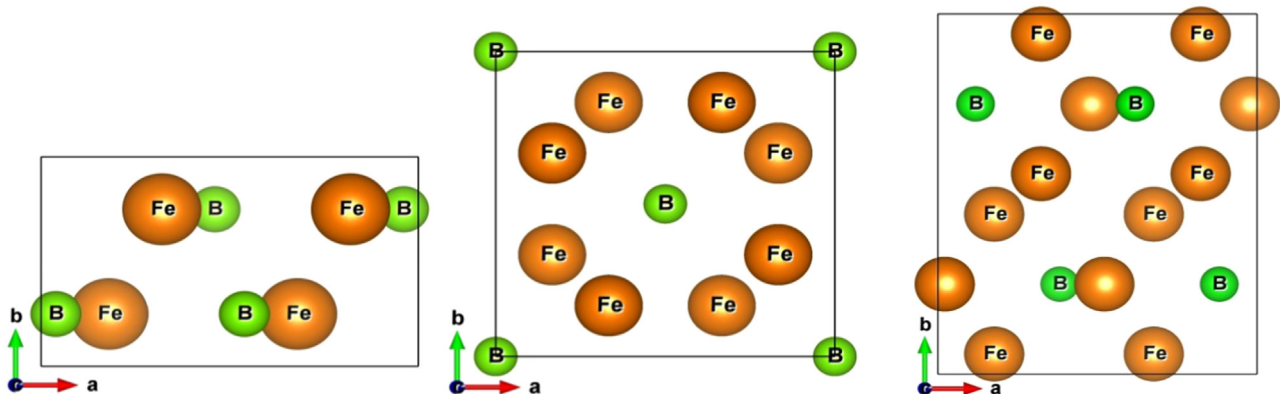


Fig. 1. Fe_xB Structures: by the left FeB, Fe₂B and Fe₃B respectively.

Table 1

The calculated ground state properties of pure elements, Fe and B. Experimental and theoretical values are listed in parentheses. Total energy of isolated atom E_{iso} (eV/atom), total cell energy E_{total} (eV/f.u.), cohesive energy E_{coh} (eV/f.u.) and volume V (\AA^3).

Ground state properties	Fe	B
E_{iso}	−859.821 (−855.913) ^a	−70.501 (−70.492) ^a
E_{total}	−865.315 (865.335) ^a	−76.953 (−76.875) ^a
E_{coh}	−5.494 (−4.28) ^{exp} (−9.422)	−6.452 (−6.383) ^a 8.652
V	11.775 (11.82) ^{exp}	(8.763) ^a

^a Ref. [63].

^{exp} Ref. [37].

Table 2

The calculated ground state properties of Fe_xB . Experimental and theoretical values are listed in parentheses. Total cell energy E_{total} (eV/f.u.), cell parameters (a, b, c in \AA), atomic positions for Fe and B atoms (fractional coordinates), volume V (\AA^3), Bulk modulus (GPa), magnetic moment (μ_B /atom), cohesive energy E_{coh} (eV/f.u.), formation energy E_f (eV/f.u.).

Parameters	FeB	Fe ₂ B	Fe ₃ B
E_{total}	−3773.900	−3618.115	−10697.2989
(a, b, c)	5.317, 2.950, 3.964 (5.495, 2.946, 4.053) ^a	5.0123, 4.209 (5.110, 4.240) ^{exp}	5.336, 6.608, 4.354 (5.397, 6.648, 4.368) ^a
Fe (x, y, z)	0.178 0.25 0.122	0.1666, 0.666, 0	0.1765 0.0560 0.3515 0.0216 0.250 0.8776 (0.1751, 0.0556, 0.3508) ^a (0.0182, 0.25, 0.8832) ^a
B(x, y, z)	0.0348 0.25 0.620	0, 0, 0.25	0.8818, 0.25, 0.4258 (0.8812, 0.25, 0.4268) ^a
V	62.176	52.872	153.52 (156.70) ^a
B	305.58 (286.6) ^b	244.59 (249.7) ^c	210 (201.6) ^b
μ_B /atom	1,126 (1.12) ^{exp1} , (1.20) ^a , (0.95) ^{exp2}	1.83 (1.96) ^a , (1.62) ^{exp2}	2.003 (2.17) ^a , (2.08) ^b
E_{coh}	−13.153	−18.92 (−26.701) ^a	−24.36
E_f	−1.207	−1.475 (−1.475) ^a , (−0.85) ^d	−1.427

^a Ref. [63].

^b Ref. [61].

^c Ref. [58].

^d Ref. [56].

^{exp1} Ref. [36].

^{exp2} Ref. [16].

^{exp} Ref. [55].

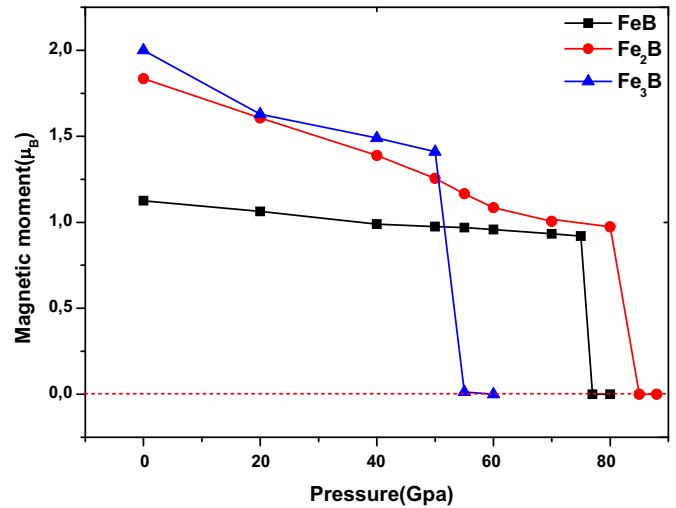


Fig. 2. Dependence of magnetic moment vs pressure for Fe_xB .

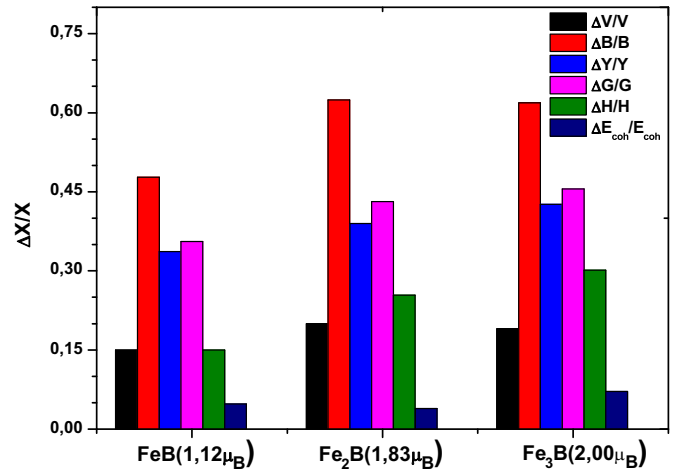


Fig. 3. The calculated relative change of atomic volume $\Delta V/V$, bulk modulus $\Delta B/B$, Young modulus $\Delta Y/Y$, Shear modulus $\Delta G/G$, Hardness $\Delta H/H$ and cohesive energy $\Delta E_{coh}/E_{coh}$ at transition pressure.

are in good agreement with previous theoretical and experimental values [16,35,36] and range from 2.0 μ_B for Fe_3B to 1.12 μ_B for FeB. These moments are smaller than the magnetic moments of elemental bcc ferromagnetic iron (2.22 μ_B) [37]. Indeed, when B atoms are inserted in Fe crystals, the volume concentration of metallic Fe–Fe bonds decreases and they replaced by newly formed covalent Fe–B and B–B, bonds.

As to the mechanical properties, it is commonly accepted that mechanical properties of 3d-metal borides are well described with the help of GGA–PBE. However, there were some doubts whether this is true also when treating magnetic moments. For this purpose, we performed also LDA calculations of magnetic moments and compared them with the experimental data. From the comparison (Table 3) one can clearly see that the GGA–PBE values agree better with experimental data than the LDA values. This comparison justifies the application of GGA–PBE approach also for magnetic moments.

The formation energy E_f , was calculated to check the probability of thermodynamic existence of Fe_xB under pressure. All formation energies are negative indicating that all structures in both pressure conditions are thermodynamically stable. The formation energies of Fe_xB in magnetic state are lower than Fe_xB in NM case by 4.7%, 3.9%, 7.1% from Fe_xB , implying that the magnetic state has higher thermodynamic stability.

volumes. This definition of critical pressure (P_c) was first employed by Mohn et al. in their work on magneto-elastic anomalies in Fe–Ni Invar alloys [29] and NiFe_3N and PdFe_3N nitrides [30]. This definition is also used in the study on magnetic transition of intermetallic bilayers and substituted iron nitrides [31–34].

The calculated changes of volume at 0 GPa and after transition pressure of our three compounds are presented in Fig. 3. We note a volume compression of 15%, 20% and 19% for FeB, Fe_2B and Fe_3B , respectively in applied pressure, which increases the bulk modulus of our compounds by 47.7%, 62% and 61.8%.

The calculated magnetic moments of our compounds at 0 GPa

Table 3

The calculated magnetic moment (μ_B/Fe) of Fe_xB . Experimental and theoretical values are listed in parentheses.

		FeB	Fe ₂ B	Fe ₃ B
		μ_B/Fe	μ_B/Fe	μ_B/Fe
Our calculations	LSDA	0.945	1.198	0.015
	GGA	1.126	1.83	2.003
Experiments		(1.12) ^{exp1}	(1.96) ^a	(2.08) ^b
		(1.20) ^a	(1.62) ^{exp2}	(2.17) ^a

^a Ref. [63].

^b Ref. [61].

^{exp1} Ref. [36].

^{exp2} Ref. [16].

3.3. Magnetic moment

Fe behaves as weak ferromagnet with a magnetic moment of $2.217 \mu_B$ [38]. The magnetic moments of iron atoms in our compounds are somewhat different: $2.003 \mu_B$, $1.83 \mu_B$ and $1.12 \mu_B$ for Fe_3B , Fe_2B and FeB , respectively. It turns out that iron atoms in Fe_3B carry a higher magnetic moment which leads to a shift in the Slater–Pauling curve [39]. The calculated total and partial densities of state DOS for Fe_xB compounds are shown in Fig. 4.

Ferromagnetic behavior is dominated by Fe–Fe bonds and any gain of the covalent Fe–B energy is accomplished by the loss of exchange energy of Fe–Fe bonds [40]. The main ferromagnetic moment of Fe_xB compounds come from spin-polarization of 3d electrons. According to the Stoner model, the magnetic phase appears when the gain in the exchange energy is larger than the loss in kinetic energy, and the condition of the existence of magnetism could be evaluated by the Stoner criterion: $N(E_F)I > 1$, where $N(E_F)$ is the non-spin-polarized partial density of states of transition metal atoms at Fermi energy and I (0.46) is the exchange–correlation integral calculated by Janak [41]. Based on the prediction of the Stoner model, Fe_xB illustrates as spontaneous criterion of spin-polarized state because $N(E_F)I > 1$ are 4.61, 8.31, and 11.06 for FeB , Fe_2B and Fe_3B respectively, much larger than the limiting value of 1. Stoner criterion is not able to predict the stability of a phase. However, it may give us some hints on the magnetic ground state of our compounds. Magnetic behavior of Fe_xB compounds is consistent with the Stoner criterion.

3.4. Density of states of Fe_xB under pressure

In order to show the dependence of the magnetic moment on the equilibrium volume, we have calculated the relative change of volume, bulk modulus and hardness between the magnetic and nonmagnetic states, they are obtained as:

$$\frac{\Delta X}{X} = \left| \frac{X_M - X_{NM}}{X_M} \right|, X = V, B \text{ and } H \quad (1)$$

where X_M and X_{NM} are the calculated volume, bulk modulus and hardness in the magnetic and non-magnetic state respectively.

The calculated relative compression in volume ranges from 0% to 15% for FeB , from 0% to 20% for Fe_2B and from 0% to 19% for Fe_3B . The magnitude of the magnetic moment is strongly related to the volume. This origin of thus dependence is due to the magneto-volume effect [42]. Because the Pauli Exclusion Principle operates for parallel spins, the electron kinetic energy of the spin-polarized state is higher, and volume expansion relaxes the kinetic energy. Consequently the magnetic (high-spin) state has a larger volume than the non-magnetic (low-spin) state [43]. In the NM state the bulk modulus B is systematically larger than in the magnetic state which increases from FeB to Fe_3B , also due to the magnetic moment eliminated (see Fig. 2). The bulk modulus in the NM state

increases by 47.7%, 62% and 61.8% for FeB , Fe_2B and Fe_3B , respectively. The low value of bulk modulus in the magnetic case points to a larger compressibility. This means that the system is “softer” when it is magnetically ordered and “harder” when it is not.

The total and partial DOS for these compounds, at ambient and critical transition pressure, are shown in Fig. 3 (Left and right panel). From these figures, it can be stated that Fe_xB total density of states at the Fermi level is predominantly due to the d electrons of Fe atoms both at ambient and under high pressure. From SP DOS Fig. 3 (Left panel) it can be seen that the energy shift between spin up and spin down population is significant for Fe-d states, which results in large magnetic moment values. The main peaks of Fe-d states for majority and minority spins are located below and above the Fermi level, respectively, and under increasing compression, they start to move towards the Fermi level. The applied pressure causes a visible reduction in the magnetic moments of Fe_xB for all materials. At approximately 77 GPa, 85 GPa and 55 GPa for FeB , Fe_2B and Fe_3B , respectively, we note that the peaks in the majority and minority DOS are the same. Thus, total DOS at the Fermi level for Fe_xB increases under pressure by 21%, 50% and 32.5% for FeB , Fe_2B and Fe_3B , respectively. This enhanced $N(E_F)$ is derived entirely from the Fe 3d states, with negligible contribution from the B 2p states. Following the above arguments we may be predict the appearance of superconductivity in Fe_xB under pressure as is the case of iron that undergoes a transition to superconducting phase above 30 GPa when it loses its magnetic moment [44].

3.5. Population analysis

Mulliken population analysis (MPA) is a method for calculating partial atomic charges based on the population of linear combined atomic orbitals (LCAO) bases. This was implemented in CASTEP by Segall et al. [45] based on the method of Sanchez-Portal [46] which provides the link between methods using LCAO and those using plane waves. Owing to the difference of electro-negativity between the Fe and B atoms, the ionic bonds are formed where Fe atoms donate some electrons to B atoms and thus become slightly positively charged. MPA method is applied for the overlap population and the charge calculations. We used the following relations to calculate the average bond length and the average overlap population:

$$L_{\text{moy}}(AB) = \frac{\sum_i L_i N_i}{\sum_i N_i} \quad (3)$$

$$P^u = \bar{n}_{AB} = \frac{\sum_i n_i^{AB} N_i}{\sum_i N_i} \quad (4)$$

Here, $L_{\text{moy}}(AB)$ and \bar{n}_{AB} are the average bond length and the mean bond population, respectively; N_i is the total number of i bond in the cell and L_i is the bond length of i type. These parameters will be used in Section 3.3 for the calculation of bond hardness.

The strongest covalent interaction is attributed to the B–B bond in FeB and Fe_2B with average calculated length of 2.322 Å and 2.105 Å respectively.

3.6. Hardness

Hardness is a measure of the resistance of materials against permanent deformations. It is usually measured by traditional techniques such as in Brinell, Rockwell, Vickers, or Knoop [47]. Materials with high hardness are technologically important for cutting tools and wear resistant coatings. It has been recognized that the hardness of strongly covalent/ionic bonded crystals is associated directly with the bond strength [48–50]. Zhang et al.

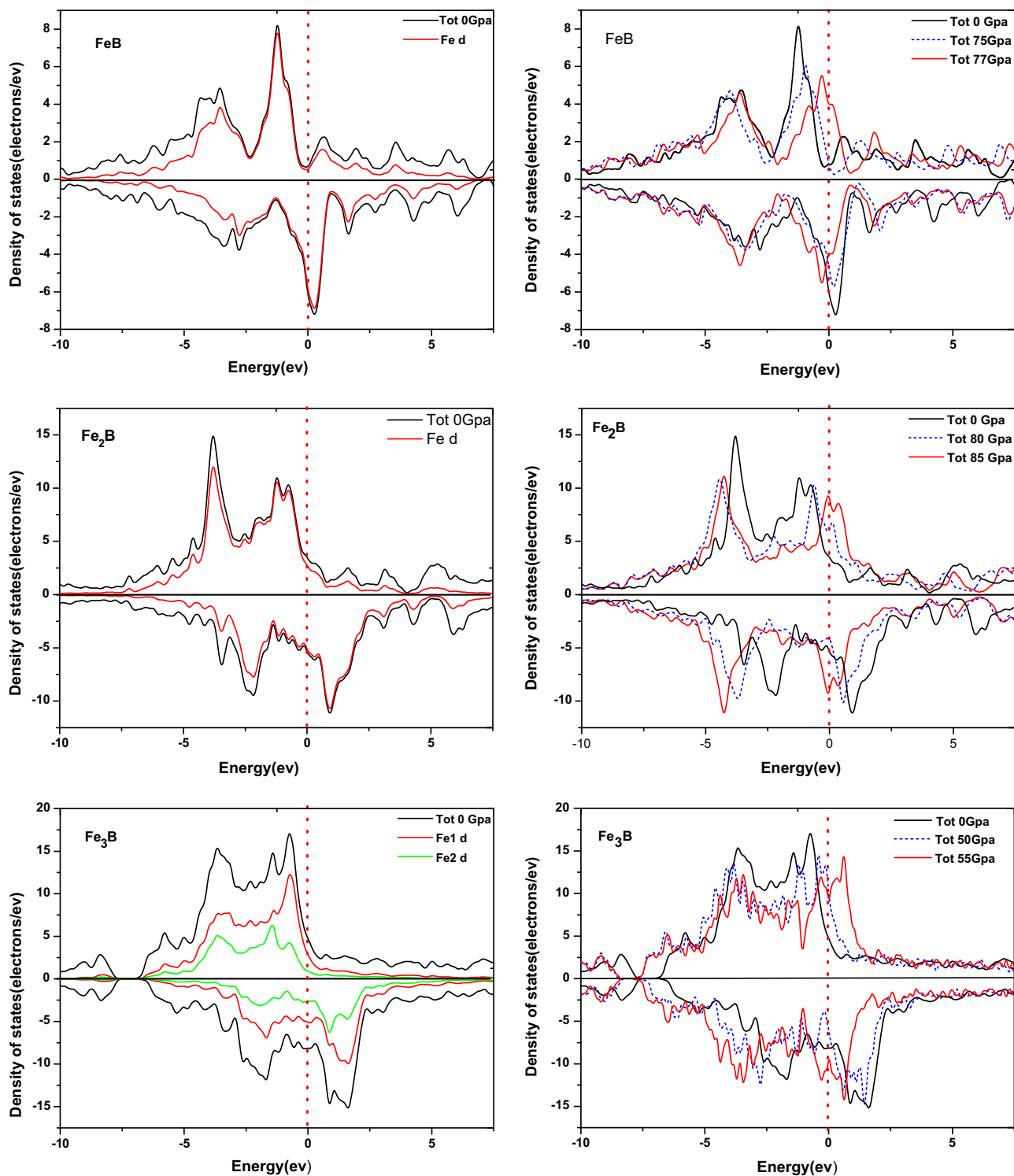


Fig. 4. The calculated total and partial DOS of Fe_xB , Left panel with spin polarization and right panel under pressure. Dashed line represents the Fermi level.

showed that GGA–PBE gives better values of bond hardness (H). It was found that GGA–PBE (USP) method can be effectively used to predict the H value [51].

In this paper, based on the previous works of Gao [52], the hardness of Fe–B and B–B bonds in each of our three compounds Fe_xB are evaluated and compared. The proposed analytical expressions have been used to determine the hardness from first-principles theory [51]. We will consider the hardness of B–B and Fe–B bonds only. The hardness of Fe–Fe bond, however, is not

taken into consideration in this work, because the hardness of metallic bond is ill defined in this method. The strength of the bond per the unit volume can be characterized by average overlap populations. For complex multi-bonding compounds, the hardness of the u type bond can be calculated as follows:

$$H_V^u (\text{GPa}) = 740P^u (v_b^u)^{(-5/3)}$$

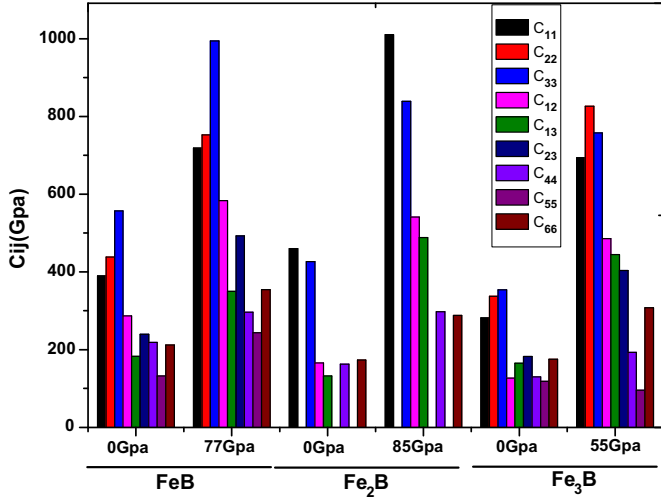


Fig. 5. Pressure dependence on the elastic constants.

$$v_b^u = \frac{(d^u)^3 \Omega}{\sum_v [(d^v)^3 N_b^v]}$$

$$H = ((H^{Fe-B})^{N^u} (H^{B-B})^{N^v})^{1/(N^u+N^v)}$$

H_v^u is the hardness of u type bond; Ω is the cell volume, d^u is the bond length; N_b^v refers to the v type bond density per cubic angstrom and the sum is over the total number of v type bonds in the cell; and P^u is overlap population of u type bond. We use Mulliken population analysis as implemented in CASTEP in order to estimate bond overlap population.

The longest Fe–B bond length considered in this work was limited to 3.1 Å because the interaction between Fe atom and the second nearest neighbor B atom is assumed to be weaker than that between the near-neighbor boron atoms.

The calculated bond length, population overlap, contribution of Fe–B and B–B bonds to the hardness H^u in FeB, Fe₂B and Fe₃B are listed in Table 4 with material hardness of our three compounds. The hardness of B–B bond H^u is significantly larger than Fe–B bond in FeB and Fe₂B compounds because of the large bond overlap population. In the case of Fe₃B the Fe–B bond is harder than B–B bond because B–B bond has the largest bond length in this compound and smaller overlap population.

The calculated hardness of FeB (26.25 GPa) and Fe₂B (18.34 GPa) are in fairly good agreement with the experimental values of $(20.4 \pm 0.017$ GPa) for Fe₂B and $(16.2 \pm 0.011$ GPa) for FeB [53]. The disagreement can be explained by the fact that

Table 4

The predicted hardness of B–B and Fe–B bonds. Experimental and theoretical values are listed in parentheses. Different pairs of atoms (B–B, Fe–B). Average bond length of nearest-neighbor atoms d^u (Å), average overlap population of u type bond, nearest-neighbor numbers N^u for different pairs of atoms, cell volume Ω (Å³), volume of a bond of u type v_b^u , hardness of u type bond H^u (GPa) and hardness H (GPa).

Species	Bond	d^u	p^u	N^u	Ω	v_b^u	H^u	H
FeB	B–B	2.322	0.725	4	62.184	3.840	56.966	26.25 (26.28) ^{exp1} (20.4 ± 0.017) ^{exp2}
	Fe–B	2.121	0.175	16			21.629	
Fe ₂ B	B–B	2.105	0.7	2	105.76	2.952	85.270	18.34 (18.2) ^a (16.2 ± 0.011) ^{exp2}
	Fe–B	2.144	0.15	32			16.658	
Fe ₃ B	B–B	3.076	−0.08	2	153.555	12.25	–	17.35
	Fe–B	2.124	0.32	32			4.798	

^{exp1} Ref. [64]

^{exp2} Ref. [53]

^a Ref. [59].

experimentally measured values of hardness of materials are very sensitive to many parameters including loading and unloading speed, applied load, anisotropy of materials, defects in the sample, method of measurement, temperature, etc. Additionally, for polycrystalline materials, hardness is a function of grain size.

3.7. Elastic properties under pressure

As well known, elastic properties can reflect the interatomic interactions and are related to some fundamental physical properties, such as, thermal expansion, phonon spectra and equations of state [54–57]. The elastic constants of single crystal Fe_xB compounds are presented in Table 5. Generally, the elastic constants along three principle axes (x , y and z) are very high, at zero and under pressure Fig. 5, which indicates the high resistance to the axial compression in these directions. However, the orders of magnitude along the three axes are different. For orthorhombic FeB and Fe₃B, the order is $C_{33} > C_{22} > C_{11}$. For tetragonal Fe₂B the orders is $C_{11} > C_{33}$. Since the tetragonal structure can be regarded as the special case of orthorhombic structure with an additional condition of $a=b$, the mechanical stability criteria can be represented in a uniform manner for orthorhombic structure [58]:

$$C_{ii} > 0 (i = 1; 2; 3; 4; 5; 6), C_{11} + C_{22} + C_{33} + 2(C_{12} + C_{13} + C_{23}) > 0$$

$$(C_{11} + C_{22} - 2C_{12}) > 0; (C_{11} + C_{33} - 2C_{13}) > 0; (C_{22} + C_{33} - 2C_{23}) > 0$$

The stability criteria of material under pressure are similar to those under zero pressure, just replacing C_{ij} with \tilde{C}_{ij} ($i = j = 1, 2, 3, 4, 5, 6$) [59]. Thus the mechanical stability leads to restrictions on the elastic coefficients under isotropic pressure as follows:

$$\tilde{C}_{ii} = C_{ii} - P > 0, (i = 1, 2, 3, 4, 5, 6), (C_{11} + C_{22} - 2C_{12} - 4P) > 0,$$

$$(C_{11} + C_{33} - 2C_{13} - 4P) > 0, (C_{22} + C_{33} - 2C_{23} - 4P) > 0,$$

$$(C_{11} + C_{22} + C_{33} + 2C_{12} + 2C_{13} + 2C_{23} + 3P) > 0$$

For tetragonal the elastic constants under pressure (P) are related to those under zero pressure, shown as follows [60],

$$\tilde{C}_{ij} = C_{ij} (i = 1, 2, 3; j = 4, 5, 6), \tilde{C}_{ii} = C_{ii} - P (i = 1, 2, 3, 4, 5, 6), \tilde{C}_{12} = C_{12} + P,$$

$$\tilde{C}_{13} = C_{13} + P, \tilde{C}_{23} = C_{23} + P, \tilde{C}_{45} = C_{45}, \tilde{C}_{46} = C_{46}, \tilde{C}_{56} = C_{56},$$

As for Fe₂B in tetragonal structure, there are six independent elastic constants, $C_{11}, C_{12}, C_{13}, C_{33}, C_{44}, C_{66}$, because of $C_{22} = C_{11}, C_{23} = C_{13}, C_{44} = C_{55}$ as a result of the crystal symmetry. The single crystal elastic coefficients (C_{ij}) satisfy the stability criteria, which,

Table 5

The calculated full set elastic constants of Fe_xB (under 0 and critical pressure, in GPa) along with other available values.

Species	Elastic constants								
	C ₁₁	C ₂₂	C ₃₃	C ₁₂	C ₁₃	C ₂₃	C ₄₄	C ₅₅	C ₆₆
FeB (0 GPa)	389.82	438.36	557.07	286.85	183.12	239.76	218.8	132.25	212.01
	373.7 ^a	434.1 ^a	503.4 ^a	246 ^a	184.4 ^a	209.1 ^a	207.4 ^a	117.7 ^a	193.7 ^a
FeB (77 GPa)	718.5	752.6	993.9	583.2	350.1	492.4	296.4	243.3	354.4
Fe ₂ B (0 GPa)	459.7		426.3	165.6	132.3		162.6		173.7
	413 ^b		389 ^b	154 ^b	132 ^b		148 ^b		157 ^b
Fe ₂ B (85 GPa)	1010.4		839	541.3	488.4		298		288.4
Fe ₃ B (0 GPa)	281.7	337.5	354	126.7	165.3	182.2	130.2	118.7	175.6
	263.3 ^a	302.7 ^a	318.4 ^a	133.5 ^a	162.8 ^a	178.6 ^a	110.2 ^a	101.2 ^a	158.7 ^a
Fe ₃ B (55 GPa)	694	826	778.5	485.5	444.75	403.6	193.1	195.8	307.7

^a Ref. [65].

^b Ref. [66].

Table 6

The calculated bulk, Young (*Y*) and Shear modulus (*G*) of Fe_xB (under 0 and critical pressure, in GPa), Poisson's ratio (*ν*) and *B/G* ratio along with other available values.

Species	<i>B</i>	<i>Y</i>	<i>G</i>	<i>ν</i>	<i>B/G</i>
FeB (0 GPa)	305.6	365.7	140.6	0.30	2.174
	286.6 ^a	360.5 ^a	139.7 ^a	0.29 ^a	2.05 ^a
FeB (77 GPa)	585	567.5	212	0.34	2.76
Fe ₂ B (0 GPa)	244.6	395.2	160.5	0.23	1.524
	222.3 ^a	355 ^a	144 ^a	0.23 ^a	1.54 ^a
Fe ₂ B (85 GPa)	651	695.4	263	0.32	2.48
Fe ₃ B (0 GPa)	210	285.3	112	0.27	1.875
	201.6 ^a	248.5 ^a	96 ^a	0.3 ^a	2.1 ^a
Fe ₃ B (55 GPa)	551	524	195.2	0.34	2.82

^a Ref. [63].

leads to the following restrictions on the elastic coefficients under isotropic pressure as follows [61]:

$$\tilde{C}_{ii} > 0, (i = 1, 2, 3, \dots, 6), \tilde{C}_{11} + \tilde{C}_{33} - 2\tilde{C}_{13} > 0,$$

$$\tilde{C}_{11} + \tilde{C}_{33} + 2\tilde{C}_{12} + 4\tilde{C}_{13} > 0, (\tilde{C}_{11} - \tilde{C}_{12}) > 0.$$

where: *C_{ij}*'s are the elements of elastic coefficient matrix. The arithmetic average of the Voigt and Reuss bounds is known as the Voigt–Reuss–Hill (VRH) average, which is regarded as the best estimate for the theoretical value of polycrystalline elastic modulus [62]:

$$G_H = (G_R + G_V)/2, B_H = (B_R + B_V)/2$$

The Young modulus and Poisson's ratio can be computed based on the above values by [63]:

$$E = 9BG/(3B + G), \nu = (3B - 2G)/(6B + 2G)$$

The ratio of *B/G* can be used to estimate the ductility or brittleness of materials, since a high (low) value is associated with ductility (brittleness), and the critical value is about 1.75. Meanwhile, the Poisson's ratio when is larger (smaller) than 0.25 can be also used to represent the ductility or brittleness of materials. The calculated values for Fe_xB compounds are presented in Table 6. It is found that FeB and Fe₃B can be classified as ductile since *B/G* is larger than 1.75 and *ν* is larger than 0.25, while Fe₂B, should be classified as brittle.

4. Conclusions

First-principles total-energy plane-wave pseudo-potential calculations were used to calculate the ground-state lattice parameters, cohesive energies, formation energies, bond length; elastic modulus and hardness of Fe_xB (*x* = 1, 2, 3) compounds. The calculated results, using PBE exchange-correlation functional and ultra-soft pseudo-potential are credible at 0 GPa to obtain the correct ground state properties of Fe_xB because our results are in good agreement with experimental data. Analysis of density of states reveals spectacular phenomena under pressure. We observe a transition from ferromagnetic to nonmagnetic states in the range of 50–90 GPa.

Disappearance of ferromagnetic order decreases the volume of the unit cell, increases the bulk modulus and also makes the solid harder. Therefore, the magnetic order in Fe_xB are sensitive to the volume, which along with the calculated value of critical pressure, indicates that those iron borides shows an Invar-like behavior.

The calculated hardness *H* from Fe–B and B–B bonds of FeB, Fe₂B and Fe₃B are predicted from Mulliken populations using GGA–PBE (USP) method. The calculated values of 26.25, 18.34 and 17.34 GPa for Fe_xB in FM agree well with the previous study and experimental Vickers hardness. It also implies that it can be an effective tool in predicting the hardness of metal-borides. It is evident that the hardness of B–B bond is significantly larger than Fe–B bond in FeB and Fe₂B compounds because of the large bond overlap population. In the case of Fe₃B, the Fe–B bond is harder than B–B bond because B–B bond has large bond length in this compound.

References

- [1] H.J. Goldschmidt, *Interstitial Alloys*, Butterworth, London, 1967.
- [2] A.Gv Matuschka, *Boronizing*, Carl Hanser Verlag, Munich, FRG, 1980.
- [3] R.C. Fisher, *Boriding and diffusion metallizing*, in: T.S. Sudarshan (Ed.), *Surface modification technologies*, Marcel Dekker Inc., New York, 1989.
- [4] O. Allaoui, N. Bouaouadja, G. Saindeman, *Surf. Coat. Technol.* 201 (2006) 3475.
- [5] M. Palumbo, G. Cacciamani, E. Bosco, M. Baricco, *Intermetallics* 11 (2003) 1293.
- [6] E. Kneller, Y. Khan, *Z. Metall.* 78 (1987).
- [7] A. Meneses-Amador, I. Campos-Silva, J. Martínez-Trinidad, S. Panier, U. Figueroa-López, A. Torres-Hernández, *Surf. Coat. Technol.* 215 (2013) 285.
- [8] G. Rodríguez-Castro, I. Campos-Silva, E. Chávez-Gutiérrez, J. Martínez-Trinidad, E. Hernández-Sánchez, A. Torres-Hernández, *Surf. Coat. Technol.* 215 (2013) 291.
- [9] Z. Huang, S. Ma, J. Xing, B. Wang, *J. Alloy. Compd.* 582 (2014) 196.
- [10] M. Zhao, Y. Feng, L. Jiao, H. Yuan, X. Zhou, M.-B. Jang, *Int. J. Hydrog. Energy* 32 (2007) 3915.
- [11] Y.H. Zhang, X.P. Dong, Gq Wang, S.H. Guo, J.Y. Ren, X.L. Wang, *Trans. Non-ferrous Met. Soc. China* 16 (2006) 800.
- [12] Y.H. Zhang, Xp Dong, S.H. Guo, Gq Wang, J.Y. Ren, X.L. Wang, *J. Alloy. Compd.* 398 (2005) 178.

- [13] R.S. Mulliken, J. Chem. Phys. 23 (1955) 1833.
- [14] L. Guangwei, W. Dingsheng, J. Phys.: Condens. Matter 1 (1989) 1799.
- [15] P.J. Brown, J.L. Cox, Philos. Mag. 23 (1971) 705.
- [16] R.S. Perkins, P.J. Brown, J. Phys. F: Met. Phys. 4 (1974) 906.
- [17] D.J. Joyner, O. Johnson, D.M. Hercules, J. Am. Chem. Soc. 102 (1980) 1910.
- [18] K.A. Murphy, N. Hershkowitz, Phys. Rev. B 7 (1973) 23.
- [19] L. Takacs, M.C. Cadeville, I. Vincze, J. Phys. F: Met. Phys. 5 (1975) 800.
- [20] W. Kohn, Rev. Mod. Phys. 71 (1999) 1253.
- [21] P. Hohenberg, W. Kohn, Phys. Rev. 136 (1964) B864.
- [22] W. Kohn, L.J. Sham, Phys. Rev. 137 (1965) A1697.
- [23] W. Kohn, L.J. Sham, Phys. Rev. 140 (1965) A1133.
- [24] S.K. Medeiros, E.L. Albuquerque, F.F. Maia Jr, E.W.S. Caetano, V.N. Freire, Chem. Phys. Lett. 435 (2007) 59.
- [25] V. Milman, B. Winkler, J.A. White, C.J. Pickard, M.C. Payne, E.V. Akhmatkaya, R.H. Nobes, Int. J. Quantum Chem. 77 (2000) 895.
- [26] Y.W. Xu, H.M. Wang, J. Alloy. Compd. 457 (2008) 239.
- [27] J.P. Perdew, K. Burke, Y. Wang, Phys. Rev. B 54 (1996) 16533.
- [28] H.J. Monkhorst, J.D. Pack, Phys. Rev. B 13 (1976) 5188.
- [29] P. Mohn, K. Schwarz, D. Wagner, Phys. Rev. B 43 (1991) 3318.
- [30] P. Mohn, K. Schwarz, S. Matar, G. Demazeau, Phys. Rev. B 45 (1992) 4000.
- [31] A.V. dos Santos, C.A. Kuhnen, Solid State Commun. 95 (1995) 537.
- [32] A.V. dos Santos, C.A. Kuhnen, J. Magn. Magn. Mater. 184 (1998) 293.
- [33] A.V. dos Santos, C.A. Kuhnen, Thin Solid Films 350 (1999) 258.
- [34] A.V. dos Santos, C.A. Kuhnen, J. Solid State Chem. 182 (2009) 3183.
- [35] W.Y. Ching, Y.-N. Xu, B.N. Harmon, J. Ye, T.C. Leung, Phys. Rev. B 42 (1990) 4460.
- [36] P. Mohn, D.G. Pettifor, J. Phys. C: Solid State Phys. 21 (1988) 2829.
- [37] C. Kittel, Introduction to Solid State Physics, Wiley, 1996.
- [38] I.R. Shein, N.I. Medvedeva, A.L. Ivanovskii, Phys. B: Condens. Matter 371 (2006) 126.
- [39] R.M. Bozorth, Ferromagnetism, Van Nostrand, New York, 1951.
- [40] Y. Bourourou, L. Beldi, B. Bentría, A. Gueddouh, B. Bouhafs, J. Magn. Magn. Mater. 365 (2014) 23.
- [41] J.F. Janak, Phys. Rev. B 16 (1977) 255.
- [42] S. Chikazumi, Physics of Magnetism, Wiley, New York, 1964.
- [43] T. Egami, B.V. Fine, D.J. Singh, D. Parshall, C. de la Cruz, P. Dai, Phys. C: Supercond. 470 (Suppl. 1) (2010) S294.
- [44] K. Shimizu, T. Kimura, S. Furomoto, K. Takeda, K. Kontani, Y. Onuki, K. Amaya, Nature 412 (2001) 316.
- [45] M.D. Segall, J.D.L. Philip, M.J. Probert, C.J. Pickard, P.J. Hasnip, S.J. Clark, M. C. Payne, J. Phys.: Condens. Matter 14 (2002) 2717.
- [46] D. Sanchez-Portal, E. Artacho, J.M. Soler, Solid State Commun. 95 (1995) 685.
- [47] B.G. Pfrommer, M. Côté, S.G. Louie, M.L. Cohen, J. Comput. Phys. 131 (1997) 233.
- [48] S. Frank, e-J. Nondestruct. Test. 7 (2002) 10.
- [49] S.-H. Jhi, S.G. Louie, M.L. Cohen, J. Ihm, Phys. Rev. Lett. 86 (2001) 3348.
- [50] J. He, E. Wu, H. Wang, R. Liu, Y. Tian, Phys. Rev. Lett. 94 (2005) 015504.
- [51] X. Zhang, X. Luo, J. Han, J. Li, W. Han, Comput. Mater. Sci. 44 (2008) 411.
- [52] F. Gao, J. He, E. Wu, S. Liu, D. Yu, D. Li, S. Zhang, Y. Tian, Phys. Rev. Lett. 91 (2003) 015502.
- [53] I. Campos-Silva, J. Martínez-Trinidad, M.A. Doñu-Ruíz, G. Rodríguez-Castro, E. Hernández-Sánchez, O. Bravo-Bárceñas, Surf. Coat. Technol. 206 (2011) 1809.
- [54] C. Zhi-Mei, W. Xin-Qiang, W. Feng, L. Li-Ya, L. Gao-Bin, D. Zhuang-Fen, N. Zhao-Xiu, Acta Phys. Sin. 60 (2011) 96301.
- [55] C.A. Ponce, R.A. Casali, M.A. Caravaca, J. Phys.: Condens. Matter 20 (2008) 045213.
- [56] H.Y. Wang, J. Cao, X.Y. Huang, J.M. Huang, Condens. Matter Phys. 15 (2012).
- [57] C. Yang, Z.F. Zhou, J.W. Li, X.X. Yang, W. Qin, R. Jiang, N.G. Guo, Y. Wang, C. Q. Sun, Nanoscale 4 (2012) 1304.
- [58] B. Xiao, J. Feng, C.T. Zhou, J.D. Xing, X.J. Xie, Y.H. Cheng, R. Zhou, Phys. B: Condens. Matter 405 (2010) 1274.
- [59] G.V. Sin'ko, N.A. Smirnov, Phys. Rev. B 71 (2005) 214108.
- [60] Z. Zhou, B. Joós, Phys. Rev. B 54 (1996) 3841.
- [61] S.K.R. Patil, S.V. Khare, B.R. Tuttle, J.K. Bording, S. Kodambaka, Phys. Rev. B 73 (2006) 104118.
- [62] R. Hill, Proc. Phys. Soc. Sect. A 65 (1952) 349.
- [63] C.T. Zhou, J.D. Xing, B. Xiao, J. Feng, X.J. Xie, Y.H. Chen, Comput. Mater. Sci. 44 (2009) 1056.
- [64] O. Culha, M. Toparli, T. Aksoy, Adv. Eng. Softw. 40 (2009) 1140.
- [65] L.H. Li, W.L. Wang, L. Hu, B.B. Wei, Intermetallics 46 (2014) 211.
- [66] A.F. Bialon, T. Hammerschmidt, R. Drautz, S. Shah, E.R. Margine, A. N. Kolmogorov, Appl. Phys. Lett. 98 (2011) 081901.

Anisotropic elastic properties of Fe_xB ($x = 1, 2, 3$) under pressure. First-principles study

A. GUEDDOUH^{1,2*}, B. BENTRIA¹, Y. BOUROUROU³, S. MAABED¹

¹Laboratoire de Physique des Matériaux, Université Amar Telidji de Laghouat; BP37G, Laghouat 03000, Algeria

²Département de Physique, Faculté des Sciences, Université A.B. Belkaid Tlemcen, BP 119, Tlemcen 13000, Algeria

³Laboratory University of Sidi Bel-Abbès, 22000 Sidi Bel-Abbès, Algeria

Spin-polarization (SP) and pressure effects have been used to better clarify and understand anisotropic elastic properties of Fe–B intermetallic compounds using the first-principles calculation with generalized gradient approximation (GGA) within the plane-wave pseudopotential density functional theory. Elastic properties, including bulk, shear and Young's moduli as well as Poisson ratio were obtained by Voigt-Reuss-Hill approximation. All studied Fe–B compounds were mechanically stable. The brittle and ductile properties were discussed using bulk to shear moduli ratio (B/G) of the studied structures in the pressure range of 0 GPa to 90 GPa in order to predict the critical pressure of phase transition from ferromagnetic (FM) to nonmagnetic (NM) state. Mechanical anisotropy in both cases was discussed by calculating different anisotropic indexes and factors. We have plotted three-dimensional (3D) surfaces and planar contours of the bulk and Young's moduli of Fe_xB ($x = 1, 2, 3$) compounds for some crystallographic planes, (1 0 0), (0 1 0) and (0 0 1), to reveal their elastic anisotropy. On the basis of anisotropic elastic properties the easy and hard axes of magnetization for the three studied compounds were predicted.

Keywords: *DFT; spin polarization; elastic properties; anisotropy; easy and hard axes*

© Wrocław University of Technology.

1. Introduction

In the past decades, the binary Fe–B alloy system has been a subject of numerous experimental and theoretical studies concerning hardness, melting point, wear resistance, corrosion resistance, and ferromagnetism [1–3]. According to the Fe–B equilibrium phase diagram, there are two stable iron borides at ambient temperature: single boride layer (Fe_2B) or double (FeB and Fe_2B) layers [4]. The metastable phase, Fe_3B , appears during formation of Fe_2B . The metastable o- Fe_3B phase has also been obtained in Fe–B glasses by quenching and annealing [5]. These compounds can be prepared using numerous equilibrium or non-equilibrium methods, such as ball milling, chemical vapor deposition (CVD), physical vapor deposition (PVD), magnetic sputtering and thermal chemical reactions. Fe_2B can also be prepared as a bulk single crystal [6]. FeB was prepared in a form

of nanoparticles by chemical reduction method [7] in order to improve the cycle stability of PuNi_3 -type hydrogen storage electrodes [8, 9]. The properties depending on process time and temperature, such as structure parameters, hardness, Young's modulus and fracture toughness of iron boride layers have been investigated experimentally [10]. The electronic structure, stability and elastic constants of the three Fe_xB compounds were calculated in the literature [11] using DFT. It was indicated that pressure affects the structure, mechanical and magnetic properties of iron borides, and spin-polarized calculations were important to obtain the correct ground state properties of Fe_xB compounds. We tried to demonstrate that the structure properties and magnetic moment change strongly with pressure.

In this work, we performed the first principles calculations of anisotropic elastic properties for the three structures Fe_xB ($x = 1, 2, 3$) at 0 GPa pressure and at a critical pressure when a ferromagnetic material undergoes transition to a nonmagnetic state

*E-mail: ghahmed2012@gmail.com

(NM). Anisotropy index A and directional dependences of bulk and Young's moduli were investigated. From the anisotropic elastic properties, the easy and hard axes of magnetization of the three compounds were predicted, which revealed that for bcc Fe the highest density of atoms is in the $\langle 1\ 1\ 1 \rangle$ direction, and consequently $\langle 1\ 1\ 1 \rangle$ is the hard magnetization axis. In contrast, the atom density is the lowest in $\langle 1\ 0\ 0 \rangle$ direction, and consequently $\langle 1\ 0\ 0 \rangle$ is the easy magnetization axis. Certainly, since bcc iron is a cubic crystal, all six cube edge orientations $\langle 1\ 0\ 0 \rangle$, $\langle 0\ 1\ 0 \rangle$, $\langle 0\ 0\ 1 \rangle$, $\langle \bar{1}\ 0\ 0 \rangle$, $\langle 0\ \bar{1}\ 0 \rangle$ and $\langle 0\ 0\ \bar{1} \rangle$ are in fact equivalent easy axes [12].

We hope that our study will provide a useful guidance for future works on the Fe–B compounds.

Finally, we concluded that spin-polarization and pressure are of significant importance in determining the anisotropic elastic properties of iron borides.

2. Structure aspects and calculation methods

FeB and Fe₃B belong to an orthorhombic space group Pnma (Fig. 1) [13–16]. Both structures contain four formula units per cell. In Fe₃B, the isotype of Fe₃C, iron atoms are distributed over two distinct lattice sites: the general Fe sites (Wyckoff position 8d) and the special Fe sites (Wyckoff position 4c). In contrast, Fe₂B (Fig. 1) belongs to the body-centered tetragonal Bravais lattice with I4/mcm space group where the unit cell contains four equivalent Fe atoms in the positions of point group mm and two equivalent B atoms in the positions of point group 42 [11]. The B atoms in Fe₂B are located between two layers of Fe atoms in a distorted, closely packed arrangement.

Total energy calculations were performed within the density functional theory (DFT) [17]. CASTEP code was used in this study. The last uses the plane wave in reciprocal space [18]. The ultrasoft Vanderbilt pseudopotentials were employed to represent the electrostatic interactions between valence electrons and ionic cores [19]. They were used with the following valence electronic configurations Fe: 3d⁶4s² and B: 2s²2p¹. Generalized

gradient approximation PBE-GGA was used for exchange-correlation energy calculations [20]. The kinetic energy cut-off value was selected as 500 eV, which was sufficient to obtain reliable results.

Total energies were evaluated in the first irreducible Brillouin zone with the following Monkhorst-pack grids [21]: (6 × 10 × 8) for FeB, (10 × 10 × 10) for Fe₂B and (10 × 12 × 8) for Fe₃B. It is known that the ground states of several Fe_xB compounds are ferromagnetic [22].

Structural and elastic properties were calculated for both FM and NM states in the three compounds. The convergence criteria of total energy and structure optimization were set to fine quality with the energy tolerance of 10^{−6} eV/atom. BFGS (Broyden-Fletcher-Goldfarbe-Shanno) optimization method was used to obtain the equilibrium crystal structures of Fe_xB with maximum atom displacement and force set to 0.002 Å and 0.001 eV/Å.

The cohesive energy (E_{coh}) of a material, (which is a useful fundamental property), is a measure of the relative binding forces. The stability of our compounds was evaluated by calculating two energy parameters, cohesive energy E_{coh} and formation energy E_f defined as:

$$E_{\text{coh}}(\text{Fe}_x\text{B}) = \frac{E_{\text{total}}(\text{Fe}_x\text{B}, \text{Cell}) - xnE_{\text{iso}}(\text{Fe}) - nE_{\text{iso}}(\text{B})}{n} \quad (1)$$

$$E_f(\text{Fe}_x\text{B}) = E_{\text{coh}}(\text{Fe}_x\text{B}) - xE_{\text{coh}}(\text{Fe}) - E_{\text{coh}}(\text{B}) \quad (2)$$

where E_{coh} (Fe_xB) is the cohesive energy of Fe_xB per unit formula; E_f (Fe_xB) is its formation energy; E_{coh} (Fe) is the cohesive energy of iron element per atom; E_{total} (Fe_xB, Cell) is the total calculated energy of Fe_xB per conventional unit cell; E_{iso} (Fe) is the total energy of an isolated Fe atom and finally n refers to the number of unit formula Fe_xB in the conventional cell. The calculation method for E_{coh} (Fe_xB) can also be used to evaluate the cohesive energy of pure elements B and Fe. Equation 1 and equation 2 require negative values of E_{coh} (Fe_xB) and E_f (Fe_xB) to refer to a thermodynamically stable structure. The crystal structures of Fe_xB

studied in this paper were built based on experimental results.

3. Results and discussion

3.1. Structural properties and stability

The calculated lattice parameters, unit cell volume, bulk modulus, cohesive energy and the formation energy for Fe_xB along with the available experimental and previous theoretical data for comparison have been discussed by Gueddouh et al. [11]. The results show that the calculated structure parameters are in good agreement with the experimental values. The calculated values of cohesive energies of FeB, Fe_2B and Fe_3B indicate that all of the Fe_xB compounds are stable. Furthermore, the cohesive energies decrease from FeB to Fe_3B , which is mainly caused by the increase in the volume concentration of Fe atoms.

3.2. Pressure effects

In order to induce a significant change in a structure, high pressure is usually needed to study the material. By increasing the pressure, a transfer from magnetic to nonmagnetic state occurs, which causes an extinction of the magnetic moment; the critical (transition) pressure was estimated as 77 GPa, 85 GPa and 55 GPa for FeB, Fe_2B and Fe_3B , respectively, as shown in Fig. 2. Usually, the critical pressure at which a ferromagnetic material undergoes transition to a NM state is defined as $P_c = -\Delta E/\Delta V$ where ΔE is the difference between NM and spin-polarized (SP) equilibrium total energy by unit cell and ΔV is the respective difference between NM and SP equilibrium volumes. This definition of critical pressure (P_c) was first employed by Mohn et al. [23, 24] in their work on magneto-elastic anomalies in Fe–Ni Invar alloys [23] and NiFe_3N and PdFe_3N nitrides [24]. This definition is also used in the study on magnetic transition of intermetallic bilayers and substituted iron nitrides [25].

The calculated percentage change of volume at 0 GPa and at transition pressure for our three compounds [11] showed a volume compression of 15 %, 20 % and 19 % for FeB, Fe_2B and Fe_3B ,

respectively, at the applied pressure, which resulted in an increase in the bulk modulus of our compounds by 47.7 %, 62 % and 61.8 %.

The formation energy E_f was calculated to check the probability of thermodynamic existence of Fe_xB under pressure. All formation energies are negative indicating that all the structures in the two pressure conditions are thermodynamically stable. The formation energies of Fe_xB in magnetic state are less than those of Fe_xB in NM state by 4.7 %, 3.9 %, 7.1 %, implying that $\text{Fe}_x\text{B}(\text{FM})$ has better thermodynamic stability.

The calculated magnetic moments of our compounds at 0 GPa are in good agreement with theoretical and experimental values [26] and are 2.003 μB , 1.83 μB and 1.12 μB for Fe_3B , Fe_2B and FeB, respectively, which results from the difference between the density of spin-up and spin-down electrons and corresponds to the saturated magnetic moment, μ_{sat} , at $T = 0$, as shown Fig. 3. It appears that Fe_3B has the highest magnetic moment which leads to a shift in the Slater-Pauling curve [27]. These moments are smaller than the magnetic moments of pure bcc ferromagnetic iron which behaves as a weak ferromagnetic with a magnetic moment of 2.217 μB [28]. Indeed, when B atoms are inserted in Fe crystal, the volume concentration of metallic Fe–Fe bonds decreases and they are replaced by the newly formed covalent Fe–B and B–B.

The magnitude of the magnetic moment is strongly related to the volume. Thus, the values of equilibrium volume obtained in the magnetic state are larger than in NM state. A possible origin of this dependence is a magneto-volume effect [29]. Because the Pauli Exclusion Principle operates for parallel spins, the electron kinetic energy in the spin-polarized state is higher, and volume expansion relaxes the kinetic energy. Consequently, the magnetic (high-spin) state has a larger volume than the non-magnetic state [30]. However, the bulk modulus decreases from FeB to Fe_3B . Also due to the pressure effect, the bulk modulus has increased from 0 % to 47.7 % for FeB, from 0 % to 62 % for Fe_2B and from 0 % to 61.8 % for Fe_3B . In the NM state the bulk modulus B is in general larger

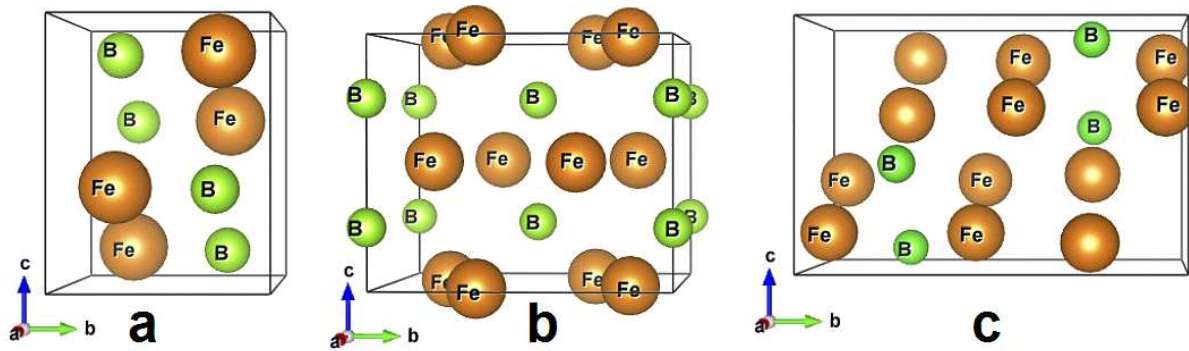


Fig. 1. Fe_xB structures: (a) FeB , (b) Fe_2B and (c) Fe_3B .

than in the magnetic state. The low value of bulk modulus in the magnetic state points out to a larger compressibility. This means that the system is “softer” when it is magnetically ordered and “harder” when it is not. The spin-polarization calculations are important to obtain the correct ground state properties of Fe_xB ferromagnetic compounds. The calculated magnetic moment as a function of pressure is presented in Fig. 2. Total DOS at the Fermi level for Fe_xB increases under pressure by 21 %, 50 % and 32.5 % for FeB , Fe_2B and Fe_3B , respectively (Fig. 3). This enhanced $N(E_f)$ is derived entirely from the Fe 3d states, with negligible contribution from the B 2p states. Following the above arguments we may predict that the appearance of superconductivity in Fe_xB under pressure is similar to the case of iron that undergoes a transition to superconducting phase above 30 GPa when it loses its magnetic moment [31]. It is easy to observe that the magnetic moment decreases with increasing pressure.

4. Elastic properties under pressure

It is well known that elastic properties reflect interatomic interactions and are related to some fundamental physical properties, such as thermal expansion, phonon spectra and equations of state [32]. The elastic constants of single crystalline Fe_xB compounds are presented in Table 1. Generally, the elastic constants C_{11} , C_{22} and C_{33} are

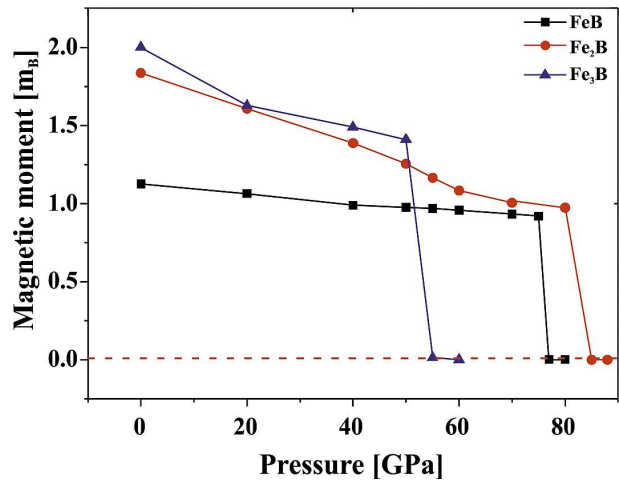


Fig. 2. Dependence of magnetic moment vs. pressure for Fe_xB [11].

very high, both at zero and critical pressure, which indicates high resistance to the axial compression in these directions. However, the magnitude orders in three axes are different. For orthorhombic FeB and Fe_3B , the order is $C_{33} > C_{22} > C_{11}$. For tetragonal Fe_2B the order is $C_{11} > C_{33}$. Since the tetragonal structure can be regarded as a special case of orthorhombic structure with an additional condition of $a = b$, the mechanical stability criteria can be represented in a uniform manner for orthorhombic structure [33]:

$$C_{ii} > 0 \quad (i = 1; 2; 3; 4; 5; 6) \quad (3)$$

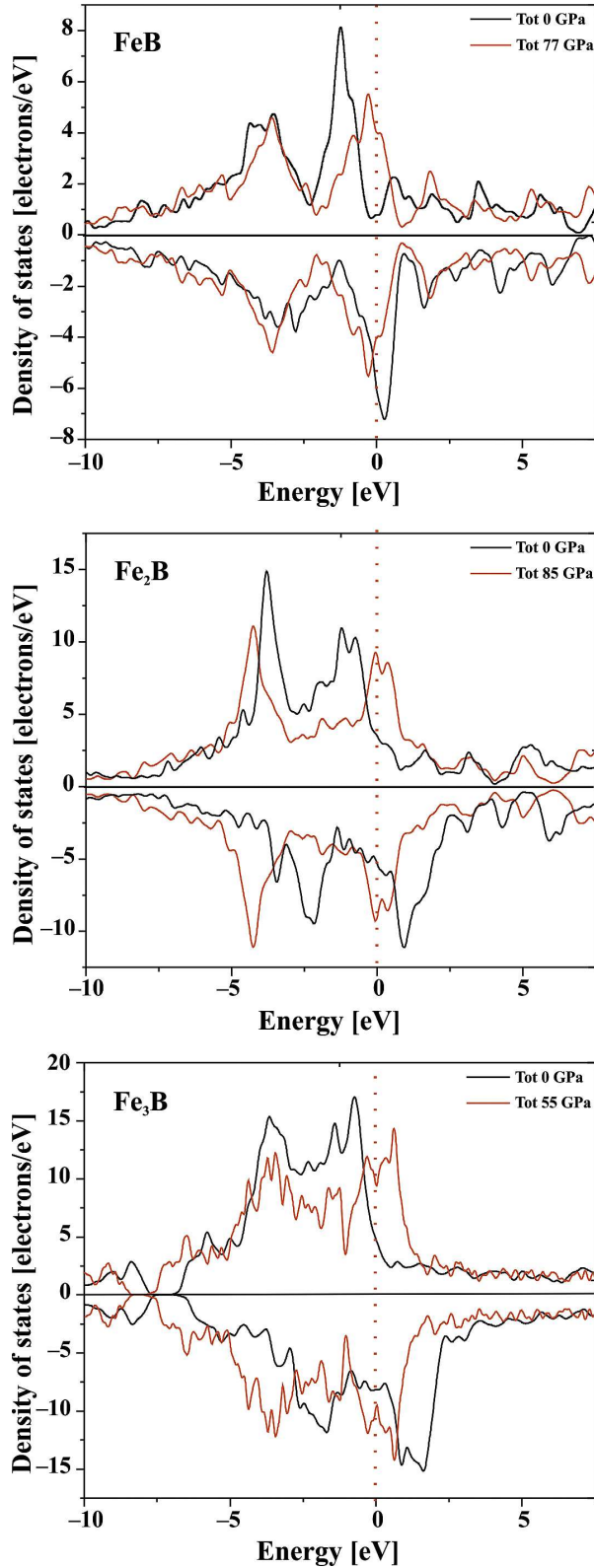


Fig. 3. The calculated total DOS with spin polarization and at critical pressure of Fe_xB .

$$\begin{aligned} C_{11} + C_{22} + C_{33} + 2(C_{12} + C_{13} + C_{23}) &> 0, \\ (C_{11} + C_{22} - 2C_{12}) > 0; (C_{11} + C_{33} - 2C_{13}) &> 0 \end{aligned} \quad (4)$$

$$(C_{22} + C_{33} - 2C_{23}) > 0 \quad (5)$$

On the other hand, the mechanical stability leads to restrictions on the elastic coefficients under isotropic pressure as follows:

$$\tilde{C}_{ii} = C_{ii} - P > 0, \quad (i = 1, 2, 3, 4, 5, 6) \quad (6)$$

$$(C_{11} + C_{22} - 2C_{12} - 4P) > 0 \quad (7)$$

For tetragonal structure the elastic constants under pressure P are related to those under zero pressure, as follows [34]:

$$\tilde{C}_{ij} = C_{ij} \quad (i = 1, 2, 3; j = 4, 5, 6) \quad (8)$$

$$\tilde{C}_{ii} = C_{ii} - P \quad (i = 1, 2, 3, 4, 5, 6) \quad (9)$$

$$\tilde{C}_{12} = C_{12} + P \quad (10)$$

$$\tilde{C}_{13} = C_{13} + P,$$

$$\tilde{C}_{23} = C_{23} + P,$$

$$\tilde{C}_{45} = C_{45},$$

$$\tilde{C}_{46} = C_{46} \quad (11)$$

$$\tilde{C}_{56} = C_{56} \quad (12)$$

The stability criteria of material under pressure are similar to those under zero pressure, just replacing C_{ij} with \tilde{C}_{ij} ($i = j = 1, 2, 3, 4, 5, 6$) [35]. As for Fe_2B in the tetragonal structure, there are six independent elastic constants, C_{11} , C_{12} , C_{13} , C_{33} , C_{44} , C_{66} , because $C_{22} = C_{11}$, $C_{23} = C_{13}$, $C_{44} = C_{55}$ as a result of the crystal symmetry. The single crystal elastic coefficients (C_{ij}) satisfy the stability criteria, which leads to the following restrictions on the elastic coefficients under isotropic pressure:

$$\tilde{C}_{ii} > 0, \quad (i = 1, 2, 3, \dots, 6), \quad \tilde{C}_{11} + \tilde{C}_{33} - 2\tilde{C}_{13} > 0 \quad (13)$$

$$2\tilde{C}_{11} + \tilde{C}_{33} + 2\tilde{C}_{12} + 4\tilde{C}_{13} > 0 \quad (14)$$

$$(\tilde{C}_{11} - \tilde{C}_{12}) > 0 \quad (15)$$

C_{ij} are the elements of elastic coefficient matrix. The arithmetic average of the Voigt and Reuss bounds is known as the Voigt-Reuss-Hill (VRH) average, which is regarded as the best estimate for the theoretical value of polycrystalline elastic modulus [11]:

$$G_H = (G_R + G_V)/2 \quad (16)$$

$$B_H = (B_R B_V)/2 \quad (17)$$

The Young's modulus and Poisson ratio can be computed from the formula [11]:

$$E = 9BG/(3B + G) \quad (18)$$

$$\nu = (3B - 2G)/(6B + 2G) \quad (19)$$

A larger B/G value (>1.75) for a solid indicates ductile behavior while a smaller B/G value (<1.75) usually means brittle material [36]. Similarly, Poisson ratio $\nu > 0.26$ relates to ductile compounds usually [36]. At both pressures studied here 0 GPa and the critical pressure, $B/G > 1.75$ and $\nu > 0.26$ is larger than 0.26 for FeB and Fe₃B (Table 3), which indicates that FeB and Fe₃B are ductile. The values of B/G and ν for Fe₂B are 1.52 and 0.23, respectively, at 0 GPa pressure which means that Fe₂B is brittle. In contrast, at critical pressure Fe₂B is ductile ($B/G = 2.48$, $\nu = 0.32$).

5. Elastic anisotropy

It is known that elastic anisotropy correlates with anisotropic plastic deformation and behavior of microcracks in material. Hence, it is important to study elastic anisotropy in intermetallics structures in order to further understand these properties and improve their mechanical durability. Most of crystals exhibit elastic anisotropy to some extent, and several criteria have been developed to describe it. The elastic anisotropy of a crystal can be characterized by the universal anisotropic index A^U and by the indexes describing the behavior in shear and compression (A_G and A_B). The universal elastic anisotropy index A^U and indexes A_G and A_B for a crystal with any symmetry may be proposed as follows [37, 38]:

$$A^U = 5 \frac{G_V}{G_R} + \frac{B_V}{B_R} - 6 \leq 0 \quad (20)$$

$$A_G = \frac{G_V - G_R}{G_V + G_R} \times 100 \quad (21)$$

$$A_B = \frac{B_V - B_R}{B_V + B_R} \times 100 \quad (22)$$

where B_V (G_V) and B_R (G_R) are the bulk modulus (shear modulus) in the Voigt and Reuss approximations respectively. $A^U = 0$ corresponds to the isotropy of the crystal. The deviation of A^U from zero defines the extent of single crystal anisotropy and accounts for both shear and bulk contribution, unlike all other existing anisotropy measures. Thus, A^U represents a universal measure to quantify a single crystal elastic anisotropy. $A_B = A_G = 0$ represents the elastic isotropic crystal, while $A_B = A_G = 1$ means the maximum elastic anisotropy [39]. From Table 2, it can be seen that the mechanical anisotropy of FeB is stronger than in other structures. In Fig. 5, we have outlined the projections of Young's modulus in (0 0 1), (0 1 0) and (1 0 0) crystal planes. We can clearly show that the anisotropy of FeB is stronger than in Fe₂B and Fe₃B in the three planes. The results are also in good agreement with the calculated anisotropic indexes in Table 2.

The shear anisotropic factors provide a measure of the degree of anisotropy in atomic bonding in different crystallographic planes. The shear anisotropic factor for an orthorhombic crystal can be measured by three factors (Zener ratios) [40–42]:

1. The shear anisotropic factor for the $\{1 0 0\}$ shear planes between $\langle 0 1 1 \rangle$ and $\langle 0 1 0 \rangle$ directions is defined as:
2. The anisotropic factor for the $\{0 1 0\}$ shear planes between $\langle 1 0 1 \rangle$ and $\langle 0 0 1 \rangle$ directions is:

$$A_2 = \frac{4C_{55}}{C_{22} + C_{33} - 2C_{23}} \quad (23)$$

and

Table 1. The calculated full set of elastic constants of Fe_xB (GPa) [11].

Species	Elastic constants								
	C_{11}	C_{22}	C_{33}	C_{12}	C_{13}	C_{23}	C_{44}	C_{55}	C_{66}
FeB (0 GPa)	389.82	438.36	557.07	286.85	183.12	239.76	218.8	132.25	212.01
	373.7 ^a	434.1 ^a	503.4 ^a	246 ^a	184.4 ^a	209.1 ^a	207.4 ^a	117.7 ^a	193.7 ^a
FeB (77 GPa)	718.5	752.6	993.9	583.2	350.1	492.4	296.4	243.3	354.4
Fe ₂ B (0 GPa)	459.7		426.3	165.6	132.3		162.6		173.7
	413 ^b		389 ^b	154 ^b	132 ^b		148 ^b		157 ^b
Fe ₂ B (85 GPa)	1010.4		839	541.3	488.4		298		288.4
Fe ₃ B (0 GPa)	281.7	337.5	354	126.7	165.3	182.2	130.2	118.7	175.6
	263.3 ^a	302.7 ^a	318.4 ^a	133.5 ^a	162.8 ^a	178.6 ^a	110.2 ^a	101.2 ^a	158.7 ^a
Fe ₃ B (55 GPa)	694	826	778.5	485.5	444.75	403.6	193.1	195.8	307.7

^a[46], ^b[47]

Table 2. Polycrystalline elastic properties and anisotropy factors of Fe-B system.

Species	B_V	B_R	G_V	G_R	A_1	A_2	A_3	A_u	A_G	A_B
FeB (0 GPa)	308.37	302.80	155.66	125.47	1.57	1.04	3.38	1.22	10.74	0.91
	287.8 ^a	284.6 ^a	148.5 ^a	130.9 ^a	1.63 ^a	0.91 ^a	2.45 ^a	0.68 ^a	5.85 ^a	0.62 ^a
FeB (77 GPa)	621.69	612.49	260.17	190.38	1.17	1.28	4.65	1.85	15.49	0.75
Fe ₂ B (0 GPa)	245.11	244.07	160.82	160.21	1.18	1.18	0.26	0.02	0.19	0.21
	222.7 ^a	221.8 ^a	144.4 ^a	143.6 ^a	1.07 ^a	1.07 ^a	1.23 ^a	0.03 ^a	0.28 ^a	0.20 ^a
Fe ₂ B (85 GPa)	655.09	646.32	266.31	260.30	1.23	1.23	0.34	0.13	1.14	0.67
Fe ₃ B (0 GPa)	213.51	207.55	118.15	107.50	1.71	1.45	1.92	0.52	4.72	1.41
	203.8 ^a	199.5 ^a	101.3 ^a	90.6 ^a	1.72 ^a	1.53 ^a	2.12 ^a	0.61 ^a	5.58 ^a	1.07 ^a
Fe ₃ B (55 GPa)	551.81	550.01	203.62	186.77	1.33	0.98	2.24	0.45	4.31	0.16

^a[46]Table 3. The calculated bulk, Young's (E) and shear modulus (G) of Fe_xB (under 0 and critical pressure, in GPa), Poisson's ratio (ν) and B/G ratio along with other available values.

Species	B	E	G	ν	B/G
FeB (0 GPa)	305.6	365.7	140.6	0.30	2.174
	286.6 ^a	360.5 ^a	139.7 ^a	0.29 ^a	2.05 ^a
FeB (77 GPa)	617.1	567.5	225.3	0.34	2.76
Fe ₂ B (0 GPa)	244.6	395.2	160.5	0.23	1.52
	222.3 ^a	355 ^a	144 ^a	0.23 ^a	1.54 ^a
Fe ₂ B (85 GPa)	651	695.4	263	0.32	2.48
Fe ₃ B (0 GPa)	210	285.3	112	0.27	1.875
	201.6 ^a	248.5 ^a	96 ^a	0.3 ^a	2.1 ^a
Fe ₃ B (55 GPa)	551	524	195.2	0.34	2.82

^a[46]

3. The anisotropic factor for the $\{0\ 0\ 1\}$ shear planes between $\langle 1\ 1\ 0 \rangle$ and $\langle 0\ 1\ 0 \rangle$ directions is:

$$A_3 = \frac{4C_{66}}{C_{11} + C_{22} - 2C_{12}} \quad (24)$$

The calculated values of anisotropic factors for iron borides are shown in Table 2. For an isotropic crystal, all three factors must be one, while any value smaller or greater than one is a measure of degree of elastic anisotropy possessed by the crystal. Our results thus indicate a very large shear anisotropy on the $(1\ 0\ 0)$ and $(0\ 0\ 1)$ planes of FeB and Fe₃B due to the anomalously high C_{44} and C_{66} relatively to C_{55} . Thus, for Fe₂B the large shear anisotropy is on the $(0\ 0\ 1)$ plane due to high C_{44} compared to C_{66} .

Taking also into account the strength characteristics of the studied compounds, which have low values of G/B ratio (0.46 for FeB, 0.66 for Fe₂B and 0.53 for Fe₃B), the ductility of the iron borides is a very important advantage and therefore they are intrinsically brittle.

The spin polarization and pressure increase the anisotropic factors A_1 by 25 % and 22 % for FeB and Fe₃B, respectively, and A_2 by 32 % for Fe₃B, but reduce the anisotropic factors A_3 by 37 % and 17 % for FeB and Fe₃B, and A_2 by 23 % for FeB, which means that the direction of easy axis of magnetization is $\langle 1\ 0\ 0 \rangle$ for FeB ($C_{11} < C_{22} < C_{33}$) and the hard axes directions are $\langle 1\ 0\ 0 \rangle$ and $\langle 0\ 1\ 0 \rangle$ (Fig. 6a and Fig. 6d). For Fe₃B the easy axis direction is $\langle 1\ 0\ 0 \rangle$ ($C_{11} < C_{22} < C_{33}$) and the hard axes directions are $\langle 0\ 1\ 0 \rangle$, $\langle 0\ 0\ 1 \rangle$ (Fig. 6c and Fig. 6f).

The anisotropy is only dependent on crystal symmetry. The structure of the crystal has been changed under spin polarized moment which varied a, b and c. Therefore, the elastic anisotropy is different because of the variations of the elastic constants with magnetic moment.

The elastic anisotropy of a tetragonal crystal can be measured by two shear anisotropy factors (Zener ratios) [43]:

$$A_1 = \frac{2C_{66}}{C_{11} - C_{12}} = A_2 \quad (25)$$

$$A_3 = \frac{C_{44}}{C_{11} + C_{33} - 2C_{13}} \quad (26)$$

$$(A^{\uparrow u} \cong 0)$$

Fe₂B has very low anisotropy.

The spin polarization has reduced the anisotropic factors A_1 and A_3 by 4 % and 30 % for Fe₂B, which means that the direction of easy axis of magnetization is $\langle 0\ 0\ 1 \rangle$ ($C_{33} < C_{11}$) and the directions of hard axes of magnetizations are $\langle 1\ 0\ 0 \rangle$, $\langle 0\ 1\ 0 \rangle$ ($(C_{11} = C_{22}) > C_{33}$).

The simplest way to illustrate the anisotropy of mechanical moduli is to plot them in the three-dimensional space as a function of direction. Here, we have plotted the bulk modulus (B) and Young's modulus (E) in different directions using spherical coordinates. For orthorhombic and tetragonal crystal class, the directional dependence of bulk modulus (B) or Young's modulus (E) can be written as:

For an orthorhombic system [44]:

$$\frac{1}{B} = (S_{11} + S_{12} + S_{13})l_1^2 + (S_{12} + S_{22} + S_{23})l_2^2 + (S_{13} + S_{23} + S_{33})l_3^2 \quad (27)$$

$$\frac{1}{E} = (S_{11} + S_{22} + S_{33})l_1^4 + (2S_{12} + S_{66})l_1^2l_2^2 + (2S_{23} + S_{44})l_2^3l_3^2 + (2S_{13} + S_{55})l_1^2l_3^2 \quad (28)$$

For a tetragonal system [44, 45]:

$$\frac{1}{E} = S_{11}(l_1^4 + l_1^4) + (2S_{13} + S_{44})(l_1^2l_3^2 + l_2^2l_3^2) + S_{33}l_3^4 + (2S_{12} + S_{66})l_1^2l_2^2 \quad (29)$$

$$\frac{1}{B} = (S_{11} + S_{12} + S_{13})(l_1^2l_2^2) - (2S_{13} - S_{33})l_3^2 \quad (30)$$

In the equations above, S_{ij} represents the compliance matrix and l_1 , l_2 and l_3 are the direction cosines, which are given as $l_1 = \sin\theta \cos\varphi$, $l_2 = \sin\theta \sin\varphi$ and $l_3 = \cos\theta$ in the spherical coordinates. The surface constructions of bulk and Young's modulus of FeB, Fe₂B and Fe₃B compounds are shown in Fig. 4 and Fig. 6. The surface constructions of the bulk and Young's moduli are

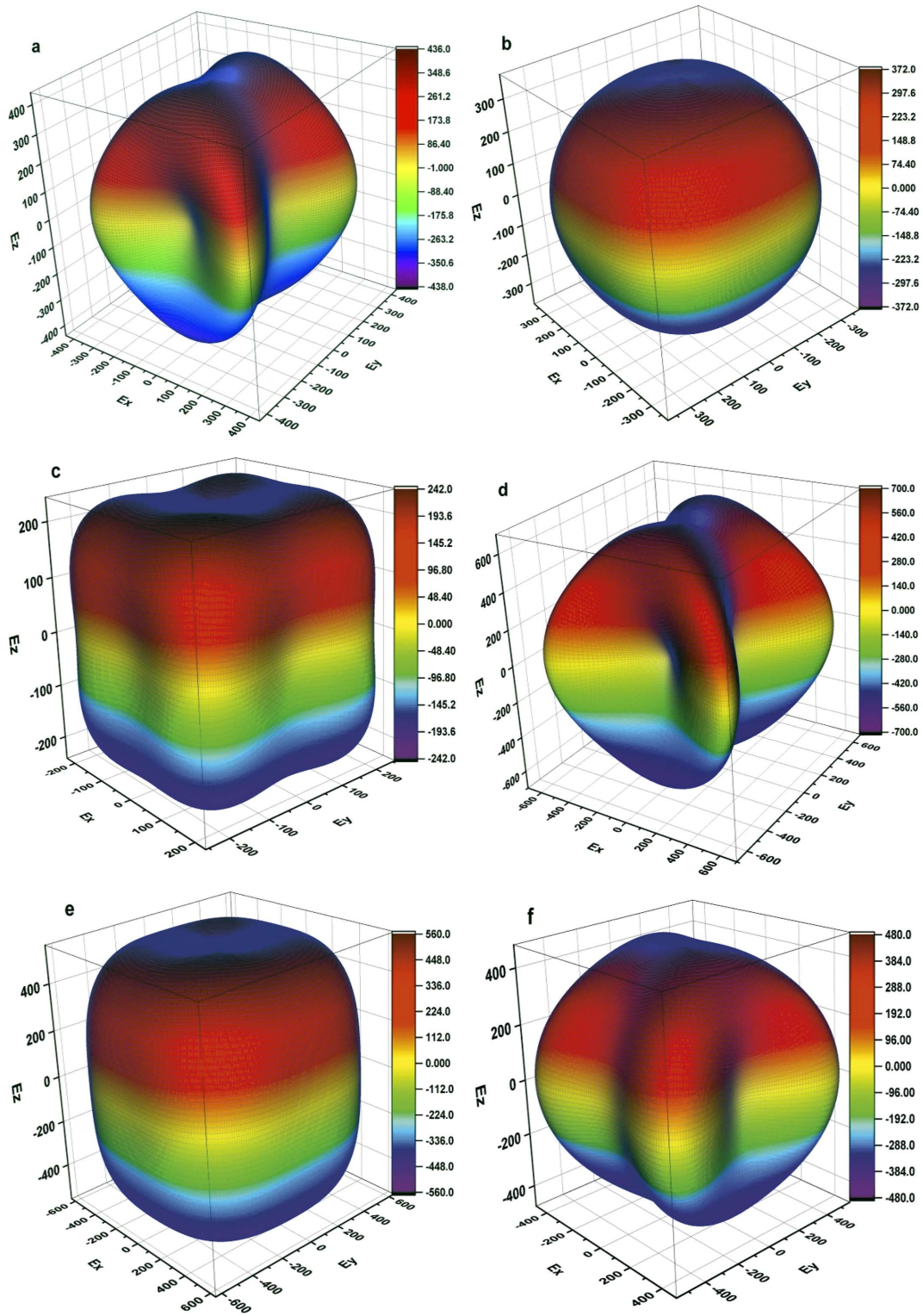


Fig. 4. Illustration of directional dependence of Young's modulus of Fe-B compounds: the left panel at 0 GPa pressure (a) FeB, (b) Fe_2B and (c) Fe_3B , and the right panel at critical pressure (d) FeB 77 GPa, (e) Fe_2B 85 GPa and (f) Fe_3B 55 GPa.

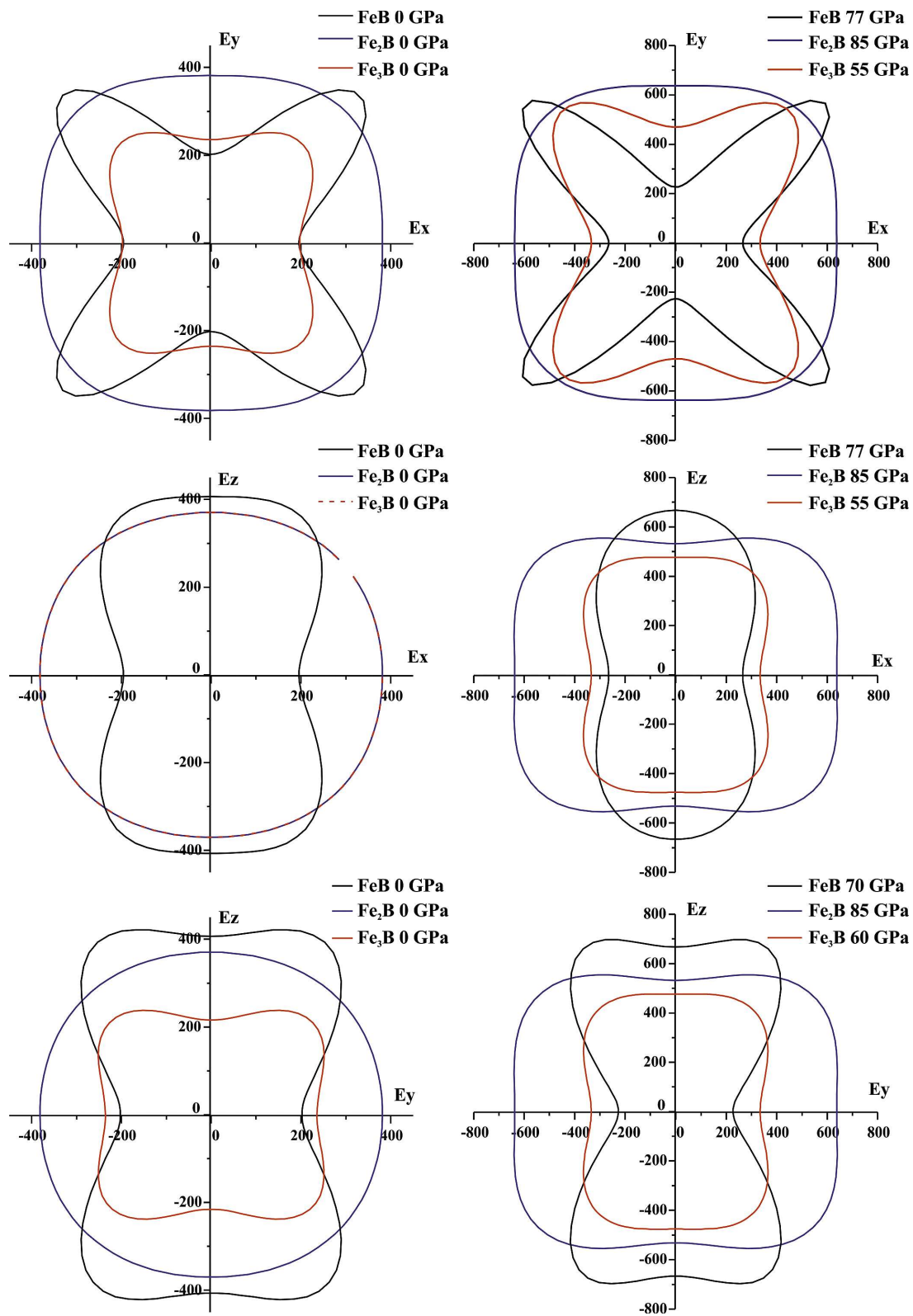


Fig. 5. Projections of Young modulus for Fe_xB compounds.

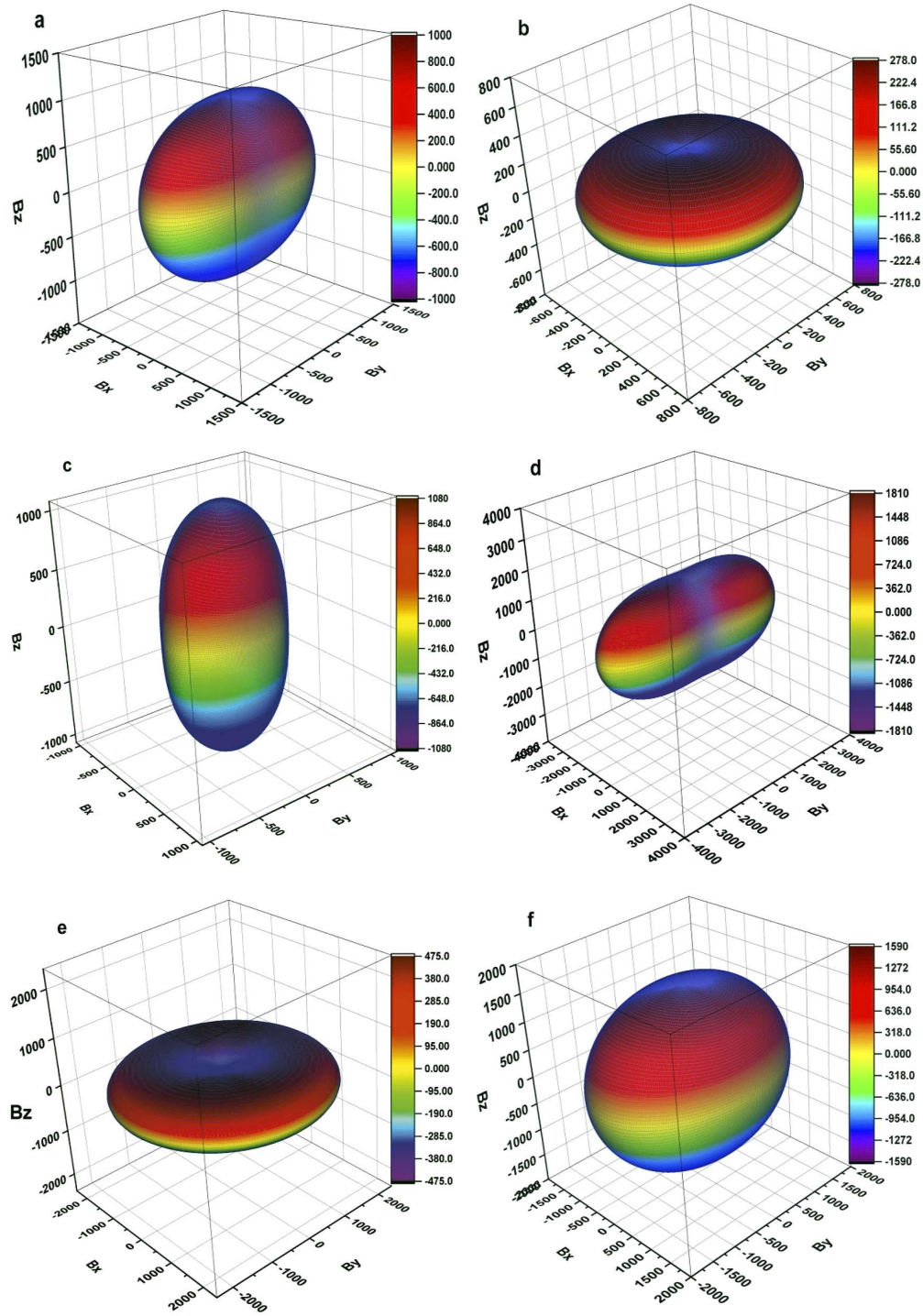


Fig. 6. Illustration of directional dependence of bulk modulus of Fe-B compounds: Left panel at 0 GPa pressure (a) FeB, (b) Fe₂B and (c) Fe₃B, and right panel at critical pressure (d) FeB 77 GPa, (e) Fe₂B 85 GPa and (f) Fe₃B 55 GPa.

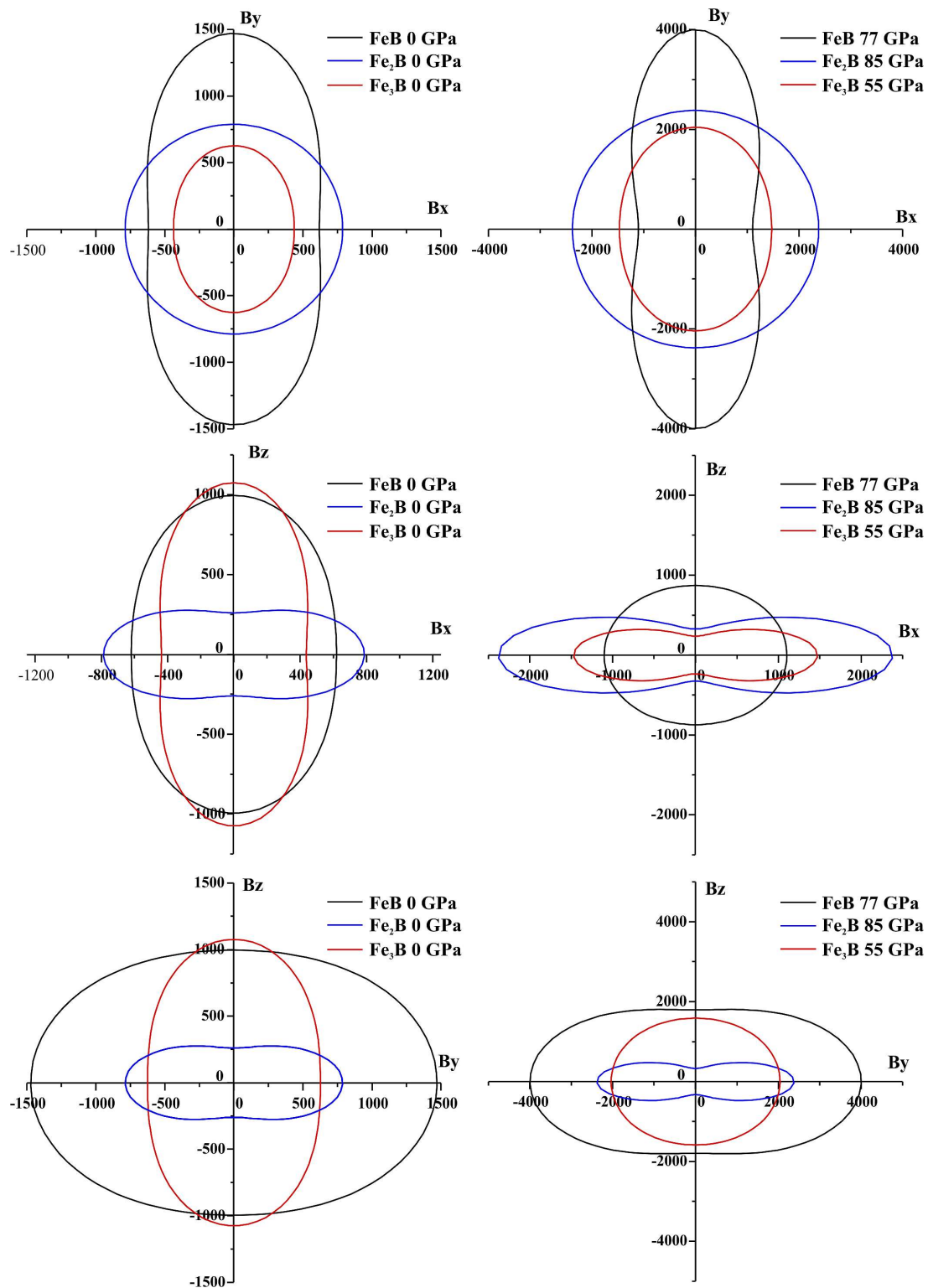


Fig. 7. Projections of bulk modulus for Fe_xB compounds.

similar to each other. The anisotropy of Young's modulus shows strong directional dependence in three crystal planes, (0 0 1), (1 0 0) and (0 1 0), for FeB structure. The projections of the mechanical moduli are plotted in Fig. 5 and Fig. 7. The results indicate that for Fe_2B the contours of bulk modulus at (0 0 1) crystal plane is spherical, implying that the bulk modulus of this phase is nearly isotropic. In the same way, the Young's modulus shows an isotropy at (0 0 1), (1 0 0) and (0 1 0) planes.

6. Conclusions

We have investigated the anisotropic elastic properties of Fe–B compounds with the help of first-principles calculations at two pressures: 0 GPa and at a critical pressure for each compound. The calculated elastic constants of all compounds clearly indicate that they are mechanically stable. Bulk modulus, shear modulus, Young's modulus and Poisson ratio have also been calculated and discussed. Disappearance of ferromagnetic order decreases the volume of the unit cell and increases the bulk modulus and also makes the solid harder. The calculated values of B/G and ν indicate that Fe_2B is ductile while FeB and Fe_3B are brittle. The degree of the elastic anisotropy for the considered Fe–B compounds follows the order $FeB > Fe_3B > Fe_2B$. We have predicted the easy and hard axes of magnetization for three compounds.

References

- [1] MATUSCHKA GRAF VON A., *Boronizing*, Hanser, Philadelphia, 1980.
- [2] CHATTERJEE-FISCHER R., *Boriding and Diffusion Metallizing*, in: SUDARSHAN T.S. (Ed.), *Surface Modification Technologies. An Engineer's Guide*, Marcel Dekker, New York, 1989, p. 567.
- [3] GOLDSCHMIDT H.J., *Interstitial Alloys*, Springer, New York, 2013.
- [4] ALLAOUI O., BOUAOUADJA N., SAINDERNAN G., *Surf. Coat. Technol.*, 201 (2006), 3475.
- [5] BATTEZZATI L., ANTONIONE C., BARICCO M., *J. Alloy. Compd.*, 247 (1997), 164.
- [6] HUANG Z., MA S., XING J., WANG B., *J. Alloy. Compd.*, 582 (2014), 196.
- [7] ZHAO M., FENG Y., JIAO L., YUAN H., ZHOU X., JANG M.B., *Int. J. Hydrogen. Energ.*, 32 (2007), 3915.
- [8] ZHANG Y.H., DONG X.P., WANG G.Q., GUO S.H., REN J.Y., WANG X.L., *T. Nonferr. Metal. Soc.*, 16 (2006), 800.
- [9] ZHANG Y.H., DONG X.P., WANG G.Q., GUO S.H., REN J.Y., WANG X.L., *J. Alloy. Compd.*, 417 (2006), 224.
- [10] MENESES-AMADOR A., CAMPOS-SILVA I., MARTINEZ-TRINIDAD J., PANIER S., FIGUEROA-LÓPEZ U., TORRES-HERNÁNDEZ A., *Surf. Coat. Technol.*, 215 (2013), 285.
- [11] GUEDDOUH A., BENTRIA B., LEFKAIER I., *J. Magn. Magn. Mater.*, 406 (2016), 192.
- [12] LU L., BANSMANN J., MEIWE-SBROER K., *J. Phys. Condens. Mat.*, 10 (1998), 2873.
- [13] BROWN P., COX J., *Philos. Mag.*, 23 (1971), 705.
- [14] PERKINS R., BROWN P., *J. Phys. F-Metal. Phys.*, 4 (1974), 906.
- [15] JOYNER D.J., JOHNSON, O., HERCULES, D. M., *J. Am. Chem. Soc.*, 102 (1980), 1910.
- [16] LI G., WANG D., *J. Phys. Condens. Mat.*, 1 (1989), 1799.
- [17] KOHN W., *Rev. Mod. Phys.*, 71 (1999), 1253.
- [18] MEDEIROS S., ALBUQUERQUE E., MAIA F., CAETANO E., FREIRE V., *Chem. Phys. Lett.*, 435 (2007), 59.
- [19] XU Y., WANG H., *J. Alloy. Compd.*, 457 (2008), 239.
- [20] WANG Y., BURKE K., PERDEW, J., *Phys. Rev. B*, 54 (1996), 16533.
- [21] MONKHORST H.J., PACK J.D., *Phys. Rev. B*, 13 (1976), 5188.
- [22] MURPHY K.A., HERSHKOWITZ N., *Phys. Rev. B*, 7 (1973), 23.
- [23] MOHN P., SCHWARZ K., MATAR S., DEMAZEAU G., *Phys. Rev. B*, 45 (1992), 4000.
- [24] MOHN P., SCHWARZ K., WAGNER D., *Phys. Rev. B*, 43 (1991), 3318.
- [25] DOS SANTOS A.V., KUHNEN C., *J. Solid State Chem.*, 182 (2009), 3183.
- [26] CHING W., XU Y.N., HARMON B., YE J., LEUNG T., *Phys. Rev. B*, 42 (1990), 4460.
- [27] BOZORT R.M., *Ferromagnetism*, Van Nostrand Company, New York, 1951, vol. 849.
- [28] KITTEL C., *Introduction to solid state physics*, John Wiley & Sons, California, 2005.
- [29] CHIKAZUMI S., GRAHAM C.D., *Physics of Ferromagnetism*, Oxford University Press, Oxford, 2009.
- [30] EGAMI T., FINE B., SINGH D., PARSHALL D., DE LA CRUZ C., DAI P., *Physica C*, 470 (2010), S294.
- [31] SHIMIZU K., KIMURA T., FUROMOTO S., TAKEDA K., KONTANI K., ONUKI Y., AMAYA K., *Nature*, 412 (2001), 316.
- [32] YANG C., ZHOU Z., LI J., YANG X., QIN W., JIANG R., GUO N., WANG Y., SUN C., *Nanoscale*, 4 (2012), 1304.
- [33] BECKSTEIN O., KLEPEIS J., HART G., PANKRATOV O., *Phys. Rev. B*, 63 (2001), 134112.
- [34] PATIL S., KHARE S., TUTTLE B., BORDING J., KODAMBAKA S., *Phys. Rev. B*, 73 (2006), 104118.

- [35] ZHOU Z., JOOS B., *Phys. Rev. B*, 54 (1996), 3841.
- [36] LEWANDOWSKI J., WANG W., GREER A., *Philos. Mag. Lett.*, 85 (2005), 77.
- [37] LIU Y., HU W.C., LI D.J., LI K., JIN H.L., XU Y.X., XU C.S., ZENG X.Q., *Comp. Mater. Sci.*, 97 (2015), 75.
- [38] ALI K., ARYA A., GHOSH P., DEY G., *Comp. Mater. Sci.*, 112 (2016), 52.
- [39] OZISIK H., COLAKOGLU K., DELIGOZ E., *Comp. Mater. Sci.*, 51 (2012), 83.
- [40] RANGANATHAN S.I., OSTOJA-STARZEWSKI M., *Phys. Rev. Lett.*, 101 (2008), 055504.
- [41] XIAO B., FENG J., ZHOU C., JIANG Y., ZHOU R., *J. Appl. Phys.*, 109 (2011), 023507.
- [42] FENG J., XIAO B., ZHOU R., PAN W., CLARKE D.R., *Acta Mater.*, 60 (2012), 3380.
- [43] GAO X., JIANG Y., ZHOU R., FENG J., *J. Alloy. Compd.*, 587 (2014), 819.
- [44] DUAN Y., SUN Y., PENG M., ZHOU S., *J. Alloy. Compd.*, 595 (2014), 14.
- [45] NYE J.F., *Physical Properties of Crystals: Their Representation by Tensors and Matrices*, Oxford University Press, Oxford, 1985.
- [46] LI L.H., WANG W.L., HU L., WEI B.B., *Intermetallics*, 46 (2014), 211.
- [47] BIALON A., HAMMERSCHMIDT T., DRAUTZ R., SHAH S., MARGINE E., KOLMOGOROV A., *Appl. Phys. Lett.*, 98 (2011), 8.

Received 2015-07-23

Accepted 2016-06-23



The effects of magnetic moment collapse under high pressure, on physical properties in mono-borides TMB (TM = Mn, Fe): a first-principles

A. Gueddouh

To cite this article: A. Gueddouh (2017): The effects of magnetic moment collapse under high pressure, on physical properties in mono-borides TMB (TM = Mn, Fe): a first-principles , Phase Transitions, DOI: [10.1080/01411594.2017.1302088](https://doi.org/10.1080/01411594.2017.1302088)

To link to this article: <http://dx.doi.org/10.1080/01411594.2017.1302088>



Published online: 27 Mar 2017.



Submit your article to this journal [↗](#)



Article views: 5



View related articles [↗](#)



View Crossmark data [↗](#)



The effects of magnetic moment collapse under high pressure, on physical properties in mono-borides TMB (TM = Mn, Fe): a first-principles

A. Gueddouh ^{a,b}

^aLaboratoire de Physique des Matériaux, Université Amar Telidji de Laghouat, Laghouat, Algeria ; ^bDépartement de Physique, Faculté des Sciences, Université A.B. Belkaid Tlemcen, Tlemcen, Algeria

ABSTRACT

In this paper, spin polarization and pressure effects on the structure, magnetic and anisotropic elastic properties of the 3d transition-metal mono-borides TMB (TM = Mn, Fe) have been investigated by using generalized gradient approximation within the framework of density functional theory. It seems that manganese in MnB carries a higher magnetic moment (1.83 μ_B) than iron in FeB (1.12 μ_B). Applied pressure ranges from 0 to 150 GPa, these ferromagnetic compounds show at a certain pressure (143 GPa for MnB and 77 GPa for FeB) a pronounced abrupt collapse of the magnetic moment (first-order quantum phase transitions). Furthermore, elastic properties, including bulk, shear and Young moduli as well as the Poisson ratio are obtained by Voigt–Reuss–Hill approximation. By the elastic stability criteria, it is predicted that MnB and FeB are stable up to the selected pressures. In both cases, mechanical anisotropies are discussed by calculating different anisotropic indexes and factors. The three-dimensional surfaces and planar contours of Young, and bulk moduli of compounds are plotted, at several crystallographic planes ((100), (010) and (001)) to reveal their elastic anisotropy.

ARTICLE HISTORY

Received 10 August 2016
Accepted 17 February 2017

KEYWORDS

Transition-metal borides;
DFT; magnetic moment
collapse; pressure;
anisotropic elastic

1. Introduction

Boride layers offer excellent surface properties in terms of high hardness, increase the wear and corrosion resistance and stability of mechanical properties at high [1–3] temperature. To understand borides as protective coatings on steel surfaces, especially mechanical properties needed the knowledge of their elastic constants, polycrystalline elastic moduli, and anisotropic elastic properties. Furthermore, the presence and nature of unconventional magnetic phases of mono-borides may be clarified by tuning them systematically with the help of an external parameter such as pressure.

Studied materials under pressure are able to provide much information on their behavior. For example, magnetic collapse, either being transitioned from ferromagnetic state (FM) to non-magnetic state (NM), or from a high-spin state to low spin state, is a widely observed phenomenon. Experiments, such as hyperfine field measurements [4], X-ray magnetic dichroism [5], nuclear forward scattering [6], may have a direct or indirect access to this phenomenon. Theoretical calculations based on density functional theory (DFT) are generally adopted to explain and predict it [7]. It was observed that the magnetic moment of MnB and FeB slowly decreases by applying pressure and

abruptly drops to zero at a critical pressure (143 GPa for MnB and 77 GPa for FeB) indicating the crystal transition from the ferromagnetic to non-magnetic state (first-order quantum phase transitions (QPT)). This is accompanied by an abrupt change in the lattice parameters, volume and elastic constants. This character of magnetic collapse is perhaps the earliest prediction of what may be called a ‘novel’ phase of magnetic metals near a QPT.

The focus of the present paper is the study of the structure, magnetic and anisotropic elastic properties of MnB and FeB compounds under pressure.

The specific feature of this investigation is the abrupt collapses of magnetic moment at a critical pressure, which resulted in the transition from ferromagnetic (FM) to non-magnetic states (NM). In these two states (FM and NM), structural and mechanical anisotropies are discussed by calculating different anisotropic indexes and factors. Thus, I have plotted the three-dimensional (3D) surfaces and planar contours of Young and bulk moduli of TMB (TM = Mn, Fe) compounds at several crystallographic planes, ((100), (010) and (001)) to reveal their elastic anisotropy.

I attempt to prove that all previous properties change strongly with increasing pressure.

I hope my study could provide a useful guidance for future works on the mono-borides TMB compounds.

2. Structural aspects and calculation methods

Both MnB and FeB crystallize with four formula units in the space group Pnma in the orthorhombic structure FeB-type. One characteristic of these structures is the presence of strong atomic interaction between non-metallic atoms in continuous zig-zag like chains [8] (Figure 1). Total energy calculations were performed within DFT [9] using CASTEP code [10] for the whole study, which uses the plane wave expansion method in reciprocal space [11]. The ultra-soft Vanderbilt pseudo-potentials were employed to represent the electrostatic interactions between valence electrons and ionic cores [12] which were used with the following valence electronic configuration’s Mn: $3d^5 4s^2$, Fe: $3d^6 4s^2$ and B: $2s^2 2p^1$. Generalized gradient approximation PBE-GGA was used for exchange–correlation energy calculations [13]. The kinetic energy cut-off value was selected as 500 eV, which was sufficient to obtain the reliable results.

Total energies were evaluated in the first irreducible Brillouin zone with the following MonkHorst–Pack grids [14]: ($8 \times 10 \times 12$) for all compounds. It is known that the ground states of MnB and FeB compounds are ferromagnetic [15–17].

Structure and anisotropic elastic properties are calculated for the both cases FM and NM. The convergence criteria of total energy and structure optimization were set to find quality with the energy tolerance of 10^{-6} eV/atom. BFGS (Broydene–Fletcher–Goldarbe–Shanno) optimization method was performed to get the equilibrium crystal structures of TMB with maximum atom displacement and force set to 0.002 Å and 10^{-4} eV/Å.

The cohesive energy (E_{coh}) of a material (a useful fundamental property) is a measure of the relative binding forces. The stability of these compounds can be evaluated by calculating two energy parameters, cohesive energy E_{coh} and formation energy E_f defined as follows:

$$E_{\text{coh}}(\text{TMB}) = \frac{E_{\text{total}}(\text{TMB, Cell}) - nE_{\text{iso}}(\text{TM}) - nE_{\text{iso}}(\text{B})}{n} \quad (1)$$

$$E_f(\text{TMB}) = E_{\text{coh}}(\text{TMB}) - E_{\text{coh}}(\text{TM}) - E_{\text{coh}}(\text{B}) \quad (2)$$

where $E_{\text{coh}}(\text{TMB})$ is the cohesive energy of TMB per unit formula; $E_f(\text{TMB})$ is its formation energy; $E_{\text{coh}}(\text{TM})$ is the cohesive energy of the transition-metal element per atom; $E_{\text{total}}(\text{TMB, Cell})$ is the total calculated energy of TMB per conventional unit cell; $E_{\text{iso}}(\text{TM})$ is the total energy of an isolated TM atom and finally n refers to the number of unit formula TMB in the conventional cell. The

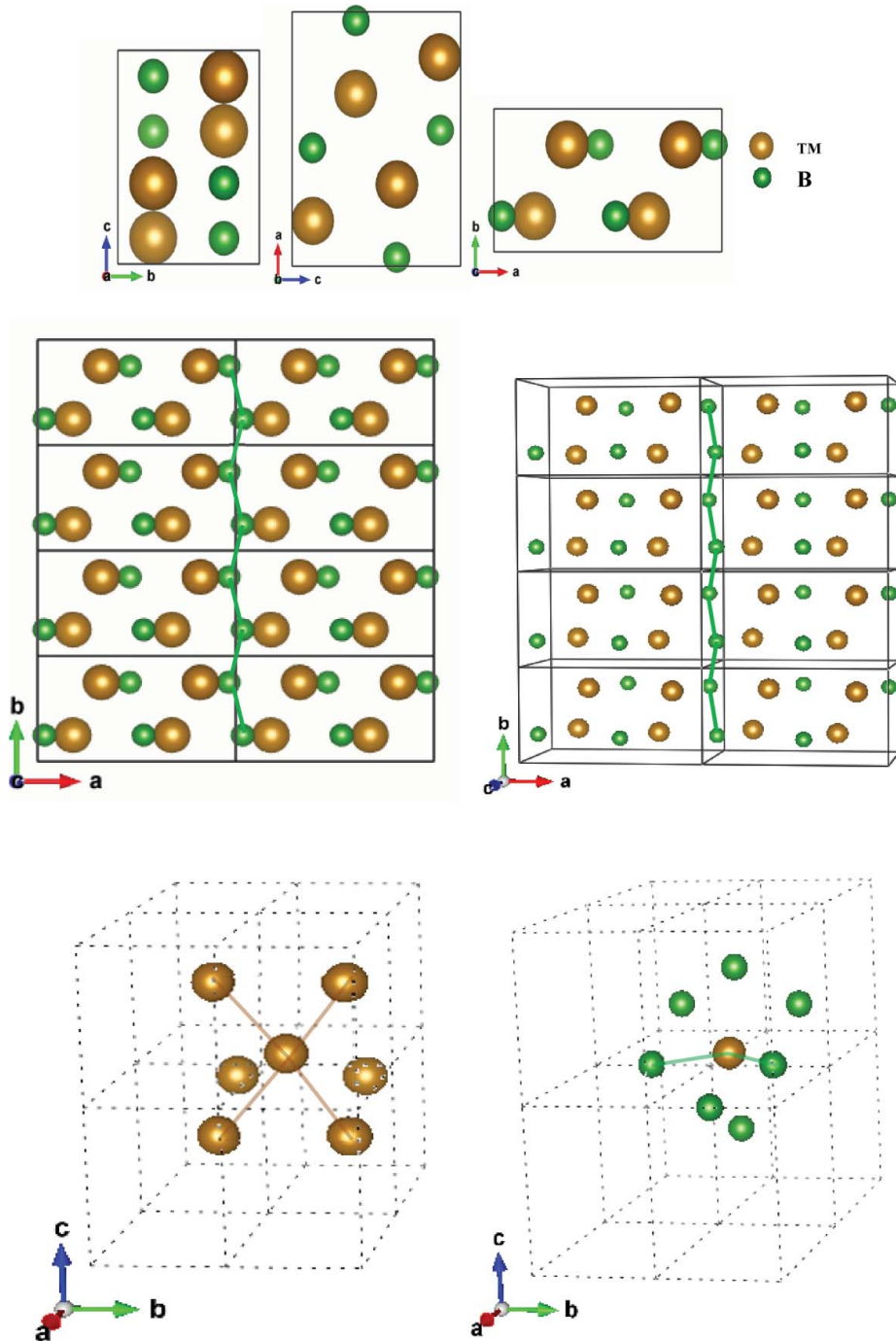


Figure 1. Crystal structure of TMB projecting onto the (100), (010) and (001) planes, the metal transition; boron atoms environment and for a section perpendicular to the plane (010) showing the zig-zag B–B chain.

calculation method for E_{coh} (TMB) can also be used to evaluate the cohesive energy of pure elements B and TM. Equations (1) and (2) require negative values of E_{coh} (TMB) and E_f (TMB) to refer to a thermodynamically stable structure. The crystal structures of TMB studied in this paper are built based on the experimental results.

3. Results and discussion

3.1. Structural properties and stability

The calculated lattice parameters, unit cell volumes, bulk modulus, cohesive and the formation energy for pure transition-metals TM, boron and TMB, with available literature data (experimental and theoretical), are shown in Tables 1 and 2. These results indicate that the calculated structure parameters are in good agreement with the experimental values. At equilibrium spin polarization, calculations show that MnB and FeB compounds carry magnetic moment with the values of 1.83 and 1.12 μ_B , respectively. The calculated value of cohesive energy is -17.01 eV for MnB and -13.153 eV per atom for FeB. Furthermore, the formation energies are -1.35 and -1.207 eV for MnB and FeB, respectively, which indicated that both of these TMB compounds are stable.

3.2. Effect of pressure and magnetic moment on the structural properties

Usually, in order to induce some significant change in materials, high pressures are needed in the study of materials. By increasing the pressure, we can see (Figure 2) that the magnetic moment decreases as a linear regression and suddenly at a critical pressure an abrupt collapse of magnetic moment (first-order QPT) occur; this critical pressure is estimated by 143 GPa for MnB and 77 GPa for FeB. This definition of critical pressure (P_c) was first employed by Mohn et al. in their work on magneto-elastic anomalies in Fe–Ni invar alloys [22] and NiFe₃N and PdFe₃N nitrides [23]. This definition is also used for the study of magnetic transition of intermetallic bilayers and substituted iron nitrides [24]. It is obvious that the volume (energy) decreases (increases) with the increase of pressure (Figure 3). At a critical pressure for both MnB and FeB compounds (Figure 3), there is a discontinuous change in slope for the structure parameters. These abrupt changes are linked with the magnetic state transition (FM to NM); these changes are even so-called isostructural phase transition [25]. In Figure 3, all the sudden changes of parameters are due to the pronounced abrupt collapse of the magnetic moment (first-order QPT) from FM to NM state, which depends on the magneto-volume (magneto-elastic) effect [26].

3.3. Density of states under pressure

The calculated magnetic moments of these compounds, at 0 GPa, are in good agreement with theoretical and experimental values. The magnetic moments values 1.83 and 1.12 μ_B for MnB and FeB comes from the difference between the total density of spin-up and spin-down electrons d of Mn and Fe, as shown in Figure 4. In the figure, the density of d electrons in the majority and minority bands are looking like the total DOS of MnB and FeB. As the Fermi energy is pinned above the pure d states, both compounds behave as strong ferromagnets. Indeed, when B atoms are inserted in TM

Table 1. The calculated ground state properties of pure elements, Mn, Fe and B. Experimental and theoretical (eV/f.u.), cohesive energy E_{coh} (eV/f.u.) and volume V (\AA^3).

Parameters	Mn	Fe	B
E_{iso}	-644.390	-859.821 (-855.913) ^a	-70.501 (-70.492) ^a
E_{total}	-653.60	-865.315 (865.335) ^a	-76.953 (-76.875) ^a
E_{coh}	-9.21	-5.494 (-4.28) ^{exp} (-9.422) ^a	-6.452 (-6.383) ^a 8.652
Volume	11.09 (11.10) ^b	11.775 (11.82) ^{exp}	8.652 (8.763) ^a

^{exp}Ref. [18].

^aRef. [16].

^bRef. [19].

Table 2. The calculated ground state properties of TMB. Experimental and theoretical values are listed in parentheses. Total cell energy E_{total} (eV/f.u.), cell parameters (a, b, c , in Å), atomic positions of TM and B atoms (fractional coordinates), volume V (Å³), Bulk modulus (GPa), magnetic moment (μ_B /atom), cohesive energy E_{coh} (eV/f.u.) and formation energy E_f (eV/f.u.).

Parameters	MnB	FeB
E_{total}	-2927.6114	-3773.900
(a, b, c)	5.493, 2.992, 4.147 (5.459, 2.984, 4.126) ^a	5.317, 2.950, 3.964 (5.495, 2.946, 4.053) ^b
TM (x, y, z)	0.175 0.25 0.123	0.178 0.25 0.122
B (x, y, z)	0.033 0.25 0.614	0.0348 0.25 0.620
V	68.153	62.176
B	261.90	305.58, (286.6) ^a
μ_B /atom	1.93	1,126 (1.12) ^{exp}
E_{coh}	-17.01	-13.153
E_f	-1.35	-1.207

^{exp}Ref. [20]

^aRef. [21].

^bRef. [16].

crystals, the volume concentration of metallic TM–TM bonds decrease and are replaced by the newly formed covalent TM–B and B–B bonds.

The magnitude of the magnetic moment is strongly related to the volume. Thus, the values of the equilibrium volume obtained in the magnetic case are larger than in NM case. A possible origin of this dependence is the magneto-volume effect [26]. Because the Pauli Exclusion Principle operates in parallel spins, the electron kinetic energy of the spin-polarized state is higher, and volume expansion relaxes the kinetic energy. Consequently, the magnetic (high-spin) state has a larger volume than the non-magnetic state [8]. The bulk modulus was increased from 0% to 67.8% for MnB and from 0% to 50.5% for FeB. In the NM state, the bulk modulus B is systematically larger than in the FM state. The low value of bulk modulus in the magnetic case points to a larger compressibility. This means that the system is ‘softer’ when it is magnetically ordered and ‘harder’ when it is not. Total DOS at the Fermi level for both MnB and FeB increases under pressure by 48.8% and 21%, respectively (Figure 4). This enhanced $N(E_f)$ is derived entirely from the TM 3d states, with a negligible contribution from the B 2p states.

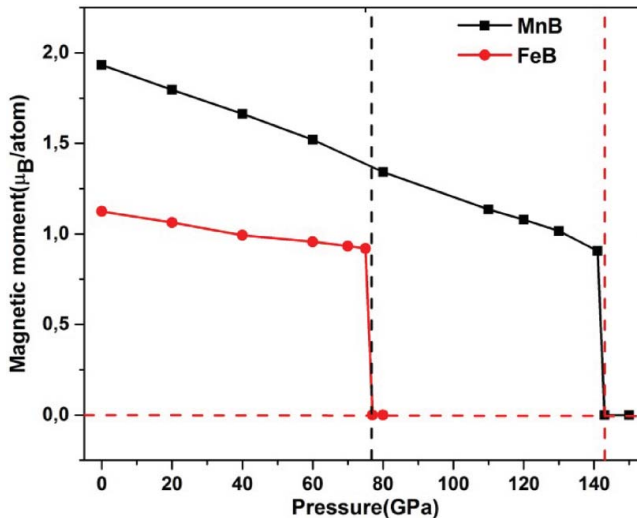


Figure 2. Dependence of magnetic moment vs. pressure.

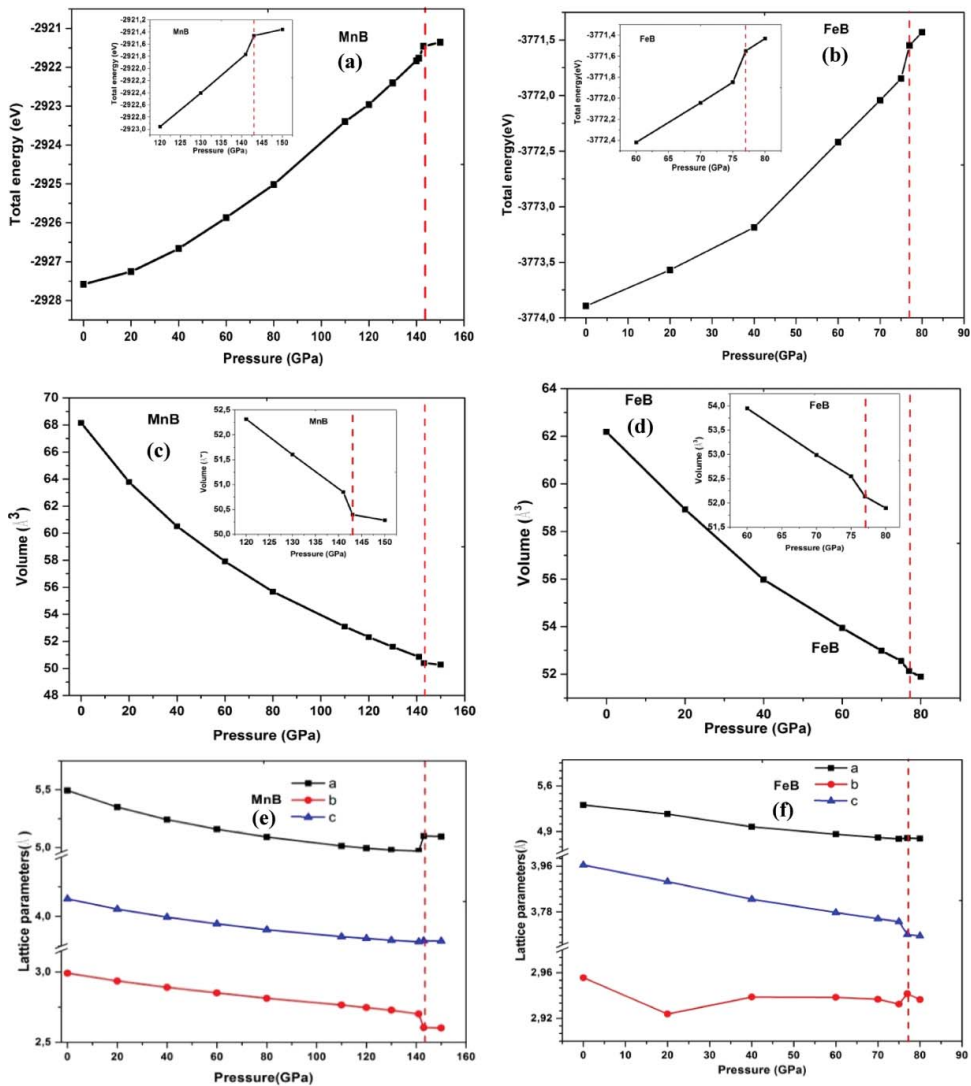


Figure 3. Pressure dependence of total energy for (a) MnB; (b) FeB, volume for (c) MnB; (d) FeB and lattice parameters for (e) MnB; (f) FeB. Dashed line represents the critical pressures.

4. Elastic properties under pressure

It is well known that elastic properties can reflect interatomic interactions and are related to some fundamental physical properties, such as thermal expansion, phonon spectra and equations of state [27,28]. The elastic constants of single orthorhombic crystalline TMB compounds are presented in Table 3. Generally, the elastic constants C_{11} , C_{22} and C_{33} are very high, both at zero and critical pressure, which indicates the high resistance to the axial compression in these directions. Moreover, it is shown in Table 3 that the elastic constants C_{11} , C_{22} and C_{33} are larger than C_{44} , C_{55} and C_{66} , indicating that TMB are mechanically anisotropic and the shear deformation is easier to take place than other deformation forms. It is well known that the elastic constant C_{44} is the most significant parameter which indirectly determining the indentation hardness of a solid [29]. A large C_{44} implies a strong resistance to monoclinic shear in the (100) plane. The highest C_{44} for FeB than those for the other compounds means that its ability to resist shear distortion in the (100) plane is the strongest.

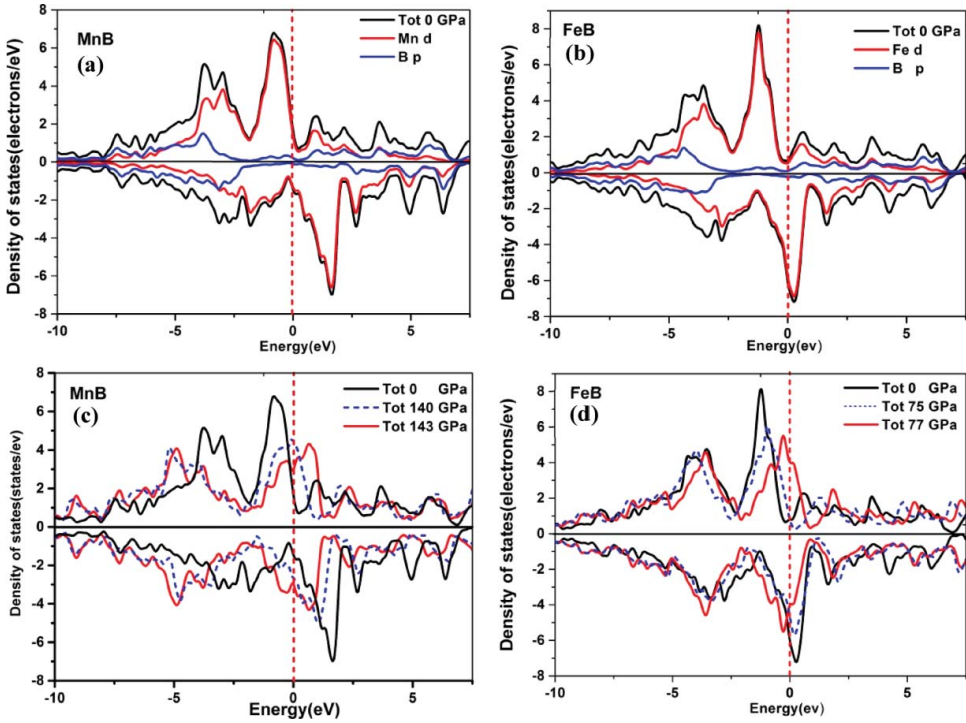


Figure 4. The calculated total and partial DOS at 0 GPa for (a) MnB; (b) FeB and at a critical pressure for (c) MnB; (d) FeB. Dashed line represents the Fermi level.

The results in Table 3 indicate that TMB have relatively strong anisotropic elastic constants resulting in the directional dependence of the moduli. Notably, the values of C_{11} (C_{66}) are relatively smaller than that of C_{33} (C_{44}) at 0 GPa and under pressure, implying that the intra-layer chemical bonds are weaker than those between the layers. Moreover, as shown in Figure 5, there are two changes of elastic constants: one appears between 0 GPa and just before a critical pressure, with linear increase with the increase of pressure, and the other one is the jump near a critical pressure; these are C_{11} (C_{66}), C_{22} (C_{55}) and C_{33} (C_{44}) for MnB and somewhat little bit for FeB. The increase (decrease) of the elastic constants for both compounds is linked directly to abrupt changes of lattice parameters a , b and c .

The calculated percentage change in lattice parameters a , b and c between FM and NM cases are 7.1%, 12.96% and 8.4% for MnB, while for FeB are 9.6%, 0.3% and 6.8%, which mean that the easy axis of magnetization for MnB is the direction $\langle 010 \rangle$, and the hard axes are the direction $\langle 100 \rangle$,

Table 3. The calculated full set elastic constants of TMB (under 0 and critical pressure, in GPa) along with other available values.

Species	Elastic constants								
	C_{11}	C_{22}	C_{33}	C_{12}	C_{13}	C_{23}	C_{44}	C_{55}	C_{66}
MnB (0 GPa)	392.05	510.74	497.17	181.33	154.92	148.61	212.11	167.69	211.28
	414.4 ^a	527.7 ^a	504.8 ^a	171.1 ^a	147.5 ^a	127.7 ^a	215.8 ^a	218.4 ^a	175.8 ^a
MnB (143 GPa)	1035	905	1300	745.2	667	560.76	442	203	561.21
FeB (0 GPa)	389.82	438.36	557.07	286.85	183.12	239.76	218.8	132.25	212.01
	373.7 ^b	434.1 ^b	503.4 ^b	246 ^b	184.4 ^b	209.1 ^b	207.4 ^b	117.7 ^b	193.7 ^b
FeB (77 GPa)	718.5	752.6	993.9	583.2	350.1	492.4	296.4	243.3	354.4

^aRef. [21].

^bRef. [30].

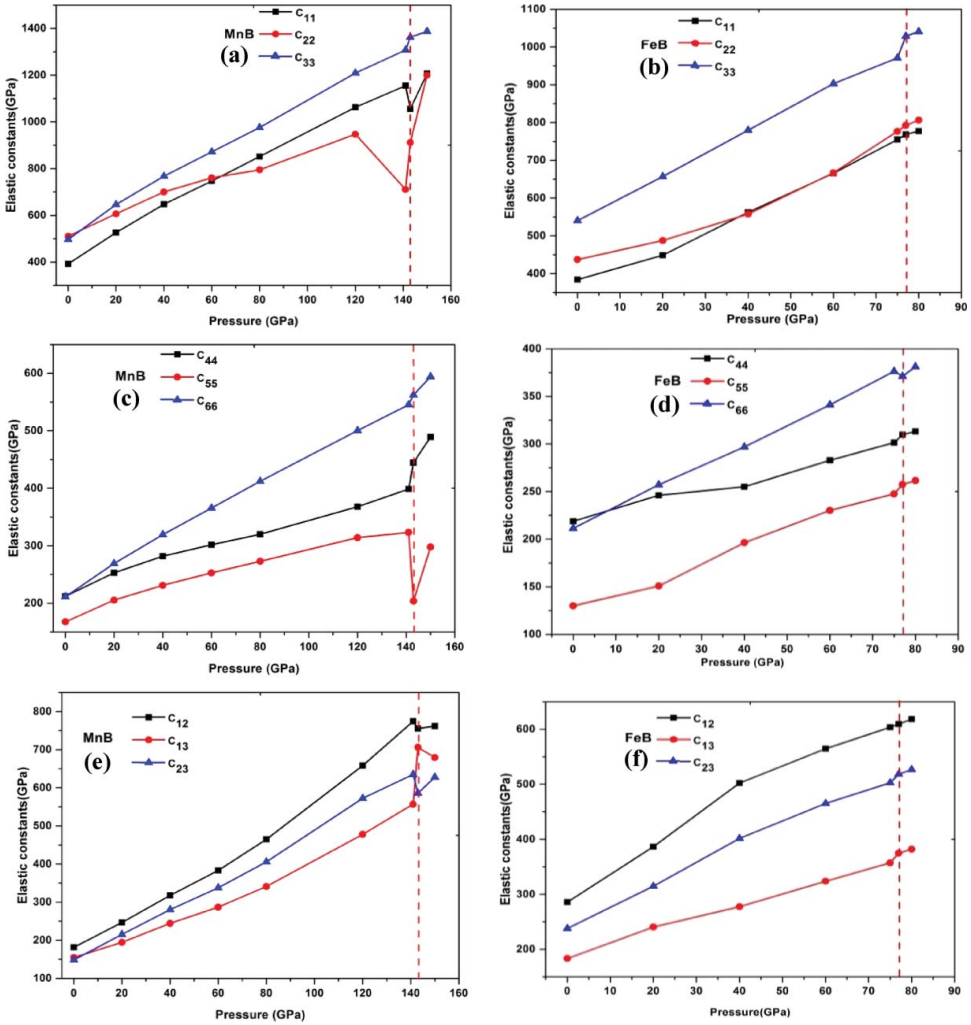


Figure 5. Pressure dependence of elastic constants: C_{11} , C_{22} and C_{33} for (a) MnB; (b) FeB, C_{44} , C_{55} and C_{66} for (c) MnB; (d) FeB and C_{12} , C_{13} and C_{23} for (e) MnB; (f) FeB. Dashed line represents the critical pressures.

(001), which is agreed with J. Park et al. [31]. However, the easy axis of magnetization for FeB is the direction $\langle 100 \rangle$, and the hard axes are the direction $\langle 010 \rangle$, $\langle 001 \rangle$, by what we know that for bcc Fe the highest density of atoms is in the $\langle 111 \rangle$ direction, and thus, $\langle 111 \rangle$ is the hard axis. In contrast, the atom density is lower in $\langle 100 \rangle$ directions and therefore $\langle 100 \rangle$ is the easy axis. Of course, since bcc iron is a cubic crystal, all six cube edge orientations $\langle 100 \rangle$, $\langle 010 \rangle$, $\langle 001 \rangle$, $\langle \bar{1}00 \rangle$, $\langle 0\bar{1}0 \rangle$ and $\langle 00\bar{1} \rangle$ are, in fact, equivalent easy axes [32]. The other compression moduli (C_{12} , C_{13} and C_{23}) are significantly different; they correspond to the intra and inter-layer moduli under bi-axial stress conditions.

The mechanical stability criteria can be represented in a uniform manner for orthorhombic structure [33]:

$$\begin{aligned}
 & C_{ii} > 0 (i = 1; 2; 3; 4; 5; 6) \\
 & C_{11} + C_{22} + C_{33} + (C_{12} + C_{13} + C_{23}) > 0, (C_{11} + C_{22} - 2C_{12}) > 0; (C_{11} + C_{33} - C_{13}) > 0 \\
 & (C_{22} + C_{33} - 2C_{23}) > 0
 \end{aligned} \quad (3)$$

On the other hand, the mechanical stability leads to restrictions on the elastic coefficients under isotropic pressure as follows:

$$\begin{aligned} \tilde{C}_{ii} = C_{ii} - P > 0, (i = 1, 2, 3, 4, 5, 6), (C_{11} + C_{22} - 2C_{12} - 4P) > 0, (C_{11} + C_{33} - 2C_{13} - 4P) > 0, \\ (C_{22} + C_{33} - 2C_{23} - 4P) > 0, (C_{11} + C_{22} + C_{33} + 2C_{12} + 2C_{13} + 2C_{23} + 3P) > 0 \end{aligned} \quad (4)$$

where C_{ij} are the elements of the elastic coefficient matrix.

In order to show the dependence of pressure at 0 GPa (FM) and at a critical pressure (NM), I have plotted the elastic constants (Figure 6) at the two pressures.

We can see that all elastic constants have an obvious increase at a critical pressure.

The arithmetic average of the Voigt and Reuss bounds is known as the Voigt–Reuss–Hill average, which is regarded as the best estimate of the theoretical value of the polycrystalline elastic modulus [34]:

$$G_H = (G_R + G_V) / 2, B_H = (B_R B_V) / 2 \quad (5)$$

The Young modulus and Poisson ratio can be computed from the formula [34]:

$$E = 9BG / (3B + G), \nu = (3B - 2G) / (6B + 2G) \quad (6)$$

Poisson's ratio ν ; characterizes the stability of the crystal against the shearing strain. For a typical metal, the value is supposed to be 0.33; for the ionic-covalent crystal, the value is situated between 0.2 and 0.3; the strong covalent crystal has even smaller Poisson's ratio, which is usually below 0.15 [35]; the calculated Poisson's ratio (0.23 and 0.32) indicates the mixture bonds in this crystal structure. It is also noted that the studied Poisson's ratios of MnB compound are smaller than other compounds.

A larger B/G value (>1.75) for a solid indicates the ductile behavior while a smaller B/G value (<1.75) usually means brittle material. Similarly, Poisson ratio $\nu > 0.26$ corresponded for ductile compounds usually [36]. At both pressures, 0 GPa and the critical pressure, FeB is ductile ($B/G > 1.75$ and $\nu > 0.26$), while MnB is brittle ($B/G < 1.75$ and $\nu < 0.26$).

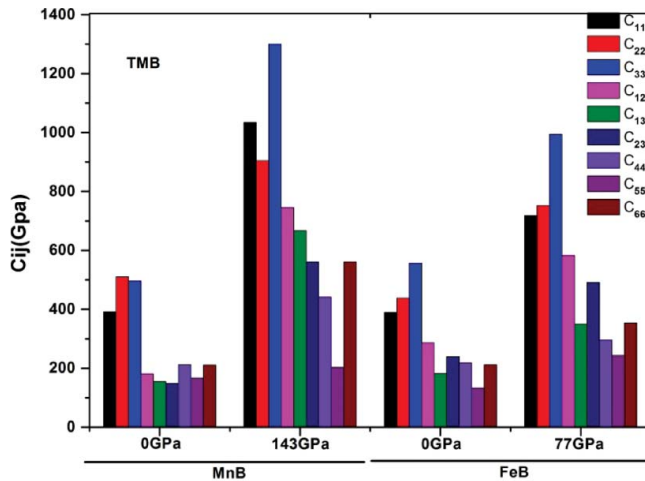


Figure 6. Pressure dependence on the elastic constants.

5. Elastic anisotropy

It is known that elastic anisotropy correlates with anisotropic plastic deformation and behavior of micro-cracks in the material. Hence, it is important to study the elastic anisotropy in intermetallic structures in order to further understand these properties and improve their mechanical durability. Most of the crystals exhibit elastic anisotropies, to some extent, and several criteria have been developed to describe it. The elastic anisotropy of a crystal can be characterized by the universal anisotropic index A^U and by the indexes describing the behavior in shear and compression (A_G and A_B). The universal elastic anisotropy index A^U and indexes A_G and A_B for a crystal with any symmetry may be proposed as follows [37,38]:

$$A^U = 5 \frac{G_V}{G_R} + \frac{B_V}{B_R} - 6 \geq 0 \quad (7)$$

$$A_G = \frac{G_V - G_R}{G_V + G_R} 100, \quad A_B = \frac{B_V - B_R}{B_V + B_R} 100 \quad (8)$$

where B_V (G_V) and B_R (G_R) are the bulk modulus (shear modulus) in terms of the Voigt and the Reuss approximations, respectively. $A^U = 0$ corresponds to the isotropy of the crystal. The deviation of A^U from zero defines the extent of single crystal anisotropy and accounts for both the shear and the bulk contributions, unlike all other existing anisotropy measures. Thus, A^U represents a universal measure to quantify the single crystal elastic anisotropy. $A_B = A_G = 0$ represents the elastic isotropic, while $A_B = A_G = 1$ means the maximum elastic anisotropy [39].

For an isotropic crystal, all three factors must be 1, while any value smaller or greater than 1 is a measure of the degree of elastic anisotropy possessed by the crystal.

The shear anisotropic factor for an orthorhombic crystal can be measured by three factors (Zener ratios):

- (1) The anisotropic factor for the $\{1\ 0\ 0\}$ shear planes between (011) and (010) directions is defined as

$$A_1 = \frac{4C_{44}}{C_{11} + C_{33} - 2C_{13}} \quad (9)$$

- (2) The anisotropic factor for the $\{0\ 1\ 0\}$ shear planes between (101) and (001) directions is

$$A_2 = \frac{4C_{55}}{C_{22} + C_{33} - 2C_{23}} \quad (10)$$

and

- (3) The anisotropic factor for the $\{0\ 0\ 1\}$ shear planes between (110) and (010) directions is

$$A_3 = \frac{4C_{66}}{C_{11} + C_{22} - 2C_{12}} \quad (11)$$

The calculated values of anisotropic factors for mono-borides TMB at 0 GPa and at the critical pressures are shown in Table 4. By a first principles study the pressure effect, between 0 GPa and a critical pressure has reduced the anisotropic factors A_1 and A_3 by 17% and 68.6% for MnB, while for FeB has reduced anisotropic factors A_2 by 18.7% and A_3 by 27.3%. For the universal anisotropic index, A^U is augmented when pressure is applied by 89.2% for MnB and 30% for FeB.

The simplest way to illustrate the anisotropy of mechanical moduli is to plot them in the 3D space as a function of direction.

Table 4. Polycrystalline elastic properties and anisotropic factors of TM-B system (under 0 and critical pressure, in GPa).

Species	B_V	B_R	G_V	G_R	A_1	A_2	A_3	A_u	A_G	A_B
MnB (0 GPa)	263.3	260.5	179.2	172.5	1.464	0.944	1.565	0.21	1.93	0.53
MnB (143 GPa)	824.8	801.0	327.7	236.6	1.766	0.749	4.993	1.95	16.14	1.47
FeB (0 GPa)	308.3	302.8	155.6	125.5	1.57	1.04	3.38	1.22	10.74	0.91
FeB (77 GPa)	287.8 ^a	284.6 ^a	148.5 ^a	130.9 ^a	1.63 ^a	0.91 ^a	2.45 ^a	0.68 ^a	5.85 ^a	0.62 ^a
FeB (77 GPa)	621.6	612.5	260.17	190.4	1.17	1.28	4.65	1.85	15.49	0.75

^a Ref. [30].

For orthorhombic crystal class, the directional dependence of the Young modulus (E) and bulk modulus (B) can be written as:

For orthorhombic system [40]

$$\frac{1}{B} = (S_{11} + S_{12} + S_{13}) l_1^2 + (S_{12} + S_{22} + S_{23}) l_2^2 + (S_{13} + S_{23} + S_{33}) l_3^2 \quad (12)$$

$$\frac{1}{E} = (S_{11} + S_{22} + S_{33}) l_1^4 + (2S_{12} + S_{66}) l_1^2 l_2^2 + (2S_{23} + S_{44}) l_2^2 l_3^2 + (2S_{13} + S_{55}) l_1^2 l_3^2 \quad (13)$$

In the above-mentioned equations, S_{ij} represents the compliance matrix and l_1 , l_2 and l_3 are the direction cosines, which are given as $l_1 = \sin \theta \cos \varphi$, $l_2 = \sin \theta \sin \varphi$ and $l_3 = \cos \varphi$ in the spherical coordinates.

From Equations (13) and (14) the 3D surface representations showing the variation of the Young, and bulk moduli are plotted in Figure 7. The plane projections ((100), (010) and (001) plans) of the directional dependences of the Young and bulk moduli are given in Figure 8 for comparisons. The surface constructions of Young moduli and bulk modulus are, respectively similar to each other. It can be clearly seen that TM-B exhibits a pronounced with the non-spherical nature (Figures 7 and 8). Thus, $A_u = 0.21(A_u = 1.95)$ and $A_u = 1.22(A_u = 1.85)$ at 0 GPa and at a critical pressure for both MnB and FeB, respectively (see Table 4). The variation of Young's modulus E in all planes and directions shows that these compounds possess a minimum of E [100] direction and a maximum of E [001] direction. Both MnB/FeB exhibit a minimum of $E_{[100]} = 304.68/195.45$ GPa, a maximum of $E_{[001]} = 422.08/407.06$ GPa and for $E_{[010]} = 413.30/201.81$ GPa. Therefore, the ordering of Young's modulus as a function of the principal crystal tensile [u v w] for TM-B is $E_{[100]} < E_{[010]} < E_{[001]}$. Additionally, it is remarkable to note that the variation of bulk modulus with B min along [100] directions and B max along [010] directions for the compounds MnB and FeB which is consistent with the predicted elastic constants along different axes (see Table 3).

6. Anisotropy of acoustic velocities

The phase velocities of pure transverse and longitudinal modes of the TM-B compounds can be calculated from the single crystal elastic constants following the procedure of Brugger [41]. The sound velocities are determined by the symmetry of the crystal and propagation direction. For example, the pure transverse and longitudinal modes can only be found in [001], [110] and [111] directions in a cubic crystal and the sound propagating modes in other directions are the quasi-transverse or quasi-longitudinal waves. In the principal directions, the acoustic velocities for orthorhombic system can be expressed by

$$\begin{aligned} [100] v_l &= \sqrt{C_{11}/\rho}; & [010] v_{t1} &= \sqrt{C_{66}/\rho}; & [001] v_{t2} &= \sqrt{C_{55}/\rho} \\ [010] v_l &= \sqrt{C_{22}/\rho}; & [100] v_{t1} &= \sqrt{C_{66}/\rho}, & [001] v_{t2} &= \sqrt{C_{44}/\rho} \\ [001] v_l &= \sqrt{C_{33}/\rho}; & [100] v_{t1} &= \sqrt{C_{55}/\rho}, & [010] v_{t2} &= \sqrt{C_{44}/\rho} \end{aligned} \quad (14)$$

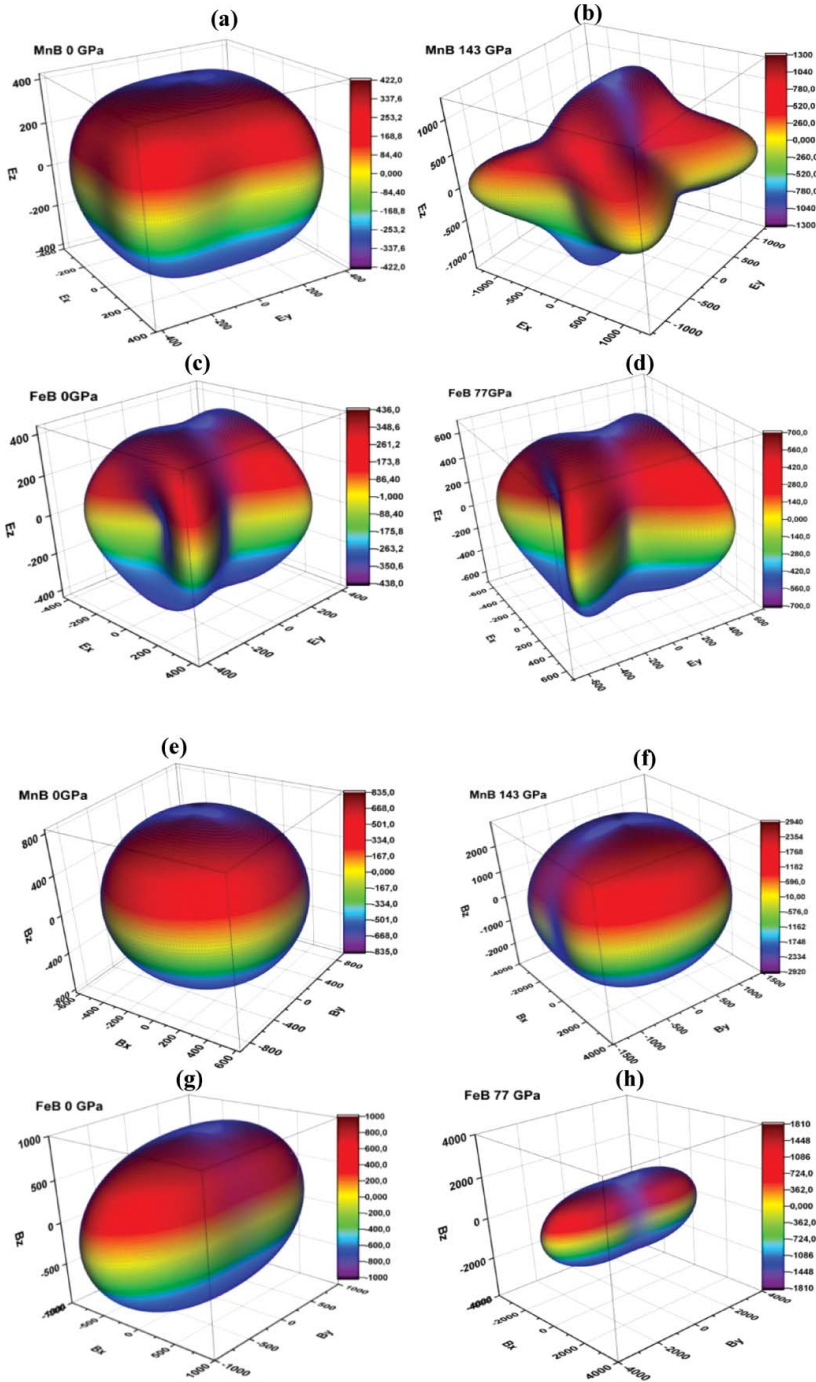


Figure 7. Illustration of directional dependent Young moduli: (a) MnB; (c) FeB at 0 GPa, and (b) MnB; (d) FeB at a critical pressure. Bulk moduli: (e) MnB; (g) FeB at 0 GPa, and (f) MnB; (h) FeB at a critical pressure.

where ρ is the density of TMB compounds; v_l is the longitudinal sound velocity; v_{t1} and v_{t2} refer the first transverse mode and the second transverse mode, respectively. The calculated densities, sound velocities and Debye temperatures at 0 GPa and critical pressure for TMB compounds are shown in Table 6. It is obvious that MnB has large sound velocities, because their density is lesser than FeB.

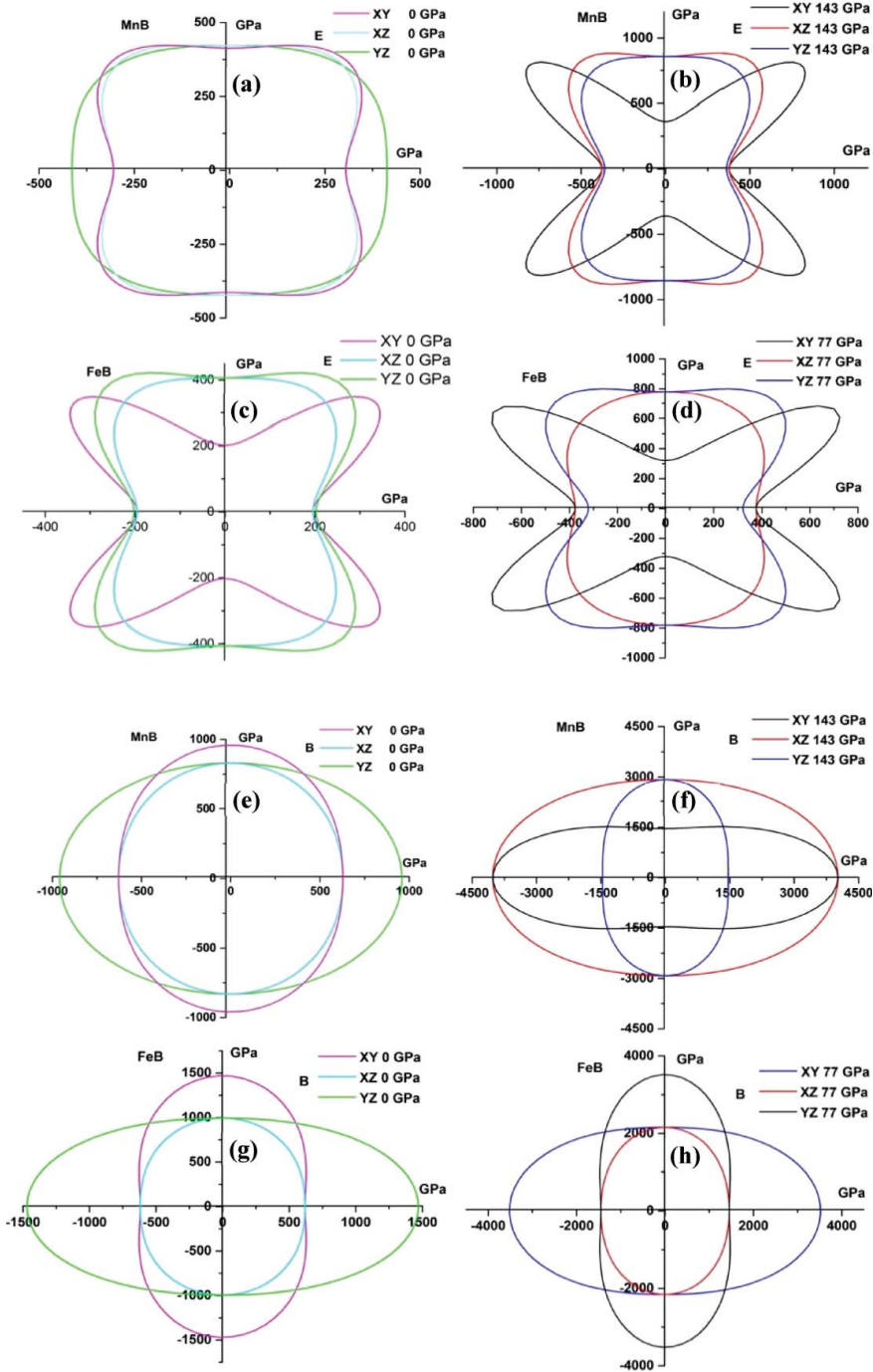


Figure 8. The projection of Young moduli at several different crystal planes (a) MnB; (c) FeB at 0 GPa and (b) MnB; (d) FeB at a critical pressure. Bulk moduli at 0 GPa for (e) MnB; (g) FeB and at a critical pressure for (f) MnB; (h) FeB.

The anisotropic properties of sound velocities indicate the elastic anisotropy in these crystals. For example, the C_{11} , C_{22} and C_{33} determine the longitudinal sound velocities along [100], [010] and [001] directions, respectively; the C_{44} , C_{55} and C_{66} correspond to the transverse modes [42].

Table 5. The calculated bulk, Young (E) and shear modulus (G) of TMB (under 0 and a critical pressure, in GPa), Poisson's ratio (ν) and B/G ratio and the calculated relative change of these parameters along with other available values.

Species	B	E	G	ν	B/G	$\Delta B/B$	$\Delta E/E$	$\Delta G/G$	$\Delta \nu/\nu$	$\Delta (B/G)/(B/G)$
MnB (0 GPa)	261.90	431.04	175.84	0.23	1.49	67.8	43.2	37.7	32.4	48.3
	259.1 ^a	450.2 ^a	186 ^a	0.21 ^a	1.49 ^a					
MnB (143 GPa)	812.95	758.70	282.16	0.34	2.88					
FeB (0 GPa)	305.6	365.7	140.6	0.30	2.174	50.5	35.6	37.6	11.8	21.2
	286.6 ^b	360.5 ^b	139.7 ^b	0.29 ^b	2.05 ^b					
FeB (77 GPa)	617.1	567.5	225.3	0.34	2.76					

^aRef. [21].^bRef. [30].

As a fundamental parameter for the materials' thermodynamic properties, Debye temperature Θ_D is related to specific heat, thermal expansion and elastic constants. The Debye temperature can be estimated from the average sound velocity by the following equation based on elastic constant evaluations [43]:

$$\Theta_D = \frac{h}{k} \left(\frac{3nN_A}{4\pi M} \right)^{1/3}$$

$$v_m = \left[\frac{1}{3} \left(\frac{1}{v_t^3} + \frac{1}{v_l^3} \right) \right]^{-\frac{1}{3}} \quad (15)$$

$$v_t = \sqrt{\frac{G}{\rho}}, \quad v_l = \sqrt{\frac{B + \frac{4G}{3}}{\rho}}$$

where B and G are isothermal bulk modulus and shear modulus, respectively; v_l is the longitudinal velocity and v_t is the transverse sound velocity. The elastic wave velocities of these compounds are relatively large, because these compounds have large mechanical moduli and large densities. For Debye temperatures, the largest Θ_D is 671 K for MnB while the lowest one is 592.8 K for FeB and the order of Θ_D for TMB compounds is MnB > FeB. It is well known that the Θ_D is the inverse to molecular weight and can be used to characterize the strength of covalent bonds in the solids. From Tables 6, I can conclude that the covalent bonds in MnB are stronger than the other borides.

In order to show the dependence of pressure at 0 GPa (FM) and at a critical pressure (NM), I have calculated the relative change of all parameters between the magnetic and non-magnetic states (Tables 5 and 6), they are obtained as

$$\frac{\Delta X}{X} = \frac{X_{FM} - X_{NM}}{X_{FM}}, \quad X = V, E_{coh}, E_f, B, E, G, \nu \text{ and } \Theta_D \dots \quad (16)$$

where $V, E_{coh}, E_f, B, E, G, \nu, \Theta$ are: the volume; cohesive energy; formation energy; bulk modulus, Young modulus, shear modulus, Poisson ratio's and the Debye temperature, respectively.

Table 6. The density (in g/cm^3), anisotropic sound velocities (in m/s), average sound velocity (in m/s), Debye temperature (in K) and the calculated relative change of these parameters for the TMB compounds.

Species	ρ	vl	vt	vm	Θ_D	$\Delta \rho/\rho$	$\Delta vl/vl$	$\Delta vt/vt$	$\Delta vm/vm$	$\Delta \Theta_D/\Theta_D$
MnB (0 GPa)	6.41	8799.7	5237.57	5798.5	671	26	25	8.24	9.6	18.23
MnB (143 GPa)	8.66	11,718.2	5708.1	6412.8	820.6					
FeB (0 GPa)	7.085	8342.2	4454.7	4976.2	592.8	19.3	18.4	12.06	12.47	18.5
FeB (77 GPa)	8.78	10,222.5	5065.6	5685.7	727.7					

^aRef. [44].

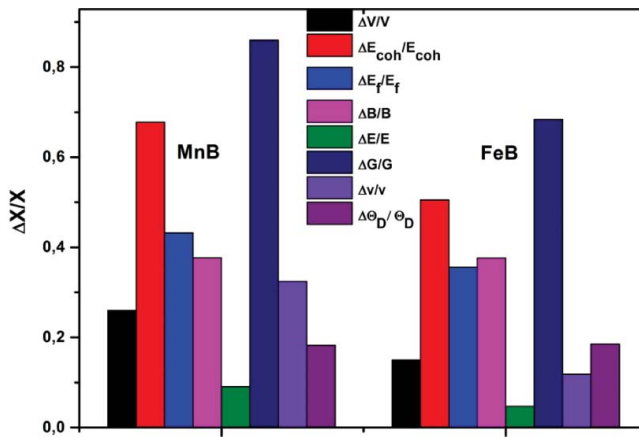


Figure 9. The calculated relative change of parameters by the top: volume cohesive and formation energy, bulk, Young and shear moduli, Poisson's ratio and Debye temperature.

The calculated percentage change of volume at 0 GPa and at a critical pressure of ferromagnetic compounds show a volume compression by 26% and 15% for MnB and FeB, respectively, in applied pressure, which increase the bulk modulus of these compounds by 67.8% and 50.5%

(Table 5). The formation energy E_f was calculated to check the probability of thermodynamic existence of TMB under pressure. All formation energies are negative, indicating that structures in two pressure conditions are thermodynamically stable (see Figure 9). The formation energy of TMB in the magnetic state is less than TMB in NM case by 85.94% and 68.35% for both MnB and FeB, respectively, implying that they have more thermodynamic stability in FM case.


7. Conclusions

The phase stability, magnetic moment, elastic moduli, elastic anisotropy properties and Debye temperatures of the TMB (TM = Mn, Fe) compounds as a function of pressure are investigated and discussed from the first-principles calculations. The equilibrium structure and formation energy show that MnB and FeB are energetically more stable at 0 GPa than at each critical pressure. Both MnB and FeB have a magnetic transition when the pressure is about 143 and 77 GPa, respectively. The elastic constants, bulk, shear, Young's modulus, acoustic velocities and Debye temperature for MnB and FeB compounds increase under pressure. The calculated ground state parameters are in good agreement with the other available theoretical data and experiment's values. The increasing B/G and ν of these compounds indicate that MnB is ductile phases under high pressures. The TMB compounds show a certain degree of mechanical anisotropy. The Debye temperatures increase with increasing pressure, and MnB has a higher Debye temperature in two pressures 0 GPa and at a critical pressure. The calculated sound velocities along [100], [010] and [001] directions for TMB under high pressure also imply the anisotropic. I believe that my findings will serve as guidance for experimental investigations.

Disclosure statement

No potential conflict of interest was reported by the author.

ORCID

A. Gueddouh  <http://orcid.org/0000-0001-6747-5770>

References

- [1] Keddad M, Chentouf SM. A diffusion model for describing the bilayer growth (FeB/Fe₂B) during the iron powder-pack boriding. *Appl Surf Sci.* **2005**;252:393–399.
- [2] Stewart K. Boronizing protects metals against wear. *Adv Mater Process.* **1997**;151:23–25.
- [3] Kartal G, Kahvecioglu O, Timur S. Investigating the morphology and corrosion behavior of electrochemically borided steel. *Surf Coat Technol.* **2006**;200:3590–3593.
- [4] Pasternak M, Taylor R, Jeanloz R, et al. High pressure collapse of magnetism in Fe_{0.94}O: mössbauer spectroscopy beyond 100 GPa. *Phys Rev Lett.* **1997**;79:5046.
- [5] Duman E, Acet M, Wassermann E, et al. Magnetic instabilities in Fe₃C vementite particles observed with Fe K-edge X-ray circular dichroism under pressure. *Phys Rev Lett.* **2005**;94:075502.
- [6] Troyan I, Gavriluk A, Sarkisyan V, et al. Transition from the antiferromagnetic to a nonmagnetic state in FeBO₃ under high pressure. *J Exp Theor Phys Lett.* **2001**;74:24–27.
- [7] Zhang W, Zhang W. Prediction of magnetic moment collapse in ZrFe₂ under hydrostatic pressure. *J Appl Phys.* **2015**;117:163917.
- [8] Bourourou Y, Beldi L, Bentria B, et al. Structure and magnetic properties of the 3d transition-metal mono-borides TM–B (TM= Mn, Fe, Co) under pressures. *J Magn Magn Mater.* **2014**;365:23–30.
- [9] Kohn W. Nobel lecture: electronic structure of matter—wave functions and density functionals. *Rev Mod Phys.* **1999**;71:1253.
- [10] Segall M, Lindan PJ, Probert M., et al. First-principles simulation: ideas, illustrations and the CASTEP code. *J Phys.* **2002**;14:2717–2744.
- [11] Medeiros S, Albuquerque E, Maia F, et al. First-principles calculations of structural, electronic, and optical absorption properties of CaCO₃ vaterite. *Chem Phys Lett.* **2007**;435:59–64.
- [12] Xu Y, Wang H. Oxidation behavior of γ /Mo₂Ni₃Si ternary metal silicide alloy. *J Alloys Compd.* **2008**;457:239–243.
- [13] Wang Y, Burke K, PERDEW J. Generalized gradient approximation for the exchange-correlation hole of a many-electron system. *Phys Rev B.* **1996**;54:16533–16539.
- [14] Monkhorst HJ, Pack JD. Special points for Brillouin-zone integrations. *Phys Rev B.* **1976**;13:5188.
- [15] Murphy KA, Hershkovitz N. Temperature-dependent hyperfine interactions in Fe₂B. *Phys Rev B.* **1973**;7:23.
- [16] Zhou C, Xing J, Xiao B, et al. First principles study on the structural properties and electronic structure of X₂B (X= Cr, Mn, Fe, Co, Ni, Mo and W) compounds. *Comput Mater Sci.* **2009**;44:1056–1064.
- [17] Kanomata T, Ise Y, Kumagai N, et al. Magnetovolume effect of Co₂B. *J Alloys Compd.* **1997**;259:L1–L4.
- [18] Kittel C. *Introduction to solid state physics.* Wiley; **2005**.
- [19] Kasper J, Roberts B. Antiferromagnetic structure of α -manganese and a magnetic structure study of β -manganese. *Phys Rev.* **1956**;101:537.
- [20] Havinga E, Damsma H, Hokkeling P. Compounds and pseudo-binary alloys with the CuAl₂ (C16)-type structure I. Preparation and X-ray results. *J Less Common Met.* **1972**;27:169–186.
- [21] Niu H, Chen X-Q, Ren W, et al. Variable-composition structural optimization and experimental verification of MnB₃ and MnB₄. *Phys Chem Chem Phys.* **2014**;16:15866–15873.
- [22] Mohn P, Schwarz K, Matar S, et al. Calculated electronic and magnetic structure of the nitrides NiFe₃N and PdFe₃N. *Phys Rev B.* **1992**;45:4000.
- [23] Mohn P, Schwarz K, Wagner D. Magnetoelastic anomalies in Fe-Ni invar alloys. *Phys Rev B.* **1991**;43:3318.
- [24] dos Santos AV, Kuhnen C. Electronic structure and magnetic properties of RuFe₃N nitride. *J Solid State Chem.* **2009**;182:3183–3187.
- [25] Müller U. *Symmetry relationships between crystal structures: applications of crystallographic group theory in crystal chemistry.* Oxford: OUP; **2013**.
- [26] Chikazumi S, Graham CD. *Physics of ferromagnetism 2e.* Oxford University Press on Demand; **2009**.
- [27] Wang H, Cao J, Huang X, et al. Pressure dependence of elastic and dynamical properties of zinc-blende ZnS and ZnSe from first principle calculation. *Condensed Matter Physics.* **2012**;15:1–10.
- [28] Yang C, Zhou Z, Li J, et al. Correlation between the band gap, elastic modulus, Raman shift and melting point of CdS, ZnS, and CdSe semiconductors and their size dependency. *Nanoscale.* **2012**;4:1304–1307.
- [29] Gao X, Jiang Y, Zhou R, et al. Stability and elastic properties of Y–C binary compounds investigated by first principles calculations. *J Alloys Compd.* **2014**;587:819–826.
- [30] Li L-H, Wang W-L, Hu L, et al. First-principle calculations of structural, elastic and thermodynamic properties of Fe–B compounds. *Intermetallics.* **2014**;46:211–221.
- [31] Park J, Hong Y-K, Kim H-K, et al. Electronic structures of MnB soft magnet. *AIP Adv.* **2016**;6:055911.
- [32] Lu L, Bansmann J, Meiwes-Broer K. Rotation of the easy-magnetization direction upon the phase transition from thin iron films to islands on W (110). *J Phys.* **1998**;10:2873–2880.
- [33] Beckstein O, Klepeis J, Hart G, et al. First-principles elastic constants and electronic structure of α -Pt₂Si and PtSi. *Phys Rev B.* **2001**;63:134112.

- [34] Gueddouh A, Bentrria B, Lefkaier I. First-principle investigations of structure, elastic and bond hardness of Fe_xB ($x= 1, 2, 3$) under pressure. *J Magn Magn Mater.* [2016](#);406:192–199.
- [35] Ding Y, Chen M, Wu W. Stability and mechanical properties of $\text{C}_2\text{N}_2\text{X}$ ($\text{X}=\text{O}, \text{NH}$ and CH_2) from first-principles calculations. *Phys B.* [2013](#);428:97–105.
- [36] Lewandowski J, Wang W, Greer A. Intrinsic plasticity or brittleness of metallic glasses. *Philos Mag Lett.* [2005](#);85:77–87.
- [37] Liu Y, Hu W-C, Li D-J, et al. Mechanical, electronic and thermodynamic properties of C14-type AMg_2 ($\text{A}=\text{Ca}, \text{Sr}$ and Ba) compounds from first principles calculations. *Comput Mater Sci.* [2015](#);97:75–85.
- [38] Ali K, Arya A, Ghosh P, et al. A first principles study of cohesive, elastic and electronic properties of binary Fe–Zr intermetallics. *Comput Mater Sci.* [2016](#);112:52–66.
- [39] Ozisik H, Colakoglu K, Deligoz E. First-principles study of structural and mechanical properties of AgB_2 and AuB_2 compounds under pressure. *Comput Mater Sci.* [2012](#);51:83–90.
- [40] Duan Y, Sun Y, Peng M, et al. Anisotropic elastic properties of the Ca–Pb compounds. *J Alloys Compd.* [2014](#);595:14–21.
- [41] Brugger K. Determination of third–order elastic coefficients in crystals. *J Appl Phys.* [1965](#);36:768–773.
- [42] Sun L, Gao Y, Xiao B, et al. Anisotropic elastic and thermal properties of titanium borides by first-principles calculations. *J Alloys Compd.* [2013](#);579:457–467.
- [43] Music D, Houben A, Dronskowski R, et al. Ab initio study of ductility in M_2AlC ($\text{M}=\text{Ti}, \text{V}, \text{Cr}$). *Phys Rev B.* [2007](#);75:174102.
- [44] Xiao B, Feng J, Zhou C, et al. The elasticity, bond hardness and thermodynamic properties of X_2B ($\text{X}=\text{Cr}, \text{Mn}, \text{Fe}, \text{Co}, \text{Ni}, \text{Mo}, \text{W}$) investigated by DFT theory. *Phys B.* [2010](#);405:1274–1278.

ملخص

هدف أطروحة الدكتوراه هذه هو الحساب الأساسي للخصائص الهيكلية، الإلكترونية، المغناطيسية، الصلابة ومرونة التباين لبعض المركبات من أحادي البورون (TMB (TM= Mn, Fe, Co, Ni) وشبه البورون: TM_2B (TM= Fe, Co, Ni). أجري الحساب في إطار نظرية الكثافة الدالية بإستعمال طريقة أشباه الكمونات (PP) مع تقريب التدرج المعمم (GGA)، المثبت في البرنامج CASTEP. الإنتقالية الكمية لا يمكن الوصول إليها إلا عن طريق التغيير في أحد الوسائط الفيزيائية، مثل الحقل المغناطيسي أو الضغط عند درجة الحرارة الصفر المطلق. الدراسة تحت الضغط لهذه المركبات و التي تحتوي على معادن مغناطيسية بينت عند قيم ضغط معينة على إنبهار مفاجئ للعزم المغناطيسي (إنتقال كمي من الدرجة الأولى) وهذه الصفة هي عادة علامة على موصل فائق للكهرباء. النتائج المتحصل عليها تمت مقارنتها مع البيانات التجريبية، وهي على إتفاق جيد مع النتائج في الحالة الأساسية. للحصول على وصف جيد للسلوك الميكانيكي للمركبات دون /تحت تأثير الضغط، فقد قمنا بحساب الثوابت المرنة C_{ij} و من خلالها دراسة خواص تباين المرونة للمركبات المدروسة، وتحقق استقرارها الميكانيكي، وتم تحديد سرعات الموجة الصوتية في الاتجاهات الرئيسية C_{ij} واستنادا إلى تقريب فويه-روس وهيل، اكتشفنا الخصائص المرورية للمركبات المدروسة لمتعدد البلورات وحدات الوسائط الفيزيائية المرورية، معامل القص G، معامل يونغ E وبواسون ν) حيث تم رسم مخططات السطوح (3D) ومخطط المستو (2D) لمعامل الانضغاط و معامل يونغ متعددة المستويات، للكشف عن تباين الخصائص المرورية.

الكلمات المفاتيح: نظرية الكثافة الدالية، أشباه الكمونات، أحادي البورون وشبه البورون، الإنتقالية الكمية، الإنهيار المفاجئ للعزم المغناطيسي، الخصائص المرورية.

Résumé:

Le but de cette thèse de doctorat est le calcul ab initio des propriétés : structurales, électroniques, magnétiques, dureté, et anisotropie élastique de quelque mono borure: TMB (TM= Mn, Fe, Co, Ni) et semi borure: TM_2B (TM= Fe, Co, Ni). Le calcul a été mené dans le cadre général de la théorie de la fonctionnelle de la densité (DFT) moyennant la méthode pseudo potentiels (PP) avec l'approximation du gradient généralisé de Perdew-Burke-Ernzerhof (GGA-PBE), qui est

implanter dans le code de calcul CASTEP. Les transitions de phase quantique ne sont accessibles que par la variation d'un paramètre physique, tel que le champ magnétique ou une pression à la température de zéro absolu. L'étude, sous l'effet de la pression de ces borures qui contiennent des métaux de transition ferromagnétiques montre à une certaine pression une avalanche brusque prononcée du moment magnétique (phase de transition quantique du premier ordre) ce caractère est généralement un signe d'un supraconducteur. Les résultats obtenus ont été commentés et comparés avec les données expérimentales disponibles. Un très bon accord a été trouvé entre les résultats calculés à l'état fondamental et ceux issus de l'expérimentale. Pour une bonne description du comportement mécanique des matériaux considérés sans/sous l'effet de la pression, nous avons calculé d'abord leurs constantes élastiques en état monocristallin, i.e., les constantes élastiques anisotropes C_{ij} . Les valeurs numériques obtenues pour les C_{ij} ont été ensuite employées pour quantifier l'anisotropie élastique des systèmes étudiés, vérifier leur stabilité mécanique et ainsi pour déterminer les vitesses d'ondes acoustiques suivant les directions principales. En utilisant toujours les valeurs des C_{ij} et en se basant sur l'approximation de Voigt-Reuss-Hill, nous avons exploré les propriétés élastiques des composés étudiés en état polycristallin : les modules d'élasticité isotropes (module de compressibilité B , module de cisaillement G , module de Young E et rapport de Poisson ν), Nous avons tracé les surfaces (3D) et les contours planes des modules (E et B à plusieurs plans cristallographiques, pour révéler leur anisotropie élastique.

Mots clés: DFT, Pseudo potentiels, Mono et Semi borures, Transitions de phase quantique, Effondrement brusque du moment magnétique, propriétés élastiques.

Abstract:

The aim of this thesis is the ab initio calculation of the properties: structural, electronic, magnetic, hardness and elastic anisotropy of a single boride: TMB (TM = Mn, Fe, Co, Ni) and semi boride: TM_2B (TM = Fe, Co, Ni). The calculation is conducted in the framework of the functional theory of density (DFT) through the pseudo potential method (PP) with the generalized gradient approximation of Perdew-Burke Ernzerhof (GGA-PBE), which is implanted in the CASTEP code. The quantum phase transitions are accessible only by the variation of a physical parameter, such as the magnetic field or pressure to the absolute zero temperature. The study, due to the pressure of these borides containing ferromagnetic transition metals shows at a certain pressure an abrupt avalanche of magnetic moment (first order quantum phase transition) this character is generally a sign of a superconductor. The results are discussed and compared with experimental data. A good agreement is found between the results in the fundamental state and those from the experimental. For a comprehensive description of the mechanical behavior of the considered without / with the effect of pressure, I first calculate their elastic constants of single crystal state, i.e., the anisotropic elastic constants C_{ij} . The values obtained for the C_{ij} are used to quantify elastic anisotropy of the systems studied, check their mechanical stability and thus to determine the acoustic wave velocities along the main directions.

Keys words: DFT, Pseudo-potential, Semi and mono borides, quantum phase transition, magnetic moment collapse, Elastic properties.

